Galactic Stellar Haloes in the CDM Model

COOPER, ANDREW,PAUL

COOPER, ANDREW,PAUL (2010) *Galactic Stellar Haloes in the CDM Model*, Durham theses, Durham University. Available at Durham E-Theses Online: http://etheses.dur.ac.uk/656/

Galactic Stellar Haloes in the CDM Model

Andrew Paul Cooper

A thesis submitted to the University of Durham
in accordance with the regulations for
admittance to the Degree of Doctor of Philosophy

Department of Physics

University of Durham
November 2010

Abstract

This thesis studies galactic stellar haloes built up through the tidal disruption of accreted dwarf galaxies. Numerical simulations are used to explore this process in the context of the Cold Dark Matter model of cosmological structure formation. We predict the properties of stellar structures that the next generation of surveys may discover in the Milky Way halo and the haloes of other nearby galaxies.

We present six simulations based on the Aquarius project, a suite of high resolution N-body simulations of individual dark matter haloes in a fully cosmological setting. We tag subsets of particles in these simulations with stellar populations predicted by the GALFORM semi-analytic model of galaxy formation. Our method self-consistently tracks the dynamical evolution and disruption of satellites from high redshift. The luminosity function and structural properties of surviving satellites, which agree well with observations, suggest that this technique is appropriate. We find that accreted stellar haloes are assembled between $1 < z < 7$ from less than 5 significant progenitors. These progenitors are old, metal-rich satellites with stellar masses similar to the brightest Milky Way dwarf spheroidals ($10^7 - 10^8$ $\mathrm{M}_{\odot}$). In contrast to previous stellar halo simulations, we find that several of these major contributors survive as self-bound systems to the present day. Both the number of these significant progenitors and their infall times are inherently stochastic. This results in great diversity among our stellar haloes, which amplifies small differences between the formation histories of their dark halo hosts. The masses ($\sim 10^8 - 10^9$ $\mathrm{M}_{\odot}$) and density/surface-brightness profiles of the stellar haloes (from 10–100 kpc) are consistent with expectations from the Milky Way and M31. Each halo has a complex structure, consisting of well-mixed components, tidal streams, shells and other subcomponents. This structure is not adequately described by smooth models. The central regions (< 10 kpc) of our haloes are highly prolate ($c/a \sim 0.3$), although we find one example of a massive accreted thick disc. Metallicity gradients in our haloes are typically significant only where the halo is built from a small number of satellites. We contrast the ages and metallicities of halo stars with surviving satellites, finding broad agreement with recent observations.

We examine these simulations from the perspective of an observer located at the position of the Sun. We discuss the apparent smoothness of the halo relative to simple 3D star counts derived from photometric tomography. We then describe a simple correlation function statistic that quantifies the amount of spatial and kinematic substructure in the distant stellar halo. We test this statistic with the simulations we have developed, and find that it can distinguish between a range of realistic alternatives for the global structure of the stellar halo. We show that current observational data from pencil beam surveys of ~ 100 tracer stars (such as the Spaghetti Survey) are not sufficient to constrain the degree of structure in the Milky Way halo with this statistic. Larger area surveys with ≥ 1000 tracer stars (such BHB stars in the Sloan Digital Sky Survey) provide much tighter constraints on comparisons between CDM models and the Milky Way.

Finally, we explore the kinematic structure of accreted stellar haloes in the CDM model. We demonstrate that multicomponent haloes like those of the Milky Way and M31 arise naturally through the accretion of stars from tidally disrupted satellite galaxies. Accreted haloes can reproduce the gross properties of the velocity ellipsoid measured in the Solar neighbourhood, although they can be far from dynamical equilibrium and have complex anisotropy profiles. In particular, halo stars do not trace the dark matter velocity distribution up to the escape velocity in the Solar neighbourhood. This suggests that mass estimates of the Milky Way based on related kinematic measurements may deviate significantly from the true mass, if the stellar halo is built largely though accretion.

To my parents.

結盧在人境
而無車馬喧
問君何能爾
心遠地自偏
採菊東籬下
悠然見南山
山氣日夕佳
飛鳥相與還
此還有真意
欲辨已忘言

– 陶渊明

Contents

1 Introduction **1**
1.1 Milky Way-like galaxies in the ΛCDM cosmogony . . . 1
1.1.1 The topic of this thesis . . . 1
1.1.2 The Cold Dark Matter cosmogony . . . 4
1.1.3 The origin of stars and galaxies . . . 9
1.1.4 Dwarf galaxies and the Local Group . . . 12
1.1.5 The fate of disrupted galactic satellites . . . 13
1.2 Simulating the Milky Way . . . 14
1.2.1 N-Body simulations: the Aquarius project . . . 14
1.2.2 Modelling gas physics and star formation . . . 16
1.3 Galactic stellar haloes . . . 20
1.3.1 The Milky Way halo . . . 20
1.3.2 The M31 halo . . . 28
1.3.3 Stellar haloes in distant galaxies . . . 29
1.4 An outline of this thesis . . . 29

2 Spatially resolved stellar populations **31**
2.1 Introduction . . . 31
2.1.1 Previous work . . . 32
2.1.2 The GALFORM Model . . . 34
2.1.3 Reionization and the satellite luminosity function . . . 34
2.1.4 Further details . . . 36
2.2 Building stellar haloes . . . 38
2.2.1 Assigning stars to dark matter . . . 38
2.2.2 Assignment criteria . . . 41
2.2.3 Defining the stellar halo and satellite galaxies . . . 51

3 Galactic Stellar Haloes in the CDM Model **53**
3.1 Results: the Aquarius stellar haloes . . . 53
3.1.1 Visualisation in projection . . . 53
3.1.2 Assembly history of the stellar halo . . . 58
3.1.3 Bulk halo properties and observables . . . 66
3.2 Conclusions . . . 78

4 Observations of Structure in the Milky Way Halo **81**
4.1 Introduction . . . 81
4.2 Starcounts . . . 81
4.2.1 Tracer star catalogues . . . 82
4.2.2 The stellar halo as seen from the Sun . . . 85
4.2.3 The field of streams in Aquarius . . . 88
4.2.4 Fractional RMS . . . 89
4.3 A two-point correlation function for kinematic substructure . . . 91
4.3.1 Previous Work . . . 91
4.4 Metrics for phase-space distance . . . 93
4.5 Observational samples: Spaghetti and SDSS . . . 96
4.6 Spaghetti survey mock catalogues . . . 97
4.7 Application of the Δ metric . . . 100
4.7.1 Distance - velocity scaling . . . 100
4.7.2 Observations of $\xi(<\Delta)$ Spaghetti and SDSS . . . 103
4.7.3 The halo-average signal and pencil-beam surveys . . . 104
4.8 Clustering of SDSS BHB stars . . . 105
4.9 Conclusions . . . 109

5 The bulk kinematics of stellar haloes **113**
5.1 Introduction 113
5.2 Halo models and rescaling 114
5.3 Global kinematic components of the halo 115
5.4 Solar neighbourhood velocity ellipsoid 121
5.5 Velocity dispersion profile 124
5.6 Hypervelocity stars and the local escape velocity 128
5.7 Discussion 132
5.8 Conclusions 134

6 Conclusions **137**
6.1 Summary 137
6.2 Further Work 138
  6.2.1 Quantifying halo structure in the Milky Way and beyond 138
  6.2.2 The contribution of in situ halo stars 141
  6.2.3 Do CDM models produce an acceptable satellite population? 142
  6.2.4 The margins of galaxy formation 144
  6.2.5 The globular cluster connection 145
6.3 Conclusion 146

List of Figures

1.1 The Millennium Simulation (*V. Springel, Virgo Consortium*) 8
1.2 The $M_\star$–M_{halo} relation of Guo et al. (2010b) 11
1.3 The Aquarius Simulation (*V. Springel, Virgo Consortium*) 15
1.4 Simplified illustration of a single halo merger tree 19
1.5 Observed [α/Fe]–[Fe/H] relation for Milky Way disc, halo and satellite stars (*Reproduced from Tolstoy et al. 2009)* 26

2.1 Cumulative V-band luminosity functions (LFs) of satellite galaxies in the Aquarius haloes, adopting the Bower (2006) GALFORM model, $V_{\rm cut} = 30\,{\rm km\,s^{-1}}$ 36
2.2 Mass-metallicity relation for Aquarius satellite galaxies with the Bower (2006) GALFORM model. 39
2.3 Individual satellite surface brightness and velocity dispersion profiles compared to observations of the Carina and Fornax dwarf spheroidals 45
2.4 Relation between magnitude and effective radius for model satellites showing the effects of different choices of most-bound assignment fraction and numerical resolution 47
2.5 Size, velocity dispersion and surface brightness of model satellites compared to observational data 49
2.6 M_{300}–L_V relation for model satellites 50

3.1 Images of the six model haloes, showing V-band surface brightness 55
3.2 As Fig. 3.1, now showing only stars associated with satellites surviving at $z = 0$ 56
3.3 Mass assembly history of the stellar halo 59
3.4 Luminosity functions of surviving satellites in each halo, compared with the luminosity functions of totally disrupted halo progenitors 61
3.5 Redshift of infall and mass contributed, for all satellites contributing significantly to the simulated stellar haloes 62
3.6 Cumulative mass fraction of each stellar halo originating in satellites of stellar mass less than $M_{\rm sat}$. 63
3.7 Number of surviving satellites (aggregated over all six haloes) which have lost a given fraction of their stellar mass through tidal stripping 64
3.8 Spherically averaged halo density profiles 66
3.9 Radially averaged halo surface brightness profiles. 68
3.10 Individual density profiles (multiplied by r^2) for stars contributed by each of the most significant progenitors of the halo 70
3.11 Redshift of host accretion for stars from disrupted and surviving satellites as a function of radial position at $z = 0$ 71
3.12 Radial profiles of luminosity-weighted metallicity 74
3.13 Metallicity distribution functions of bright satellites, faint satellites and stellar haloes 76
3.14 Tails of the cumulative luminosity-weighted metallicity distribution (halo, Solar shell, bright satellites, faint satellites) 77
3.15 Cumulative luminosity-weighted stellar age distributions for halo and satellite stars 78

4.1 Distribution of halo stars as seen from the Solar position in halo Aq-A, for a range of distances from the observer 85
4.2 Distribution of halo stars as seen from the Solar position in five haloes, at distances between 10 and 30 kpc. 87
4.3 Distribution of halo stars as seen from the Solar position in four haloes, at distances between 30 and 50 kpc 87
4.4 Distribution of MSTO stars in the Aquarius 'Field of Streams 89
4.5 Fractional RMS of MSTO counts in simulated haloes, compared to SDSS data . 91
4.6 *4-distance* cumulative correlation function for Spaghetti and SDSS BHB data. . . 95

4.7 Sky distribution of halo RGB stars in simulation Aq-A 98
4.8 Fiducial realisation of a Spaghetti-like survey in halo Aq-A 99
4.9 Correlation functions in space separation (blue) and velocity separation (red) for stars in halo Aq-A, illustrating choice of w_v parameter 101
4.10 Δ metric cumulative correlation function $\xi(<\Delta)$ for mock Spaghetti surveys in halo Aq-A 102
4.11 Δ metric cumulative correlation function for Spaghetti and SDSS data 104
4.12 $\xi(<\Delta)$ for an 'enhanced' Spaghetti-like survey (in halo Aq-A) having 200 pencil beams at high latitude in each Galactic hemisphere 105
4.13 $\xi(<\Delta)$ of 20 Solar-shell observers with a SDSS-like survey, showing effects of the choice of galactic plane and observational errors 108

5.1 Velocity distribution functions in spherical polar coordinates and metallicity distribution functions for individual halo components in regions corresponding to the Solar neighbourhood 116
5.2 As Fig. 5.1, but here showing only halo Aq-A in different radial bins 117
5.3 Velocity distributions in cylindrical coordinates for a halo component resembling a thick disc 119
5.4 Velocity distributions for stars in two randomly chosen Solar neighbourhood volumes 123
5.5 Galactocentric velocity dispersion of accreted halo stars compared to the dark matter and observational data 126
5.6 Velocity anisotropy profiles of accreted halo stars, compared to the dark matter 127
5.7 Distribution of halo star and dark matter particle velocities in the Solar neighbourhood, relative to the escape velocity 130
5.8 Galactocentric radial velocity diagram for particles in haloes Aq-C, Aq-D and Aq-E 131

List of Tables

1.1 Properties of the six Aquarius dark matter halo simulations 16

3.1 Properties of the six simulated haloes 54
3.2 Axial ratios $q = c/a$ and $s = b/a$ of stellar-mass-weighted three-dimensional ellipsoidal fits to halo stars within a galactocentric radius of 10 kpc. 57

5.1 Rescaling factors for each Aquarius halo in Chapter 5 115
5.2 Moments of the velocity distribution of accreted halo stars and dark matter in regions corresponding to the Solar neighbourhood 120
5.3 Observational estimates of the principle axes of the halo velocity ellipsoid in spherical polar coordinates 122

Acknowledgements

Shaun Cole remained calm, insightful and confident, and Carlos Frenk supplied a unique combination of boundless enthusiasm, sagacious advice and erudite humour. I am grateful indeed for their scientific and professional guidance and for their generous support of my travels. I thank Simon White, Amina Helmi, Julio Navarro, Volker Springel, Andrew Benson, Gabriella De Lucia, Adrian Jenkins and Vince Eke for their proofreading and patient advice. I am indebted, as are all at the ICC, to the unstinting technical and moral support provided by Lydia Heck.

Friends and colleagues have been a constant source of strength. I thank LVS, SK and ES in particular for their company and hospitality. Officemates NKM, VGP, BJL, OP and ML suffered my scatterbrained opinions more often than most. I thank John Helly for all his help and hard work, without which this thesis would have been impossible. FM will have forgotten why she appears in this list, and I hope by now she might have forgiven my poor sense of direction. Space is limited, so I hope everyone else will include themselves in my collective but no less heartfelt thanks.

The generosity of Gao Liang allowed me to draft the first chapters of this thesis in Beijing, in the heat of the days around 七夕. I'm not sure how this came to be such a fitting conclusion to the last four years, and who can say what the future holds? But for now I am caught up, 世事波上舟, 沿洄安得住, and so 天涯若比鄰. I owe a great deal of my faith in human nature to my wonderful friends CSH and WJ, who help me to keep calm and carry on. 知音世所稀. I don't know where you belong, LY-S, but here you are, and it is a pleasure to share your indignation about the many things that neither of us understand. I am fortunate and glad to have, from time to time, the company of GQ, who keeps my spirits up, and of WJ, who listens with such patience to my rambling thoughts on ancient history, the painting of sunsets and the stripes of tigers.

CYC, with you it has been my privilege to pass long hours with likeminded conversations and contented silences, to share a few idle enthusiasms and too much faulty erudition, to think lightly of everything and nothing. This universe of ours, with its dark corners and its distant lights, its complications and all the useful and useless things in it – we'll never work them out, but what good fun we'll have!

And finally you, XDD. How should I thank you, and for what? For your company on a handful of journeys that might have been real or imaginary? For all our talk of hills and stars, near and far at the same time? For your insights and surprises? Or for inspiring me with your brave spirit, your kindness and your unpredictable dreams? No, I'll never have the words. Perhaps one day I'll find a moment when the world is peaceful, and my heart is quiet – then, at least, I'll think of all these things that I appreciate so very much, and of you, dear friend.

Munich
January 16th, 2011

Larga y final andanza,
sobre la arrebatada exaltación del ala del viaducto;
el viento, a nuestros pies, busca velámenes,
y las estrellas laten intensidad.
Bien paladeado el gusto de la noche,
traspasados de sombre,
vuelta ya una costumbre de nuestra carne, la noche.

Noche postrer de nuestro dialogo,
antes nos separen las leguas.
Aun es nuestro silencio donde
como praderas resplandecen las voces;
aun el alba es una pájaro
perdio en la vileza más remota del mundo.
Ùltima noche, resguardada del gran viento de ausencia.

Es trágic entraña del adiós,
como de todo acontecer en que es notorio el tiempo;
es duro realizar que ni tendremos en commún las estrellas.

Cuado la tarde sea quietud en mi patio,
de tus carillas surgirá la mañana.
Será la sombre de mi verano en tu invierno,
y tu luz será la gloria de mi sombre.
Aun persistimos juntos;
aun las dos voces lagran convivir,
como la intensidad y la tenura
en las puestas del sol.

— *Jorge Luis Borges*

探春笑道：“只恐又是你的杜撰”

寶玉笑道：“除《四書》外，杜撰的太多，偏只我是杜撰不成？”

Declaration

The work described in this thesis was undertaken between October 2006 and October 2010, during which time the author was a research student under the supervision of Professor Shaun Cole, Professor Carlos Frenk and Dr. Adrian Jenkins in the Department of Physics at the University of Durham. This work has not been submitted for any other degree at the University of Durham or any other University.

The author was supported by a PPARC/STFC studentship and received travel grants from the Royal Astronomical Society and the Institute of Physics C.R. Barber Trust. He is grateful for the hospitality of the Max-Planck Instiut für Astrophisik (Munich), the Kavli Institute for Theoretical Physics (Santa Barbara), the Kapteyn Institute (Groningen) and the National Astronomical Observatories of the Chinese Academy of Sciences (Beijing).

Chapters 2 and 3 of this thesis have been published in the form of a paper:

- Cooper, A. P., Cole, S., Frenk, C. S., White, S. D. M., Helly, J., Benson, A. J., De Lucia, G., Helmi, A., Jenkins, A., Navarro, J. F., Springel, V. and Wang, J., Galactic Stellar Haloes in the CDM Model, *Monthly Notices of the Royal Astronomical Society*, 406, 744, 2010

Chapter 4 has been submitted in the form of two separate papers:

- Cooper, A. P., Cole, S. and Frenk, C. S., A Two-Point Correlation Function for Halo Stars, *Monthly Notices of the Royal Astronomical Society*, submitted
- Helmi, A., Cooper, A. P., White, S.D.M., Cole, S., Frenk, C. S. and Springel, V., Sagittarius and its siblings in the Aquarius Simulations, *Astrophysical Journal Letters*, submitted

This chapter makes use of data from the Spaghetti Survey, kindly provided by Else Starkenburg, Heather Morrison and the Spaghetti Team.

Chapter 5 is being prepared for submission in the form of a paper:

- Cooper, A. P., Cole, S., Frenk, C. S., et al., The Kinematic Structure of CDM Stellar Haloes, in preparation

This thesis also discusses work associated with the paper in preparation:

- Font, A.S., Benson, A.J., Bower, R.G., Frenk., C.S., Cooper, A.P., Helmi, A., Li, Y-S., McCarthy, I.G., Navarro, J.F., Springel, V., Starkenburg, E. and Wang, J., A new model for the satellites of the Milky Way in the ΛCDM cosmology, *Monthly Notices of the Royal Astronomical Society*, in preparation

1

Introduction

1.1 Milky Way-like galaxies in the ΛCDM cosmogony

1.1.1 The topic of this thesis

The Milky Way is wonderful to see, a subtle band arching from horizon to horizon, near and far at the same time, wherever one finds oneself on Earth[1]. This river in heaven is made of myriad stars. On the clearest, darkest evenings, on the tops of mountains or by the sea, by accident or on purpose, each of us has stood in silence, head back, shivering (with cold, perhaps) and in awe of it.

And yet, this beautiful, familiar and profoundly peculiar arrangement of the universe was all but ignored by most early scientific cosmologies[2]. The humble philosopher Thomas Wright[3] was the first to recognise that the Milky Way was an effect of perspective, and could be explained if the Sun occupied an off-centre position in an extensive three-dimensional stellar system with a complex (possibly flattened) geometry[4]. Wright believed that universe consisted of many such Milky Ways, each a cloud of stars in motion about a common centre (Wright 1750). By determining the true structure of our own star cloud, the organisation of the entire cosmos could be understood. Wright's insight, slow to be recognised and rarely attributed, began the work of understanding the Milky Way and its place in the natural world. More than two hundred and fifty years have passed, many profound discoveries have been made, and still that work is a long way from being finished.

---

[1] Here the author relies mostly on the view from Grasmere on dark winter evenings. He has been lucky enough to see the centre of the Galaxy from Goleta beach and its anticentre from Beijing.

[2] The Milky Way has always had a more prominent place in the richer field of unscientific cosmology. For instance, for approximately 2500 years it has been noted that α Aquilae and α Lyrae lie on *opposite* sides of a well-defined Galactic plane (most of the time).

[3] 1711–1786; of Byers Green, County Durham. Following an accident-prone youth and a disastrous foray into the compilation of almanacs, Wright found success as a tutor of surveying and mathematics. Cosmology was an interlude: in later life he turned his attention to the design of elaborate gardens.

[4] Wright suggested shell or ring configurations, but did not claim the stars were distributed in a continuous disc.

At the turn of the 20^{th} century, the most fundamental cosmic distance scales were yet to be established. Only philosophical arguments and tentative observational hints suggested that the Universe was any more or less extensive than the Milky Way star system (Kant 1755; Scheiner 1899). Determining the structure of the Galaxy using increasingly accurate measurements of stellar motions and distances was then a problem at the forefront of cosmology (e.g. Shapley 1919; Kapteyn 1922; Kapteyn & van Rhijn 1922). An important milestone in the study of Galactic structure was the recognition of two distinct 'populations' of stars in a photometric study of M31 and its companions (Baade 1944). One of these (dubbed population II by Baade) was identified with a kinematic subdivision of stars in the Solar neighbourhood first recognised by Oort (1926). It had already been noted[5] that the properties of the predominantly old stars in this component (such as their near-spherical spatial distribution and chemical composition) were similar to those of the globular star cluster system revealed by the extensive studies of Shapley (1918). Kinematic measurements were critical in establishing this link(for example, the correlation between population II metallicity and velocity noted by Roman 1954). Both the population II stars and the Milky Way globular cluster system appeared to be supported by their internal velocity dispersion, forming a diffuse 'halo' around the Galaxy distinct from the thin, coherently rotating disc population that defines the night-sky appearance of the Milky Way. Today, stellar populations with halo properties can be detected at distances in excess of 100 kpc by observations of their most luminous 'tracers', such as RR Lyraes, blue horizontal branch stars and K giants (e.g. Yanny et al. 2000; Morrison et al. 2000; Vivas & Zinn 2006). Explaining the motion and distribution of halo stars and globular clusters has remained one of the most important objectives for theories of the formation of our Galaxy for almost a century.

Before the current standard model of cosmology was introduced, debate about the origin of halo stars and their theoretical implications centred around the seminal model of Eggen et al. (ELS; 1962). These authors argued (in summary; see e.g. Sandage 1990 and Majewski 1993) for a galaxy formed in the collapse of a single protogalactic gas cloud. This argument was based on an apparent correlation between the chemical enrichment (metallicity) and orbital eccentricity of stars in the entire Milky Way system (including the disc). ELS hypothesised that halo stars are more metal-poor and have more eccentric orbits than disc stars because they formed from unstable gaseous fragments on the free-fall timescale of the cloud ($\sim 10^8$ years). Following this turbulent free-fall[6] period the parent cloud virialised. Enriched gas subsequently had time to

---

[5] For example by Oort (1927) and Lindblad (1927) (following Lindblad 1925), and later by Baade (1944).

[6] The collapse could not have been pressure supported, as the available evidence indicated no strong abundance gra-

settle into a rotationally supported disc, forming stars on circular orbits. This argument was refined by Searle & Zinn (1978), who suggested that the chemical homogeneity observed among globular clusters and halo stars indicated that the halo had been assembled from a number of discrete sub-units. They conjectured that these sub-units collapsed rapidly in independent overdensities of gas, which were brought together by merging over a much longer timescale ($\sim 10^9$ years). The Searle & Zinn model[7] foreshadowed many of the characteristic predictions of the now-standard ΛCDM cosmogony[8].

In comparison to the pace of discovery in extragalactic astronomy and cosmology as a whole, data concerning the properties of the Milky Way's stellar halo have accumulated slowly, and still present a very uncertain picture. For example, the tidal streams of the disrupting Sagittarius dwarf galaxy, a highly significant irregularity in the stellar halo, went undetected until 1994 (Ibata et al. 1994). The current concordance theory of the formation of Milky Way-like galaxies is heavily reliant on data gathered from outside the Milky Way – in particular, from galaxy surveys and the Cosmic Microwave Background. This evidence supports a particular model of the origin and evolution of structure in the Universe, the ΛCDM model, in which the growth of cosmic structure is driven by the gravitational clustering of non-baryonic dark matter. This model provides a well-defined framework within which the formation and evolution of galaxies can be explored from 'first principles'.

As recognised by the pioneering models described above, halo stars in the Milky Way[9] have a pivotal role to play in the study of galaxy formation. Their kinematics, distribution and chemical abundances provide a direct record of the assembly history of the galaxy extending far back in time, before the formation of the disc. We describe below how these properties can be used to explore the close relationship between galaxy formation and cosmological structure formation predicted by the Cold Dark Matter model.

Efficient large-scale star surveys in the next decade (such as PanSTARRS[10], LAMOST[11],

---

dient in the halo.

[7] A similar model of galactic assembly was proposed by Shapley in 1918, albeit on weaker grounds. As quoted in a letter to A.S. Eddington (see e.g. Smith 1985): *'[The Galaxy] may have originated in a combination of two clusters and has grown, as it appears to be growing now, by the accretion of other stellar systems – adding the smaller units such as the globular clusters with ease, and the larger ones such as the Magellanic Clouds with some difficulty, if at all. It appears to be an example on a grand cosmic scale of survival of the fittest, that is, survival of the most massive and most stable.'*

[8] The essential argument of the ELS/Searle & Zinn debate continues with regard to the formation of the thick disc (e.g. Majewski 1993) as well as the stellar halo. We return to this point in Chapter 6.

[9] Although halo stars can now be studied in many other galaxies, the Milky Way will always remain a uniquely detailed test case for the rest of the Universe.

[10] Panoramic Survey Telescope and Rapid Response System: `http://pan-starrs.ifa.hawaii.edu/`

[11] The Guo Shoujing Telescope: `http://www.lamost.org/`

Gaia[12] and the LSST[13]) will allow these models of galaxy formation to be tested in even greater detail with huge, systematically sampled datasets from the Milky Way and M31 – almost two decades after highly efficient redshift surveys began a similar (and still ongoing) revolution in the understanding of large-scale structure. In the Milky Way as in the rest of the Universe, detailed predictions based on the prevailing cosmological model are necessary to guide and interpret the observations. The numerical simulations that we describe in this thesis aim to predict the properties of stellar haloes in the ΛCDM model. The work we describe links together galaxy formation theory and simulations of cosmological structure formation at the resolution necessary to confront the next generation of Galactic surveys.

1.1.2 The Cold Dark Matter cosmogony

Throughout this thesis we will assume an inflationary big-bang model of cosmogony in a flat Universe, with an energy budget dominated by a 'cosmological constant' (Λ, dark energy) and a matter budget dominated by a weakly interacting, massive, non-baryonic fundamental particle (cold dark matter, CDM). Hereafter, this cosmogony will be referred to as ΛCDM. At the time of writing, both of the key ingredients in this model are hypothetical, based on indirect evidence with no experimental confirmation or even a single strong theoretical foundation. ΛCDM nevertheless represents the current scientific consensus, in large part because its predictions for the evolution and structure of the Universe accord remarkably well with observational data. In this section, we summarise the ΛCDM model and discuss some of its implications for the formation of a Milky Way-like galaxy. We note that Λ plays only a minor role in this thesis (by affecting the global expansion history of the universe). Our primary concern will be stars tracing the gravitational clustering of dark matter. For this reason, we will frequently refer to the 'CDM model' in cases where Λ is not relevant.

A cosmological framework

The hot big bang model describes the evolution of the Universe as a process of expansion and cooling in a mixture of 'fluids' (in ΛCDM these are baryonic matter, pressureless dark matter, radiation and dark energy), beginning from an initially dense high-temperature equilibrium. The dimensionless scale factor, $a(t)$, parameterizes the expansion as a function of elapsed time, t, such that $a(t_0) = 1$ at the present day ($t = t_0$). Assuming an isotropic and homogeneous

---

[12] `http://gaia.esa.int/`

[13] Large Synoptic Survey Telescope: `http://www.lsst.org/`

Universe, the rate of growth of this parameter is given by the Friedmann equation[14],

$$H^2 = \frac{8\pi G}{3}\rho - k\frac{c^2}{a^2} + \frac{\Lambda}{3}, \tag{1.1}$$

where G is the gravitational constant, ρ is the density of the composite cosmic fluid, k parameterizes the curvature of space, c is the speed of light, and Λ denotes a cosmological constant. H in this equation is the Hubble parameter,

$$H(a) = \frac{\dot{a}}{a}, \tag{1.2}$$

(e.g. Peacock 1999). The redshift of a photon emitted at time t and observed at $t = t_0$ is given by $z = a(t)^{-1} - 1$. Redshift is often used as a proxy for age when describing the observable Universe in the epoch of structure formation.

Here we consider only a flat Universe ($k = 0$), for which the condition $\Omega \equiv \rho/\rho_c = 1$ holds[15]. In a Universe containing pressureless matter and dark energy (such as a cosmological constant), an alternative statement of this condition is

$$\Omega_{\rm m} + \Omega_\Lambda = 1. \tag{1.3}$$

Here $\Omega_{\rm m}(a) = \rho_{\rm m}(a)/\rho_c(a)$ and $\Omega_\Lambda = \rho_\Lambda/\rho_c(a)$ are the density parameters of matter and dark energy respectively (defining $\rho_\Lambda \equiv \Lambda/8\pi G$). Much progress in cosmology over the last few decades has followed from rapidly improving constraints on the present-day values of $\Omega_{\rm m}$ and Ω_Λ, and from measurements of the temperature anisotropies in the Cosmic Microwave Background (CMB) radiation, relic photons from the epoch of recombination[16]. From the CMB measurements, the 'initial conditions' of the density distribution at recombination can be derived[17]. Given these ingredients (together with the corresponding equations of state for matter and dark energy), this model can be used to make predictions for the subsequent expansion history of the Universe.

---

[14] To solve Equation 1.1 for the evolution of the density of the Universe requires equations of state relating density and pressure in each constituent of the cosmic fluid.

[15] $\rho_{\rm c}(a) = 3H(a)^2/8\pi G$ is the critical density required for a flat Universe.

[16] *Iamne vides igitur quam puncto tempore imago aetheris ex oris in terrarum accidat oras?* Lucretius asks, in the fourth book of *De Rerum Natura*.

[17] The yields of elements created in primordial nucleosynthesis (hydrogen, helium, lithium and deuterium) also provide important constraints on the Universal expansion history and composition.

The recombination-era constraints provided by the CMB are particularly important. At this time in the early history of the expansion ($z \sim 1100$), the temperature and density of the Universe became low enough to allow neutral atoms to remain stable against photoionization. Thereafter were no longer confined by scattering encounters with free electrons. The background field of photons propagating around the transitional time of 'last scattering' now has an extremely low temperature of ~ 2.73 K (due to redshifting), is uniform across the sky to one part in 10^5 K, and has a near-perfect black-body spectrum, an indication that the Universe was once in a state very close to thermal equilibrium.

The existence and overall isotropy of the CMB provide strong support for an initial hot big bang. Experiments such as COBE and WMAP have nevertheless detected minute anisotropies in the temperature of the CMB over a wide range of angular scales. These anisotropies (which correspond to variations in density) are thought to have originated in quantum-mechanical fluctuations in the very early Universe, enlarged to their current scale by a period of rapid inflation (Guth 1981; Narlikar & Padmanabhan 1991).

Assuming a model of particle physics that describes the fundamental constituents of the Universe and their interaction, measurements of the properties of the CMB and its anisotropies tightly constrain the history of cosmic expansion (including the age of the Universe) and the fraction of mass-energy in each of the components governing that expansion (i.e. $\Omega_{\rm m}$ and Ω_Λ). Observations with the WMAP satellite have now determined these fundamental cosmological parameters to remarkable precision[18].

Against the background of universal expansion, the ΛCDM model predicts that *collapsing* structures form in the distribution of dark matter as the result of gravitational clustering, which amplifies the initially small overdensities seeded by inflation. The collapse of these overdense regions (in practice, calculated from an empirical spectrum of density fluctuations derived from the CMB) can be related to the observable properties of large and small-scale cosmic structure at the present day. Of particular interest are predictions for the distribution of galaxies and galaxy clusters, which observations clearly show to be inhomogeneous on scales below $\sim 100\,\mathrm{Mpc}$ (e.g.

---

[18] Assuming ΛCDM, the 7-Year WMAP measurements of Larson et al. (2010) imply a flat Universe (with density parameter $\Omega = 1$), comprising a dominant contribution from dark energy $\Omega_\Lambda = 0.734 \pm 0.029$, a cold dark matter component $\Omega_{\rm c}h^2 = 0.1109 \pm 0.0056$, and a baryonic component $\Omega_{\rm b} = 0.0449 \pm 0.0028$. The derived Hubble parameter, H_0, is $71.0 \pm 2.5\,\mathrm{km\,s^{-1}\,Mpc^{-1}}$. These parameters correspond to an age for the Universe of $t_0 = 13.75 \pm 0.13\,\mathrm{Gyr}$. The slope of the primordial power spectrum of density fluctuations is $n = 0.963 \pm 0.014$, with normalization $\sigma_8 = 0.801 \pm 0.03$ (the rms overdensity fluctuation in spheres of radius $8h^{-1}$ Mpc). Note however that as explained in Section 1.2.1 the cosmological parameters adopted for the work in this thesis are *not* those derived from the latest WMAP analysis. They are chosen instead to match the parameters used in the Millennium Simulation (Springel et al. 2005).

Bahcall & Soneira 1983; Peacock & Dodds 1994). The following sections briefly describe how, given a set of cosmological parameters and initial conditions, the ΛCDM model treats both the growth of cosmic structure and the process of galaxy formation.

The growth of cosmic structure

The linear evolution of the dark matter density fluctuations imprinted on the CMB can be described analytically (although collapsing overdensities and expanding underdensities eventually enter a nonlinear regime, which is of most practical interest for studying the formation and structure of individual galaxies). Collapse occurs first around the most overdense peaks in the density field, and thereafter successively larger regions turn around from the global expansion, collapse and virialise (i.e. become supported against further collapse by random internal motions, as dark matter in this model is assumed to be collisionless). The characteristic feature of this process in the CDM model is that small, early-collapsing regions within larger, shallower overdensities merge with one another, while their 'host' regions continue to virialise around them. The smaller objects in this hierarchy can be destroyed over time by tidal forces as they orbit inside their more massive hosts. Thus all individual virialised dark matter overdensities (haloes) may grow through the accretion of 'smooth' (unbound) dark matter and through the disruption of smaller bound systems (e.g. Wang et al. 2010).

The evolution of structure in the nonlinear regime is usually explored using numerical N-body simulations (Section 1.2.1). These simulations represent the smooth density field of dark matter with discrete collisionless tracer particles. The Millennium Simulation (MS; Springel et al. 2005) exemplifies N-body simulations of cosmological structure formation in the ΛCDM cosmogony[19]. Fig. 1.1 shows a slice through the MS periodic volume (a cube of side length $500\,h^{-1}\,\mathrm{Mpc}$). The distribution of dark matter on large scales is dominated by interlinking filaments tracing the edges of 'empty' void regions. Individual haloes are embedded in this filamentary structure, and clusters of haloes form at the intersection of filaments.

High resolution N-body simulations of individual Milky Way-like CDM haloes (such as the Aquarius simulations; Section 1.2.1) show that they host a substantial population of smaller subhaloes at the present day. The most massive of these has typically $\sim 1\%$ of the host halo mass (Boylan-Kolchin et al. 2010). These subhaloes have passed within the virial radius of their host halo but have survived tidal stripping for as long as a Hubble time. They may even be ejected

---

[19] The models and codes underlying the work in this thesis are derived from those used to run and postprocess the Millennium Simulation.

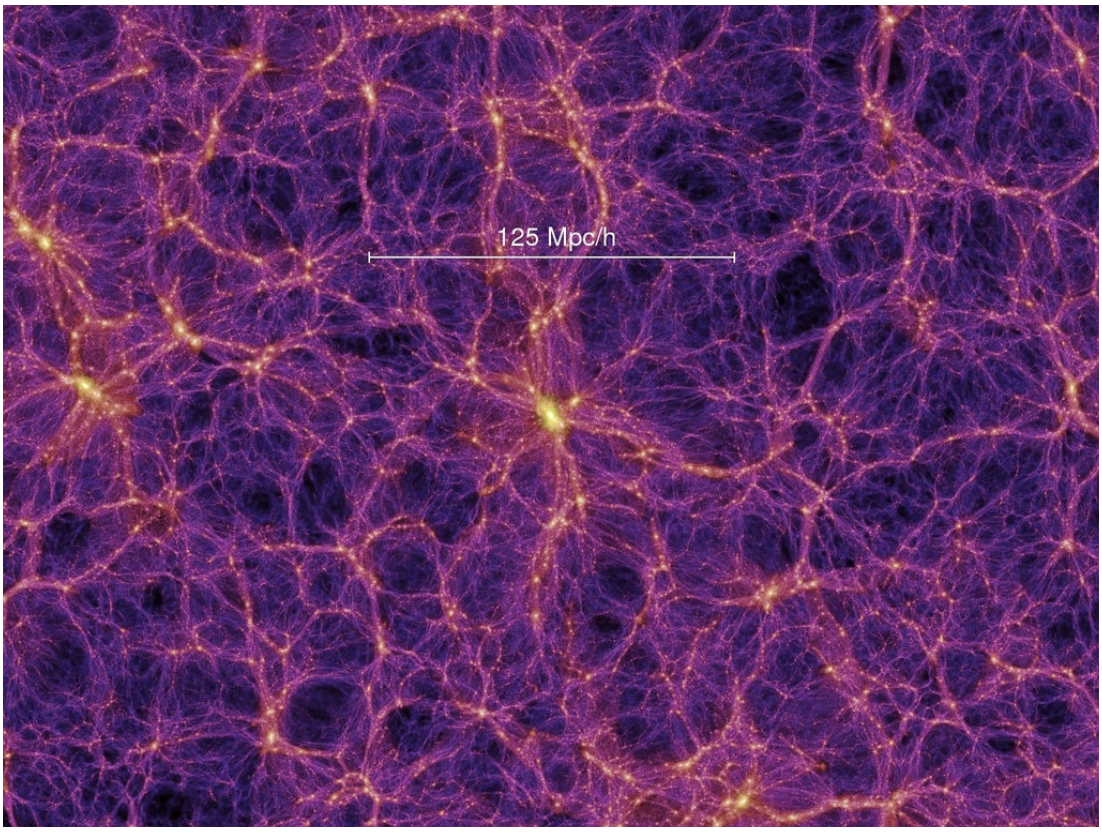

Figure 1.1: The large-scale structure of dark matter in the Millennium Simulation. This slice through the simulation box is $15\,h^{-1}\mathrm{Mpc}$ thick. Intensity corresponds to surface density and colour to velocity dispersion. *Image from Volker Springel / Virgo Consortium.*

from their host halo altogether as the result of three-body encounters (Sales et al. 2007a). Some subhaloes are themselves massive enough to retain their own (sub-)subhaloes; this hierarchy of haloes-within-haloes continues down to the smallest mass scale at which structures can form (roughly one Earth mass, $3 \times 10^{-6}\mathrm{M}_{\odot}$, in the case of neutralino dark matter Hofmann et al. 2001). Hence, in principle, studying the phenomenology of subhaloes in N-body simulations requires very high numerical resolution.

As described in the following section, however, baryonic physics creates a natural 'cut-off' scale in halo mass[20] below which star formation in inhibited altogether (e.g. Benson et al. 2002b; Stringer et al. 2010). These thresholds make the deep hierarchy of the subhalo population irrelevant to the study of luminous galaxies. The latest generation of N-body simulations that we employ in this thesis adequately resolves subhaloes at this scale.

---

[20] Imposed either by inefficient radiative cooling of atomic hydrogen, or by heating by ionizing photons; in either case, where the halo virial temperature falls below $\sim 10^4$ K, corresponding to approximately $M_{\mathrm{vir}} \sim 10^7\ \mathrm{M}_{\odot}$

1.1.3 The origin of stars and galaxies

Stellar populations

The now-standard picture of galaxy formation in a CDM-like cosmogony was outlined by White & Rees (1978)[21]. In this model, ionized gas from the diffuse inter-galactic medium (IGM) is accreted and confined by dark matter haloes, within which it subsequently collapses to very high densities through radiative cooling. Galaxies are thus highly concentrated in their host haloes, and can only grow efficiently while the radiative cooling and collapse time of the trapped gas is short relative to the lifetime of the halo (from the time it virialises to the time it is accreted into a more massive halo).

The first stars are likely to form in early-collapsing regions of 10^5–$10^6\mathrm{M}_{\odot}$ (e.g. Couchman & Rees 1986; Tegmark et al. 1997), where the trapped primordial IGM cools efficiently through the transitions of molecular hydrogen. This first generation of stars is thought to have been massive, short-lived and very different from subsequent generations (e.g. Bromm & Larson 2004). They may have transformed the primordial IGM through the input of supernova energy and heavy elements (metals), and produced a radiative background which affected subsequent star formation. However, the formation of these stars and their effects on the IGM are not at all well constrained by observations, and are typically not included in *ab initio* models of galaxy formation, including those used in this thesis.

The majority of stars in the present-day Universe form inside dense molecular clouds, which in turn form through clumping of gas in thin, rotationally supported discs. Disc-like morphologies are common in the observed galaxy population – as discussed below, most of the stars in the Milky Way lie in a thin disc. These galactic discs arise naturally in the CDM model as the result of conservation of angular momentum (acquired through tidal torques) by the gas cooling within dark matter haloes (e.g. Fall & Efstathiou 1980; Mo et al. 1998).

Many disc galaxies (though perhaps not all; Kautsch et al. 2006) harbour a dispersion-supported concentration of stars at their centre (a bulge) which may result from the hierarchical accretion and disruption of less massive galaxies. It may also be possible to form these central bulges through secular instabilities (such as dynamical bars) arising in the disc itself. Entirely dispersion-supported galaxies (ellipticals) are thought to be the 'limiting case' of this process, in which a merger with a galaxy of similar mass (or else the onset of violent dynamical instabilities) has completely scrambled the orbits of stars.

---

[21] See also White & Frenk (1991)

Although the model outlined above provides a good overall description of the morphologies of galaxies and their subcomponents, almost all of the details are highly uncertain. The model has not been extensively tested for the smallest galaxies observed in the nearby Universe (the dwarf irregulars and spheroidals, discussed below), or for rapidly-growing (or rapidly-assembling) galaxies at high redshift. The role of mergers in transforming galaxy morphology and creating dispersion supported components is still under debate (e.g. Parry et al. 2009).

Consequently, there is currently no single well-developed model for the origin of components in disc galaxies other than the thin discs themselves. Substantially more theoretical and observational work is required to understand the origin of the thick discs, bulges and stellar haloes of galaxies like the Milky Way, and their relationship to the thin disc, if any. These are among the primary goals of studies of the Milky Way in a cosmological context, the topic of this thesis. In particular, we will focus on the role of satellite accretion in building haloes (and bulges).

Mass-to-light ratios

The overall efficiency with which dark matter haloes are populated with stars over the lifetime of the Universe (regardless of how those stars are formed and distributed) is encapsulated in their ratio of total mass to luminosity (M/L). This ratio is modulated by the capacity of a halo to accrete baryons from the IGM and to cool those baryons to the temperature and density at which stars can form. As discussed below in the specific case of dwarf galaxies, M/L is an observable quantity, in principle.

One approximate means of studying the overall efficiency of the galaxy formation process in terms of M/L is to match the abundance of dark matter haloes as a function of mass in a ΛCDM cosmological simulation to the observed abundance of galaxies as a function of luminosity. Guo et al. (2010b) performed this abundance matching using the Millennium Simulation and data from the Sloan Digital Sky Survey (SDSS). Their results are shown in Fig. 1.2. It is clear that haloes in the plausible range of MW dark halo masses form stars more efficiently than those of substantially lower or higher mass: the Milky Way dark halo is slightly more massive than the peak of the recovered $M_{\star} - M_{DM}$ relation if its stellar mass is $5.5 \times 10^{10}\,\mathrm{M}_{\odot}$ (Flynn et al. 2006). Guo et al. find a corresponding dark halo mass of $2.0 \times 10^{12}\,\mathrm{M}_{\odot}$ (with a 10-90% range of $0.8 \times 10^{12}\mathrm{M}_{\odot}$ to $4.7 \times 10^{12}\mathrm{M}_{\odot}$). This estimate is consistent with the Milky Way-M31 'timing argument' (Li & White 2008), although it is sensitive to the adopted Milky Way stellar mass and implicitly assumes that the Milky Way is a typical galaxy. As we discuss further in Chapter 5, it is slightly higher than earlier dynamical estimates based on the velocity dispersion profile

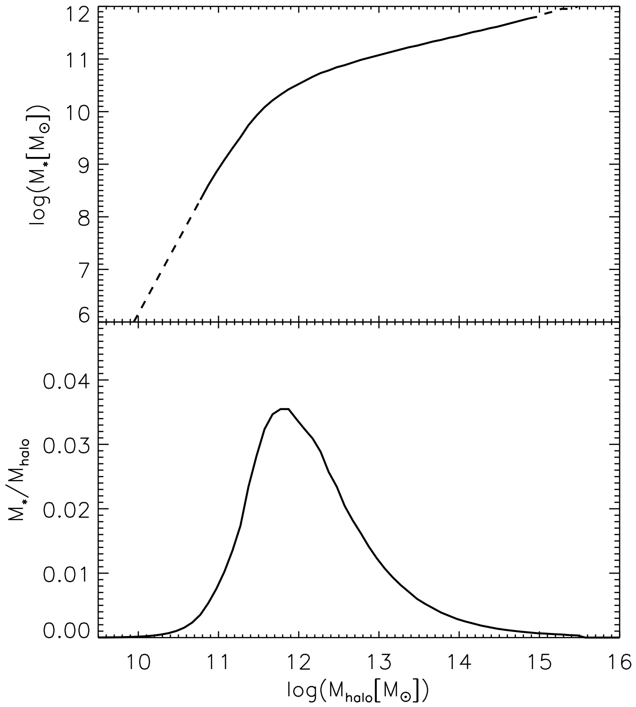

Figure 1.2: Figure 2 of Guo et al. (2010b), showing (upper panel) the stellar mass – halo mass relation obtained from matching the abundance of haloes in the Millennium and Millennium II simulations to the SDSS stellar mass function (dashed lines are extrapolations beyond the mass range of the simulations). The lower panel shows the ratio of stellar to dark mass, indicating the suppressed efficiency of star formation in large and small haloes. The peak efficiency ($\sim 20\%$ of baryons converted to stars) occurs at $10^{11.8}\,\mathrm{M}_{\odot}$, somewhat below the halo mass inferred for the Milky Way assuming $M_{\star} = 5.5 \times 10^{10}\,\mathrm{M}_{\odot}$ (Flynn et al. 2006). *Reproduced with thanks to Guo Qi.*

of halo stars (e.g. Battaglia et al. 2005; Smith et al. 2007; Xue et al. 2008). The corresponding efficiency with which baryons are converted to stars in Milky Way haloes is somewhat less than $\sim 20\%$, much lower than predicted by most hydrodynamic simulations of galaxy formation (Guo et al. 2010b).

A variety of self-regulating feedback mechanisms have been invoked to explain the inefficient conversion of gas to stars in DM haloes. On large scales (i.e. in the central galaxies of groups and clusters) the intracluster medium may be heated by relativistic jets powered by accretion onto a central supermassive black hole, suppressing further cooling (e.g. Bower et al. 2006; Croton et al. 2006). This process becomes less important at a mass scale roughly corresponding to that of MW-like galaxies (e.g. Croton et al. 2006).

On the scales of relevance to this thesis (galaxies of MW mass and below), energy injected into the ISM by supernovae in regions of active star-formation is the most important feedback mechanism (e.g. Benson et al. 2003). This energy can drive large-scale outflows of gas (galactic winds). Supernova feedback has (in principle) a similar strength per unit stellar mass in all galaxies (Larson 1974): gas is thus much more easily ejected altogether from haloes of lower mass (i.e. from shallower potential wells). Regulation of star formation by gas ejection gives rise to a relationship between galaxy mass and metallicity (see Chapter 2). Finally, as noted above, the heating of the IGM by ionizing photons may also suppress star formation in very small haloes by limiting the amount of baryons they can accrete (e.g. Benson et al. 2002b; Hoeft et al. 2006).

1.1.4 Dwarf galaxies and the Local Group

The Local Group is dominated by two massive disc galaxies, the Milky Way and M31. These galaxies have ~ 24 and ~ 15 known dwarf satellites respectively; some of these are unconfirmed and new candidate satellites are being discovered regularly in wide-area photometric surveys (e.g. Belokurov et al. 2010). Beyond these two systems a large number of faint galaxies lie within a sphere of $\sim 1\,\mathrm{Mpc}$ (Mateo 1998). Many of these are dwarf irregulars (dIrr), containing a measurable quantity of cold gas and showing ongoing star formation. This contrasts with the majority of galactic satellites, which are gas-free and consist of predominantly old stars (e.g. Tolstoy et al. 2009).

In Chapter 2 we discuss constraints on galaxy formation models provided by the large number of so-called ‘ultra-faint’ satellites recently discovered around the Milky Way[22] and M31. These discoveries have gone some way towards alleviating the simplest formulation of the so-called ‘missing satellites problem’ (Klypin et al. 1999; Moore et al. 1999) – an apparent discrepancy between the number of observed Milky Way satellites and the number of subhaloes found in N-body simulations of Milky Way analogues. Clearly, extending the expectation of one satellite galaxy per subhalo to arbitrarily low masses is incorrect given the rapidly declining efficiency of star formation in the smallest haloes (e.g. Kauffmann et al. 1993; Benson et al. 2002b). Nevertheless, the solution of this ‘problem’ is an extremely basic test for CDM. As we discuss further in Chapter 6, the question of whether or not current models of halo and galaxy formation are consistent with the known properties of Milky Way satellites remains open (e.g. Kravtsov 2010).

The dwarf galaxies associated with the Milky Way have extremely high M/L ratios, of the order ~ 10 to 1000 (Mateo 1998). These important observational results have been obtained

---

[22] Almost entirely in SDSS data (e.g. Martin et al. 2008, and references therein)

through Jeans modelling of the satellites (e.g. Binney & Tremaine 1987), based on a small number (typically tens to hundreds) of line-of-sight velocity measurements for their individual stars (Walker et al. 2009a; Wolf et al. 2010). Such high mass-to-light ratios are broadly consistent with the expectation of the standard CDM model, as outlined above. However, these measurements are difficult and often controversial in the case of the faintest dwarf galaxies (e.g. Adén et al. 2009), for which very few data are available at present.

Based on such measurements, Strigari et al. (2007) determined the mass within the central $300\,\mathrm{pc}$ of the 'classical' satellites and a number of the 'ultra-faints'. They found that this M_{300} measure was approximately constant over five decades in satellite luminosity. Taken at face value, this result supports claims for a minimum mass below which star formation is inhibited – or below which no dark matter haloes exist, corresponding for example to the free-streaming scale of a warm dark matter cosmogony (e.g. Strigari et al. 2008). In fact, this uniformity is a natural outcome of well-understood scaling relations in dark matter haloes and thresholds in standard galaxy formation physics (Stringer et al. 2010). Furthermore, it is likely that there is a strong systematic bias against the detection of low surface-brightness satellites (Koposov et al. 2008; Tollerud et al. 2008) and that these may inhabit structurally different dark haloes (e.g. Bullock et al. 2010). We discuss these issues further in the context of our models in Chapter 2.

1.1.5 The fate of disrupted galactic satellites

Not all subhaloes accreted by a Milky Way-like dark matter halo survive to the present day. Any subhalo with an orbit that carries it deep into the potential well of its parent will experience strong tidal forces capable of unbinding its dark matter and, if the subhalo hosts a dwarf galaxy, its stars. This tidal stripping may eventually destroy the satellite as a self-bound entity. Stripped stars themselves will survive, of course, and continue to orbit the parent galaxy, conserving their phase-space density (e.g. Binney & Tremaine 1987; Johnston et al. 1996). The typical result is a diffuse stream of stars following the orbit of the now-defunct satellite. Stellar haloes formed from the superposed debris of disrupted satellites are thus a natural byproduct of hierarchical galaxy formation in the ΛCDM cosmogony, which predicts many such encounters in the history of a Milky Way-like halo. As we discuss further in Section 2.2.3, in addition to forming components of the accreted stellar halo, infalling satellites may cause dynamical heating of the thin disc (e.g. Toth & Ostriker 1992; Velazquez & White 1999; Benson et al. 2004; Kazantzidis et al. 2008) and may also contribute material to an accreted thick disc (Abadi et al. 2006) or central bulge.

The disruption of luminous satellites and the formation of a diffuse accreted stellar halo is intimately connected to the CDM hierarchy and the physics of galaxy formation in small haloes, particularly at high redshift. Much of the assembly history of a galaxy like the Milky Way may be encoded in the kinematics metallicities, ages and spatial distributions of its halo stars. 'Reading' this record of the Galaxy's assembly through observations of halo stars – so called 'galactic archaeology' – can provide useful insights into aspects of the CDM model that are hard (or impossible) to study in any other way.

1.2 Simulating the Milky Way

The models described in this thesis focus on the evolution of Milky Way-like galaxies. They are based on a combination of two large computational projects. One of these is the Aquarius suite of six high-resolution N-body simulations of Milky Way-like dark matter haloes. The other is the GALFORM code, a semi-analytic model of galaxy formation (Cole et al. 2000; Baugh et al. 2005; Bower et al. 2006; Benson & Bower 2010). The work presented in this thesis is part of a larger study of galaxy formation on small scales with this semi-analytic model. More technical details and modifications are discussed in the following chapter.

1.2.1 N-Body simulations: the Aquarius project

Aquarius (Springel et al. 2008a) is a suite of high-resolution simulations of six dark matter haloes having virial masses[23] within the range $1-2\times10^{12}\,\mathrm{M}_{\odot}$, comparable to values typically inferred for the Milky Way halo (see Section 1.1.3). In this thesis we use the 'level 2' Aquarius simulations, the highest level of resolution at which all six haloes were simulated. A comprehensive account of the entire simulation suite and demonstrations of numerical convergence are given by Springel et al. (2008a,b). The outstanding resolution of these simulations is clear from the $z=0$ snapshot shown in Fig. 1.3.

The Aquarius haloes were selected from a lower resolution version of the MS-II (Boylan-Kolchin et al. 2009), based only on their mass (a loose isolation criterion at $z=0$ was also applied). Haloes of this mass show wide variation in properties such as the mass of their most massive subhalo, spin parameter, concentration and mass assembly history (Navarro et al. 2010b; Boylan-Kolchin et al. 2010; Wang et al. 2010). Boylan-Kolchin et al. (2009, 2010) have shown that the Aquarius haloes are in most respects an unbiased sample of haloes in their

---

[23] We define the virial mass of a halo as M_{200}, the mass enclosed within a sphere of mean density 200 times the critical density for closure. The radius of this sphere is r_{200}. These definitions are used throughout.

Figure 1.3: The small-scale structure of dark matter in the Aquarius Simulation. A single Milky Way-mass halo (Aq-A) is shown, together with its subhalo population. Intensity corresponds to surface density and colour to velocity dispersion. *Image from Volker Springel / Virgo Consortium*.

mass range selected from the entire MS-II[24]. However, as noted above, it is possible that these haloes are not themselves representative of the Milky Way, as some estimates of its dark halo mass lie towards the upper limit of the range covered by the Aquarius sample.

Each Aquarius halo was individually resimulated using a multi-mass particle (‘zoom’) technique (Power et al. 2003). In the initial conditions of the original low-resolution simulation, the Lagrangian volume enclosing particles belonging to a sphere around each target halo at $z = 0$ was identified. Each of these volumes was resampled with many more particles of much lower mass to create a high-resolution region. The spectrum of density fluctuations used to seed the initial displacements of particles in the original simulation was also applied to the resimulation, with identical amplitude and phase on all scales common to the two simulations. Power in smaller-scale fluctuations can be included, because of the denser sampling

---

[24] The clearest discrepancy is that five of the six Aquarius haloes have spin parameters lower than the median for haloes of their mass – see figure 4 of Boylan-Kolchin et al. (2010).

Table 1.1: Properties of the six Aquarius dark matter halo simulations (Springel et al. 2008a) on which the models in this thesis are based. The first column labels the simulation (abbreviated from the notation Aq-A-2, Aq-B-2 etc.). From left to right, the remaining columns give the particle mass $m_{\rm p}$, the number of particles within r_{200}, the virial radius at $z = 0$; the virial mass of the halo, M_{200}; and the maximum circular velocity, $V_{\rm max}$, and corresponding radius, $r_{\rm max}$.

	$m_{\rm p}$ $[10^3 {\rm M}_\odot]$	N_{200} $[10^6]$	M_{200} $[10^{12} {\rm M}_\odot]$	r_{200} [kpc]	$V_{\rm max}$ $[{\rm km\,s^{-1}}]$	$r_{\rm max}$ [kpc]
A	13.70	135	1.84	246	209	28
B	6.447	127	0.82	188	158	40
C	13.99	127	1.77	243	222	33
D	13.97	127	1.74	243	203	54
E	9.593	124	1.19	212	179	56
F	6.776	167	1.14	209	169	43

of the high resolution region in the resimulation. The full volume of the parent simulation ($100\,h^{-1}\,{\rm Mpc/side}$) is retained in the resimulation, with higher-mass particles used outside the high-resolution region to represent the long-range tidal field[25]. No more than a few high-mass 'boundary' particles entered the high-resolution region in any of the simulations.

We list relevant properties of each halo/simulation in Table 1.1. The simulations were carried out with the parallel Tree-PM code GADGET-3, an updated version[26] of GADGET-2 (Springel 2005). The Aq-2 simulations used a fixed comoving Plummer-equivalent gravitational softening length of $\epsilon = 48\,h^{-1}$ pc. ΛCDM cosmological parameters were adopted as $\Omega_{\rm m} = 0.25$, $\Omega_\Lambda = 0.75, \sigma_8 = 0.9, n_{\rm s} = 1$, and Hubble constant $H_0 = 100h\,{\rm km\,s^{-1}Mpc^{-1}}$. A value of $h = 0.73$ is assumed throughout this thesis. These parameters are identical to those used in the Millennium Simulation, consistent with WMAP 1-year constraints, and marginally consistent with WMAP 5-year constraints (Spergel et al. 2003; Komatsu et al. 2009).

1.2.2 Modelling gas physics and star formation

Hydrodynamic simulations

N-body integration codes can be combined with schemes to to solve for collisional interactions in fluids. The IGM can be treated in this way in cosmological simulations, typically with a Lagrangian method (similar to the dark matter) using 'smoothed particles'. These Smooth Particle Hydrodynamic (SPH) codes can explicitly track the evolution of the temperature and density of the IGM (subject to an imperfect treatment of shock physics). However, even the

---

[25] In practice, a gradient of particle mass is used outside the high-resolution region.

[26] The principal improvements in GADGET-3 relate to computational speed and improved scaling behaviour for large numbers of parallel processing cores (Springel et al. 2008a).

'macroscopic' processes that directly govern star formation[27] occur on scales many orders of magnitude smaller the effective spatial and mass resolution of a typical cosmological simulation. Such simulations therefore rely on simplified prescriptions for physics occurring on these small scales. These 'sub-resolution' prescriptions are controlled by free parameters, which must be adjusted empirically to obtain results consistent with observations. On the whole, while the large-scale gas physics are reasonably well understood, the sub-resolution models remain almost completely ad hoc. This difficulty has motivated the development of an alternative technique known as semi-analytic modelling.

The GALFORM semi-analytic model

Semi-analytic models are numerical codes which make simplified numerical approximations for the large-scale 'macroscopic' physics of galaxy formation – for example, by assuming the dark matter haloes are spherically symmetric, and that their accretion of dark matter and gas can be described analytically (see Baugh 2006 and Benson 2010 for a comprehensive discussion of the principles of semi-analytic modelling). This allows the evolution of star formation in a population of dark matter haloes to be simulated in a fraction of the time required for a full hydrodynamic calculation, at the cost of a fully general solution and the introduction of a large number of numerical parameters. However, the computational simplicity of these models permits a very rapid exploration of different combinations of parameters. A large number of galaxies can be modelled in a very short time, producing results that can be compared against the statistical properties of the entire observed galaxy population. The most common 'test' of this sort is the field galaxy luminosity function at $z = 0$.

The Durham semi-analytic model, GALFORM, is used in this thesis to postprocess the Aquarius N-body simulations. The version we use throughout is that of Bower et al. (2006), which updates the Cole et al. (2000) models for the accretion and cooling of gas from the IGM, the formation of gaseous and stellar discs, disc instabilities, bulge growth through mergers, supernova feedback and gas ejection. The Bower et al. (2006) model implements additional prescriptions for AGN feedback (hydrostatic and rapid-cooling regimes) and the associated growth of supermassive black holes. The GALFORM code is controlled by a number of interdependent parameters which are constrained in part by theoretical limits and results from hydrodynamical simulations. Parameters that cannot be constrained in this way ('free' parameters) are adjusted such

---

[27] For example, the formation and disruption of molecular clouds, the Jeans instability and the coupling of radiative and supernova feedback energy to the interstellar medium.

that the model satisfies statistical comparisons with several datasets, for example the galaxy luminosity function measured in different wavebands (e.g. Baugh et al. 2005; Bower et al. 2006; Font et al. 2008). However, such statistical constraints on large scales do not guarantee that the same model, with no modifications, will provide a good description of the evolution of a single 'Milky Way' halo and its satellites. A model that results in a *satellite* galaxy luminosity function consistent with observations is a fundamental prerequisite for the work presented here, in which a proportion of the total satellite population provides the raw material for the assembly of a stellar halo. In Chapter 2 we demonstrate that the key processes driving galaxy formation on small scales are modelled reasonably well with the GALFORM model and parameter values of Bower et al. (2006).

The 'units of analysis' in most semi-analytic models are individual dark matter haloes. The growth of structure is modelled by representing these haloes as nodes in a directed network graph known as a *merger tree*. Each merger tree is 'rooted' in a single halo at $z = 0$, but will comprise many hierarchical 'branches' at higher redshift. Nodes are grouped by discretized time levels. Each node at timestep i has links to zero or more *progenitors* at the earlier time $i - 1$ and to a single *descendant* at the later time $i + 1$. On each time level, the semi-analytic model evolves the properties of galaxies in each node (halo) forwards in time, from progenitors to their descendants.

Merger trees can be constructed with statistical methods based on Press-Schechter theory (Press & Schechter 1974; Bond et al. 1991; Bower 1991; Cole 1991; Lacey & Cole 1993; Parkinson et al. 2008). This technique has been shown to be an excellent approximation to the growth of haloes observed in N-Body simulations (e.g. Cole et al. 2008), but it neglects all spatial information on the haloes concerned (their positions and velocities) and cannot treat subhaloes. For these reasons, it is often useful to construct merger trees directly from a pre-existing N-body simulation. To do this, haloes must be identified at each simulation output timestep, using group-finding methods to isolate self-bound sets of particles whose overdensity corresponds to that typical of virialised objects[28].

For the purpose of constructing merger trees for the MS, MS-II and Aquarius simulations, the Friends-Of-Friends (FOF) and SUBFIND algorithms were used to identify haloes (Davis et al. 1985; Springel et al. 2001). FOF links together all particles within a certain distance of one another to form groups. The linking length, b, is specified as a fraction of the mean interparticle separation. With the choice $b = 0.2$, the FOF procedure efficiently isolates all closed regions

---

[28] Approximately 200 times the critical density for closure, ρ_c, as noted above (e.g. Navarro et al. 1996).

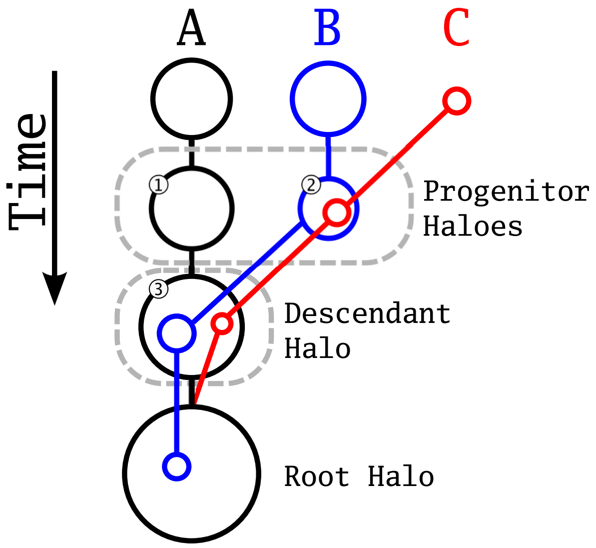

Figure 1.4: Simplified illustration of a single halo merger tree. The tree has four time levels (time increases down the page) and contains three branches (A,B and C) ordered by mass from left to right. At the first step (top), all the haloes are independent entities. Branch C (red) becomes a subhalo of B (blue) at the second step (labelled 2). Branch B becomes a subhalo of A at the third step and survives as a subhalo to the final time. The subhalo branch of C terminates at the third step – it is deemed to have merged into branch A between the third and fourth steps. The concept of progenitor and descendant is illustrated in the case of the *halo* merger tree used by GALFORM (i.e. ignoring subhaloes). The haloes labelled 1 and 2 (step 2) are the progenitors of the halo labelled 3 (step 3). Halo 1 is the most massive progenitor of halo 3; this chain of most massive progenitors followed upwards from the root node defines branch A as the main branch of the tree.

with mean overdensities of ~ 200 (Lacey & Cole 1994; Cole & Lacey 1996). The purpose of SUBFIND is to decompose the overdensities identified by FOF into physical (i.e. gravitationally self-bound) haloes. In addition to a 'main halo' in each FOF group, SUBFIND identifies a hierarchy of self-bound subhaloes[29]. In each 'snapshot' of the simulation, a set of progenitors is identified for every subhalo at the *preceding* step, using the methods described by Helly et al. (2003). Every subhalo is associated with zero or one fragments from that earlier time – typically the most massive of its progenitors – which can be identified with the subhalo itself. The chain of direct progenitors and descendants followed through the lifetime of a particular halo or subhalo is referred to as its *branch* in the merger tree (see Fig. 1.4). All merger trees terminate in a single subhalo at redshift zero; the branches of these 'root' haloes are referred to as the *main* branches of their respective merger trees. The branches of all other subhaloes terminate when they are no longer identified as the main progenitor of the subhalo to which they descend.

---

[29] In practice GALFORM operates on the merger trees of the 'main' subhaloes of FOF groups (referred to as haloes). The principles of merger tree construction are equivalent for haloes and subhaloes.

The technique of post-processing an N-body simulation with a semi-analytic model using merger trees is well established (Kauffmann et al. 1999; Springel et al. 2001; Helly et al. 2003; Hatton et al. 2003; Kang et al. 2005; Bower et al. 2006; De Lucia et al. 2006), although only a few studies have applied 'standard' semi-analytic modelling to high-resolution simulations of individual haloes similar to those of the Aquarius project[30] (e.g. Li et al. 2010, also Font et al., in preparation).

Unlike a 'typical' cosmological volume simulation, the Aquarius simulations focus on a single dark halo, the mass of which (at $z = 0$) is significantly greater than any other subhalo in the simulated region. Where necessary, we refer to the branch of this particular subhalo as the *principal* branch of the simulation[31]. In the following chapters, we distinguish between accretion (the transition from halo to subhalo, in the context of our group-finding algorithms) and disruption (the termination of a merger tree branch, occurring when the particles defining a halo at one output time cannot subsequently be identified as a self-bound entity). We return to these technical details in Chapter 2.

1.3 Galactic stellar haloes

We conclude this introduction with a short summary of the basic observational results and previous theoretical work concerning the stellar haloes of the Milky Way, M31 and other galaxies. Further details are given in the following chapters, where relevant. This section relies heavily on reviews by Freeman & Bland-Hawthorn (2002) and Helmi (2008).

1.3.1 The Milky Way halo

Definition: Theory

From a theoretical point of view, the stellar halo component of a massive disc galaxy like the Milky Way is easy to define. In such systems most stars have a characteristic coherent high-velocity bulk rotation, following nearly circular orbits confined to a thin plane. In contrast, by definition, a 'halo' component is supported by its intrinsic velocity dispersion rather than

---

[30] As part of the work described in this thesis, the Helly et al. (2003) algorithms have been refined further. All the results presented here are based on the previously published algorithms.

[31] Although such semantic distinctions are not essential for understanding the work presented in this thesis, we stress that *all* the merger trees in the simulation, each defined by a root (sub)halo at $z = 0$, are processed by our model. We do not follow the common terminology in which one branch of one particular merger tree – that hosting the formation of the notional 'Milky Way' – is referred to as *the* main branch. Rather, it is *a* main branch, one of many in the simulation. Hence we distinguish this 'special' branch as the *principal* branch of the simulation as a whole (a peculiarity of 'zoom' resimulations).

rotation, and is characterised by eccentric orbits carrying its stars out of the plane of the disc. In a given galaxy there may be more than one such component (or none at all). The sum of these velocity dispersion-supported components make up a stellar envelope that can be clearly distinguished from a thin disc. This definition of a stellar halo is close to another widely used term, 'galactic spheroid', most often used to describe the combination of a bulge and a halo.

This highlights the important (and still largely unresolved) ambiguity concerning bulges in current theories of galaxy formation. At least three alternative origins are commonly proposed for bulges (e.g. Kormendy & Kennicutt 2004). A bulge may be the innermost region of a larger extended halo (formed through one or more minor mergers); a transient dynamical instability in the disc (e.g. a bar); or else a completely separate component with an obscure origin in the early stages of galactic evolution (as bulges are typically old). The first two of these origins are well-defined and common interpretations of observed bulges. Both interpretations have been proposed for the Milky Way bulge.

This uncertainty over the nature of bulges makes it hard to draw a simple distinction between bulges and haloes. In the scenario in which both are built by minor mergers (i.e. from accreted stars), there is no difference between the 'innermost' halo and the bulge[32]. As bulges may be built in more than one way, however, there is no straightforward empirical separation between 'accreted' bulge stars and 'in situ' bulge stars. As we discuss in Section 2.2.3, particular care over definition is needed when comparing simulations of 'the stellar halo' with observations, because of this ambiguity[33].

Confusion between in situ formation and accretion extends to the halo. Other means of building up kinematically hot metal-poor stellar haloes around galaxies like the Milky Way have been proposed, in addition to the stripping of stars from tidally disrupted satellites (the mechanism on which we will focus, which we refer to throughout as *accretion*). One of these is the tidal scattering of disc stars from circular to eccentric orbits during mergers or disc instabilities (*disc disruption*, e.g. Purcell et al. 2010). Another is the formation of stars far away from the galaxy on initially eccentric orbits (e.g. in 'cold clouds' formed by thermal instabilities in a halo cooling flow, or else in gas stripped from satellites or torn from the disc; *extragalactic star formation*). Usually, disc disruption and extragalactic star formation are referred to collectively as the 'in situ' contribution to a stellar halo. Quantifying the relative importance of accreted

---

[32] This need not mean that they are a single 'simple' component with a seamless transition. As noted throughout this thesis, mergers between haloes in CDM are inherently stochastic and this gives rise to a complex internal structure in the accreted component of a galaxy.

[33] A similar argument applies to the thick disc, as discussed further in Section 2.2.3.

and in-situ halo assembly has been an important problem for theories of galaxy formation and galactic structure since the work of Searle & Zinn (1978). In this thesis we explore the extent to which mismatches between observations and simulations of the accreted halo indicate that in situ halo formation is significant.

Definition: Observations

Prior to the current era of large-scale photometric star surveys and efficient spectroscopic campaigns[34], work on the Milky Way's stellar halo was characterised by a large number of small-scale observational programmes. In these studies, particular selections for 'halo' stars were used, typically based on kinematics (isolating stars with eccentric orbits) or colours (isolating stars of low metallicity). In the case of colour selections, follow-up spectroscopy can distinguish faint stars at genuinely large distances from foreground interlopers. Alternatively, stars of a specific type with standard-candle properties can be searched for systematically (e.g. RR Lyraes or horizontal branch stars). Globular clusters have also been used as halo tracers. Past 'halo star' samples were extremely heterogeneous, with complicated (mostly unquantified) selection functions and biases – the definition of the stellar halo has varied from author to author over time. The historical progression of work on the stellar halo is therefore rather complicated, in part because many potentially 'different' haloes were being studied at once under the same name. In recent years SDSS data has allowed a more homogeneous approach to the selection of halo stars.

At least two kinematically distinct 'smooth' halo components have been claimed[35] based the motions of stars in the Solar neighbourhood (Sommer-Larsen & Zhen 1990; Carollo et al. 2007, 2010). These components are usually termed the 'inner' and 'outer' halo. The inner halo component is more metal rich and does not rotate, whereas the outer component shows some evidence for bulk rotation (Carollo et al. 2010, but see also Deason et al. 2010). This dichotomy has lead some authors to suggest that the inner halo was built through in situ processes (Carollo et al. 2007; Zolotov et al. 2009) 'on top of' an accreted halo which now dominates only at large radii (in this picture, bulk rotation is a natural consequence of accretion). The Milky Way halo shows a break in its power-law density profile at ~ 30 kpc which may mark the transition between these components (Ivezić et al. 2000; Bell et al. 2008; de Jong et al. 2010; Carollo et al.

---

[34] Very approximately defined by the first releases of SDSS and 2MASS (Skrutskie et al. 2006) circa. 2000

[35] In addition to one or more 'thick discs' (Gilmore & Reid 1983; Carollo et al. 2010), which partly overlap the distributions of halo star metallicity and kinematics (e.g. Majewski 1993).

2010). A similar inner/outer halo dichotomy has been observed in M31, where the inner halo component appears to be much brighter than that of the Milky Way (e.g. Koch et al. 2008). These are 'minimal' structure models: many large, diffuse substructures have been discovered in the Milky Way halo wherever sufficiently deep tracer star counts have been carried out (e.g. Newberg et al. 2002; Rocha-Pinto et al. 2004; Jurić et al. 2008; Belokurov et al. 2007a; Watkins et al. 2009; de Jong et al. 2010). As noted below, studies of different halo tracers do not always agree even on the slope of the inner halo density profile.

Indeed, when different 'tracer' stellar populations are studied in isolation, the halo is seen to be extremely inhomogeneous and poorly represented by smooth models even with two components (Bell et al. 2008; Sesar et al. 2007; Watkins et al. 2009; Bell et al. 2010). Morrison et al. (2009) report a highly flattened ($c/a \sim 0.2$) dispersion-supported component in nearby halo stars, distinct from the inner halo of Carollo et al. (2010) but also having a net prograde rotation. Even more recently, Deason et al. (2010) have found evidence for two families of SDSS BHB stars showing bulk rotation, with $\langle v_\phi \rangle = -(25 \pm 7)\,\mathrm{km\,s^{-1}}$ and $\langle v_\phi \rangle = 15 \pm 8\,\mathrm{km\,s^{-1}}$ in the region $10 < r < 50\,\mathrm{kpc}$. Their prograde BHB population is more metal rich than the retrograde BHB population and may be associated with a cold velocity clump suggestive of an accretion remnant. The authors propose that the detection of a retrograde component is an artifact of uncertainty in the velocity of the local standard of rest and hence the bulk of the outer halo is *not* rotating. The 'halo' globular cluster population of the Milky Way shows a net prograde rotation (e.g. Frenk & White 1980) of $\sim 58 \pm 27\,\mathrm{km\,s^{-1}}$ according to Deason et al. (2010). This is similar to their metal-rich BHB population, which it also overlaps in space and metallicity.

Mass

The canonical mass of the Milky Way stellar halo is $\sim 10^9\,M_\odot$ although this value (derived from the slope of the halo density profile $\rho \propto r^n$, typically $n \sim -3$, a normalization in the Solar neighbourhood, and an assumption about the behaviour of the profile as $r \to 0$) is not at all well-constrained. Bell et al. (2008) estimated $\sim 3 \times 10^8\,\mathrm{M_\odot}$ in the range $3 < r < 40\,\mathrm{kpc}$ from their best-fit double power-law model of turnoff star counts in SDSS (see however Jurić et al. 2008; Ivezić et al. 2008). Thus the halo is unlikely to be much more massive than the 'conventional' $\sim 10^9\,M_\odot$.

Observational estimates of the halo mass necessarily includes both accreted and in-situ halo stars. However, the most distinctive accreted substructure in the halo, the stream of the Sagittarius galaxy, is sometimes explicitly *excluded* (for example, in the density profile fits of Bell et al. 2008). Niederste-Ostholt et al. (2010) have estimated the total luminosity in the stream to be 6.6–$9.2 \times 10^7\ \mathrm{L}_\odot$, a significant fraction of the total luminosity of the halo. Thus, when comparing with models, the decision to include or exclude this stream is as arguably significant as the definition of the bulge and thick disc.

Extent, shape and density profile

The extent of the Milky Way's stellar halo is unknown (and not well-defined). Halo stars are known to ~ 100 kpc and the most distant Galactic globular cluster lies at ~ 120 kpc (e.g. Harris 1996). As stars have been found travelling with speeds in excess of the local escape velocity (e.g. Abadi et al. 2009) it seems reasonable to suppose that *some* stars will be found out to the virial radius of the Milky Way.

Many attempts have been made to measure the shape and density profile of the halo using different tracers, producing similar but not identical results (see for example the discussion in Majewski 1993; Helmi 2008; Carollo et al. 2010). As we have noted above, observations indicate that the halo is highly structured. Most studies assume that the majority of halo stars belong to one or a few smoothly distributed components. A power law profile is typically used to fit the density profile of the halo overall. A wide range of exponents (from -2 to -5) have been measured for this profile, with each measurement probing different distance ranges and different tracer populations. Recent work by Carollo et al. (2010) based on a large sample of nearby halo stars suggests a double power-law model[36] comprising a steep inner halo profile $\rho_{\mathrm{inner}} \propto r^{-3.17\pm0.12}$ and a shallow outer halo profile $\rho_{\mathrm{outer}} \propto r^{-1.79\pm0.29}$.

Many studies seem to support the existence of a flattened (oblate) component in the halo (e.g. Sommer-Larsen & Zhen 1990) with a minor-to-major axis ratio as extreme as $c/a \sim 0.5$ (e.g. Lemon et al. 2004; Du et al. 2006), although a range of values up to $c/a \sim 0.9$ have been found in other work. The current consensus is $c/a \sim 0.6$ (Jurić et al. 2008; Helmi 2008). It is possible that confusion between the inner halo and the thick disc in the kinematic and chemical regions in which they overlap contributes to this uncertainty (Majewski 1993). Whatever the degree of flattening, the minor axis of the inner halo appears to be aligned (roughly) with the rotation axis of the Galaxy.

Measurements of the slope of the density profile are, of course, sensitive to the assumed shape. In light of the considerable amount of halo substructure discovered recently, it is unclear how existing measurements of halo shape and density should be interpreted, or indeed

---

[36] This well-established dichotomy in the properties of the halo is mirrored in the globular cluster system.

how the ‘shape’ of an intrinsically lumpy halo (made up from the superposition of different components) should be defined. We return to this point later in this thesis.

Chemical composition and age

Milky Way halo stars are characteristically metal poor, and on this basis are typically assumed to be old, although precise age determinations are few and highly uncertain (see e.g. Helmi 2008). The distribution of metallicities[37] for kinematically selected halo stars is broad, with a mean in the solar neighbourhood of [Fe/H] ~ -1.6 (e.g. Ryan & Norris 1991; Carollo et al. 2010). The tail of this distribution extends to the most metal-poor stars known (e.g. Schöerck et al. 2008), although the abundances of comparably ‘extremely metal-poor’ stars have been investigated recently in a number of satellites (e.g. Frebel et al. 2010b,a). Remnants of the first generations of star formation may survive among the halo stars (e.g. Gao et al. 2010).

Beyond [Fe/H] metallicities, the abundances of individual chemical elements can provide a detailed insight into the formation history of the halo. Abundances of the α elements (O, Mg, Si, Ca, S, Ti) in particular are widely used as a ‘clock’ timing the star formation rate of a population. The ratio of [α/Fe] remains constant as the population is enriched by type II supernovae (SNe), but then declines rapidly after approximately 1 Gyr, when type Ia SNe begin to recycle more iron than α-elements into the interstellar medium. A plot of [α/Fe] against [Fe/H] for a given population will form a track starting from the highest [α/Fe] and lowest [Fe/H] values of the population, which represent the conditions at the onset of star formation. These tracks evolve to increasing [Fe/H] and exhibit a characteristic ‘knee’ at the value of [Fe/H] reached after $\sim$ 1 Gyr. Populations formed rapidly will show this knee at higher metallicities than those formed gradually **(e.g. Tinsley 1979; Matteucci & Brocato 1990; Gilmore & Wyse 1991, 1998)**.

Significant application of this idea to the formation of the stellar halo has followed from the key work of Venn et al. (2004), who constructed [α/Fe] – [Fe/H] tracks for the Milky Way disc and thick disc, for a large sample of halo stars, and for a number of satellite galaxies. Their results are shown in Fig. 1.5, along with a compilation of measurements for four dwarf spheroidal satellites (this figure is reproduced from Tolstoy et al. 2009). Results such as those shown in Fig. 1.5 suggest that more luminous satellites (such as Sagittarius) were formed in short, intense and rapidly truncated star formation episodes, while less luminous satellites had less efficient, more extended star formation histories, and hence show a knee at lower [Fe/H]

---

[37] Here observed abundances Z are given in the form $[\mathrm{Z/H}] = \log_{10}(Z/X) - \log_{10}(Z_{\odot}/X_{\odot})$. Here Z may stand for either one element, such as iron, or a group of elements, such as the α elements or ‘metals’ (all nuclei more massive than Helium).

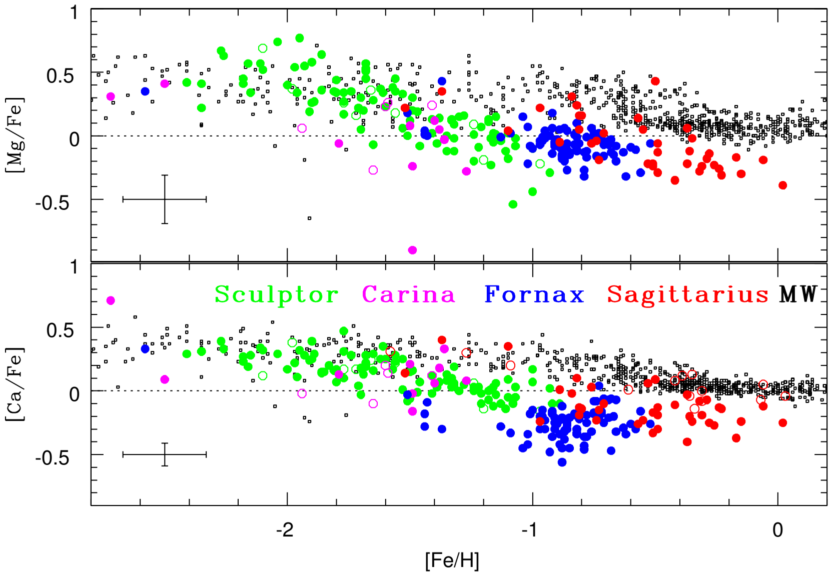

Figure 1.5: α-elements (Mg and Ca) in the dwarf galaxies Sagittarius (red), Fornax (blue), Sculptor (green) and Carina (magenta). The small black symbols are a compilation of MW disc and halo star abundances, from Venn et al. (2004). The 'knee' corresponding to the onset of type Ia supernovae is evident at $[\mathrm{Fe/H}] \sim -0.8$ dex for the Milky Way stars and (though less well-defined) at lower metallicities for the satellites. *Reproduced from Tolstoy et al. (2009); citations to individual observational results are given in that paper.*

.

(Tolstoy et al. 2009). The stellar halo sample follows this trend (the halo considered as a single component is presumably more massive than any of these satellites), but does not *overlay* any of the satellite tracks at high [Fe/H]. All the tracks overlap at a common threshold in $[\alpha/\mathrm{Fe}]$ at low metallicity, however, and show remarkably little scatter.

The differences between halo and satellite tracks in these diagrams, together with an apparent lack of extremely metal-poor stars in the classical dwarf spheroidals relative to the halo, has lead to suggestions (e.g. Helmi et al. 2006) that the progenitors of the halo (often called 'building blocks') did not have similar star formation histories to the surviving satellites. Of course, this result does not rule out the possibility that the halo was built by satellite accretion. Instead it implies simply that the present day 'survivors' of the hierarchical assembly of the Milky Way have systematically different histories to their siblings that did *not* survive. This in turn hints that the assembly of the stellar halo was stochastic and (given its mean metallicity and α enrichment) dominated by a small number of massive objects. These arguments have been supported by the simulations of Robertson et al. (2005) and Font et al. (2006a) and are discussed extensively in the context of our simulations in Chapter 3.

Considerable uncertainty remains in the sampling of the metal-poor tail of the halo metallicity distribution function (MDF). Schöerck et al. (2008) correct the metal-poor star counts in the Hamburg/ESO Survey (HES; Beers & Christlieb 2005; Christlieb et al. 2008) for selection bias. With this correction, they demonstrate a much closer agreement between the metal-poor tail of the halo MDF and those of the bright satellites than the earlier work on which the argument of Helmi et al. (2006) was based. Meanwhile, Kirby et al. (2008) have found a significant number of very metal-poor stars ($[\mathrm{Fe/H}] < -3.0$) in samples from the 'ultra-faint' dSphs, suggesting that the halo could more plausibly be built from a population resembling these faint satellites. Abundance measurements of halo stars, including those far beyond the Solar neighbourhood, also support the view that populations comparable to those of the very metal poor faint satellites have contributed (if only at a low level) to the halo (e.g. Fulbright 2002; Ivans et al. 2003; Roederer 2009; Ishigaki et al. 2010).

In principle, halo stars belonging to a common progenitor will share a common and 'unique' abundance pattern (assuming that an enriched intergalactic medium was not well-mixed between different progenitors). Searching for clustering of stars in the multi-dimensional space defined by many abundance ratios is (in theory) a powerful tool for identifying the different contributors of the halo despite their presently well-mixed state (Freeman & Bland-Hawthorn 2002). The detection in the Solar neighbourhood halo of two metal-rich populations with different abundance patterns by Nissen & Schuster (2010) is an early example of this idea in practice.

Substructure

In recent years, large samples of halo-star velocities (e.g. Morrison et al. 2000; Starkenburg et al. 2009) and 'galactic tomography' with photometric and spectroscopic surveys have demonstrated conclusively that the stellar halo is not a single smoothly-distributed entity, but instead a superposition of many components (Jurić et al. 2008; Bell et al. 2008; Carollo et al. 2007, 2009; Yanny et al. 2009). The striking SDSS 'field of streams' image of Belokurov et al. (2006) provided the first panoramic view of the halo, showing most of the currently known substructures. These include the broad stream of stars from the disrupting Sagittarius dwarf galaxy (Ibata et al. 1994, 2001b), a number of extensive, diffuse overdensities (clouds; Jurić et al. 2008; Belokurov et al. 2007a; Watkins et al. 2009; Kollmeier et al. 2009; Sesar et al. 2010), the Monoceros 'ring' or low-latitude stream (Newberg et al. 2002; Ibata et al. 2003; Yanny et al. 2003) and the narrow orphan stream (Belokurov et al. 2007b). Other kinematically cold debris has been tentatively identified (e.g. Schlaufman et al. 2009b). The true nature of many of these features remains to be established, and more continue to be found even in pre-existing data (e.g. Sharma et al. 2010).

In the Solar neighbourhood (e.g. within ~ 2.5 kpc of the Sun), proper motions are available for a substantial number of halo stars. Together with radial velocity measurements and accurate distances, these 6D coordinates can be used to isolate groups of stars with coherent motions. From such data Gould (2003) determined that no more than 5% of nearby halo stars could be contained in one single stream[38]. The available data is reviewed by Klement (2010), who lists 16 (tentative) stream detections in the literature to date. Amongst these, the stream discovered by Helmi & White (1999) seems to be particularly secure (Klement 2010). Smith et al. (2009a) determine that up to $\sim 7\%$ of nearby subdwarfs belong to this stream. Attempts have been made to link another significant stream on kinematic and chemical grounds with ω Centauri, an anomalous globular cluster widely suspected of being the nucleated core of a former dwarf galaxy (e.g. Meza et al. 2005, Nissen & Schuster 2010; further details of possible relationships between streams and ω Centauri are summarised by Klement 2010). The *Gaia* mission (Perryman et al. 2001) will soon revolutionise these studies in the Solar neighbourhood.

1.3.2 The M31 halo

Recent surveys of M31 (e.g. Ferguson et al. 2002; Irwin et al. 2005; Kalirai et al. 2006; Ibata et al. 2007; McConnachie et al. 2009) have revealed an extensive halo (to at least $\sim 150\,\mathrm{kpc}$) also containing abundant substructure. The halo of M31 is qualitatively different to that of the Milky Way, containing (in its inner regions) a much younger stellar population superimposed on a more Milky Way-like metal-poor component (e.g. Koch et al. 2008). The M31 halo also contains more luminous tidal features, most notably the giant southern stream (Ibata et al. 2001a). There are other differences between the two galaxies: their satellites differ in their distributions of effective radii and their collective spatial distribution (McConnachie & Irwin 2006); the bulge of M31 is more extensive and less clearly distinguished from the halo (Merrett et al. 2006); an irregular rotating 'extended disc' has been identified, although the relationship of this component to the thick disc of M31 (or the Milky Way) is unclear (Ibata et al. 2005; Collins et al. 2010); and the globular cluster distribution of M31 is richer than that of the Milky Way and more clearly associated with tidal features in the halo (Mackey et al. 2010). In addition, the disc of M31 shows signs of warps and bursts of star formation suggesting recent disturbance. Taken together these features suggest that M31 has experienced a more active recent accretion history than the Milky Way.

---

[38] This refers only to individual clumps in velocity space, and does not preclude more than one stream per progenitor, for example from different wraps in an evolving orbit (e.g. Smith et al. 2009a).

1.3.3 Stellar haloes in distant galaxies

Low surface-brightness features seen in projection around other galaxies inform the interpretation of the Milky Way's stellar halo, and vice versa. Diffuse concentric 'shells', fans and tails of stars on scales up to 100 kpc around otherwise regular elliptical galaxies are not uncommon (e.g. Schweizer 1980; Quinn 1984; Schweizer & Seitzer 1992; van Dokkum 2005; Tal et al. 2009). Most recently a catalogue of such features round elliptical galaxies in SDSS Stripe 82 observations has been compiled by Kaviraj (2010). This reveals many interesting extended features and highlights the fact that a large number of elliptical galaxies also possess stellar haloes, which can be used to probe their recent accretion histories.

A handful of deep observations beyond the Local Group suggest that stellar haloes around late-type galaxies are almost ubiquitous and highly diverse (e.g. Sackett et al. 1994; Shang et al. 1998; Malin & Hadley 1999; Martínez-Delgado et al. 2008, 2009; Faúndez-Abans et al. 2009). The surroundings of nearby bright spiral galaxies are now being targeted by observations using resolved star counts capable of reaching very low effective surface brightness limits. However, as yet no systematic survey has been carried out to a depth sufficient to detect analogues of the features discovered in the M31 halo (e.g. Zibetti & Ferguson 2004; McConnachie et al. 2006; de Jong et al. 2008; Barker et al. 2009; Ibata et al. 2009). Early results from the HST GHOSTS survey[39] suggest that the haloes of nearby spirals are often compact and flattened, with relatively high metallicity even at large galactocentric radii (e.g. de Jong et al. 2008).

1.4 An outline of this thesis

In this thesis, we will address several questions concerning the consistency between the CDM model, concordance theories of galaxies formation, and observations of stellar haloes (primarily those of the Milky Way and M31). We will use the N-body and semi-analytic techniques described above to simulate the assembly of the dark matter and stellar haloes of six Milky Way-like galaxies. The models we adopt have been calibrated using observations on much larger scales: we will examine their predictions for the population of satellite galaxies surviving around the Milky Way, and for the disrupted galaxies that build the stellar halo. We will seek to characterise the assembly of stellar haloes in terms of the number of contributing objects, their mass, time of arrival and stellar populations. Our ultimate aim is to relate observables, such as the spatial distribution and kinematics of halo stars, to the assembly of their

---

[39] `http://www-int.stsci.edu/~djrs/ghosts/`

host dark haloes. We take the first steps in making quantitative comparisons between existing observational data and our models.

The structure of this thesis is as follows. In Chapter 2 we describe the technical basis of our stellar halo model, a combination of GALFORM and the Aquarius simulations. We discuss important computational issues and support our parameter choices. In Chapter 3, we discuss the gross properties of the stellar haloes that we obtain with this model. In Chapter 4 we examine observations of substructure in the Milky Way halo in the context of our models and propose a simple statistic for quantifying this substructure. In Chapter 5 we explore the multi-component nature and large-scale kinematic properties of the stellar halo, and contrast these with those of the dark halo. Chapter 6 summarises our conclusions and discusses future prospects for theoretical models of the stellar halo, including extensions of the work in this thesis.

2

Spatially resolved stellar populations in semi-analytic models

2.1 Introduction

This chapter describes our approach to combining GALFORM with the Aquarius simulations[1]. Our aim is to predict the distribution of individual stellar populations in phase space, by adding a further step to the post-processing of the underlying N-body simulation. In this extra step, the stellar populations forming in each dark matter halo (according to the semi analytic model) are associated with sets of individual dark matter particles – we refer to these dark matter particles as being ‘tagged’ with stellar populations.

We use the positions and velocities of these tagged dark matter particles to track the evolving spatial distribution and kinematics of the associated stars. We are particularly concerned with those stars that are stripped from the satellites of the principal DM halo, building up a stellar halo. A standard semi-analytic approach, in which the structure of each galaxy is represented by a combination of purely *analytic* density profiles, would not be able to recover this information.

Tagging particles in this way is physically reasonable only if baryonic mass does not dominate anywhere in the total potential and perturb the collisionless dynamics of the dark matter. We assume, in effect, that adding baryons to the simulations would not significantly alter the positions and velocities of the dark matter particles we tag. This assumption is fundamental to our approach, but it is clearly violated in systems where the self-gravity of gas and stars is significant, such as the Milky Way’s thin disc. The structure and kinematics of these massive galactic discs are the result of dissipative processes. Although the semi-analytic component of our model self-consistently accounts for the growth of a thin disc and the adiabatic response of the dark halo (Cole et al. 2000), this cannot be easily extended to our dark matter tagging

---

[1] Hereafter we refer to these simulations simply as ‘Aquarius’.

scheme. For example, as we discuss below, it would be particularly difficult to identify a sufficient number of dark matter particles on circular orbits of comparable energy. For this reason, and also to avoid confusion with our accreted halo stars, we do not attempt to tag dark matter to represent stars forming in situ in a thin disc at the centre of the main halo.

This limitation restricts the method we describe to systems in which dark matter dominates the gravitational potential (less restrictive methods may be developed in future). The dwarf satellites of the Milky Way and M31 appear to be ideal candidates, as their measured velocity dispersions indicate high mass-to-light ratios (as discussed in Chapter 1; e.g. Simon & Geha 2007; Walker et al. 2009b). In this thesis, we concentrate on Milky-Way like stellar haloes assembled through the disruption of dwarf satellite galaxies such as these.

2.1.1 Previous work

There have been a number of earlier studies of Milky Way-like stellar haloes using approaches that resemble our particle-tagging scheme. White & Springel (2000) identified star-forming haloes in an N-body simulation of a galaxy cluster using a semi-analytic model, and tracked the most-bound particles in those haloes. This work was the first to link together the spatial and kinematic evolution of individual particles in an N-body simulation with predictions for the properties of their associated stellar populations. It established several fundamental results concerning the assembly of the spheroidal component in a Milky Way-like ΛCDM galaxy. Among these were that 'spheroids' (bulges and haloes) are formed from a small number of progenitors; that the accreted bulge contains most of the spheroid stars and is assembled at early times from relatively massive progenitors; and that even old halo stars can be metal rich.

The more recent work of De Lucia & Helmi (2008) reprised this approach, again post-processing a fully cosmological N-body simulation with a semi-analytic model to identify the star-forming progenitor haloes of a Milky Way analogue. As in our work, groups of tightly bound dark matter particles were selected in these haloes and tagged with appropriate stellar populations. Although the simulations used by De Lucia & Helmi (2008) had sufficient resolution to resolve the most significant stellar halo progenitors and the overall structure of the halo, they could not resolve structural details comparable with observations (in particular, stellar streams).

An important variant of this technique was used by Bullock et al. (2001). These models, unlike the work of White & Springel (2000) and De Lucia & Helmi (2008), simulated the evolution of *individual* satellite galaxies in the potential of a Milky Way-like host (described analytically).

Several accretion histories were generated for a Milky Way-mass halo using the extended Press-Schechter formalism (Press & Schechter 1974; Bond et al. 1991; Bower 1991; Lacey & Cole 1993).

A stellar population (specifically, the abundance of RR Lyrae stars) was determined for each accreted halo, using a simple semi-analytic prescription specifically tuned to reproduce observations of the Milky Way satellites (as opposed to more general models of cosmology and galaxy formation). Each satellite was 'injected' into a spherically symmetric analytic central halo potential along an orbit randomly selected from parameter distributions consistent with cosmological simulations. The orbit of each satellite was integrated in the host potential and populated with points representing RR Lyrae stars, again according to analytic recipes. The orbital decay of the satellite due to dynamical friction was also modelled analytically, as was its tidal disruption.

This approach sacrifices generality for increased resolution. It allowed Bullock et al. to predict the structure of the stellar halo (i.e. the density profile of halo RR Lyrae stars) and to show that a high degree of substructure is expected at large radii, where the halo is dominated by 'dynamically young' streams that have not been phase-mixed. In their simulations Bullock et al. (2001) did not include the contribution to the stellar halo made by progenitor satellites that merge with the central galaxy, but only those made by satellites that are tidally disrupted before reaching the centre of the halo.

The most widely cited simulations of Milky Way-like stellar haloes to date are those of Bullock & Johnston (2005), further analysed by Font et al. (2006a,b), Robertson et al. (2005) and Johnston et al. (2008). Following the approach of Bullock et al. (2001), eleven distinct accretion histories were generated for haloes of mass $1.4{\times}10^{12}\mathrm{M}_{\odot}$. However, in the Bullock & Johnston (2005) simulations, one full N-Body simulation was performed for each accretion event. The growth of the central halo potential (now assumed axisymmetric, including a thin disc contribution) was modelled by assuming smooth increase in mass.

Satellites in the Bullock & Johnston models were based on an NFW dark matter halo (Navarro et al. 1996, 1997), set up for each individual case by rescaling a single set of initial conditions. The stellar component within each satellite halo was set up to follow a 'massless' King model density profile in dynamical equilibrium within the potential well of the dark matter, by tagging particles with a mass-to-light ratio according to their binding energy. The parameters of the King model were fixed in each case by assuming linear scalings with satellite luminosity, calibrated to match the slope of the relation between half-light radius and M_{V} for the classical Milky Way satellites. Hence, all properties of the model satellites were fixed *a priori*.

The Bullock & Johnston (2005) models achieved a high level of resolution for individual satellites by making similar approximations to Bullock et al. (2001) and by running one simulation per satellite (neglecting interactions between substructures within the halo). Many results have followed from the work of Bullock & Johnston (2005), demonstrating the value of this technique for studying the assembly of stellar haloes under idealised conditions. These simulations cannot be easily compared to observational results, however, because they are not based on a fully general and self-consistent ΛCDM galaxy formation model, and because the simplifying assumptions they employ (such as a smooth potential and spherically symmetric satellite accretion) do not represent the full complexity of ΛCDM structure formation. These shortcomings motivate the more general model that we present in this thesis.

2.1.2 The GALFORM Model

Many of the physical processes of greatest relevance to galaxy formation on small scales were explored within the context of semi-analytic modelling by Benson et al. (2002b). Of particular importance are the suppression of baryon accretion and cooling in low mass haloes (the result of photoheating by a cosmic ionizing background), and the effect of supernova feedback in shallow potential wells. Together, these effects constitute a straightforward astrophysical explanation for the disparity between the number of low mass dark subhaloes found in N-body simulations of Milky Way-mass hosts and the far smaller number of luminous satellites observed around the Milky Way (the so-called 'missing satellite' problem). Recent discoveries of faint dwarf satellites and an improved understanding of the completeness of the Milky Way sample (Koposov et al. 2008; Tollerud et al. 2008, and references therein) have reduced the deficit in the number of *observed* satellites, which is now in agreement with the predictions of Benson et al. (2002b). At issue now is the quality (rather than the lack) of agreement between such models and the data. The model we adopt here gives a reasonable match to the observed satellite luminosity function, but is far from complete (see Chapter 6). In our description of the model, we pay particular attention to the suppressive effect of photoheating. This is a significant process for shaping the faint end of the satellite luminosity function when, as we assume, the strength of supernova feedback is fixed by constraints on the galaxy population as a whole.

2.1.3 Reionization and the satellite luminosity function

A simple model of reionization heating based on a halo mass dependent cooling threshold (Benson et al. 2003) is implemented in the Bower et al. (2006) model of GALFORM. This threshold is set by parameters termed V_{cut} and z_{cut}. No gas is allowed to cool within haloes having a circular velocity below $V_{\rm cut}$ at redshifts below $z_{\rm cut}$. This scheme approximates the more detailed model of Benson et al. (2002b), in which photoheating of the intergalactic medium was modelled explicitly. It reproduces the link between the suppression of cooling and the evolution of the 'filtering mass' (as defined by Gnedin 2000). In practice the value of $V_{\rm cut}$ is most important in this simple model. Variations in $z_{\rm cut}$ within plausible bounds have a less significant effect on the $z = 0$ luminosity function.

The GALFORM implementation and parameters of Bower et al. (2006) have been shown to give a good match to the properties of the large-scale galaxy population. We therefore adopt the model of Bower et al. (2006) as a fiducial model. However, we make a single parameter change, lowering the value of $V_{\rm cut}$ from $50\,{\rm km\,s^{-1}}$ to $30\,{\rm km\,s^{-1}}$. This choice is motivated by recent *ab initio* cosmological galaxy formation simulations incorporating the effects of photoionization self-consistently (Hoeft et al. 2006; Okamoto et al. 2008; Okamoto & Frenk 2009; Okamoto et al. 2009). These studies find that values of $V_{\rm cut} \sim 25 - 35\,{\rm km\,s^{-1}}$ are preferable to the higher value suggested by the results of Gnedin (2000) and adopted in previous semi-analytic models (e.g. Somerville 2002; Bower et al. 2006; Croton et al. 2006; Li et al. 2009a). Altering this value affects only the very faint end of the galaxy luminosity function, and so should not change the results of Bower et al. (2006). The choice of a fiducial set of semi-analytic parameters in this thesis illustrates the flexibility of our approach to modelling stellar haloes. The N-body component of our models (Aquarius) represents a considerable investment of computational time. In contrast, the semi-analytic post-processing can be re-run in only a few hours, and can be easily 'upgraded' (by adding physical processes and constraints) to provide more detailed output, to explore the consequences of parameter variations, or to compare alternative semi-analytic models.

The V-band satellite luminosity functions shown in Fig. 2.1 result from applying the GALFORM model described above to each Aquarius halo. Satellites are defined as all galaxies within a radius of 280 kpc from the centre of potential in the principal halo, equivalent to the limiting distance of the Koposov et al. (2008) completeness-corrected observational sample. These luminosity functions are measured from the *particle* realisations of satellites that we describe in the following section, and not directly from the semi-analytic model. They therefore account for the effects of tidal stripping, although these are minor: the fraction of satellites brighter than $M_{\rm V} = -10$ is reduced very slightly in some of the haloes by stripping. In agreement with the findings of Benson et al. (2002a), the model matches the faint end of the luminosity function well, but fewer bright satellites are found in each of our six models than are observed in the mean of the Milky Way + M31 system (although the number of objects concerned is small). The

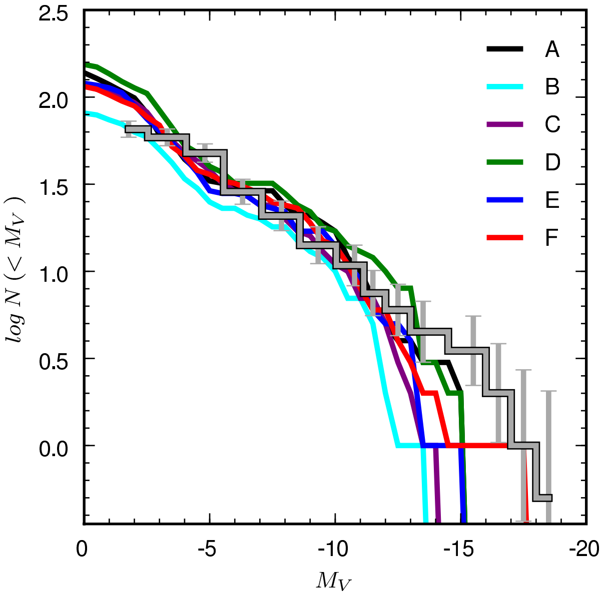

Figure 2.1: The cumulative V-band luminosity functions (LFs) of satellite galaxies for the six Aquarius haloes, adopting the GALFORM parameters of Bower et al. (2006) with $V_{\mathrm{cut}} = 30\,\mathrm{km\,s^{-1}}$. These LFs *include* the effects of tidal stripping measured from our assignment of stars to dark matter particles (Section 2.2), although this makes only a small difference to the LF obtained from our semi-analytic model alone. All galaxies within 280 kpc of the halo centre are counted as satellites. The stepped line (grey, with error bars) shows the observed luminosity function found by Koposov et al. (2008) for the mean of the MW and M31 satellite systems (also to 280 kpc), assuming an NFW distribution for satellites and correcting for SDSS sky coverage and detection efficiency below $M_{\mathrm{v}} = -10$. The colour-coding of haloes in this figure is used throughout this thesis.

true abundance of bright satellites for Milky Way-mass hosts is poorly constrained at present, so it is unclear whether or not this discrepancy reflects sample variance, a disparity in mass between the Aquarius haloes and the Milky Way halo, or a shortcoming of our fiducial Bower et al. (2006) model. A modification of this model in which the tidal stripping of hot gas coronae around infalling satellites is explicitly calculated (rather than assuming instantaneous removal; see Font et al. 2008) may increase the abundance of bright satellites.

2.1.4 Further details

Unresolved satellite haloes

Within GALFORM, when the host subhalo of a satellite galaxy is no longer identified at the resolution limit imposed by SUBFIND, its cold gas is transferred instantly to the disc of the central galaxy. In the Aq-2 simulations this limit corresponds to a minimum resolved dark halo mass of $\sim 3 \times 10^5 \mathrm{M}_{\odot}$. In the GALFORM model of Bower et al. (2006), which does not include tidal stripping or a separate 'stellar halo' component, the satellite galaxy is considered to be fully disrupted (merged) at this point and its stars are also transferred to the bulge component of the central galaxy. In contrast, the particle representation we describe in Section 2.2 allows us to follow the *actual* fate of the satellite stars, independent of the semi-analytic model. The component to which the semi-analytic model assigns the satellite stars is therefore largely a matter of 'book-keeping'.

Semi-analytic models based on N-body simulations often choose to 'follow' satellites with dark haloes falling below the numerical resolution by calculating an appropriate merger timescale from the last-known N-body orbital parameters, accounting for dynamical friction. However, the resolution of Aquarius is sufficiently high to make a simpler and more self-consistent approach preferable in this case as it preserves the one-to-one correspondence between star-forming semi-analytic galaxies and self-bound dark matter haloes in the simulation. We have checked that allowing semi-analytic galaxies to survive without resolved subhaloes, subject to the treatment of dynamical friction used by Bower et al. (2006), affects only the faintest ($M_{\mathrm{v}} \sim 0$) part of the survivor luminosity function. This approach does not prematurely merge galaxies in the semi-analytic model that are still capable of seeding new stellar populations into the particle representation. The true nature and survival of these extremely faint sub-resolution galaxies remains an interesting issue to be addressed by future semi-analytic models of galactic satellites.

Central Galaxy Properties

In Table 3.1 (Section 3.1) we list the V-band magnitudes and total stellar masses, M_{gal}, of the central galaxies that form in the six Aquarius haloes. A wide range is evident, from an M31-analogue in halo Aq-C, to an M33-analogue in Aq-E. This is not unexpected: the Aquarius dark haloes were selected only on their mass and isolation, and these criteria alone do not guarantee that they will host close analogues of the Milky Way. The scaling and scatter in the predicted relationship between halo mass and central galaxy stellar mass are model-dependent. With the GALFORM parameter values of Bower et al., the mean central stellar mass in a typical Aquarius halo ($M_{\mathrm{halo}} \sim 1.4 \times 10^{12}\mathrm{M}_{\odot}$) is $\sim 1.5 \times 10^{10}\,\mathrm{M}_{\odot}$, approximately a factor of 3–4 below typical estimates of the stellar mass of the Milky Way ($\sim 6 \times 10^{10}\,\mathrm{M}_{\odot}$; Flynn et al. 2006). The scatter in M_{gal} for our central galaxies reflects the overall distribution produced by the model of Bower et al. (2006) for haloes of this mass. The model of De Lucia et al. (2006) was also constrained using statistical properties of bright field and cluster populations. This model produces a mean central stellar mass of $\sim 4 \times 10^{10}\,\mathrm{M}_{\odot}$ for the typical halo mass of the Aquarius simulations, as well as a smaller scatter about the mean value.

In light of these modelling uncertainties and because the true Milky Way dark halo mass has not yet been determined to within a factor of two, we prefer not to re-scale the Aquarius haloes to a specific common mass for 'direct' comparison with the Milky Way[2]. The results we present concerning the assembly and structure of stellar haloes and the ensemble properties of satellite systems should be insensitive to whether or not their galaxies are predicted to be direct analogues of the Milky Way by the Bower et al. (2006) GALFORM model. Therefore, in interpreting the *absolute* values of quantities compared to observational data in the following sections, it should be borne in mind that we model a *range* of halo masses that might lie below the most likely Milky Way value (see Chapter 5).

Mass-metallicity relation

The Bower et al. (2006) implementation of GALFORM predicts a stellar mass-metallicity relation for faint galaxies which is slightly steeper than that derived from the satellites of the Milky Way and M31 (e.g. Mateo 1998; Kirby et al. 2008; see also Tremonti et al. 2004 and references therein). As shown in Fig. 2.2our model galaxies are on average $\sim 0.5\,\mathrm{dex}$ more metal-poor in $[\mathrm{Fe/H}]$ than the observed relation at magnitudes fainter than $M_{\mathrm{V}} \sim -10$. Whilst it would be straightforward to make adjustments to the model parameters in order to match this relation, doing so may violate the agreement established between the Bower et al. (2006) parameter set and a wide range of statistical constraints from the bright ($M_V < -19$) galaxy population. As we prefer to retain our fiducial model, we accept this shortcoming (see also Font et al. 2011, in preparation). We also note that the offset with the observed mass-metallicity relation is smallest for the brightest satellites, which contribute the majority of halo stars.

2.2 Building stellar haloes

2.2.1 Assigning stars to dark matter

Observations of the stellar velocity distributions of dwarf spheroidal satellites of the Milky Way imply that these objects are dispersion-supported systems with extremely high mass-to-light ratios, of order 10–1000 (e.g. Mateo 1998; Simon & Geha 2007; Strigari et al. 2007; Wolf et al.

---

[2] Specifically, we do not rescale the simulations in any of the results presented in chapters 2, 3 and 4. We do carry out a rescaling in Chapter 5, however.

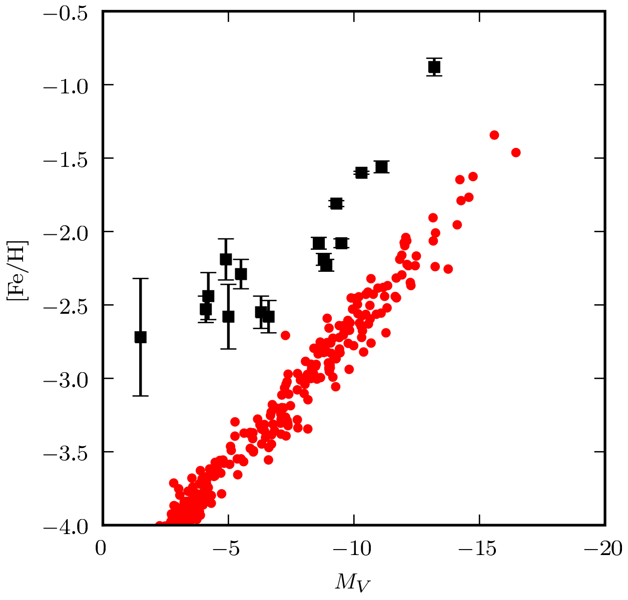

Figure 2.2: Mass-metallicity relation for all Aquarius satellite galaxies with the fiducial GALFORM model used in this thesis (red points). Black points show observational data for the Milky Way satellites from Norris et al. (2010).

2009; Walker et al. 2009b). As we describe in this section, in order to construct basic models of these high-M/L systems without simulating their baryon dynamics explicitly, we will assume that their stars are formed 'dynamically coupled' to a strongly bound fraction of their dominant dark matter component, and that they continue to trace that component. Here we further assume that the depth at which stars form in a halo potential well depends only on the total mass of the halo. As a description of stellar dynamics in such systems, these assumptions are really too simplistic to be compared directly with structural and kinematic observations. Nevertheless, we show that they result in half-light radii and line-of-sight velocity dispersions in agreement with those of Milky Way dwarf spheroidals. Hence we assume that the disruption of a fraction of these model satellites by tidal forces in the main halo will reproduce tidal streams and similar features at a level of detail sufficient to investigate the assembly and gross structure of stellar haloes. We stress that we use these comparisons with observations as constraints on the single additional free parameter introduced by our model. They are not intended as predictions for the satellite population.

In the context of our GALFORM model, a given satellite can be thought of as a superposition of many distinct stellar populations, each defined by a particular formation time and metallicity. The N-body halo merger tree used as input to GALFORM is discretized by the finite number of output times (snapshots) available from the simulation. However, much finer interpolating timesteps are taken between these snapshots when solving the differential equations governing star formation. Hence a large number of distinct populations are 'resolved' by GALFORM. Even so, we can only update our particle (dynamical) data and assign stars to dark matter at the output times of the pre-existing N-body simulation. For the purposes of performing star-to-dark-matter assignments we must restrict ourselves to these timesteps, and reduce the fine-grained information computed by GALFORM between each pair of snapshots to a single aggregated population of 'new stars' for each galaxy.

The aim of our method here is to select a sample of representative particles from the parent N-body simulation to trace *each such stellar population*, individually. First we will describe the general objective of our selection process, and then we will examine the selection criteria that we apply in practice.

Consider first the case of a single galaxy evolving in isolation. At a given simulation snapshot (B) the total mass of new stars formed since the previous snapshot (A) is given by the difference in the stellar mass of the semi-analytic galaxy recorded at each time by the semi-analytic model,

$$\Delta M_{\star}^{AB} = M_{\star}^{B} - M_{\star}^{A}. \tag{2.1}$$

In our terminology, $\Delta M_{\star}^{AB}$ is the mass of a single stellar population formed between two snapshots[3]. The total mass in metals within the population is determined in the same way as the stellar mass[4]. In a similar manner, the luminosity of the new population (at $z = 0$) is given by the difference of the total luminosities (corrected for evolution to $z = 0$) at successive snapshots.

We select a set of particles to be tracers of the stellar population $\Delta M_{\star}^{AB}$ from among those identified with the dark matter halo of the galaxy at B. The exact criteria for selection are explained below. Particles in this tracer set are 'tagged', i.e. are identified with data describing the stellar population. We give equal 'weight' (fraction of stellar mass, luminosity and metals in $\Delta M_{\star}^{AB}$) to each particle in the set of tracers. We repeat this process for all snapshots, applying our criteria to *obtain a new set of DM tracers each time new stars are formed* in a particular galaxy. In the scheme we adopt, the same DM particle can be selected as a tracer at more than one output time (i.e. the same DM particle can be tagged with more than one stellar population). Hence a given DM particle will accumulate its own individual star formation history. The dynamical

---

[3] We do not track the small amount of mass lost during subsequent stellar evolution.

[4] We do not follow individual chemical elements.

evolution of satellite haloes determines whether or not a particular particle is eligible for the assignment of new stars during any given episode of star formation.

So far we have considered a completely isolated galaxy. In practice, we apply this technique to merger trees, in which 'central' galaxies grow by the accretion of satellites as well as by *in situ* star formation. In the expression (2.1) above, the total stellar mass at A, $M_\star^A$, is simply modified to include a sum over N immediate progenitor galaxies in addition to the galaxy itself i.e.,

$$\Delta M_\star^{AB} = M_\star^B - M_{\star,0}^A - \sum_{i>0} M_{\star,i}^A \tag{2.2}$$

where $M_{\star,0}^A$ represents the galaxy itself and $M_{\star,i}^A$ is the total stellar mass (at A) of the i'th progenitor deemed to have merged with the galaxy in the interval AB. Stars forming in the progenitors during the interval AB and stars forming in the galaxy itself are treated as a single population.

This procedure requires that a one-to-one correspondence exists between a galaxy and a dark matter halo (or subhalo) from which particles can be chosen as tracers of its newly formed stars. As discussed in Section 2.1.4, a satellite galaxy whose host subhalo can no longer be identified by SUBFIND has its cold gas content transferred immediately to the central galaxy of its parent halo and forms no more new stars. In the semi-analytic model, the stars of the satellite are also added to the bulge component of the central galaxy. This choice is irrelevant in our particle representation, as we can track the actual fate of these stars.

2.2.2 Assignment criteria

Selection of dark matter particles

In this section we describe how we choose the dark matter particles within haloes that we want to tag with a newly formed stellar population. In Section 2.1.1 we described the particle-tagging method employed by Bullock & Johnston (2005), the philosophy of which might be termed '*in vitro*', as it uses idealised initial conditions to simulate accretion events individually in a 'controlled' environment. By contrast, our approach is to *postprocess* fully cosmological simulations '*in vivo*'[5]. In a fully cosmological N-body simulation the growth of the central potential, the structure of the halo and the orbits, the accretion times and the tidal disruption of subhaloes are all fully consistent with one another. The central potential can have an arbitrary triaxial shape (although no disc component is included in our dynamical model) and can grow

---

[5] This terminology should not be taken to imply that 'star particles' themselves are included in the N-body simulation; here stellar populations are simply tags affixed to dark matter particles.

through violent mergers as well as through smooth accretion. Therefore, our model can be applied at high redshift when the halo is undergoing rapid assembly. These complexities in the halo potential encountered in a fully cosmological simulation are likely to influence the dynamics of satellites (e.g. Sales et al. 2007a) and the evolution of streams, through the effects of phase-mixing and orbital precession (e.g. Helmi & White 1999).

Our approach to selecting dark matter particles for stellar tagging is different to that of Bullock & Johnston (2005), because we are postprocessing a cosmological N-body simulation rather than constructing idealised initial conditions for each satellite. Rather than assigning the mass-to-light ratio of each tagged particle by comparing stellar and dark matter energy distribution functions in the halo concerned, *we assume that the energy distribution of newly formed stars traces that of the dark matter*. We order the particles in the halo by binding energy[6] and select a most-bound fraction f_{MB} to be tagged with newly-formed stars. As previously described, stars are shared equally among the selected DM particles.

This approach constitutes an extremely simplistic dynamical model for stars in dwarf galaxies. However, the main results of this thesis do not concern the satellites themselves; instead we focus on the debris of objects that are totally (or largely) disrupted to build the stellar halo. As we describe below, we compare the structure and kinematics of our model satellites (those that survive at $z = 0$) to Local Group dwarf galaxies in order to fix the value of the free parameter, f_{MB}. Since we impose this constraint, our method cannot predict these satellite properties *ab initio*. Constraining our model in this way ensures reasonable structural properties in the population of progenitor satellites, and allows us to make predictions for the stellar halo. More complex models are certainly possible, in which f_{MB} is not a free parameter but is instead physically determined based on the semi-analytic model. It would also be possible to use a more complicated tagging scheme that better represents star formation in a disc, for example. However, such models would add substantial complexity to the method and there are currently very few observational constraints on how stars are actually formed in satellite galaxies. Thus, we believe that a simple model suffices for our present study of the stellar halo.

Our approach has similarities with that of De Lucia & Helmi (2008), who tag the most bound 10% of particles in satellite haloes. However, De Lucia & Helmi perform this tagging only *once* for each satellite, at the time at which its parent halo becomes a subhalo of the main halo

---

[6] Here, the most bound particle is that with the most negative total energy, including both kinetic and gravitational contributions. Binding energies are computed relative to the bound set of particles comprising an object identified by SUBFIND.

(which we refer to as the time of infall[7]). Their approach (like that of Bullock & Johnston 2005) defines the end result of the previous dynamical evolution of an infalling satellite, the former by assuming light traces dark matter and the latter with a parameterized King profile.

In our model each newly-formed stellar population is assigned to a subset of DM particles, chosen according to the 'instantaneous' dynamical state of its host halo (independently of any previous star formation in the same halo). The overall structure structure of a satellite at any point in the simulation is determined by the dynamical evolution of the many tracer sets it contains.

Further criteria imposed on particle selections

Implementing a particle-tagging scheme within a fully cosmological simulation requires a number of additional issues to be addressed, which we summarise here along with our solutions.

1. *Subhalo assignments*: Star formation in a satellite galaxy will continue to tag particles regardless of the level of its halo in the hierarchy of bound structures (halo, subhalo, subsubhalo etc.). The growth of a dark matter halo ends when it becomes a subhalo of a more massive object, whereupon tidal stripping starts to reduce its mass. The assignment of stars to particles in the central regions should, of course, be insensitive to the stripping of dark matter at larger radii. However, choosing a fixed fraction of dark matter tracer particles to represent new stellar populations couples the number of particles chosen to the total mass of the subhalo. Therefore, when assigning stars to particles in a subhalo (rather than the main halo of a FOF group), we select a fixed *number* of particles rather than a fix fraction. This number is equal to the number in the most-bound fraction f_{MB} at the time of the infall of the subhalo.

2. *Equilibrium criterion*: To guard against assigning stars to sets of tracer particles that are temporarily far from dynamical equilibrium, we adopt the conservative measure of deferring assignments to any halo in which the centres of mass and potential are separated by more than 7% of the half-mass radius $r_{1/2}$. We select $0.07\,r_{1/2}$ in accordance with the criterion of $0.14\,r_{\mathrm{vir}}$ used to select relaxed objects in the study of Neto et al. (2007), taking $r_{\mathrm{vir}} \sim 2\,r_{1/2}$. These deferred assignments are carried out either at the next snapshot at

---

[7] In both Bullock & Johnston (2005) and De Lucia & Helmi (2008) only satellites directly accreted by the main halo 'trigger' assignments to dark matter; the hierarchy of mergers and accretions forming a directly-infalling satellite are subsumed in that single assignment.

which the halo satisfies this criterion, or when it becomes a subhalo of a more massive halo.

3. *No in situ star formation*: Stars formed in the principal galaxy in each Aquarius simulation[8] are never assigned to DM particles. This exclusion is applied over the entire history of that galaxy. Stars formed in situ are likely to contribute to the innermost regions of the stellar halo, within which they may be redistributed by mergers. However, the dynamics of stars formed in a dissipationally-formed, baryon-dominated thin disc cannot be represented with particles chosen from a dark matter-only simulation. Our technique would still offer the possibility of extracting *some* information on a fraction of in situ stars if we were to assign them to dark matter particles (those contributing to the bulge or forming at early times, for example). However, we choose to omit this additional complexity here and study the accreted component in isolation. SPH simulations of stellar haloes (which naturally model the in situ component more accurately than the accreted component) suggest that the contribution of in situ stars to the halo is small beyond ~ 20 kpc (Abadi et al. 2006; Zolotov et al. 2009).

   At early times, when the principal halo in each simulation is growing rapidly and near-equal-mass mergers are common, the definition of the 'main' branch of its merger tree can become ambiguous. Also, the main branch of the galaxy merger tree need not follow the main branch of the halo tree. Hence, our choice of which branch to exclude (on the basis that it is forming 'in situ' stars) also becomes ambiguous. Indeed, it is not clear that any of these 'equivalent' early branches should really be excluded.

   Later we will show that two of our haloes have concentrated density profiles. We have confirmed that these *do not* arise from making the 'wrong' choice in these uncertain cases, i.e. from tagging particles in the dynamically robust core of the 'true' main halo. Making a different choice of the excluded branch in these cases (before the principal branch can be unambiguously identified) simply replaces one of these concentrated components with another very similar component. Therefore, we adopt the stated definition of the galaxy main branch when excluding in situ stars.

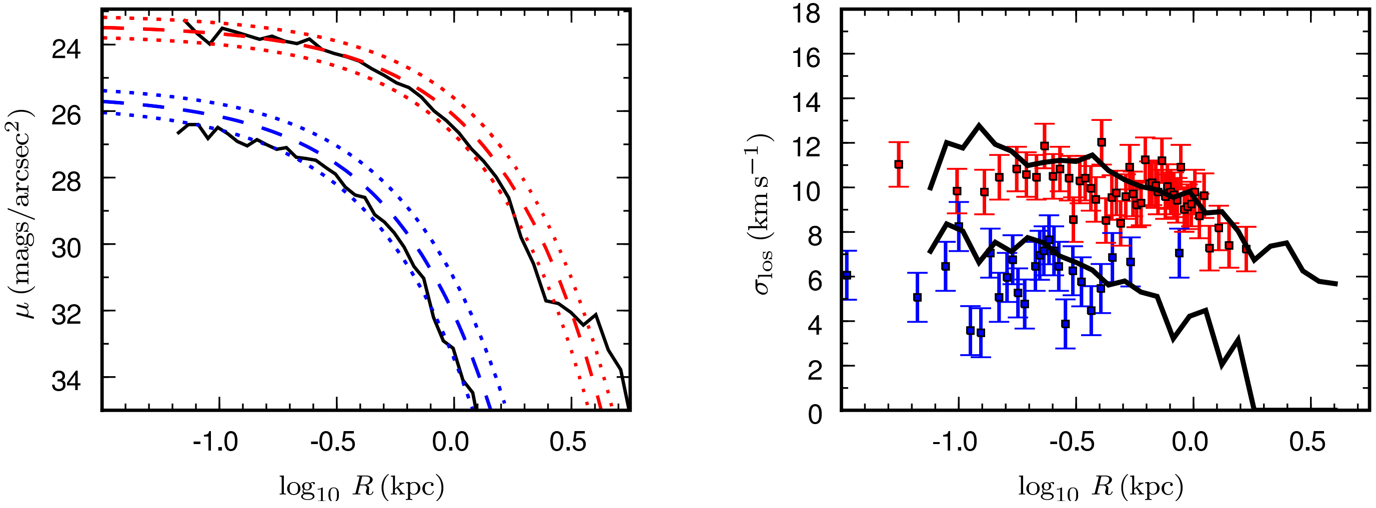

Figure 2.3: Examples of individual satellites in our models (solid black lines), compared to Fornax (red) and Carina (blue), showing surface brightness (left, Irwin & Hatzidimitriou 1995) and line-of-sight velocity dispersion (right, Walker et al. 2009a). With our fiducial GALFORM model, simultaneous matches to both $\sigma(R)$ and $\mu(R)$ for these datasets are found only among satellites that have undergone substantial tidal stripping (see text).

Individual satellites

In the following section we show that, with a suitable choice of the most-bound fraction, our method produces a population of model satellites at $z = 0$ that is consistent with observed relationships between magnitude, half-light radius/surface brightness and velocity dispersion for the satellite populations of the Milky Way and M31. In Fig. 2.3 we show profiles of surface brightness and velocity dispersion for two individual satellites from our models at $z = 0$, chosen to give a rough match to observations of Fornax and Carina. That we can find any close analogues of these satellites suggests that our galaxy formation model and the simple prescription for the spatial distribution of star formation is capable of producing realistic stellar structures within dark haloes. However, while it is possible to match these individual observed satellites with examples drawn from our models, we caution that we can only match their observed surface brightness and velocity dispersion profiles *simultaneously* by choosing model satellites that have suffered substantial tidal stripping. This is most notable in the case of our match to Fornax, which retains only 2% of its dark matter relative to the time of its accretion to the main halo, and 20% of its stellar mass.

We have tested our method with assignments for each satellite delayed until the time of infall, as in De Lucia & Helmi (2008). This results in slightly more compact galaxies than our standard approach, where mergers and tidal forces (and relaxation through two-body encounters for objects near the resolution limit) can increase the energies of tagged dark matter particles over time. However, we find that this makes little difference to the results that we discuss below.

Parameter constraints and convergence

We now compare the $z = 0$ satellite populations of our models with trends observed in the dwarf companions of the Milky Way and M31. We do this in order to determine a suitable choice for the fixed fraction, f_{MB}, of most-bound dark matter particles that we select for each assignment of stars. Our aim is to study the stellar halo, so we use the sizes of our surviving satellites as a constraint on f_{MB} and as a test of convergence. We find that within the range of f_{MB} that produces plausible satellites, the gross properties of our stellar haloes, such as total luminosity, change by only a few percent.

In Fig. 2.4, we show the relationship between the absolute magnitudes, M_{V}, of satellites

---

[8] Identified as the central galaxy of the most massive dark halo at $z = 0$.

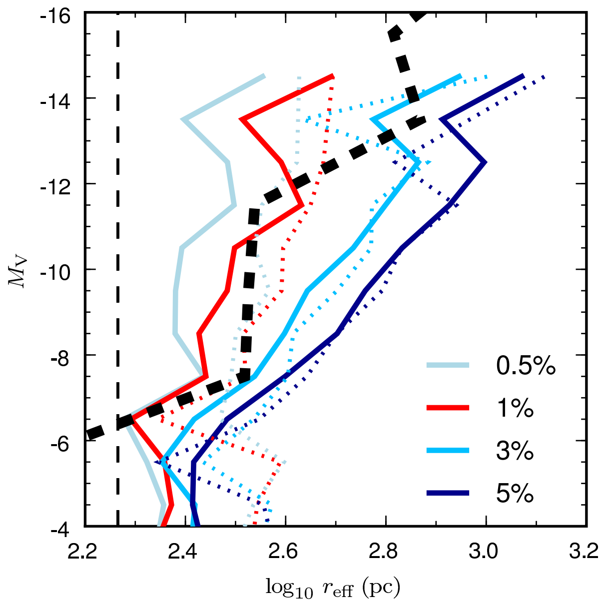

Figure 2.4: Median effective radius $r_{\rm eff}$ (enclosing half of the total luminosity in projection) as a function of magnitude for model satellites in haloes Aq-A and Aq-F at $z = 0$. A thin vertical dashed line indicates the softening scale of the simulation: $r_{\rm eff}$ is unreliable close to this value and meaningless below it. *Thick lines* represent our standard high-resolution simulations (Aq-2) using a range of values for $f_{\rm MB}$, the fraction of most bound particles chosen in a stellar population assignment. *Dotted lines* correspond to lower resolution simulations (Aq-3) of the same haloes. A *thick dashed line* shows the median relation from observations of Local Group dwarf galaxies. These galaxies, and our model data points for all haloes in the Aq-2 series with $f_{\rm MB} = 1\%$, are plotted individually in Fig. 2.5.

(combining data from two of our simulations, Aq-A and Aq-F), and the projected radius enclosing one half of their total luminosity (which we refer to as the effective radius, $r_{\rm eff}$). We compare our models to a compilation of dwarf galaxy data in the Local Group, including the satellites of the Milky Way and M31. The slope of the median relation for our satellites agrees well with that of the data for $f_{\rm MB} = 1\%$ to 3%. It is clear that a choice of 5% produces bright satellites that are too extended, while for 0.5% they are too compact. We therefore prefer $f_{\rm MB} = 1\%$. A more detailed comparison to the data at this level is problematic: the observed sample of dwarf galaxies available at any given magnitude is small, and the data themselves contain puzzling features such as an apparently systematic difference in size between the bright Milky Way and M31 satellites (McConnachie & Irwin 2006).

Fig. 2.4 also shows the same results for our model run on the lower-resolution simulations of haloes Aq-A and Aq-F (as dotted lines). The particle mass in the Aq-3 series is approximately three times greater than that of the Aq-2 series, and the force softening scale is larger by a factor of two. We concentrate on the convergence behaviour of our simulations for galaxies larger than the softening length, and also where our sample provides a statistically meaningful number of galaxies at a given magnitude; this selection corresponds closely to the regime of the brighter dwarf spheroidal satellites of the Milky Way and M31, $-15 < M_{\mathrm{V}} < -5$. In this regime, Fig. 2.4 shows convergence of the median relations brighter than $M_{\mathrm{V}} = -5$ for $f_{\mathrm{MB}} = 3\%$ and 5%. The case for $f_{\mathrm{MB}} = 1\%$ is less clear-cut. The number of particles available for a given assignment is set by the mass of the halo, and so haloes near the resolution limit (with ~ 100 particles) will have only ~ 1 particle selected in a single assignment. In addition to this poor resolution, galaxies formed by assignments to a small number of central particles are more sensitive to spurious two-body heating in the innermost regions of subhaloes. We therefore expect the 'tagged particle' galaxies in small subhaloes to be dominated by few-particle 'noise' and to show poor convergence behaviour.

On the basis of Fig. 2.4 *we adopt $f_{\mathrm{MB}} = 1\%$ as a reasonable match to the data*[9]. We believe the resulting satellites to be sufficiently well-converged at the resolution of our Aq-2 simulations with this choice of f_{MB} to permit a statistical study of the disrupted population (the stellar halo). We offer the following heuristic argument to support this assertion. The increase in resolution from Aq-3 to Aq-2 results in approximately three times more particles being selected at fixed f_{MB}; likewise, a change in f_{MB} from 1% to 3% selects three times more particles at a fixed resolution. Therefore, as $f_{\mathrm{MB}} = 3\%$ has converged at the resolution of Aq-3, it is reasonable to expect that $f_{\mathrm{MB}} = 1\%$ selects a sufficient number of particles to ensure that satellite sizes are not dominated by noise, at the resolution of Aq-2. We show below that the most significant contribution to the halo comes from a handful of well resolved objects with $M_{\mathrm{V}} < -10$, rather than from the aggregation of many fainter satellites. So our results should not be sensitive to the treatment of objects at the resolution limit. Additionally, as demonstrated for example by Peñarrubia et al. (2008a,b, 2009), there is a 'knife-edge' between the onset of stellar stripping and total disruption for stars deeply embedded within the innermost few percent of the dark matter in a halo. We conclude that premature stripping resulting from an over-extension of very small satellites in our model is unlikely to alter the gross properties of our stellar haloes.

The points raised above in connection with Fig. 2.4 make clear that our *in vivo* particle tagging approach demands extremely high resolution, near the limits of current cosmological N-body simulations. Also, we stress that the choice of $f_{\mathrm{MB}} = 1\%$ in this approach (from an acceptable range of $1 - 3\%$) is not arbitrary. For example, choosing $f_{\mathrm{MB}} = 10\%$ (either as a

---

[9] Noting also that it lies close to the power-law fit employed by Bullock & Johnston (2005) to map luminosities to satellite sizes.

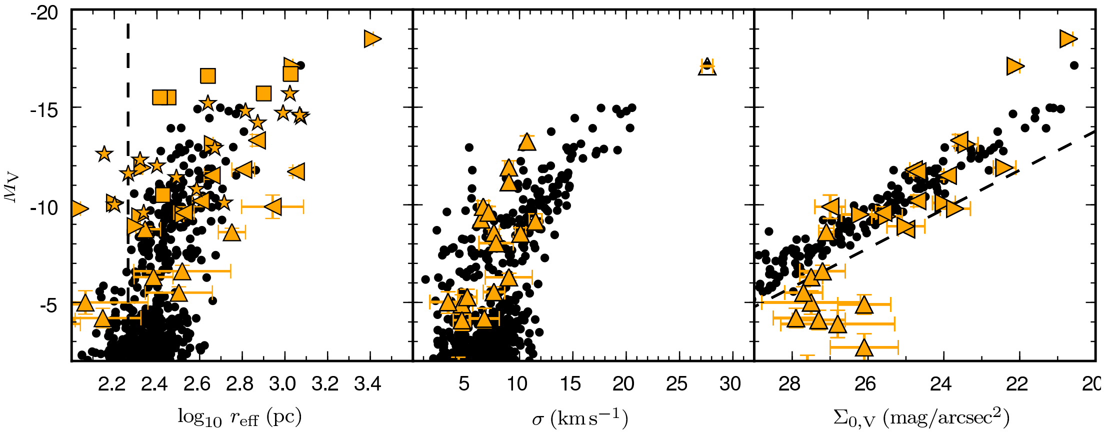

Figure 2.5: Projected half-light radius (left), mean luminosity-weighted 1D velocity dispersion (centre) and central surface brightness (right) of simulated satellite galaxies (defined by $r_{\rm GC} < 280\,{\rm kpc}$) that survive in all haloes at $z = 0$, as a function of absolute V-band magnitude. Observational data for Milky Way and M31 satellites are shown as orange symbols; values are from Mateo (1998) and other authors as follows: bright satellites (triangles pointing right, Grebel et al. 2003); faint MW satellites discovered since 2005 (triangles pointing up, Martin et al. 2008); M31 dwarf spheroidals (triangles pointing left, McConnachie et al. 2006; Martin et al. 2009); M31 ellipticals (squares); Local Group 'field' dwarf spheroidals and dwarf irregulars (stars). In the central panel we use data for Milky Way satellites only tabulated by Wolf et al. (2010) and for the SMC, Grebel et al. (2003). In the rightmost panel, we plot data for the Milky Way and M31 (Grebel et al. 2003; Martin et al. 2008). A dashed line indicates the surface brightness of an object of a given magnitude with $r_{\rm eff} = 2.8\epsilon$, the gravitational softening scale (see Section 1.2.1).

round-number estimate, or as necessitated by limited resolution, as in the work of De Lucia & Helmi 2008) would produce unrealistically extended satellites.

For the remainder of this thesis we concentrate on the higher resolution Aq-2 simulations. In Fig. 2.5 we fix $f_{\rm MB}$ at 1% and compare the surviving satellites from all six of our haloes with observational data, looking at three properties correlated with absolute magnitude: effective radius, $r_{\rm eff}$, mean luminosity-weighted line-of-sight velocity dispersion, σ, and central surface brightness, μ_0 (although the latter is closely related to $r_{\rm eff}$). In all cases our model satellites agree well with the trends and scatter in the data for satellites brighter than $M_{\rm V} = -5$.

The force softening scale of the simulation (indicated by dashed lines in the first and third panels of Fig. 2.5) effectively imposes a maximum density on the dark haloes hosting our satellites. At this radial scale we would expect the relation between $r_{\rm eff}$ and $M_{\rm V}$ to break down for numerical reasons. Fig. 2.5 shows that the $r_{\rm eff}(M_{\rm V})$ relation becomes steeper for galaxies fainter than $M_{\rm V} \sim -9$, corresponding to $r_{\rm eff} \sim 200\,{\rm pc}$. This resolution-dependent maximum density corresponds to a minimum surface brightness at a given magnitude. We note that the low-surface-brightness limit in the Milky Way data shown in the right-hand panel of Fig. 2.5

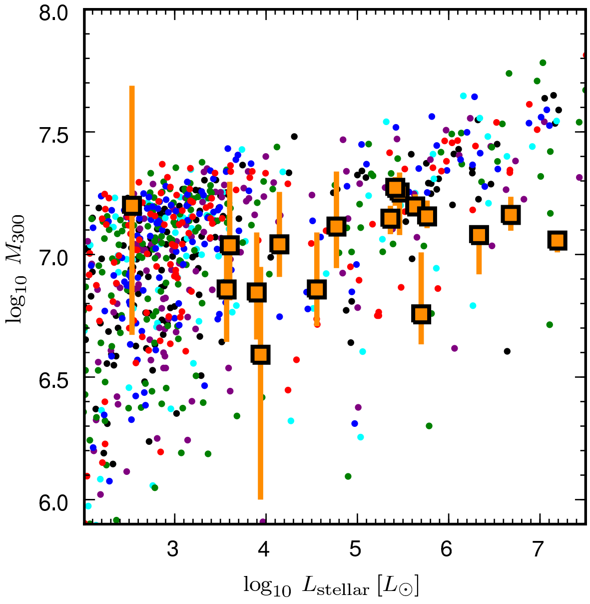

Figure 2.6: Mass in dark matter enclosed within 300 pc (M_{300}) as a function of luminosity (V-band) for satellites in each of our simulated haloes (coloured points, colours as Fig. 2.1). Maximum likelihood values of M_{300} for Milky Way dwarf spheroidals from Strigari et al. (2008) are shown (orange squares), with error bars indicating the range with likelihood greater than 60.6% of the maximum.

corresponds to the completeness limit of current surveys (e.g. Koposov et al. 2008; Tollerud et al. 2008). The lower surface brightness satellite population predicted by our model is not in principle incompatible with current data.

Finally, in Fig. 2.6 we show the relationship between total luminosity and the mass of dark matter enclosed within 300 pc, M_{300}, for our simulated satellites (in all haloes). This radial scale is well-resolved in the Aq-2 simulations (see also Font et al. 2011, in preparation). Our galaxies show a steeper trend than the data of Strigari et al. (2008), with the strongest discrepancy (0.5 dex in M_{300}) for the brightest satellites. Nevertheless, both show very little variation, having $M_{300} \sim 10^7\,\mathrm{M}_\odot$ over five orders of magnitude in luminosity. In agreement with previous studies using semi-analytic models and lower-resolution N-body simulations (Macciò et al. 2009; Busha et al. 2009; Li et al. 2009b; Koposov et al. 2009), and N-body gasdynamic simulations (Okamoto & Frenk 2009), we find that this characteristic scale arises naturally as a result of astrophysical processes including gas cooling, star formation and feedback (Stringer et al. 2010).

2.2.3 Defining the stellar halo and satellite galaxies

To conclude this chapter, we summarise the terminology we adopt to describe our results. Tagged dark matter particles in the self-bound haloes and subhaloes identified by SUBFIND constitute our 'galaxies'. Our stellar haloes comprise all tagged particles bound to the principal halo in the simulation, along with those tagged particles not in any bound group[10]. All galaxies within 280 kpc of the centre of the main halo are classed as 'satellites', as in the luminosity functions shown in Fig. 2.1. Centres of mass for the stellar haloes and satellites are determined from tagged particles only, using the iterative centring process described by Power et al. (2003).

As described in Section 1.3.1, many structural elements of a galaxy intermix within a few kiloparsecs of its centre. Our definition of the innermost regions of a stellar halo also requires a careful and unambiguous definition of the other components present. This is especially important when distinguishing between those galactic components that are represented in our model and those that are not, because there may be no straightforward way to make a similar separation in the observational data. Therefore, before describing our haloes, we first summarise some of these possible sources of confusion, clarify what is and is not included in our model, and define a range of galactocentric distances on which we will focus for our analysis of the stellar halo.

As discussed above, our model does not use particles to track the motions of any stars formed in situ in the central 'Milky Way' galaxy, whether in a rotationally supported thin disc or otherwise[11]. For this reason we refer to the halo stars that *are* included in our model as *accreted* and those that form in the central galaxy (and hence are *not* explicitly tracked in our model) as *in situ*. Observational definitions of the 'stellar halo' cannot distinguish between accreted and in situ stars, only between components separated empirically by their kinematic, spatial and chemical properties.

Confusion between accreted and in situ halo stars is likely to be most acute near the plane of the disc. Observations of the Milky Way and analogous galaxies frequently distinguish a 'thick disc' component (Gilmore & Reid 1983; Carollo et al. 2010) thought to result either from dynamical heating of the thin disc by minor mergers (e.g. Toth & Ostriker 1992; Quinn et al. 1993; Velazquez & White 1999; Font et al. 2001; Benson et al. 2004; Kazantzidis et al. 2008) or from accretion debris (Abadi et al. 2003b; Yoachim & Dalcanton 2005, 2008). In principle, our

---

[10] Note that below we impose an additional cut in galactocentric radius to further refine our definition of the stellar halo.

[11] This central galaxy is included in the underlying semi-analytic model

model will follow the formation of accreted thick discs. However, the stars in our model only feel the potential of the dark halo; the presence of a massive baryonic disc could significantly alter this potential in the central region and influence the formation of an accreted thick disc (e.g. Velazquez & White 1999).

Our models include that part of the galactic bulge built from accreted stars, but they do not include any of the other possible processes of bulge formation (starbursts, bars etc.). However, the interpretation of this component, the signatures of an observational counterpart and the extent to which our simulation accurately represents its dynamics are all beyond the scope of the work we present in this thesis. Instead, we will consider stars within 3 kpc of the dark halo potential centre as 'accreted bulge', and define those between 3 kpc and a maximum radius of 280 kpc as the 'stellar halo'. We will focus our analysis on these stars. This arbitrary radial cut is chosen to exclude the region in which the observational separation of 'bulge' and 'halo' stars is most difficult. At least near the Galactic plane, this region is implicitly excluded from observational studies of the stellar halo. Our choice of 3 kpc is *not* intended to reflect a physical scale-length or dichotomy in our stellar haloes, analogous to that claimed for the Milky Way in recent work (e.g. Carollo et al. 2007, 2010). Beyond 3 kpc we believe that the ambiguities discussed above and the 'incompleteness' of our models with regard to stars formed *in situ* should not substantially affect the comparison of our *accreted* stars with observational data that follows in Chapter 3. However, we will revisit this issue in later chapters.

3

Galactic Stellar Haloes in the CDM Model

3.1 Results: the Aquarius stellar haloes

In this chapter, we present the six stellar haloes resulting from the application of the method described in the previous chapter to the Aquarius simulations. Here our aim is to characterise the assembly history of the six haloes and their global properties. Quantities measured for each halo are collected in Table 3.1. These include a measure of the number of progenitor galaxies contributing to the stellar halo, N_{prog}. This last quantity is not the total number of accreted satellites, but instead is defined as $N_{\mathrm{prog}} = M_{\mathrm{halo}}^2 / \sum_i m_{\mathrm{prog,i}}^2$ where $m_{\mathrm{prog,i}}$ is the stellar mass contributed by the i'th progenitor. N_{prog} is equal to the total number of progenitors in the case where each contributes equal mass, or to the number of significant progenitors in the case where the remainder provide a negligible contribution.

3.1.1 Visualisation in projection

A $300 \times 300\,\mathrm{kpc}$ projected surface brightness map of each stellar halo at $z = 0$ is shown in Fig. 3.1. Substantial diversity among the six haloes is apparent. Haloes Aq-B and Aq-E are distinguished by their strong central concentration, with few features of detectable surface brightness beyond $\sim 20\,\mathrm{kpc}$. Haloes Aq-A, Aq-C, Aq-D and Aq-F all show more extended envelopes to 75-100 kpc. Each envelope is a superposition of streams and shells that have been phase-mixed to varying degrees.

Analogues of many morphological features observed in the halo of M31 (Ibata et al. 2007; Tanaka et al. 2009; McConnachie et al. 2009) and other galaxies (e.g. Martínez-Delgado et al. 2008) can be found in our simulations. For example, the lower left quadrant of Aq-A shows arc-like features reminiscent of a complex of 'parallel' streams in the M31 halo labelled A, B, C and D by Ibata et al. (2007) and Chapman et al. (2008), which have surface brightnesses of $30 - 33\,\mathrm{mag\,arcsec^{-2}}$ and a range of metallicities (Tanaka et al. 2009). These streams in Aq-A can also be traced faintly in the upper right quadrant of the image and superficially resemble

Halo	$L_{V,\mathrm{halo}}$ $[10^8\mathrm{L}_\odot]$	$M_{\star,\mathrm{halo}}$ $[10^8\mathrm{M}_\odot]$	$M_{\star,\mathrm{bulge}}$ $[10^8\mathrm{M}_\odot]$	M_{gal} $[10^{10}\mathrm{M}_\odot]$	M_V	N_{sat}	f_{sat}	f_{surv}	N_{prog}	$r_{1/2}$ [kpc]	n_{in}	n_{out}	r_{brk} [kpc]
A	1.51	2.80	1.00	1.88	-20.3	161	0.61	0.065	3.8	20	-2.7	-8.2	80.4
B	1.27	2.27	3.33	1.49	-20.1	91	0.07	0.036	2.4	2.3	-4.2	-5.8	34.6
C	1.95	3.58	0.34	7.84	-21.3	150	0.28	0.667	2.8	53	-2.0	-9.4	90.8
D	5.55	9.81	1.32	0.72	-19.1	178	0.35	0.620	4.3	26	-2.0	-5.9	37.7
E	0.90	1.76	16.80	0.45	-18.6	135	0.11	0.003	1.2	1.0	-4.7	-4.4	15.2
F	17.34	24.90	6.42	1.36	-20.1	134	0.28	0.002	1.1	6.3	-2.9	-5.9	14.0

Table 3.1: For each of our simulated haloes we tabulate: the luminosity and mass of halo stars (in the range $3 < r < 280$ kpc); the mass of accreted bulge stars ($r < 3$ kpc); the total stellar mass and V-band magnitude of the central galaxy in GALFORM; the number of surviving satellites (brighter than $M_{\mathrm{V}} = 0$); the fraction of the total stellar mass within 280 kpc bound in surviving satellites at $z = 0$, f_{sat}; the fraction of *halo* stellar mass ($r < 280$ kpc) contributed by these surviving satellites, f_{surv}; the number of halo progenitors, N_{prog} (see text); the half-light radius of the stellar halo ($r < 280$ kpc); the inner and outer slope and break radius of a broken power-law fit to the three-dimensional density profile of halo stars ($3 < r < 280$ kpc).

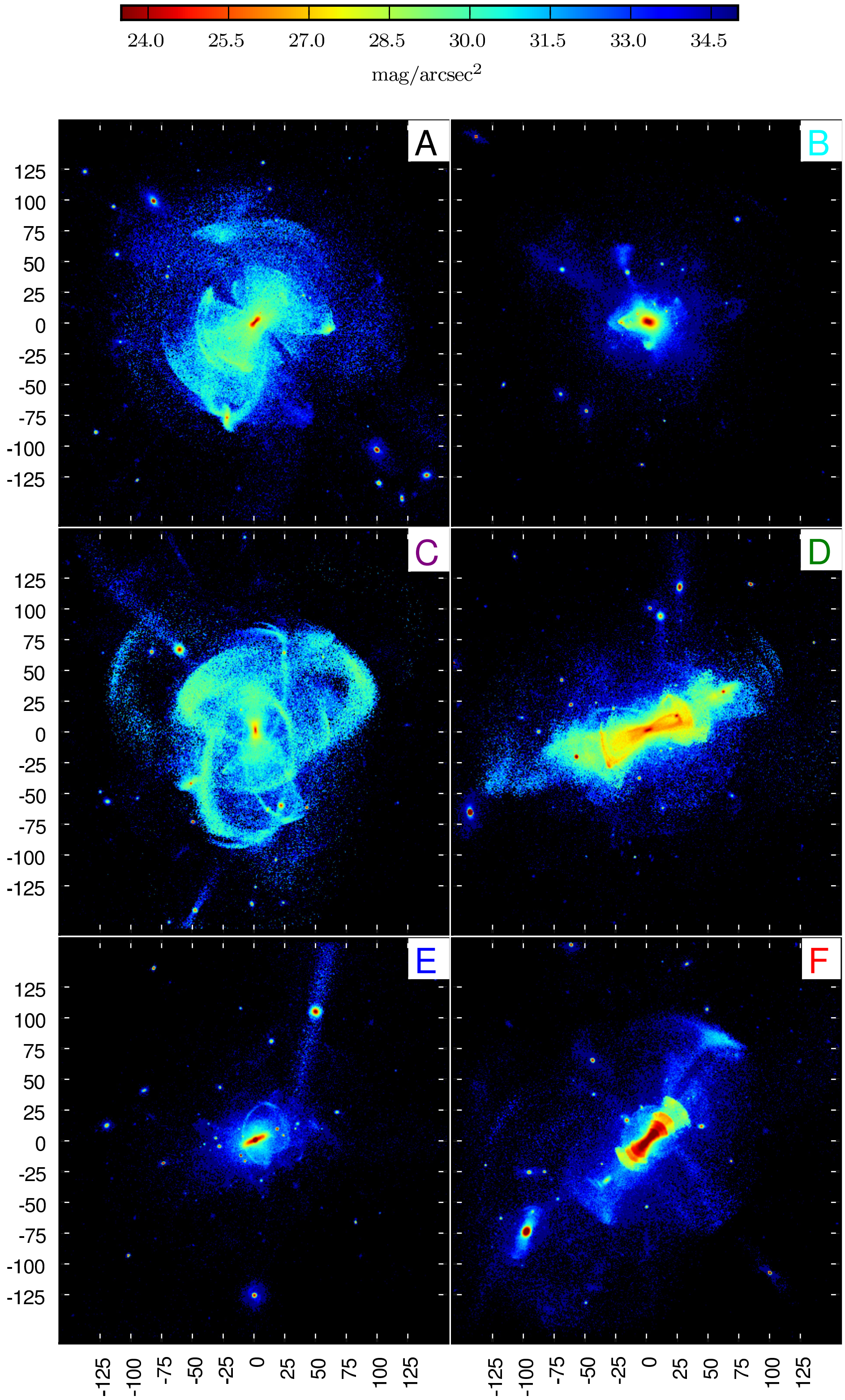

Figure 3.1: V-band surface brightness of our model haloes (and surviving satellites), to a limiting depth of $35\,\mathrm{mag/arcsec^2}$. The axis scales are in kiloparsecs. Only stars formed in satellites are present in our particle model; there is no contribution to these maps from a central galactic disc or bulge formed in situ (see Section 2.2.3).

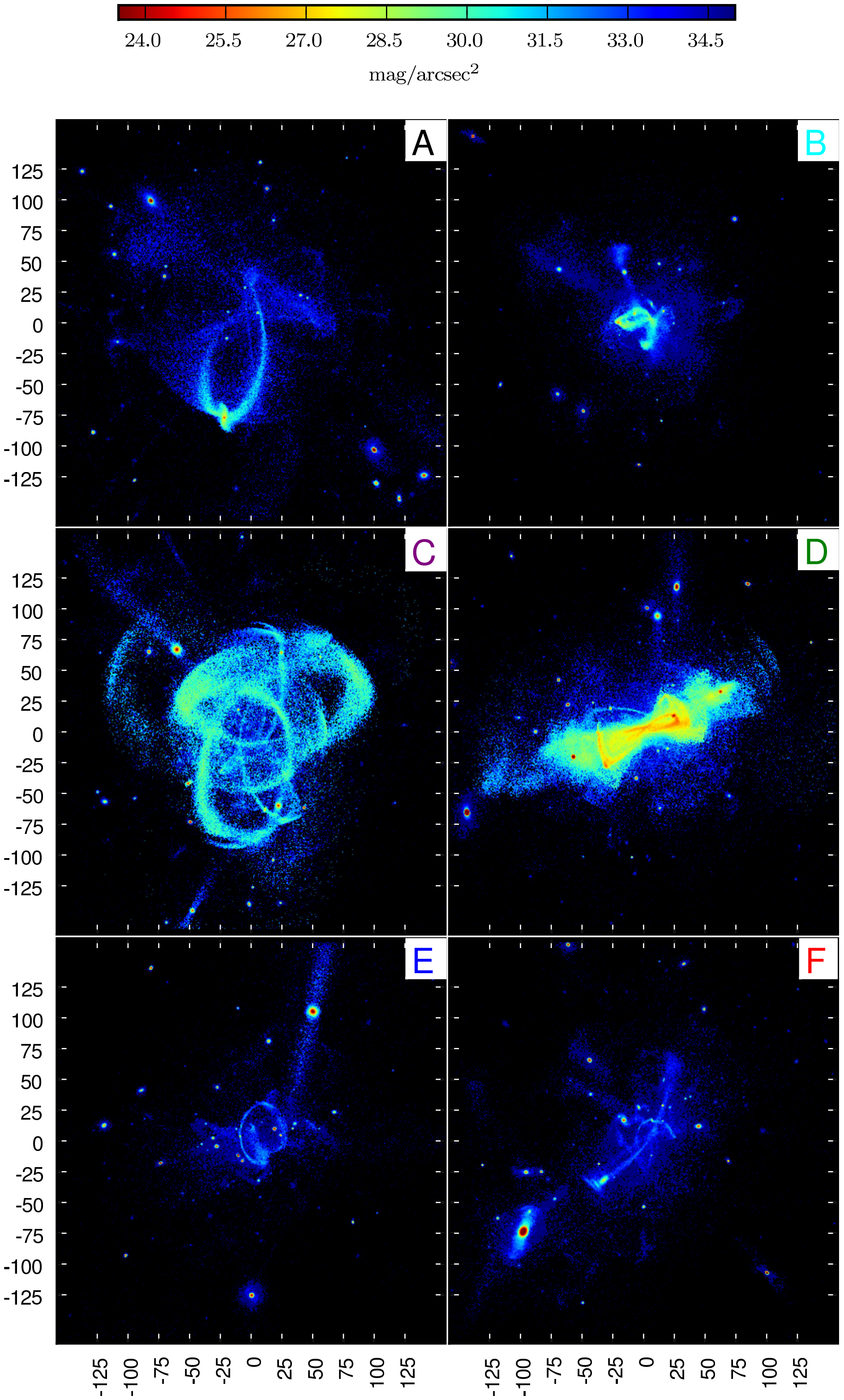

Figure 3.2: As Fig. 3.1, but here showing only those stars stripped from satellites that survive at $z = 0$.

Table 3.2: Axial ratios $q = c/a$ and $s = b/a$ of stellar-mass-weighted three-dimensional ellipsoidal fits to halo stars within a galactocentric radius of 10 kpc. These were determined using the iterative procedure described by Allgood et al. (2006), which attempts to fit the shapes of self-consistent 'isodensity' contours. A spherical contour of $r = 10$ kpc is assumed initially; the shape and orientation of this contour are then updated on each iteration to those obtained by diagonialsing the inertia tensor of the mass enclosed (maintaining the length of the longest axis). The values thus obtained are slightly more prolate than those obtained from a single diagnonalization using all mass with a spherical contour (i.e. the first iteration of our approach), reflecting the extremely flattened shapes of our haloes at this radius. The oblate shape of Aq-E is not sensitive to this choice of method.

Halo	A	B	C	D	E	F
q_{10}	0.27	0.28	0.29	0.33	0.36	0.21
s_{10}	0.30	0.32	0.32	0.42	0.96	0.25

the edges of 'shells'. In fact, they result from two separate progenitor streams, each tracing multiple wraps of decaying orbits (and hence contributing more than one 'arc' each). Seen in three dimensions, these two debris complexes are elaborate and irregular structures, the true nature of which is not readily apparent in any single projection. They are among the most significant contributors to the Aq-A halo.

The brightest and most coherent structures visible in Fig. 3.1 are attributable to the most recent accretion events. To illustrate the contribution of recently-infalling objects (quantified in Section 3.1.2), we show the same projections of the haloes in Fig. 3.2, but include only those stars whose parent satellite survives at $z = 0$. In haloes Aq-C and Aq-D, stars stripped from surviving satellites constitute $\sim 60-70\%$ of the halo, while in the other haloes their contribution is $\lesssim 10\%$. Not all the recently-infalling satellites responsible for bright halo features survive; for example, the massive satellite that merges at $z \sim 0.3$ and produces the prominent set of 'shells' in Aq-F.

Fig. 3.1 shows that all our haloes are notably flattened, particularly in the central regions where most of their light is concentrated. Table 3.2 gives axial ratios $q = c/a$ and $s = b/a$ of three-dimensional ellipsoidal fits to halo stars within 10 kpc of the halo centre (these fits include stars within the accreted bulge region defined above). Most of our haloes are strongly prolate within 10 kpc. Halo Aq-E is very different, having a highly oblate (i.e. disc-like) shape in this region – this structure of ~ 20 kpc extent can be seen 'edge on' in Fig. 3.1 and can be described as an 'accreted thick disc' (e.g. Abadi et al. 2003b; Peñarrubia et al. 2006; Read et al. 2008). We examine this interesting object in more detail in Chapter 5. Beyond 10–30 kpc, the stellar mass in our haloes is not smoothly distributed. These regions consist of a number of discrete streams, plumes and other irregular structures. Fits to all halo stars assuming a smoothly varying ellipsoidal distribution of mass interior to a given radius do not accurately describe these sparse outer regions.

Few observations of stellar halo shapes are available for comparison with our models. M31 is the only galaxy in which a projected stellar halo has been imaged to a depth sufficient to account for a significant fraction of halo stars. Pritchet & van den Bergh (1994) measured a projected axial ratio for the M31 halo at ~ 10 kpc of ~ 0.5. Ibata et al. (2005) describe a highly irregular and rotating inner halo component or 'extended disc' (to $\sim 40\,\mathrm{kpc}$) of $27-31\,\mathrm{mag/arcsec}^2$, aligned with the thin disc and having an axial ratio ~ 0.6 in projection. Zibetti & Ferguson (2004) find a similar axial ratio for the halo of a galaxy at $z = 0.32$ observed in the Hubble ultra-deep field. Evidence for the universality of flattened stellar haloes is given by Zibetti et al. (2004), who find a best-fitting projected axial ratio of $\sim 0.5 - 0.7$ for the low surface brightness envelope of ~ 1000 stacked edge-on late-type galaxies in SDSS. A mildly *oblate* halo with $c/a \sim 0.6$ is reported for the Milky Way, with an increase in flattening at smaller radii (< 20 kpc; e.g. Chiba & Beers 2000; Bell et al. 2008; Carollo et al. 2007). Interestingly, Morrison et al. (2009) present evidence for a highly flattened halo ($c/a \sim 0.2$) component in the Solar neighbourhood, which appears to be dispersion-supported (i.e. kinematically *distinct* from a rotationally supported thick disc).

The shapes of components in our haloes selected by their kinematics, chemistry or photometry may be very different to those obtained from the aggregated stellar mass. A full comparison, accounting for the variety of observational selections, projection effects and definitions of 'shape' used in the measurements cited above, is beyond the scope of this chapter. We emphasize, however, that the flattening in our stellar haloes cannot be attributed to any 'baryonic' effects such as a thin disc potential (e.g. Chiba & Beers 2001) or star formation in dissipative mergers and bulk gas flows (e.g. Bekki & Chiba 2001). Furthermore, it is unlikely to be the result of a (lesser) degree of flattening in the dark halo. Instead the structure of these components is most likely to reflect the intrinsically anisotropic distribution of satellite orbits. In certain cases (for example, Aq-D and Aq-A), it is clear that several contributing satellites with correlated trajectories are responsible for reinforcing the flattening of the inner halo.

3.1.2 Assembly history of the stellar halo

We now examine when and how our stellar haloes were assembled. Fig. 3.3 shows the mass fraction of each stellar halo (*including* the accreted bulge component defined in Section 2.2.3) in place (i.e. unbound from its parent galaxy) at a given redshift. We count all 'star particles'

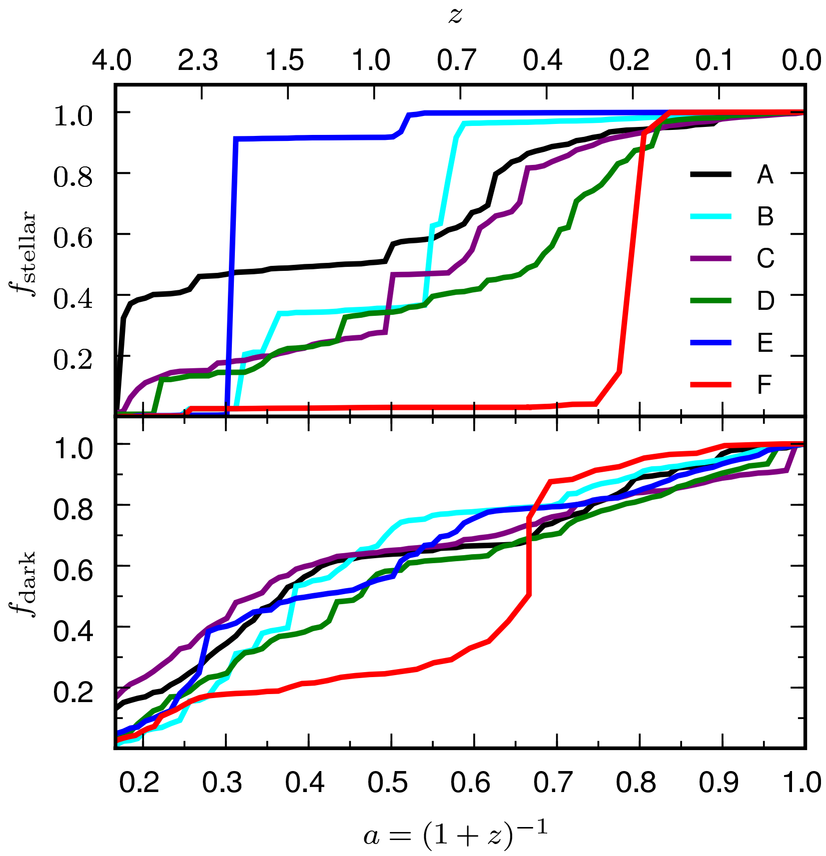

Figure 3.3: The mass assembly history of the stellar halo (*upper panel*) and the dark matter halo (the principal branch; *lower panel*) as a function of expansion factor (*bottom axis*) or redshift (*top axis*). Lines show the mass fraction of each halo in place at a given time. Stars are counted as belonging to the stellar halo when the DM particle that they tag is assigned to the principal halo, or is not bound to any SUBFIND group.

bound to the main dark halo and within 280 kpc of its centre at $z = 0$ as belonging to the stellar halo. We compare the growth of the stellar haloes with that of their corresponding host dark haloes. It is clear that our sample spans a range of assembly histories for haloes even though the haloes have very similar final mass.

Not surprisingly, the growth of the dark halo is considerably more smooth than that of the stellar halo. The 'luminous' satellite accretion events contributing stars are a small subset of those that contribute to the dark halo, which additionally accretes a substantial fraction of its mass in the form of 'diffuse' dark matter (Wang et al. 2010). As described in detail by Peñarrubia et al. (2008a,b) the dark haloes of infalling satellites must be heavily stripped before the deeply embedded stars are disrupted. This gives rise to time-lags seen in Fig. 3.3 between the major events building dark and stellar haloes.

To characterise the similarities and differences between their histories, we subdivide our sample of six stellar haloes into two broad categories: those that grow through the gradual accretion of many progenitors (Aq-A, Aq-C and Aq-D) and those for which the majority of stellar mass is contributed by only one or two major events (Aq-B, Aq-E and Aq-F). We refer to this latter case as 'few-progenitor' growth. The measure of the number of 'most-significant' progenitors given in Table 3.1, $N_{\rm prog}$, also ranks the haloes by the 'smoothness' of their accretion history, reflecting the intrinsically stochastic nature of their assembly.

Fig. 3.4 compares the luminosity functions (LFs) of surviving satellites with the LF of totally disrupted satellites, measuring luminosity at the time of infall in both cases. In general, there are fewer destroyed satellites than survivors over almost all luminosities, although the numbers and luminosities of the very brightest contributors and survivors are comparable in each halo. The deficit in the number of disrupted satellites relative to survivors is most pronounced in the few-progenitor haloes Aq-B and Aq-F.

Fig. 3.5 summarises the individual accretion events that contribute to the assembly of the stellar halo, plotting the stellar mass of the most significant progenitor satellites against their redshift of infall (the time at which their host halo first becomes a subhalo of the main FOF group). Here we class as significant those satellites which together contribute 95% of the total halo stellar mass (this total is shown as a vertical line for each halo) when accumulated in rank order of their contribution. By this measure there are (5,6,8,6,6,1) significant progenitors for haloes (A,B,C,D,E,F). We also compare the masses of the brightest Milky Way satellites to the significant contributors in our stellar haloes. Typically the most significant contributors have masses comparable to the most massive surviving dwarf spheroidals, Fornax and Sagittarius.

With the exception of Aq-F, all the most significant contributors to our stellar haloes were accreted more than 8 Gyr ago. We highlight (as filled squares) those contributors whose cores survive as self-bound objects at $z = 0$. We find that surviving satellites accreted before $z = 1$ are the dominant contributors to the many-progenitor haloes Aq-C and Aq-D. The extreme case of Aq-F is atypical: more than 95% of the halo was contributed by the late merger of an object of stellar mass greater than the SMC infalling at $z \sim 0.7$, which does not survive. By contrast, the two least massive haloes Aq-B and Aq-E are built by many less massive accretions at higher redshift, with surviving satellites making only a minor contribution ($< 10\%$). Halo Aq-A represents an intermediate case, in which stars stripped from a relatively late-infalling survivor add significantly ($\sim 10\%$) to the mass of a halo predominantly assembled at high redshift. The relative contributions to the halo from all accretion events are illustrated in Fig. 3.6. Each line in this figure indicates the fraction of the total halo stellar mass that was contributed by satellites donating less than a given fraction of this total *individually*. An interesting feature

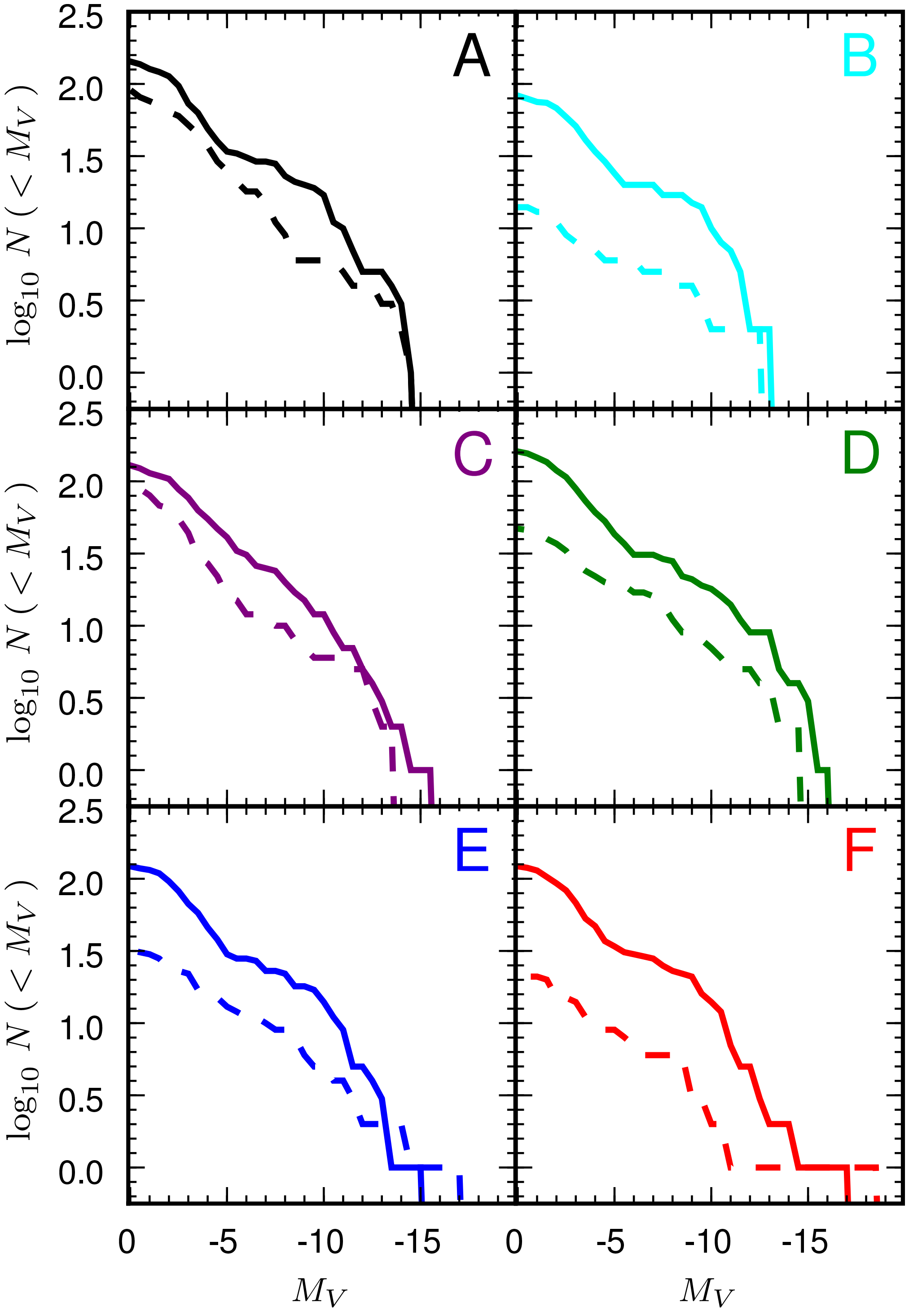

Figure 3.4: Luminosity functions of surviving satellites (solid) in each of our six haloes, compared with those of totally disrupted halo progenitors (dashed). These are constructed using only stars formed in each satellite before the time of infall (the halo-subhalo transition). The luminosity of each population is that after evolution to $z = 0$.

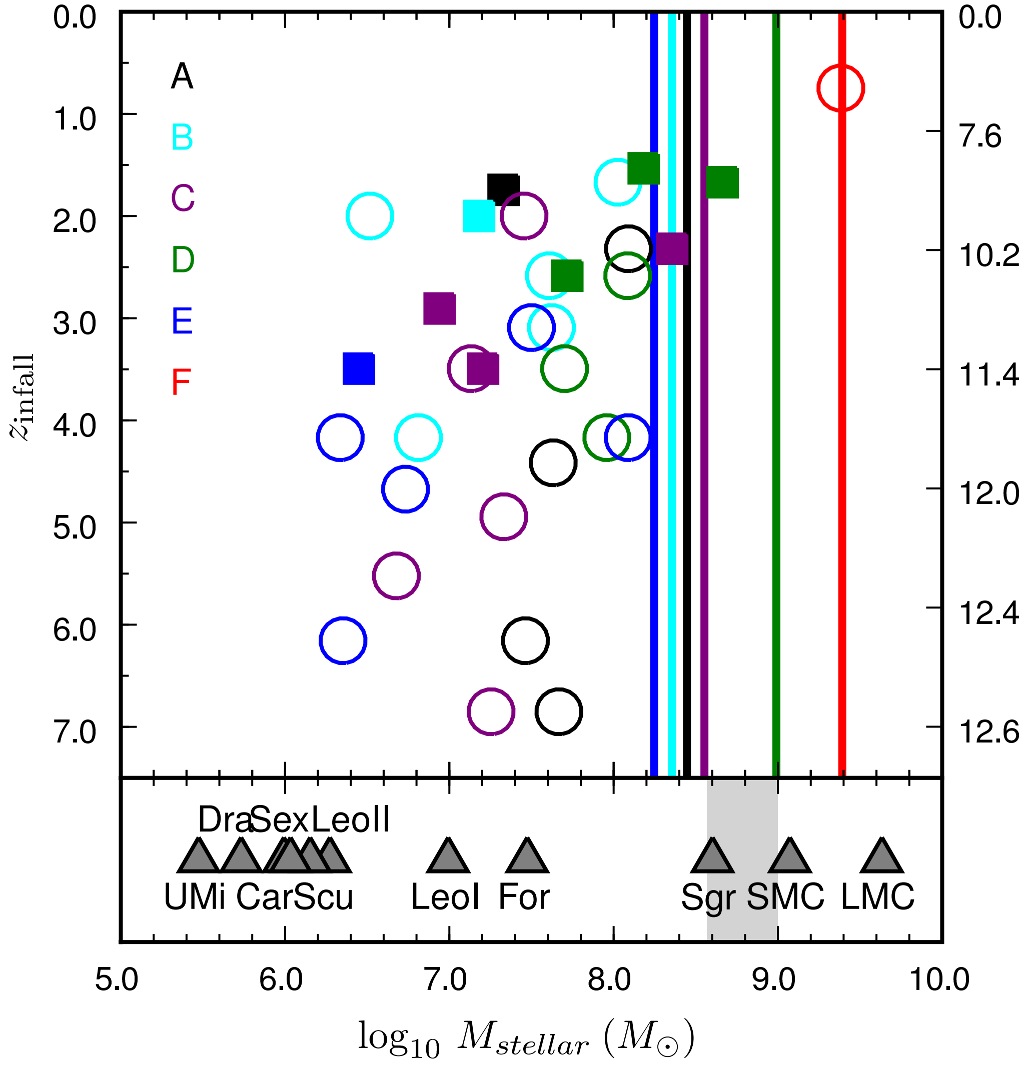

Figure 3.5: *Main panel*: for satellites that have been stripped to form the stellar haloes, symbols show the redshift of infall and total mass contributed to the stellar halo at $z = 0$ (in the range $3 < r < 280\,\mathrm{kpc}$). Vertical lines indicate the total mass of each stellar halo in this radial range. The right-hand y-axis is labelled by lookback time in gigayears. We plot only those satellites whose individual contributions, accumulated in rank order from the most significant contributor, account for 95% of the total stellar halo mass. Satellites totally disrupted by $z = 0$ are plotted as open circles, surviving satellites as filled squares (in almost all cases the contributions of these survivors are close to their total stellar masses; see text). *Lower panel:* symbols indicate the approximate masses of bright MW satellites, assuming a stellar mass-to-light ratio of 2; the Sgr present-day mass estimate is that given by Law et al. (2005). The shaded region indicates an approximate range for the MW halo mass in our halo regime (see e.g. Bell et al. 2008).

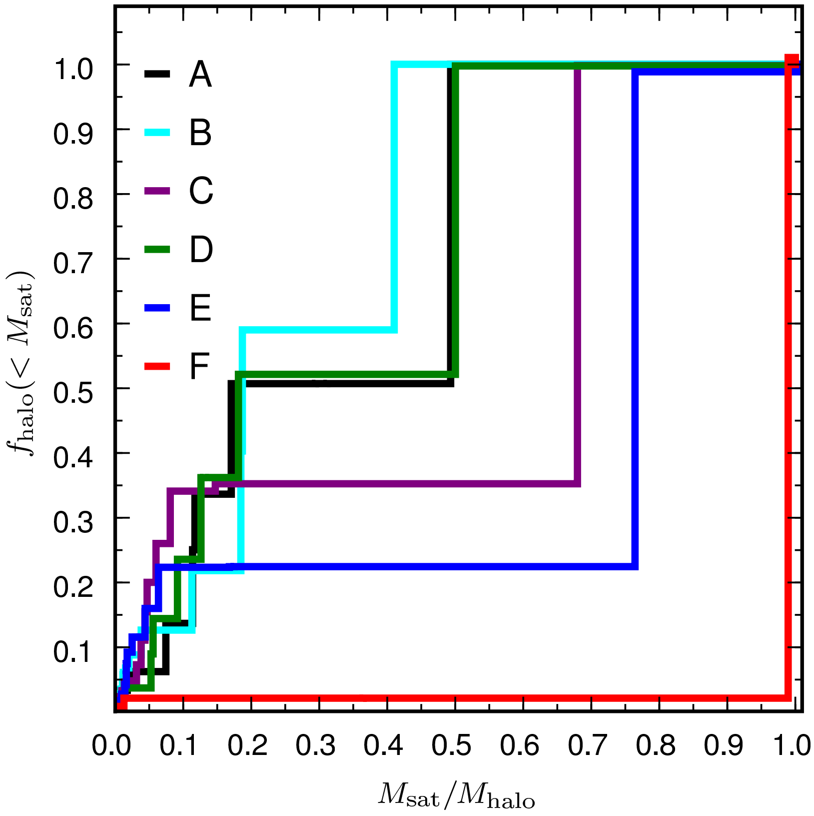

Figure 3.6: Cumulative mass fraction of each stellar halo originating in satellites of stellar mass less than $M_{\rm sat}$. Satellite masses are normalised to the total stellar halo mass $M_{\rm halo}$ in each case, as defined in Section 2.2.3.

illustrated by this figure concerns Aq-B, one of our few-progenitor haloes (shown as light blue in all figures). Although Fig. 3.3 shows that the assembly of this halo proceeds over time by a series of concentrated 'jumps' in mass, its final composition is even less biased to the most significant progenitor than any of the many-progenitor haloes.

In general, surviving contributors to the halo retain less than 5% of the total stellar mass that formed in them. A small number of surviving contributors retain a significant fraction of their mass, for example, the surviving contributor to Aq-A, which retains 25%. In Fig. 3.7, we show histograms of the number of all surviving satellites (combining all six haloes) that have been stripped of a given fraction of their mass. Most satellites are either largely unaffected or almost totally stripped, indicating that the time spent in an intermediate disrupting state is relatively short.

In Table 3.1, we give the fraction of mass in the stellar halo that has been stripped from surviving satellites, $f_{\rm surv}$. As previously stated, this contribution is dominant in haloes Aq-C

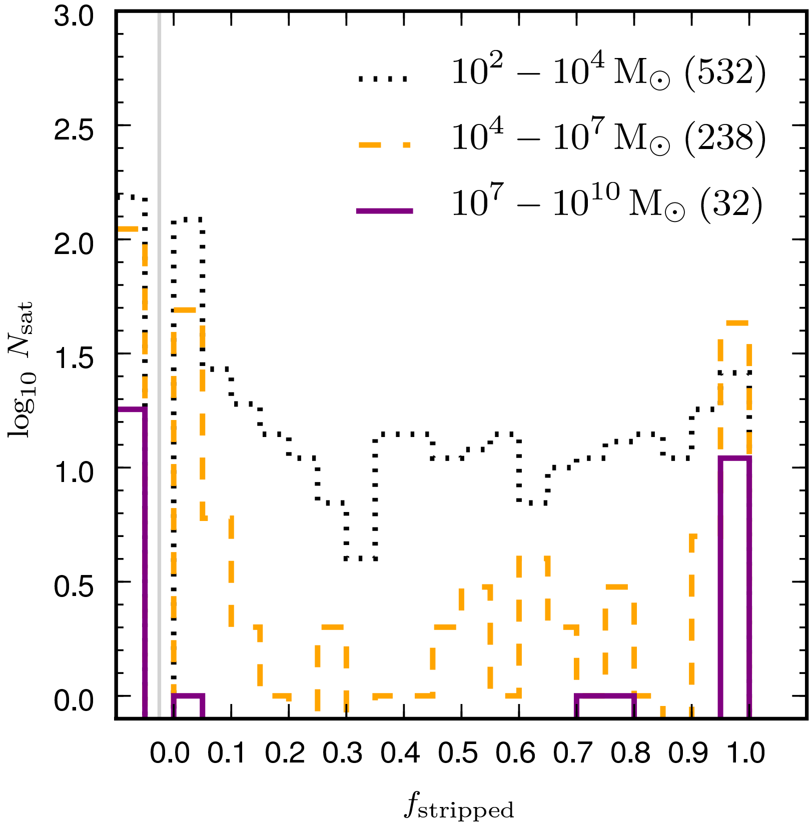

Figure 3.7: Number of surviving satellites (aggregated over all six haloes) which have lost a fraction, $f_{\rm stripped}$, of the stellar mass through tidal stripping. Satellites are divided into three mass bins: massive (purple), intermediate (dashed orange) and low-mass (dotted black) as quantified in the legend. The leftmost bin (demarcated by a vertical line) shows the number of satellites that have not suffered any stellar mass loss.

(67%) and Aq-D (62%), significant in Aq-A (7%) and Aq-B (4%) and negligible in Aq-E and Aq-F. Sales et al. (2007b) find that only $\sim 6\%$ of stars in the eight haloes formed in the SPH simulations of Abadi et al. (2006) are associated with a surviving satellite. The lack of surviving satellites may be attributable to the limited resolution of those simulations; clearly, the number of 'survivors' is sensitive to the lowest mass at which remnant cores can be resolved. However, Bullock & Johnston (2005) and the companion study of Font et al. (2006a) also conclude that the contribution of surviving satellites is small ($< 10\%$ in all of their 11 haloes and typically $< 1\%$). As the resolution of their simulations is comparable to ours, the predominance of surviving contributors in two of our haloes is significant.

Bullock & Johnston find that their haloes are built from a similar (small) number of massive objects to ours (e.g. figure 10 of Bullock & Johnston 2005) with comparable accretion times ($>$ 8 Gyr), suggesting that there are no fundamental differences in the infall times and masses of accreted satellites. Notably, Font et al. (2006a) observe that no satellites accreted > 9 Gyr ago survive in their subsample of four of the Bullock & Johnston haloes, whereas we find that some satellites infalling even at redshifts $z > 2$ may survive (see also Fig. 3.11 below). The discrepancy appears to stem from the greater resilience of satellites accreted at $z > 1$ in our models, including some which contribute significantly to the stellar haloes. In other words, our model does not predict any more late-infalling contributors than the models of Bullock & Johnston. The more rapid disruption of massive subhaloes in the Bullock & Johnston models may be attributable to one or both of the analytic prescriptions employed by those authors to model the growth of the dark matter halo and dynamical friction in the absence of a live halo. It is also possible that the relation between halo mass and concentration assumed in the Bullock & Johnston model results in satellites that are less concentrated than subhaloes in the Aquarius simulations.

Current observational estimates (e.g. Bell et al. 2008) imply that the stellar halo of the Milky Way is intermediate in mass between our haloes Aq-C and Aq-D. If its accretion history is qualitatively similar to these many-progenitor haloes, Fig. 3.5 implies that it is likely to have accreted its four or five most significant contributors around $z \sim 1 - 3$ in the form of objects with masses similar to the Fornax or Leo I dwarf spheroidals. Between one and three of the most recently accreted, and hence most massive contributors, are expected to retain a surviving core, and to have a stellar mass comparable to Sagittarius ($M_{\mathrm{sgr}} \sim 5 \times 10^{8}\,\mathrm{M_{\odot}}$ or $\sim 50\%$ of the total[1] halo mass, infalling at a lookback time of $\sim 5\,\mathrm{Gyr}$; Law et al. 2005). It is also possible that the Canis Major overdensity (with a core luminosity comparable to that of Sagittarius; Martin et al. 2004) associated with the low-latitude Monoceros stream (Newberg et al. 2002; Yanny et al. 2003; Ibata et al. 2003) should be included in the census of 'surviving contributors' (although this association is by no means certain; e.g. Mateu et al. 2009). Therefore, the picture so far established for the Milky Way appears to be in qualitative agreement with the presence of surviving cores from massive stellar halo contributors in our simulations.

---

[1] Both the Sagittarius and Milky Way halo stellar mass estimates are highly uncertain; it is unclear what contribution is made by the Sgr debris to estimates of the halo mass, although both the stream and the Virgo overdensity were masked out in the analysis of Bell et al. (2008) for which a value of $\sim 3 \times 10^{8}\,\mathrm{M_{\odot}}$ in the range $3 < r < 40\,\mathrm{kpc}$ was obtained from a broken power-law fit to the remaining 'smooth' halo.

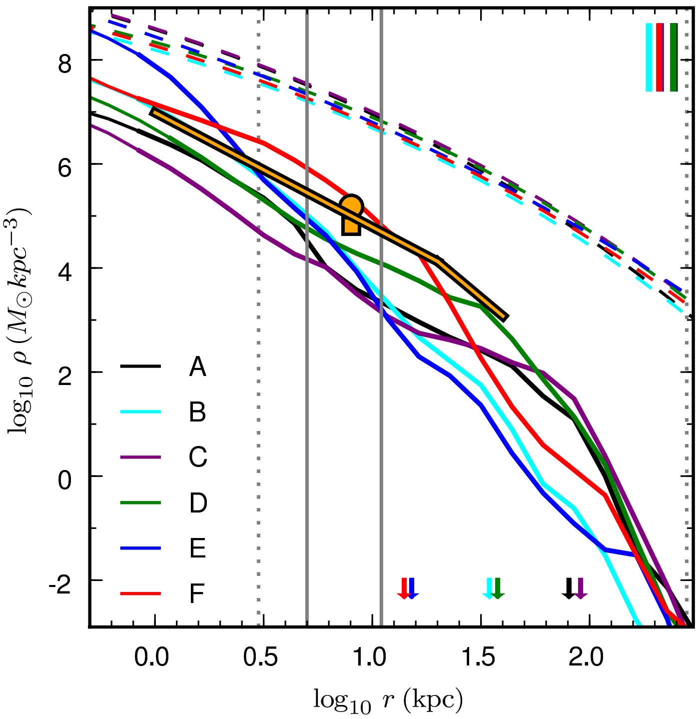

Figure 3.8: Spherically averaged density profiles for our six stellar haloes (shown as thin lines below the $\kappa = 7$ radius of Navarro et al. 2008, at which the circular velocity of the dark matter halo has converged to an accuracy of 1%). Arrows mark the break radii of broken power-law fits to each profile. Dashed lines show Einasto profile fits to the corresponding dark matter haloes (Navarro et al. 2008). Grey vertical lines demarcate our outer halo region (dotted) and the Solar neighbourhood (solid); coloured vertical bars indicate r_{200} for the dark haloes. For reference we overplot representative data for the Milky Way (orange): estimates of the halo density in the Solar neighbourhood (symbols) from Gould et al. (1998, square) and Fuchs & Jahreiß (1998, circle), and the best-fitting broken power-law of Bell et al. (excluding the Sagittarius stream and Virgo overdensity).

3.1.3 Bulk halo properties and observables

Distribution of mass

In Fig. 3.8 we show the spherically averaged density profiles of halo stars (excluding material bound in surviving satellites, but making no distinction between streams, tidal tails or other overdensities, and a ‘smooth’ component). The notable degree of substructure in these profiles contrasts with the smooth dark matter haloes, which are well-fit by the Einasto profiles shown in Fig. 3.8. As discussed further below, this stellar substructure is due to the contribution of localised, spatially coherent subcomponents within the haloes, which are well resolved in our particle representation.

The shapes of the density profiles are broadly similar, showing a strong central concentration and an outer decline considerably steeper than that of the dark matter. We overplot in Fig. 3.8 an approximation of the Milky Way halo profile (Bell et al. 2008) and normalization (Fuchs & Jahreiß 1998; Gould et al. 1998). The gross structure of our three many-progenitor haloes (Aq-A, Aq-C and Aq-D) can be fit with broken power-law profiles having indices similar to the Milky Way ($n \sim -3$) interior to the break. Bell et al. (2008) note that their best-fitting observational profiles do not fully represent the complex structure of the halo, even though they mask out known overdensities (our fits include all halo substructure). Our fits decline somewhat more steeply than the Bell et al. data beyond their break radii. We suggest that the Milky Way fit may represent variation at the level of the fluctuations seen in our profiles, and that an even steeper decline may be observed with a representative and well-sampled tracer population to > 100 kpc (for example, Ivezić et al. 2000 find a sharp decline in counts of RR Lyr stars beyond ~ 60 kpc). In contrast with the many-progenitor haloes, two of our few-progenitor haloes (Aq-B and Aq-E) have consistently steeper profiles and show no obvious break. Their densities in the Solar shell are none the less comparable to the many-progenitor haloes. Aq-F is dominated by a single progenitor, the debris of which retains a high degree of unmixed structure at $z = 0$ (see also Fig. 3.10).

We show projected surface brightness profiles in Fig. 3.9. As with their three-dimensional counterparts, two characteristic shapes distinguish the many- and few-progenitor haloes. The few-progenitor haloes are centrally concentrated and well fit in their innermost $\sim 10\,\mathrm{kpc}$ by Sersic profiles with $1.5 < n < 2.2$. Beyond $10\,\mathrm{kpc}$, extended profiles with a more gradual rollover (described by Sersic profiles with $n \sim 1$ and $25 < r_{\mathrm{eff}} < 35$ kpc) are a better fit to the many-progenitor haloes. In their centres, however, the many-progenitor haloes display a steep central inflection in surface brightness. As a consequence of these complex profiles, Sersic fits over the entire halo region (which we defined to begin at 3 kpc) are not fully representative in either case. To illustrate this broad dichotomy in Fig. 3.9, Sersic fits to a smoothly growing halo (Aq-C) *beyond* 10 kpc and a few-progenitor halo (Aq-E) *interior to* 10 kpc are shown. Abadi et al. (2006) found the average of their simulated stellar haloes to be well-fit by a Sersic profile ($n = 6.3$, $r_{eff} = 7.7$ kpc) in the radial range $30 < r < 130$ kpc, which we show as an orange dashed line in Fig. 3.9. This profile is close to the 'mean' profile of our halos A, C and D interior to 30 kpc (neglecting the significant fluctuations and inflections within each individual halo in Fig. 3.9), but does not capture the sharp decline of our haloes at radii beyond 150 kpc. Fig. 3.9 also shows (as dashed grey lines) the fits of Ibata et al. (2007) to the haloes of M31 (comprising an $r^{1/4}$ spheroid and shallow powerlaw tail at large radii) and M33 (powerlaw tail only).

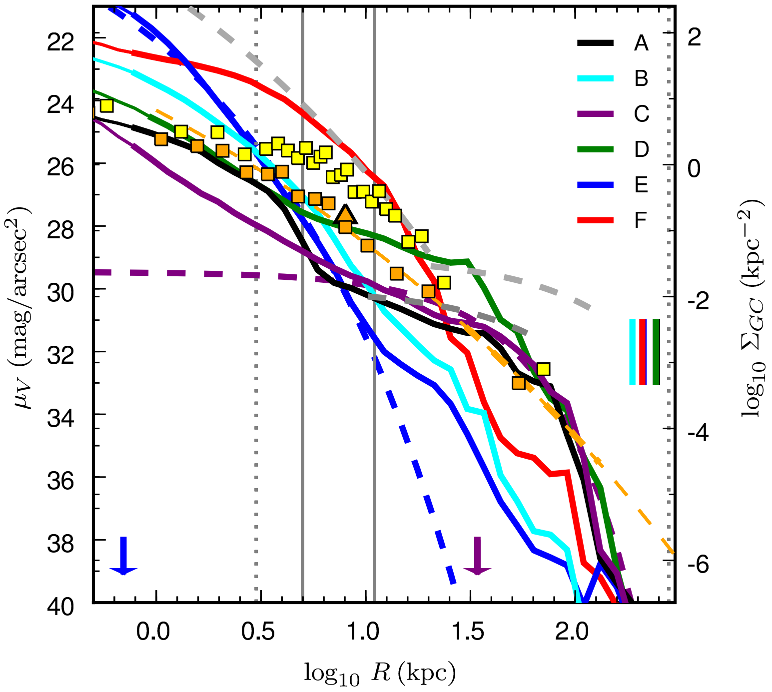

Figure 3.9: Radially averaged surface brightness profiles. Dashed lines show illustrative Sersic fits to haloes Aq-E and Aq-C (see text), with arrows indicating the corresponding scale radii. We show sections of equivalent profiles for the haloes of M31 (including the inner $r^{1/4}$ 'spheroid') and M33 (beyond 10 kpc) as dashed grey lines (Ibata et al. 2007). We overplot the surface number density (right-hand axis) of globular clusters in M31 (yellow squares) and the Milky Way (orange squares), with 40 and 10 clusters per bin, respectively. These profiles have been arbitrarily normalized to correspond to an estimate of the surface brightness of halo stars in the Solar neighbourhood from Morrison (1993), shown by an orange triangle. Vertical lines are as in Fig. 3.8.

There is evidence for multiple kinematic and chemical subdivisions within the Galactic globular cluster population (e.g. Searle & Zinn 1978; Frenk & White 1980; Zinn 1993; Mackey & Gilmore 2004, and references therein). This has led to suggestions that at least some of these cluster subsets may have originated in accreted satellites (Bellazzini et al. 2003; Mackey & Gilmore 2004; Forbes et al. 2004). Support for this conclusion includes the presence of five globular clusters in the Fornax dwarf spheroidal (Hodge 1961) and the association of several Galactic clusters with the Sagittarius nucleus and debris (e.g. Layden & Sarajedini 2000; Newberg et al. 2003; Bellazzini et al. 2003). Similarities with the 'structural' properties of stellar populations in the halo have motivated a longstanding interpretation of globular clusters as halo (i.e. accretion debris) tracers (e.g. Lynden-Bell & Lynden-Bell 1995). We therefore plot in Fig. 3.9 the surface density profile of globular clusters in the Milky Way (Harris 1996) and M31 (confirmed GCs in the Revised Bologna Catalogue – RBC v3.5, March 2008 Galleti et al. 2004, 2006, 2007; Kim et al. 2007; Huxor et al. 2008). The Milky Way data have been projected along an arbitrary axis, and the normalization has been chosen to match the surface density of Milky Way clusters to an estimate of the surface brightness of halo stars in the Solar neighbourhood ($\mu_V = 27.7\,\mathrm{mag/arcsec^2}$; Morrison 1993). We caution that the RBC incorporates data from on-going surveys as it becomes available: the M31 GC profile shown here is therefore substantially incomplete, particularly with regard to the sky area covered beyond $\sim$ 20–30 kpc.

Abadi et al. (2006) showed that their average stellar halo Sersic fit also approximates the distribution of globular clusters in the Milky Way and M31. As stated above, the inner regions of our haloes Aq-A, Aq-C and Aq-D are in broad agreement with the Abadi et al. halo profile, and hence show some similarities with the observed globular cluster profiles also. Both the halo and cluster samples show strong variations from halo to halo, however, and the comparison of these small samples is inconclusive. A close correspondence between accreted halo stars and globular clusters would be expected only if the majority of clusters are accreted, if accreted satellites contribute a number of clusters proportionate to their stellar mass, and if all stripped clusters have an equal probability of surviving to $z = 0$. None of these assumptions is realistic, and further work is required to better constrain the relationship between globular clusters and stellar haloes.

The multicomponent nature of our haloes, which gives rise to the local structure in their overall profiles, is examined in more detail in Fig. 3.10. Here the density profiles of the major contributors shown in Fig. 3.5 are plotted individually (progenitors contributing $< 5\%$ of the halo have been added to the panel for Aq-F). It is clear from these profiles that material from a given progenitor can be deposited over a wide range of radii. The few-progenitor haloes show strong gradients in ρr^2 while more uniform distributions of this quantity are seen in their sub-dominant contributors and in most contributors to the many-progenitor haloes.

Finally, we show in Fig. 3.11 the time at which the satellite progenitors of halo stars at a given radius were accreted (this infall time is distinct from the time at which the stars themselves were stripped, which may be considerably later). An analogous infall time can be defined for the surviving satellites, which are shown as points in Fig. 3.11. We would expect little information to be encoded in an instantaneous sample of the radii of surviving satellites, but their infall times can none the less be usefully compared with those of halo stars.

A gradient to earlier infall times with decreasing radius is apparent in both the satellites and the many-progenitor haloes. In the case of the haloes, this reflects the fact that relatively larger apocentres are associated with later-infalling satellites, which enable them to deposit material over a greater radial range. Assembly in this manner is arguably not adequately characterised as ‘inside out’ formation. Late infalling material is added at all radii but has a greater maximum

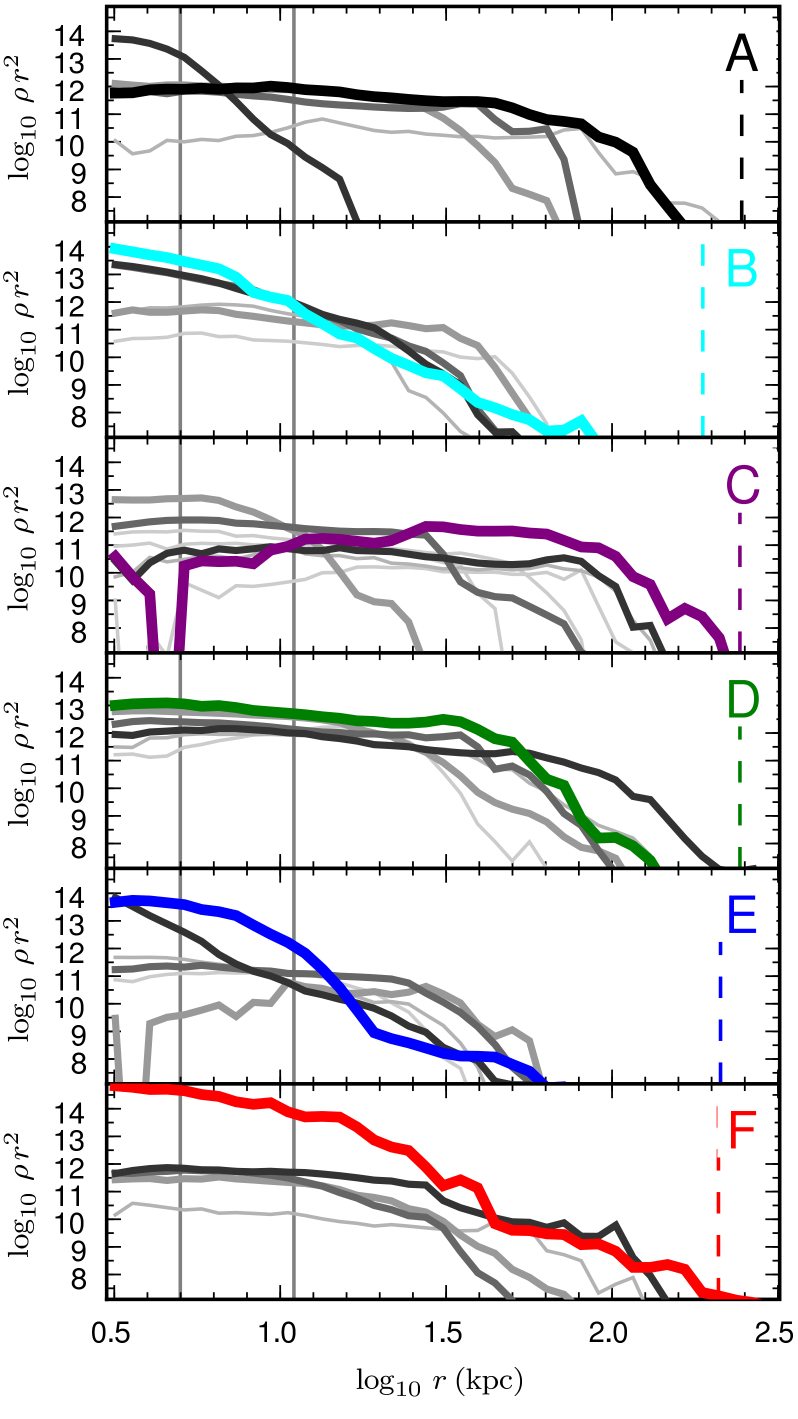

Figure 3.10: Individual density profiles (multiplied by r^2) for stars contributed by each of the most significant progenitors of the halo (defined in Section 2.2.3). Line types indicate the rank order of a progenitor contribution: the bold coloured line in each panel indicates the most significant contributor, while lesser contributions are shown by increasingly lighter and thinner lines. Vertical solid and dashed lines indicate the Solar shell and virial radius respectively, as Fig. 3.8. Individual stellar halo components contribute over a wide radial range, and different components 'dominate' at particular radii. This figure can be used to interpret the radial trends shown in other figures.

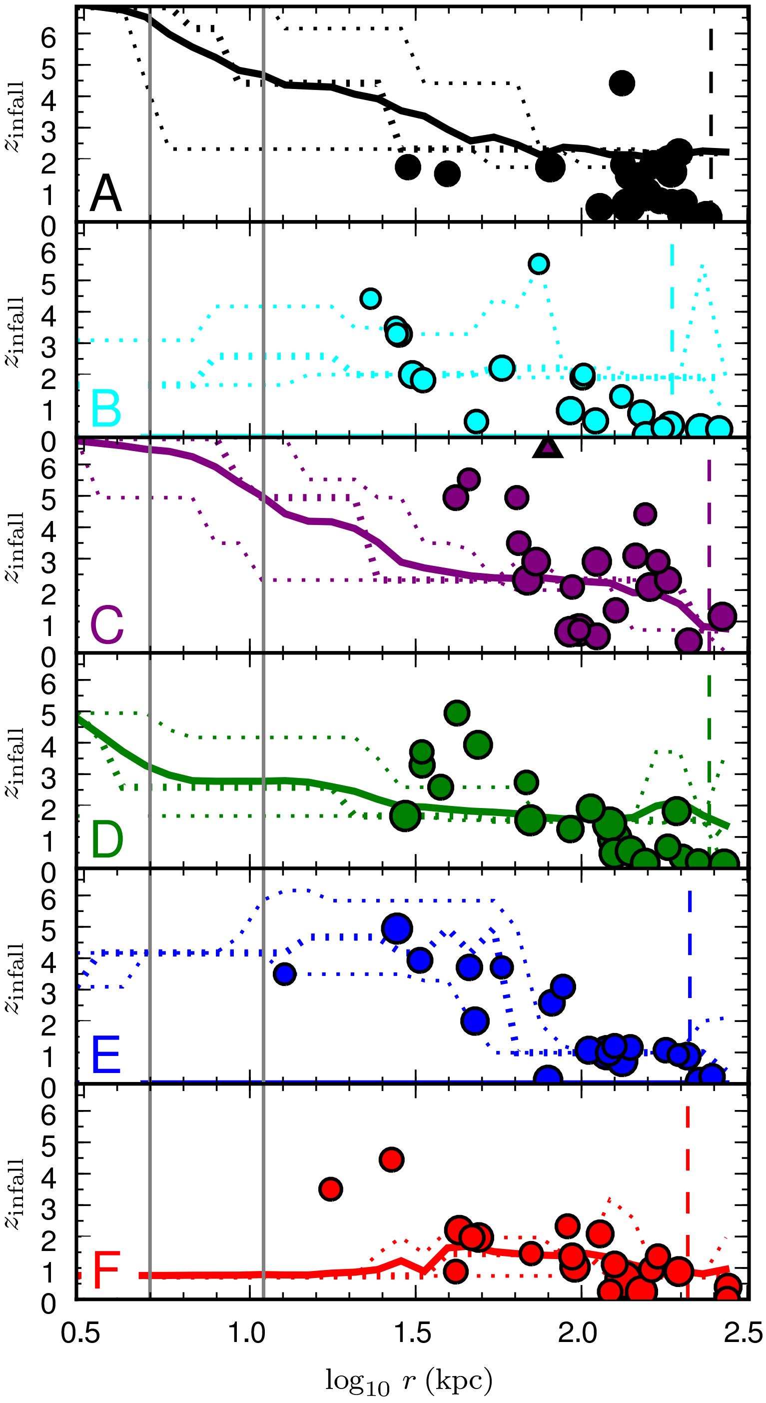

Figure 3.11: Lines show, for halo stars at a given radius at $z = 0$, the mean (solid), median and 10/90th percentile (dotted) redshift at which their parent galaxy was accreted on to the main halo (*not* the time at which the stars themselves were stripped). Filled circles show the redshift at which surviving satellites were accreted; triangles indicate satellites accreted before $z = 7$. Within the Solar shell, the stellar halo is typically old in this 'dynamical' sense, whereas beyond 100 kpc its young 'dynamical' age is comparable to that of the surviving satellite population. In many cases the innermost satellites represent a relic population that is 'older' than the stellar halo at comparable radii.

extent than earlier-infalling material. The result is that earlier-infalling material comes to *dominate* towards the centre. For the few-progenitor haloes the profile of infall time is essentially flat (or shows sharp transitions between populations), more closely reflecting the contributions of individual progenitors.

Further to our discussion of satellite survival in our haloes in Section 3.1.2, it is interesting that amongst the surviving satellites, we observe several accreted at $z > 1$. For example, in the case of Aq-E, six surviving satellites are accreted at $z \sim 3.5$. At the present day this group is found in association with a concentration of halo stars from a stellar halo progenitor also infalling at this time. The majority of survivors in each halo are accreted recently, however, and typically more recently than the stellar halo progenitors. The opposite is true for the earliest-accreted survivors, which are accreted earlier than the halo at the notably small radii at which they are now found. In general, at any given instant the majority of satellites are more likely to be located nearer to the apocentre of their orbit than the pericentre. Furthermore, the orbits of the most massive satellites are likely to have been more circular than their disrupted siblings and dynamical friction may act to reinforce such a trend. Therefore, the locations of early-infalling survivors are likely to be fairly represented by their radius in Fig. 3.11. Dynamical friction acts to contract but also to circularize orbits. Plausibly these survivors are those that have sunk slowly as the result of their initially low orbital eccentricities.

Stellar populations

In this section, we show how the multicomponent nature of our stellar haloes is reflected in their metallicity profiles, and contrast the stellar populations of surviving satellites with those of halo progenitors. We caution that a full comparison of the relationship between the stellar halo and surviving satellites will require more sophisticated modelling of the chemical enrichment process than is included in our fiducial model, which adopts the instantaneous recycling approximation and does not follow individual elemental abundances. The model we adopt here tracks only total metallicity, defined as the total mass fraction of all metals relative to the Solar value, $Z/\mathrm{Z}_{\odot}$ (the absolute value of which cannot be compared directly with measurements of [Fe/H]). This model can nevertheless address the *relative* enrichment levels of different populations.

Fig. 3.12 shows the spherically averaged metallicity gradient in each halo. Haloes with many progenitors are characterised by a metallicity distribution of width ~ 1 dex and approximately constant mean value, fluctuating by less than ± 0.5 dex over a range of 100 kpc. This is comparable to observations of the M31 halo, which show no significant gradient (metallicities varying by ± 0.14 dex) in the range 30–60 kpc (Richardson et al. 2009). Localised structure is most apparent in the few-progenitor haloes: Aq-F shows a clear separation into two components, while Aq-B and Aq-E exhibit outwardly declining metallicity gradients. In all cases the mean metallicity within the Solar radius is relatively high. These features can be explained by examining the relative weighting of contributions from individual progenitors at a given radius, as shown in the density profiles of Fig. 3.10, bearing in mind the mass-metallicity relation for satellites that arises in our model. Where massive progenitors make a significant luminosity-weighted contribution, the haloes are seen to be metal-rich. Overall, metallicity gradients are shallower in those haloes where many significant progenitors make a comparable contribution, smoothing the distribution over the extent of the halo. Conversely, metallicity gradients are steeper where only one or two disproportionately massive satellites make contributions to the halo (as indicated by the luminosity functions of Fig. 3.4). Sharp contrasts are created between the radii over which this metal-rich material is deposited (massive satellites suffer stronger dynamical friction and sink more rapidly, favouring their concentration at the centres of haloes) and a background of metal-poor material from less massive halo progenitors. This effect is clearly illustrated by the sharp transition in Aq-F and at two locations (centrally and at $\sim 100\,\mathrm{kpc}$) in Aq-E.

It follows that the process by which our smooth haloes are assembled, which gives rise to the steep gradients of progenitor infall time with redshift shown in Fig. 3.11, also acts to *erase* metallicity gradients. As a result, measurements of (for example) $[\mathrm{Fe/H}]$ alone do not constrain the local infall time: a metal-poor halo need not be 'old' in the sense of early assembly. A particularly notable example of this is Aq-E, where the centrally dominant metal-rich material was assembled into the halo considerably *earlier* ($z \sim 3$) than the diffuse outer envelope of relatively metal-poor material ($z \sim 1$). This is a manifestation of a mass-metallicity relation in satellites: at fixed luminosity, an earlier infall time is 'compensated for' by more rapid star formation, resulting in a comparable degree of overall enrichment as that for a satellite with similar luminosity infalling at lower redshift. Abundance ratios such as $[\alpha/\mathrm{Fe}]$ indicate the time taken by a given stellar population to reach its observed level of enrichment, and so distinguish between rapidly forming massive populations, truncated by early accretion to the halo, and populations reaching similar mass and metallicity through gradual star formation (e.g. Shetrone et al. 2001; Tolstoy et al. 2003; Venn et al. 2004; Robertson et al. 2005).

Fig. 3.13 shows luminosity-weighted metallicity distribution functions (MDFs) for two selections of halo stars: a 'Solar shell' ($5 < r < 12\,\mathrm{kpc}$; dashed lines) and the entire halo as defined in Section 2.2.3 (dotted). We compare these to MDFs for stars in the surviving satellites in each

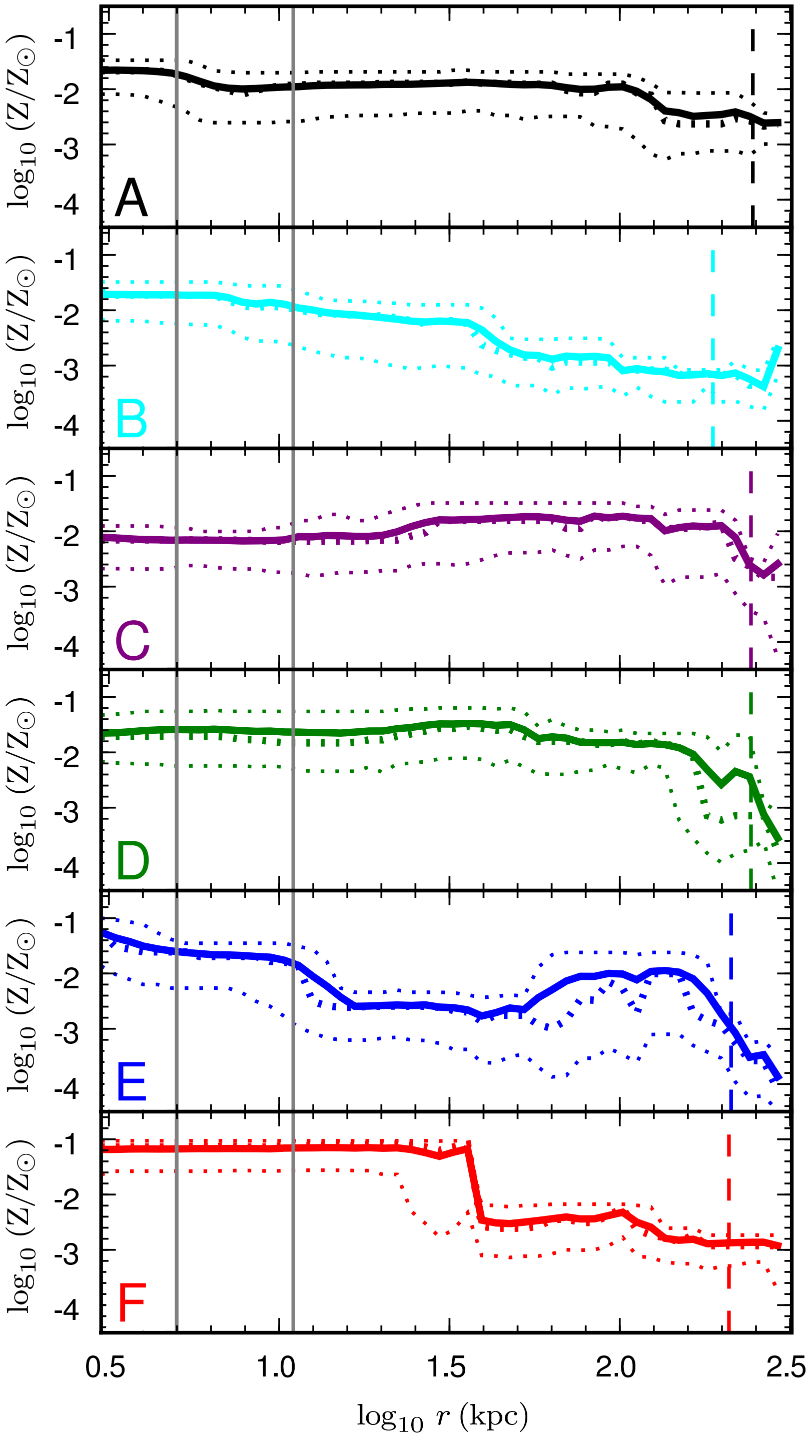

Figure 3.12: Radial profiles of luminosity-weighted metallicity (ratio of total metal mass fraction to the Solar value) for spherical shells in our six haloes, showing the mean (solid) and median (thick dotted) profiles, bracketed by the 10th and 90th percentiles (dotted).

halo, separating bright ($M_\mathrm{V} < -10$, $r < 280\,\mathrm{kpc}$; thick, coloured) and 'faint' ($-10 < M_\mathrm{V} < -5$; thin, grey) subsets. All distributions are normalized individually to the total luminosity in their sample of stars.

The MDF of Solar-shell halo stars is typically broad, and tends to peak at slightly higher metallicity (by < 0.5 dex) than the aggregated surviving bright satellites. The halo as a whole is comparable to the Solar shell. A clear disparity is only evident in Aq-E, where the halo appears to reflect more closely the distribution of fainter, lower-metallicity satellites. In all cases, the MDF of these faint satellites peaks at considerably lower metallicity than in the halo or brighter satellites.

In Section 1.3.1 we discussed the chemical evidence for a halo built by satellite accretion: specifically, the inferred difference in star formation histories for halo progenitors and surviving satellites, and the relative fractions of metal-poor stars in these two groups. The low metallicity tails of *cumulative* metallicity distributions are shown in Fig. 3.14. The three panels show (from top to bottom) distributions for halo stars (the mean of which is indicated by a solid orange line common to all three panels), faint satellites (mean dark green) and bright satellites (mean light green). We find that the 'average' halo has an equivalent number of very metal-poor stars to the surviving bright satellites, although there are clear exceptions in individual cases. The fainter satellites have a substantially greater fraction of very metal-poor stars, in accordance with their low mean metallicities[2] (Fig. 3.13). Surviving satellites contain a greater fraction of moderately metal-poor stars ($\log_{10}(Z/\mathrm{Z}_\odot) < -2.5$) than the halo.

Our halo models suggest that similar numbers of comparably luminous (and hence metal-rich) satellites contribute to the bright end of both the halo-progenitor and the surviving-satellite luminosity functions, and that these bright satellites are the dominant contributors to the halo. This supports the view that halo MDFs should resemble those of bright survivor satellites in their metal-poor tails. At very low metallicities the halo is dominated by the contribution of low-luminosity satellites which are exclusively metal-poor; the stars associated with these faint contributors are expected to represent only a very small fraction of the total halo luminosity.

Finally, Fig. 3.15 compares the luminosity-weighted age distributions of halo stars in the Solar shell with those in the surviving satellites ($M_\mathrm{V} < -5$), separated into bright and faint subsets. The average of all six haloes contains essentially no stars younger than 5 Gyr (if we

---

[2] That the fainter dwarfs may appear disproportionately metal-poor is a consequence of the steep mass-metallicity relation for these galaxies in our models.

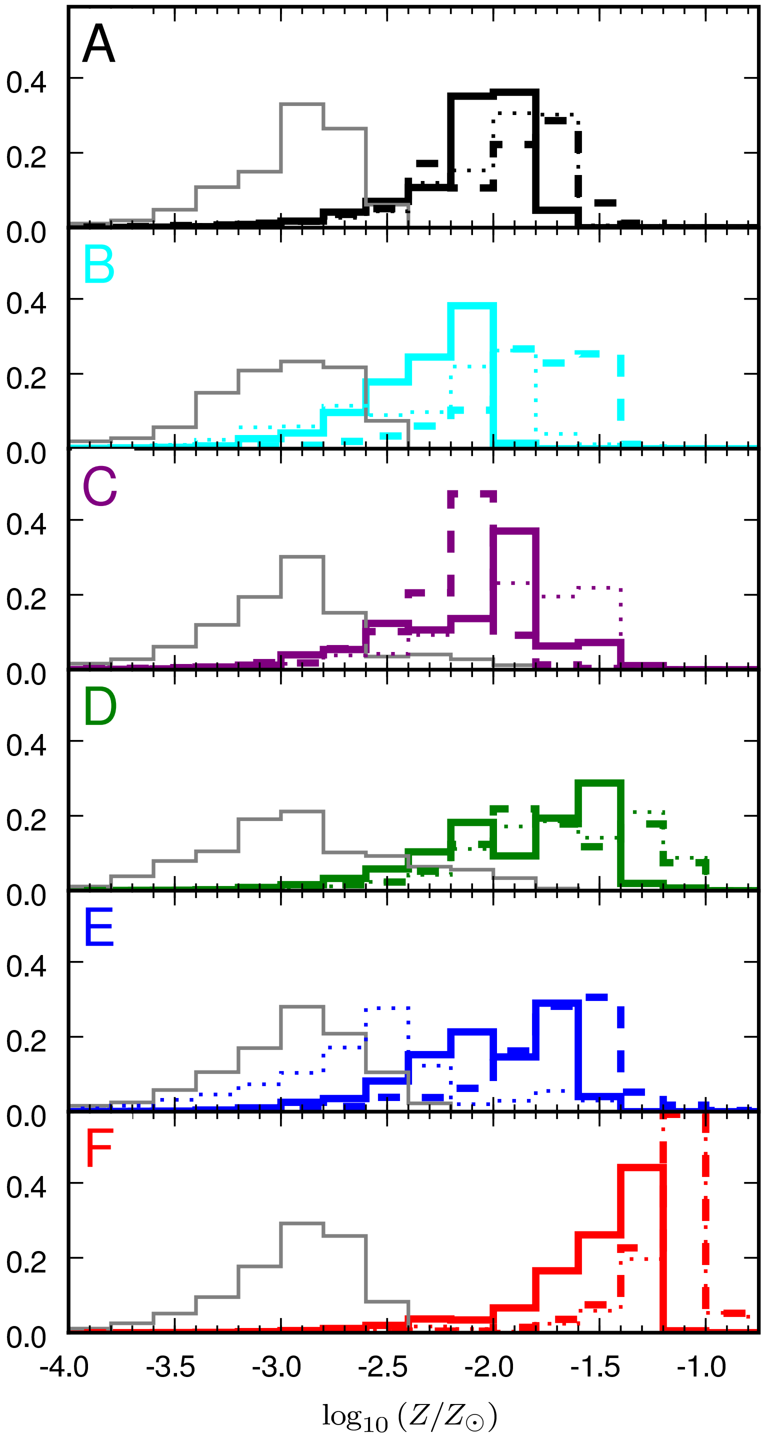

Figure 3.13: Metallicity distribution functions of bright ($M_V < -10$; solid coloured) and faint ($-10 < M_V < -5$; solid grey) satellites, halo stars in the 'Solar shell' (dashed) and the entire halo ($3 < r < 280$ kpc, dotted). Z is the total mass fraction of all metals.

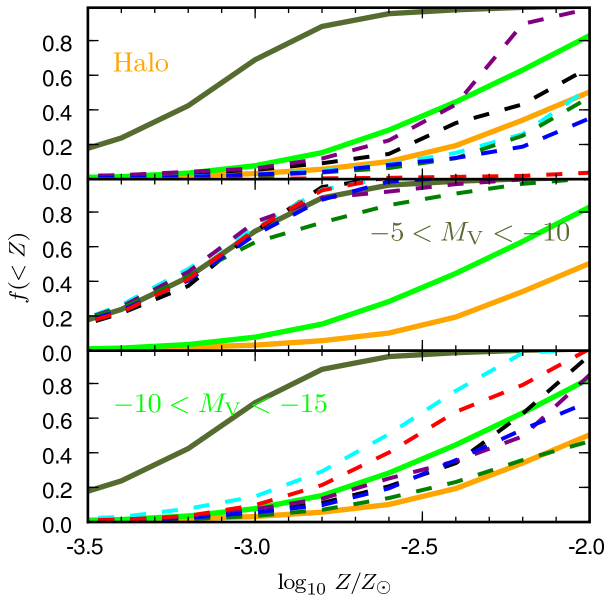

Figure 3.14: Tails of the cumulative luminosity-weighted metallicity distribution (mean of all six simulations) for halo stars in the Solar shell ($5 < r < 12$ kpc, orange, top panel) compared to bright ($-15 < M_V < -10$; light green, bottom) and faint ($-10 < M_V < -5$; dark green, centre) satellites ($M_V < -10$), showing individual contributions from each halo (dashed, colours as in previous figures) to the mean value represented by each panel. The total stellar masses of these three components over all haloes are 1.04×10^9, 7.45×10^8 and 3.45×10^8 $\mathrm{M}_\odot$, respectively.

exclude halo Aq-F, which is strongly influenced by the late accretion of an SMC-like object, this minimum age rises to 8 Gyr). The median age of halo stars is $\sim$ 11 Gyr. By contrast, the brightest satellites have a median age of $\sim$ 8 Gyr and a substantial tail to young ages (with $\sim 20\%$ younger than 4 Gyr and $\sim 90\%$ younger than the median halo age). The distribution of old stars in the faintest surviving satellites is similar to that of the halo.

The true age distribution of halo stars is poorly constrained in comparison to that of the satellites (e.g. Tolstoy et al. 2009). By comparing the colour and metallicity distributions of Milky Way halo stars to those of the Carina dSph, Unavane et al. (1996) have argued that similar satellites (i.e. those with a substantial fraction of intermediate-age stars) could not contribute more than $\sim 1\%$ to the halo (equivalent to a maximum of $\sim$ 60 halo progenitors of Carina's luminosity). A corresponding limit of $\leq$ 6 Fornax-like accretions in the last $\sim$ 10 Gyr was derived from an analysis of higher metallicity stars by the same authors, consistent with the progenitor populations of our simulated stellar haloes.

It is important in this context that the satellites themselves form hierarchically. In our models, between ten and twenty progenitors are typical for a (surviving) galaxy of stellar mass comparable to Sagittarius, or five to ten for a Fornax analogue. Satellites in this mass range

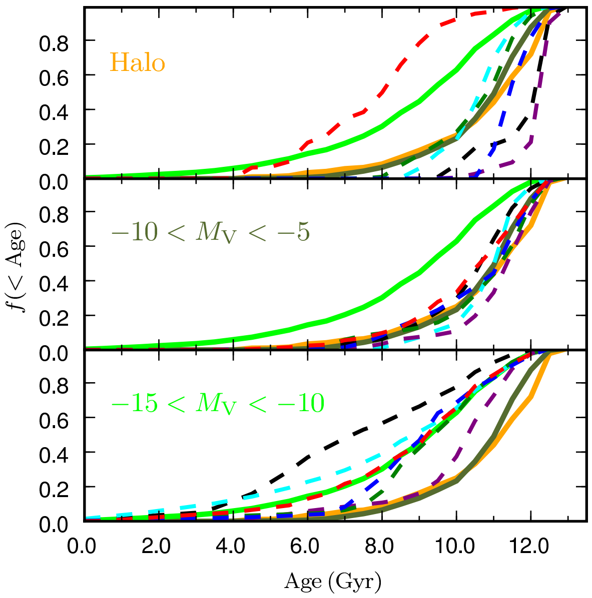

Figure 3.15: The cumulative luminosity-weighted age distributions of halo and satellite stars. Lines and panels are as Fig. 3.14

are the most significant contributors to our stellar haloes. Their composite nature is likely to be reflected in their stellar population mix and physical structure, which could complicate attempts to understand the halo 'building blocks' and the surviving satellites in terms of simple relationships between mass, age and metallicity.

3.2 Conclusions

We have presented a technique for extracting information on the spatial and kinematic properties of galactic stellar haloes that combines a very high resolution fully cosmological ΛCDM simulation with a semi-analytic model of galaxy formation. We have applied this technique to six simulations of isolated dark matter haloes similar to or slightly less massive than that of the Milky Way, adopting a fiducial parameterization of the GALFORM semi-analytic model. The structural properties of the surviving satellites have been used as a constraint on the assignment of stellar populations to dark matter. We found that this technique results in satellite populations and stellar haloes in broad agreement with observations of the Milky Way and M31, if allowance is made for differences in dark halo mass.

Our method of assigning stellar populations to dark matter particles is, of course, a highly simplified approach to modelling star formation and stellar dynamics. As we discuss further in Chapter 6, the nature of star formation in dwarf galaxy haloes remains largely uncertain. In future, observations of satellites interpreted alongside high-resolution hydrodynamical simulations will test the validity of approaches such as ours. As a further simplification, our models do not account for a likely additional contribution to the halo from scattered *in situ* (disc) stars, although we expect this contribution to be minimal far from the bulge and the disc plane. The results outlined here therefore address the history, structure and stellar populations of the accreted halo component in isolation.

Our results can be summarised as follows:

- Our six stellar haloes are predominantly built by satellite accretion events occurring between $1 < z < 3$. They span a continuum of assembly histories, from 'smooth' growth (with a number of roughly equally massive progenitors accreted steadily over a Hubble time) to growth in one or two discrete events.
- Stellar haloes in our model are typically built from fewer than 5 significant contributors. These significant objects have stellar masses comparable to the brightest classical dwarf spheroidals of the Milky Way; by contrast, fewer faint satellites contribute to the halo than are present in the surviving population.
- Typically, the most massive halo contributor is accreted at a lookback time of between 7 and 11 Gyr ($z \sim 1.5 - 3$) and deposits tidal debris over a wide radial range, dominating the contribution at large radii. Stars stripped from progenitors accreted at even earlier times usually dominate closer to the centre of the halo.
- A significant fraction of the stellar halo consists of stars stripped from individual *surviving* galaxies, contrary to expectations from previous studies (e.g. Bullock & Johnston 2005). It is the most recent (and significant) contributors that are likely to be identifiable as surviving bound cores. Such objects have typically lost $\sim 90\%$ of their original stellar mass.
- We find approximately power-law density profiles for the stellar haloes in the range $10 < r < 100$ kpc. Those haloes formed by a superposition of several comparably massive progenitors have slopes similar to those suggested for the Milky Way and M31 haloes, while those dominated by a disproportionally massive progenitor have steeper slopes.
- Our haloes have strongly prolate distributions of stellar mass in their inner regions ($c/a \sim 0.3$), with one exception, where an oblate, disc-like structure dominates the inner $10 - 20$ kpc.

- Haloes with several significant progenitors show little or no radial variation in their mean metallicity ($Z/\mathrm{Z}_{\odot}$) up to 200 kpc. Those in which a small number of progenitors dominate show stronger metallicity gradients over their full extent or sharp transitions between regions of different metallicity. The centres of these haloes are typically more enriched than their outer regions.
- The stellar populations of the halo are likely to be chemically enriched to a level comparable to that of the bright surviving satellites, but to be as old as the more metal-poor surviving ‘ultra faint’ galaxies. The very metal-poor tail of the halo distribution is dominated by contributions from a plethora of faint galaxies that are insignificant contributors to the halo overall.

4

Observations of Structure in the Milky Way Halo

4.1 Introduction

The previous chapter demonstrated qualitatively that the CDM model predicts a high degree of structure in the stellar haloes of Milky Way-like galaxies. The properties of this structure are sensitive to the accretion history of the dark halo (e.g. Johnston et al. 2008). A large number of similar structures and substructures have been detected in the Milky Way and M31 haloes, but it is difficult to compare these discoveries to the expectations of CDM with models that lack resolution (e.g. De Lucia & Helmi 2008) or a full cosmological context (e.g. Johnston et al. 2008). In this chapter we discuss two aspects of 'global' structure in our high resolution cosmological models, which address both of these shortcomings.

4.2 Starcounts

Counting the predicted number of halo stars over different regions of the sky is a straightforward way to compare the structure of our model haloes to real Milky Way data. The previous chapter presented spherically averaged density profiles and radially averaged surface brightness profiles. These were broadly consistent with the global structure of the Milky Way and M31, although most of our fiducial models are less dense and luminous than the Milky Way halo at the Solar neighbourhood. Here we are concerned with substructure rather than the absolute normalization of these profiles. Hence, we examine the *fluctuations* in counts of stars across the sky, as seen by an observer at the location of the Sun. We do this in a manner that is independent, in principle, of the overall normalization in the density of halo stars. Quantifying deviations from a smooth halo in this way is a very simple statistical comparison, but nevertheless it highlights some important issues that more detailed comparisons will need to address.

We compare with data obtained by Bell et al. (2008), who attempted to isolate metal-poor main sequence turn-off (MSTO) stars in SDSS (DR5) by selecting objects classified as stars with $0.2 < g-r < 0.4$. Distances were estimated for these stars by assuming that MSTOs are approximate 'standard candles', with only a small intrinsic dispersion about a mean absolute magnitude $M_r \sim 4.5$. These photometric distances allowed Bell et al. (2008) to study the distribution of stars on the sky in radial bins, from ~ 7 to ~ 40 kpc. The sky distribution was quantified by counting stars in $2.5^\circ \times 2.5^\circ$ cells and calculating the root mean square (RMS) deviation of the observed counts around those predicted by a smoothly distributed halo model[1]. A number of smooth models were considered and a 'best-fit' halo model was derived by minimising the RMS.

Although Bell et al. searched a large parameter space, they found all their smooth models to be a poor fit to the data. This suggests that the smooth halo has a more complex structure than a broken power law, or equivalently, that there is a large amount of substructure in the halo (substructure contributes the 'intrinsic residuals' in these smooth fits). This difficulty in recovering an adequate smooth model motivates a simpler comparison between our models and the Milky Way MSTO data, in the first instance. We therefore examine the simple 'fractional rms' statistic $\sigma_{\mathrm{rms}}/\rho$, where σ_{rms} is the RMS of counts in individual cells, and ρ is the mean count over all cells in the survey.

The outputs of the simulations described in Chapter 2 cannot be treated directly as catalogues of halo stars for the purpose of the comparisons with observations that we make in this chapter. Each tagged dark matter particle in the simulation outputs represents a different amount of stellar mass, and this 'density field' must be converted to a corresponding *number* of individual stars before it can be treated as mock observational data. The following section describes how we generate mock catalogues of tracer stars from the simulation outputs.

4.2.1 Tracer star catalogues

Using the simulations described in Chapter 2, we construct catalogues of tracer stars (for example MSTO, RGB or BHB stars) by converting the stellar mass assigned to each dark matter particle into an appropriate number of stars. Each DM particle can give rise to many tracer stars if it is tagged with sufficient stellar mass.

---

[1] The 'σ/total' statistic used by Bell et al. is formally insensitive to Poisson noise

We assign individual positions and velocities to each tracer star by interpolating between the near neighbours of its parent DM particle in phase space. To accomplish this, the 32 nearest phase space neighbours of each tagged particle are identified using a procedure which we describe below. The mean dispersion in each of the six phase-space coordinates is then calculated for each particle by averaging over these neighbours. These dispersions define a six-dimensional ellipsoidal Gaussian kernel centred on the particle, from which the positions and velocities of the tracer stars that it generates are drawn randomly. Each progenitor object (a set of tagged DM particles accreted as members of a single subhalo) is treated individually in this smoothing operation, i.e. particles are smoothed using only neighbours from the same progenitor (so there is no 'cross talk' between streams from different progenitors). This procedure can be thought of as a crude approximation to running our original simulation again including each tracer star as a test particle.

The 'distance in phase space' used to identify neighbours in the interpolation scheme is defined by a scaling relation between distances in configuration space and velocity space[2]. For each progenitor, we adopt an individual scaling which corresponds to making the median pairwise interparticle separation of its particles in configuration space (at $z = 0$) equal to their median separation in velocity space. In practice the value of this scaling parameter makes very little difference to the results we present, when compared to the extreme choice of selecting only 32 velocity or position neighbours (disregarding the other three coordinates in each case). Giving more weight to configuration-space neighbours smears out velocity substructure within the debris of a progenitor (for example, where two wraps of a stream pass near one another). Giving more weight to velocity neighbours has the opposite effect; stars can be interpolated over arbitrarily large separations in configuration space, but coherent velocity structures are preserved. Therefore, one 'optimal' choice is the scaling which balances smoothing in configuration space against smoothing in velocity space.

To quantify this balance between smoothing in configuration and velocity, we compute six smoothing lengths for each particle, $\epsilon_{x,i}$ and $\epsilon_{v,i}$, where i represents a single dimension in space or velocity. We compute these as the spherically averaged dispersion in position and velocity, respectively, taken over the 32 phase-space neighbours of the particle. We define the 'optimum' choice of scaling for *each* progenitor galaxy as that which minimises the quantity

---

[2] In this part of the calculation, we are only interested in finding neighbours, so the absolute values of these distances are not important. This scaling of velocity space to configuration space for the purpose of resampling the simulations should not be confused with the Δ metric we define for our analysis of clustering.

$$\sigma_{\epsilon}^{2} = \left(\frac{1}{\bar{\epsilon}_{x,\mathrm{min}}} \sum_{i=0}^{3} \epsilon_{x,i} \right)^{2} + \left(\frac{1}{\bar{\epsilon}_{v,\mathrm{min}}} \sum_{i=0}^{3} \epsilon_{v,i} \right)^{2} . \tag{4.1}$$

This is the sum in quadrature of the mean smoothing lengths in configuration and velocity space, normalized respectively by $\bar{\epsilon}_{x,\mathrm{min}}$, the 'minimal' mean smoothing length in configuration space (obtained from the 32 nearest configuration space neighbours) and $\bar{\epsilon}_{v,\mathrm{min}}$, the 'minimal' mean smoothing length in velocity space (obtained from the 32 nearest velocity space neighbours). We find that the scaling obtained by matching the median interparticle separations in position and velocity as described above is typically a good approximation to this optimal value – a similar result is discussed in more detail by Maciejewski et al. (2009).

Each N-body dark matter particle in our simulation contributes a number of tracer stars to our mock observations, depending on the mass of the stellar population with which it has been 'tagged'. Where we compare to the data of Bell et al. (2008) these tracers are MSTO stars detected by SDSS; likewise, in the case of our comparison to Spaghetti, the tracers are RGB stars meeting the (complex) selection criteria of that survey. Here we assume a global scaling between the stellar mass associated with each N-body particle, $M_{\star}$, and the number of tracers it contributes to our mock catalogues, i.e. $N_{\mathrm{T}} = f_{\mathrm{T}} M_{\star}$ where f_{T} is the number of tracer stars per unit mass of the original stellar population[3]. For each N-body particle, the actual number of stars generated is drawn from a Poisson distribution with mean N_{T}.

In the analysis that follows, we obtain distances and radial velocities to each tracer star assuming a randomly oriented vector of length $r_{\odot} = 8$ kpc linking the observer to the galactic centre. Each random placement of the observer on the 'Solar shell' is referred to below as one *random realisation* of the mock catalogue. Wherever the observer is placed on this spherical shell, galactic longitude and latitude are defined in the same way with respect to the footprint of the survey, with $(l, b) = (0, 0)$ being the vector directed from the observer to the centre of the halo. As there is no galactic plane in our simulations (which contain only the accreted component of the halo and the bulge), there is no direct constraint on the orientation of the 'rotation axis' of the galaxy seen by the observer (this is more significant in the context of the SDSS survey: in Section 4.8 we use the shape of the halo to fix the orientation of the galactic plane). To derive line-of-sight velocities we adopt a Solar motion of $U, V, W = (10, 5.2, 7.2)\,\mathrm{km\,s^{-1}}$ and a velocity of the local standard of rest about the galactic centre $v_{\mathrm{LSR}} = 220\,\mathrm{km\,s^{-1}}$.

---

[3] We do this as we prefer to make only a simple comparison with the observational data here. In principle, the age and metallicity information associated with each stellar population in our model could be used to populate an individual colour-magnitude diagram for each tagged N-body particle.

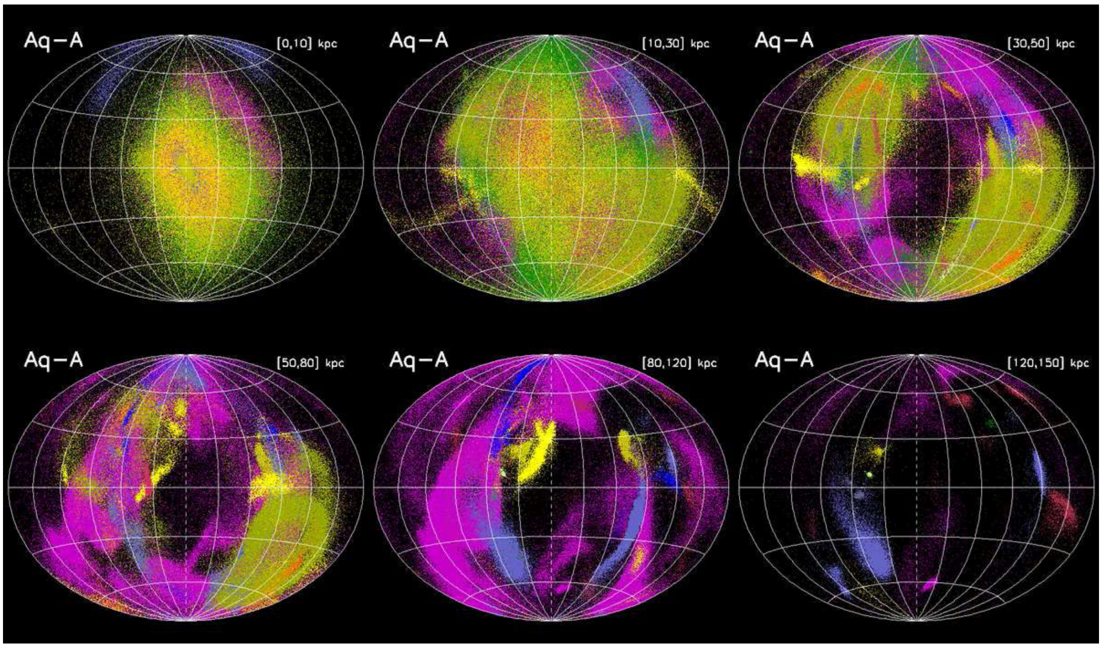

Figure 4.1: Sky distribution of stars brighter than the main sequence turn-off in halo Aq-A. Panels show a range of distance bins, measured from the Solar position. Colours correspond to unique progenitor galaxies. The total number of progenitors is 163, of which 53 contribute a stellar mass greater than $1 \times 10^4 \mathrm{M}_{\odot}$. 35 different progenitors contribute more than 50 tracer stars to the innermost bin, and 48 progenitors contribute to the bin from 10 and 30 kpc. Only 10 progenitors contribute more than 50 stars in the most distant bin shown here. Hence the diversity of the Aq-A stellar halo is most apparent at distances from 10 and 30 kpc. *(Figure produced by A. Helmi)*

4.2.2 The stellar halo as seen from the Sun

To illustrate the overall sky distribution of halo stars, we first select a fiducial sampling fraction $f_T = 0.025\,\mathrm{M}_{\odot}{}^{-1}$. This corresponds approximately to the total number of halo stars above the MSTO[4] in the models of Marigo et al. (2008).

Fig. 4.1 shows the sky distribution of stars in halo Aq-A. The different panels in Fig. 4.1 correspond to stars located at increasing distance from the Sun, which is assumed to be located at $(-8, 0, 0)$ kpc with respect to the halo centre (for this prolate halo, the major axis is very nearly aligned with the z-axis of the simulation reference frame). Particles with the same colour correspond to stars accreted from the same parent galaxy.

---

[4] Specifically, to the total number of stars more massive than $\sim 0.77\,\mathrm{M}_{\odot}$ for a 12 Gyr population with $[\mathrm{Fe/H}] = -1.5$, assuming a Chabrier et al. (2000) lognormal IMF. This and other values quoted in this chapter in relation to the mix of stellar populations were obtained using the online interface to the Padova isochrones at `http://stev.oapd.inaf.it/cgi-bin/cmd`

This figure shows that the distribution of stars in the accreted halo is very smooth in the inner 10 kpc, as expected. Substructures become apparent at ~ 20 kpc and dominate the halo beyond $\sim$30 kpc. These substructures are often diffuse, particularly at small distances from the galactic centre. This is because their progenitor satellites are relatively massive. For example, the most prominent streams in Fig. 4.1 are those in purple (visible at all distances), green (dominant in the very centre), light blue (which we describe below as a Sagittarius analogue) and light green (prominent beyond 30 kpc). These contribute 1.3×10^8, 1.4×10^8, 2.2×10^7 and 4.5×10^7 $\mathrm{M}_{\odot}$ respectively. Taken together these features account for 85% of the stellar mass in the halo of Aq-A.

The distribution of substructure on the sky is anisotropic, and appears to be preferentially found along a 'ring'. In this region, a system of streams very similar to those of the Sagittarius dwarf galaxy is apparent (shown in light blue). These streams lie at a similar distance and cover a similar area of the sky as the Sagittarius streams in the Milky Way halo[5]. Even the central regions of the stellar halo of Aq-A are not isotropic on the sky – a bar-like feature is visible towards the galactic centre. As we discussed in Chapter 3, the central regions of our stellar haloes are prolate or triaxial (there is some evidence for this in the case of the Milky Way, Newberg & Yanny 2006). It is likely that the degree of triaxiality would decrease if a massive stellar disk was included in the simulation (Tissera et al. 2010; Abadi et al. 2010).

Fig. 4.2 and Fig. 4.3 show the distance ranges 10 to 30 kpc and 30 to 50 kpc, respectively, for our other simulated haloes. In Fig. 4.2 we highlight the object in Aq-A resembling the Sagittarius dwarf, which is particularly interesting. It shows that such streams may come close to the Galactic centre, and remain coherent for many gigayears. This object became a satellite at redshift 1.74 (9.7 Gyrs ago), at which time its total mass was $2.9 \times 10^{10}\,\mathrm{M}_{\odot}$ and its stellar mass was $2.7 \times 10^7\,\mathrm{M}_{\odot}$. A bound core has survived until the present day with approximately 25% of the initial stellar mass.

We also find structures that resemble the Orphan stream (Belokurov et al. 2007b). Although they are not common at small radii, very low surface brightness thin streams are present, and can be found as close as 10 kpc to the halo centre. They have very elongated orbits, with typical apocentres between 30 and 40 kpc, extending up to 100 kpc in some case. This explains why they have remained coherent despite the triaxial shape of the halo and the graininess of the potential. These streams originate in low mass galaxies. For example, the stream shown in red

---

[5] Note, however, that in subsequent sections, we will adopt an orientation for the galactic plane such that this pseudo-Sgr stream is planar, not polar.

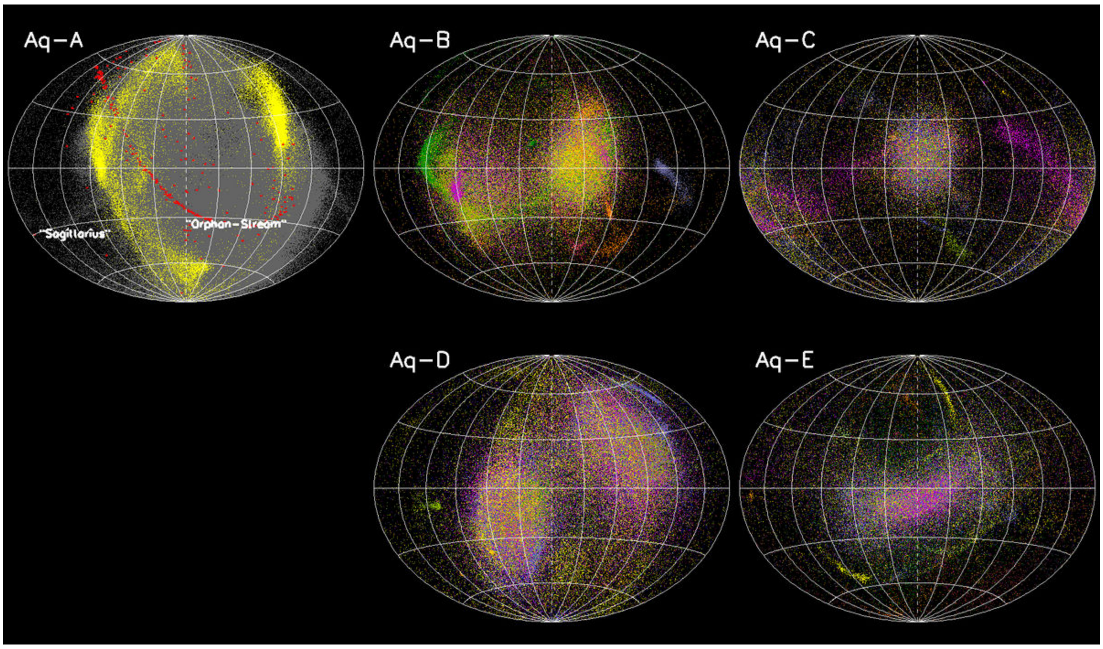

Figure 4.2: Sky distribution of stars brighter than the main sequence turnoff, located at distances between 10 and 30 kpc from the Solar position for five of the six Aquarius stellar haloes *(Figure produced by A. Helmi)*

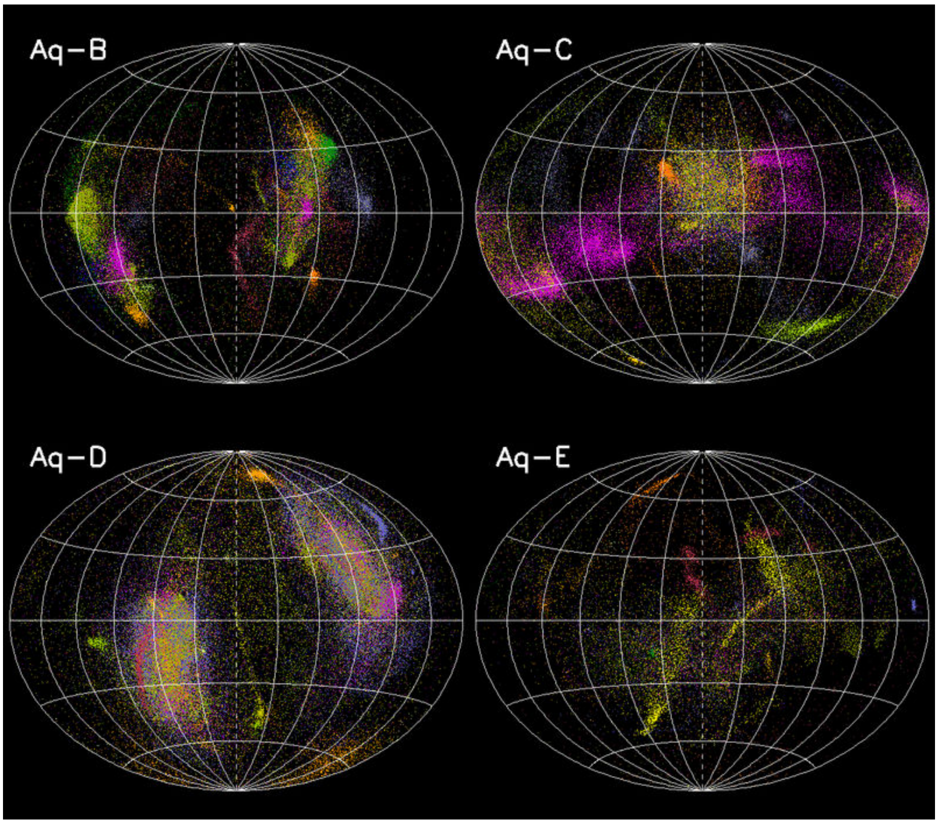

Figure 4.3: As Fig. 4.2, now for all stars brighter than the main sequence turn-off, at distances between 30 and 50 kpc from the Solar position. *(Figure produced by A. Helmi)*

in the first panel of Fig. 4.2 corresponds to a satellite with a total mass of $1.2 \times 10^8\,\mathrm{M}_\odot$, stellar mass of $10^5\,\mathrm{M}_\odot$ and accretion redshift 4.94 ($\sim$ 12.5 Gyr ago).

4.2.3 The field of streams in Aquarius

To create a catalogue of main sequence turn-off stars, we adopt $f_T = 0.2\,\mathrm{M}_\odot{}^{-1}$ (as assumed by Bell et al. 2008). This value[6] results in $\sim 5.5 \times 10^7$ MSTO stars for halo Aq-A, up to $\sim 1.83 \times 10^8$ MSTO stars for halo Aq-D (the brightest of our stellar haloes). These numbers are comparable to those inferred by Bell et al. (2008) for the whole stellar halo of the Milky Way.

The previous figures show that in our simulations, streams from different progenitors frequently appear to overlap on the sky. In large part this is due to the correlated infall directions of the progenitor satellites which give rise to these streams. For example, Aq-A remains embedded in the same coherent filament for $\sim 10\,$Gyr before the present day, and many of its satellites form in this structure (Libeskind et al. 2005; Lovell et al. 2010, Vera-Ciro et al. in prep.).

The top panel of Fig. 4.4 shows the distribution of MSTO stars (generated according to our simple prescription) for Aq-A in a thin distance slice through a region similar to the portion of the SDSS footprint known as the 'Field of Streams' (Belokurov et al. 2006).

The characteristics of this Aquarius 'Field of Streams' are similar to those observed in SDSS. In particular, we see streams of stars that follow similar paths on the sky, resembling the bifurcation discovered by Fellhauer et al. (2006), as well as various broad overdensities. The bottom panel reveals the origin of these features in our simulations. Different colours indicate different progenitor systems. Note that some of the apparent bifurcations visible in the top panel do not necessarily arise from the overlap of streams on the same orbit with slightly different phase, but instead correspond to the overlap of streams of different origin. This implies that measurements of angular position and distance alone may be insufficient to associate overdensities in nearby regions of the sky with a single parent object. This caution is particularly significant where such associations are used to constrain the shape of the underlying gravitational potential.

---

[6] The number of MSTO stars per Solar mass adopted by Bell et al. (2008) is much higher than predicted, for example, by the models of Marigo et al. (2008). These models give $\sim 0.02\,\mathrm{M}_\odot{}^{-1}$ for halo isochrones as mentioned above, an order of magnitude fewer stars than Bell et al. assume.

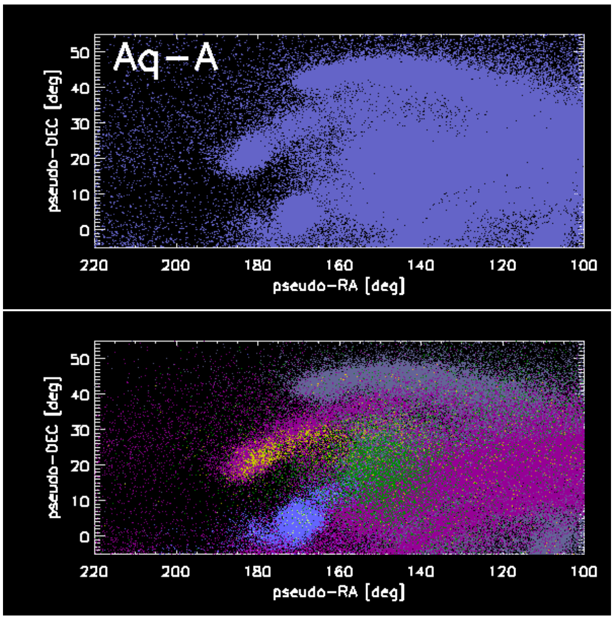

Figure 4.4: Distribution of MSTO stars in the Aquarius 'Field of Streams'. The region of the sky shown here has a similar extent to the SDSS footprint, but the model 'stars' are located in a thin slice of 1 kpc width at a distance of ~ 35 kpc. In the bottom panel the colours indicate different progenitors. *(Figure produced by A. Helmi)*

4.2.4 Fractional RMS

Following Bell et al. (2008), we have selected stars from SDSS-DR7 with $140^\circ \leq \alpha \leq 220^\circ$ and $0^\circ \leq \delta \leq 60^\circ$, colours in the range $0.2 < (g - r) < 0.4$ (characteristic of the halo MSTO) and apparent magnitudes $18.5 \leq r \leq 22.5$. Assuming an absolute magnitude $M_r \sim 4.5$ for MSTO stars, these stars would probe distances from 7 to 35 kpc. In practice this simple 'tomography' of the halo is subject to several uncertainties.

For example, using data from SDSS Stripe 82, Jurić et al. (2008) estimated that at the bright end of the above magnitude range, 5% of the point-like sources with $0.2 < (g - r) < 0.3$ are quasars. At $r \sim 22$, this fraction increases to 34%. Extrapolated to $r \sim 22.5$ this implies a contamination level of 50%. Furthermore, while the individual photometric errors in g and r are relatively small, the colour error at the faint end is $\sigma_{g-r} \sim 0.2$. This is comparable to the width of the MSTO colour selection box (Ivezic et al. 2008). This may scatter a large number of lower main sequence stars into the MSTO region, effectively broadening the effective dispersion in absolute magnitude. We consider both these effects in our simulations.

We measure the root mean square fluctuation (RMS) in the surface density of sources identified as halo MSTO stars in the SDSS by the above cuts. We bin stars by their apparent magnitude and in cells of 2×2 deg^2. Likewise, for each tracer particle in our resampling of the simulations in Chapter 2, we derive an apparent magnitude as $m_r = 5\log_{10} d - 5 + M_r + \Delta M_r$, where d is the distance from the observer, M_r is a random variable following a Gaussian distribution with $\langle M_r \rangle = 4.5$ and $\sigma = 0.9$ (this mimics spread in the absolute magnitude of the MSTO; Bell et al. 2008), and

$$\Delta M_r = u\,\sigma_{g-r}\,\frac{dM_r}{d(g-r)}. \tag{4.2}$$

In this final term, the derivative term describes the displacement of the absolute magnitude of stars along the main sequence as the $(g-r)$ colour changes, σ_{g-r} is the typical error in SDSS $(g-r)$ colour and u is a Gaussian random variable.

We place eight observers around a circle of 8 kpc radius from the halo centre, in a plane perpendicular to the minor axis of the dark matter halo. We select simulated tracer (MSTO) stars located in the same region of the sky and with the same apparent magnitude range as the SDSS sample. We measure the RMS in the projected surface number density of these stars for each of our haloes. Finally we add contamination by quasars following the model of Jurić et al. (2008). In this way, we obtain fractional RMS measurements which may be compared to those we obtain from SDSS.

The top panel of Fig. 4.5 shows that our haloes have systematically larger median fractional RMS values than the objects selected from SDSS. In this panel we have included the Jurić et al. (2008) estimate of the quasar contribution to each bin (uniformly distributed across the sky). Without this contribution the disagreement is even larger at faint magnitudes. In general, the largest deviations are those corresponding to observers whose sky contains a single high surface brightness substructure but is nearly empty otherwise.

In the bottom panel of Fig. 4.5 we have assumed an extra MSTO component following a Hernquist density profile with a scale radius of 1.25 kpc, and a total mass equivalent to 10% of the stellar halo mass. Our results are not strongly dependent on the exact value of the scale radius. This component may represent halo stars formed in situ, as discussed in Chapter 1 (Section 1.3.1). Its effect is to lower the contrast between cells, particularly at bright and intermediate magnitudes (at $r \sim 19$, the contribution of this extra component is $\sim 30\%$). The result is a substantially improved agreement with the apparent absence of structure in the data.

This comparison is extremely simple and severely limited by our understanding of the uncertainties in the method of MSTO tomography. However, at face value, it suggests that a non-negligible fraction of stars in the Milky Way halo may not be accounted for by our model based on accretion alone.

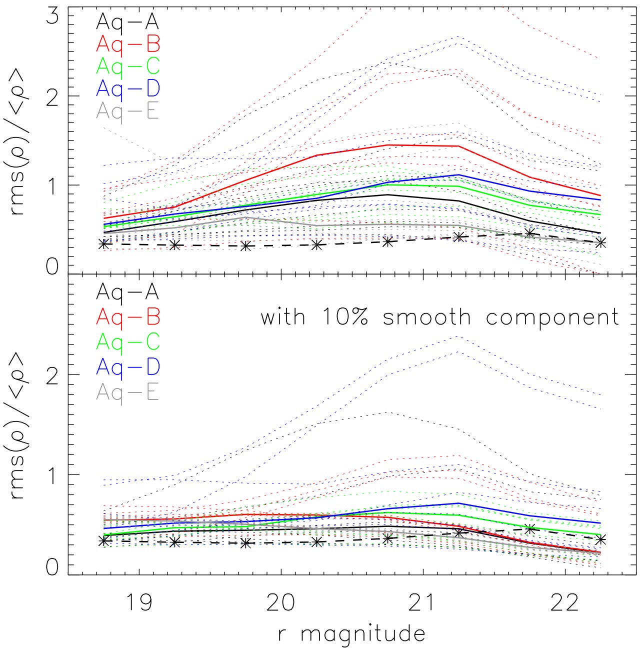

Figure 4.5: Fractional RMS of MSTO counts (*RMS* divided by the mean density) for five of our resampled stellar haloes as a function of apparent magnitude (here a proxy for distance). These results correspond to a region of the sky similar in location and extent to the SDSS-footprint. Dotted lines show the individual profiles measured by eight observers placed around the Solar circle. The median profiles are shown as solid lines. In the simulations shown in the top panel, we include a contaminating contribution from quasars as described in the text. Dashed lines/black asterisks correspond to Milky Way data from SDSS. In the bottom panel, in addition to quasar contamination, we have also included a smoothly distributed component.*(Figure produced by A. Helmi)*

4.3 A two-point correlation function for kinematic substructure

The previous section discussed a 'tomographic' view of the halo based on very large samples of stars with imprecise distance estimates. Another approach to quantifying substructure is to use more limited spectroscopic samples, which typically have two significant advantages: more precise distance estimates and radial (i.e. line-of-sight) velocity measurements. In addition, bright tracers (such as RGB stars and horizontal branch stars) can be observed at very large distances. In this section we present a simple statistical technique that aims to quantify the substructure these spectroscopic datasets using spatial and kinematic information.

4.3.1 Previous Work

Algorithms already exist for identifying substructure in huge multidimensional datasets (e.g. Sharma & Johnston 2009), such as the *Gaia* data supplemented by chemical abundance measurements (Freeman & Bland-Hawthorn 2002). These algorithms can also be applied to simulations, although this is not straightforward. One problem is that current (cosmological) hydrodynamic simulations still fall short of the star-by-star 'resolution' of the *Gaia* data, particularly in the Solar neighbourhood (e.g. Brown et al. 2005).

In the outer halo, longer mixing times allow ancient structures to remain coherent in configuration space for many gigayears. However, 6D *Gaia* data is restricted to relatively bright stars, so studies of the outer halo in the near future will continue to rely on a modest number of bright 'tracer' populations (giants and horizontal branch stars) for which typically only angular positions and (more uncertain) estimates of distance and radial velocity are available. Current simulations contain as many particles as there are (rare) tracer stars in observational samples. This motivates the simple comparison that we present here between models and data in the distant halo, particularly as suitable data are already available. Here we focus on quantifying the degree of structure in rare tracer stars in a generic way, which we apply to these data and to simulations of stellar haloes.

Most studies of spatial and kinematic structure in the Milky Way halo have given priority to the discovery of individual overdensities (exceptions include Bell et al. 2008 and Xue et al. 2009). Relatively few have investigated global statistical quantities for the entire stellar halo, although several authors have suggested an approach based on clustering statistics. Re Fiorentin et al. (2005) analysed velocity-space clustering among a small number of halo stars in the Solar neighbourhood, using a correlation function statistic. Following early work by Doinidis & Beers (1989), Brown et al. (2004) examined the angular two-point correlation function of photometrically selected blue horizontal branch (BHB) stars in the Two Micron All Sky Survey catalogue (Skrutskie et al. 2006), probing from $\sim 2 - 9$ kpc. They detected no significant correlations at latitudes $|b| \gtrsim 50^{\circ}$, but did detect correlations on small scales (1°, ~ 100 pc) at lower latitudes, which they attributed to structure in the thick disc. Lemon et al. (2004) performed a similar analysis for nearby F stars in the Millennium Galaxy Catalogue and found no significant clustering. Starkenburg et al. (2009) used a correlation function in *four* dimensions (which we discuss in detail below) to identify substructures in the Spaghetti pencil-beam survey of the distant halo, from which they obtained a significant detection of clustering and set a lower limit on the number of halo stars in all substructures. Similarly, Schlaufman et al. (2009a) constrain the mass fraction of the halo in detectable substructure by estimating the completeness of their overdensity detection algorithm. Respectively, Starkenburg et al. and Schlaufman et al. conclude that $> 10\%$ (by number of stars) and $\sim 30\%$ (by volume) of the Milky Way halo belongs to groups meeting their individual definitions of phase space substructure. These methods were tested on 'mock catalogues' of tracer stars constructed from simplified models of the stellar halo. Also of particular relevance to this work is the study of Xue et al. (2009), who considered the pairwise radial velocity separation of a large sample of halo BHB stars as a function of their separation in space, but found no evidence of clustering.

The statistic we develop below is more general than the otherwise similar approach of Starkenburg et al. (2009) and more sensitive than that of Xue et al. (2009). Following Starkenburg et al. (2009), we define a two-point correlation function using a metric which combines pairwise separations in the four most readily-obtained phase space observables for halo stars (angular position, radial distance and radial velocity). We apply this statistic to the data analysed by Xue et al. (2009) and demonstrate that a significant signal can be recovered.

A metric of the kind we propose can be tuned to probe a specific scale of clustering by adjusting the weight given to each of its components (e.g. Starkenburg et al. 2009). However, it is not clear what signal is to be expected from a 'typical' ΛCDM stellar halo (a superposition of many sub-components with a complex assortment of morphologies in phase space). We can identify no clearly 'optimal' metric. Instead we make a fiducial choice of scaling which we will test using our accreted-halo models. Having defined our metric, we are able to make direct comparisons between these simulations and the data of Xue et al. (2008). We show that even though both the metric and our choice of scaling are simplistic, this approach has the power to discriminate quantitatively between qualitatively different stellar haloes.

We describe the basis of our method in Section 4.4 and the observational data to which we compare in Section 4.5. We have already described our method for constructing mock catalogues of tracer stars in Section 4.2.1. In Section 4.6 we discuss how our technique relates to the similar approach of Starkenburg et al. (2009) in the context of the Spaghetti Survey (Morrison et al. 2000). We show that the number of stars in this survey is too small to give useful constraints with our approach. In Section 4.8 we apply our method to a much larger sample of BHB stars (Xue et al. 2008) from the 6th data release (DR6) of the Sloan Digital Sky Survey (SDSS SEGUE), and compare these data to our simulations. Our conclusions are given in Section 4.9.

4.4 Metrics for phase-space distance

The most readily obtained phase-space observables for distant halo stars are their galactic angular coordinates l and b, heliocentric radial distance d, and heliocentric line-of-sight velocity v_{hel}. From their angular position and distance estimate, each star can be assigned a three-dimensional position vector in galactocentric Cartesian coordinates, $r\,(X, Y, Z)$, and a radial velocity corrected for the Solar and local standard of rest motions, v_{GSR} (hereafter v). We begin by defining a scaling relation (metric), Δ, which combines these observables into a simple 'phase-space separation' between two stars:

$$\Delta_{ij}^2 = |r_i - r_j|^2 + w_v^2 (v_i - v_j)^2. \tag{4.3}$$

Here, $|r_i - r_j|$ is the separation of a pair of stars in coordinate space (in kiloparsecs), and $v_i - v_j$ is the difference in their radial velocities (in $\mathrm{km\,s^{-1}}$). The scaling factor w_v has units of $\mathrm{kpc\,km^{-1}\,s}$, such that Δ has units of kiloparsecs. The choice of w_v is arbitrary unless a particular 'phase space scale' of interest can be identified. This is not straightforward; we discuss some simple choices below.

Our definition of Δ is similar to the *4-distance* metric of Starkenburg et al., who define the phase-space separation of two stars, δ_{4d}, to be

$$\delta_{4d,ij}^2 = \tilde{w}_\phi \phi_{ij}^2 + \tilde{w}_d (d_i - d_j)^2 + \tilde{w}_v (v_i - v_j)^2. \tag{4.4}$$

The observables in Equation 4.4 are the same as those in Equation 4.3. In this definition the distance in configuration space between two stars is split into an angular component, ϕ, and a radial component, d. The constant scaling factors $\tilde{w}$ normalize each component to its maximum observable value in the Spaghetti survey (described below). Starkenburg et al. choose $\tilde{w}_\phi = 1/\pi^2$, $\tilde{w}_d = \eta_{d,ij}/(130\,\mathrm{kpc})^2$, and $\tilde{w}_v = \eta_{v,ij}/(500\,\mathrm{km\,s^{-1}})^2$. The η_{ij} terms are intended to incorporate into the metric itself the observational errors, $\sigma_{d,v}$, on d and v. They are defined relative to the typical error of a star in the survey:

$$\eta_{d,ij} = \frac{(\sigma_{d,i}/d_i)^2 + (\sigma_{d,j}/d_j)^2}{2\langle\sigma_d/d\rangle^2} \tag{4.5}$$

$$\eta_{v,ij} = \frac{\sigma_{v,i}^2 + \sigma_{v,j}^2}{2\langle\sigma_v\rangle^2}\,. \tag{4.6}$$

If these η terms are neglected (i.e. $\eta_{d,v} = 1$), the metric of Starkenburg et al. can be related to Equation 4.3 by separating radial distance into transverse and parallel components, i.e. $r^2 = r_\parallel^2 + r_\perp^2$. The $r_\parallel$ term is exactly equivalent to d in Equation 4.4, but transforming the angular separation of the stars to a transverse distance $r_\perp$ is less straightforward[7]. At small angles,

---

[7] Separating the components of distance in the metric in this way is natural where radial distance error dominates the uncertainty. One simple way to proceed may be to include an '$r\,d\theta$' term in the angular separation, where r is defined (for example) as the mean distance of the two stars. In a modified Equation 4.4 this could be achieved by setting $w_{\phi,ij} \propto \sqrt{d_i d_j}$. With this definition, larger values of Δ result for pairs of the same angular separation lying at larger mean absolute distances (note that this is not the case in the Starkenburg et al. formulation of Equation 4.4). However,

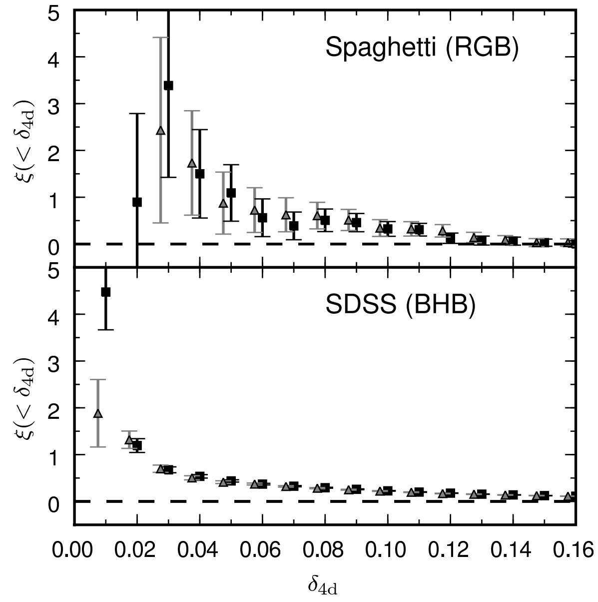

Figure 4.6: Upper panel: the *4-distance* cumulative correlation function $\xi(<\delta_{4\mathrm{d}})$ defined by Starkenburg et al. (black squares with Poisson error bars) for 101 RGB stars from the Spaghetti survey (Starkenburg et al. 2009). Grey triangles (slightly offset in $\delta_{4\mathrm{d}}$ for clarity) show the same function setting $\eta = 1$ in the metric of Starkenberg et al. (see text). Lower panel: correlation functions in the same metric for 2558 BHB stars ($6 < r < 60\,\mathrm{kpc}$) from the SDSS DR6 sample of Xue et al. (2008).

where $r_{\perp}^2 = r^2 - r_{\parallel}^2 \approx w_{\phi}^2 \phi_{ij}^2$, the scaling between our metric and that of Starkenburg et al. corresponds to $\Delta = (130\,\mathrm{kpc}) \times \delta_{4\mathrm{d}}$, with $w_{\phi} = 130/\pi \sim 41.4\,\mathrm{kpc\,rad^{-1}}$ and $w_v = 0.26\ \mathrm{kpc\,km^{-1}\,s}$.

Starkenburg et al. suggest that pairs of stars separated by a suitably small $\delta_{4\mathrm{d}}$ can be regarded as a 'group'. To determine the optimum value of $\delta_{4\mathrm{d}}$ to define groups in a given survey[8], they examine the cumulative two-point correlation function defined by

$$1 + \xi(<\delta_{4\mathrm{d}}) = \frac{DD(<\delta_{4\mathrm{d}})}{\langle RR(<\delta_{4\mathrm{d}})\rangle}. \tag{4.7}$$

Here $DD(<\delta_{4\mathrm{d}})$ counts the number of pairs in the sample separated by less than $\delta_{4\mathrm{d}}$, and $\langle RR(<\delta_{4\mathrm{d}})\rangle$ is the equivalent count averaged over a number of random realisations. Starkenburg et al. compute $\langle RR\rangle$ by repeatedly 'reshuffling' the distances and velocities of stars in the sample amongst their (fixed) angular coordinates (l, b).

Fig. 4.6 shows two such correlation functions in the Starkenburg et al. metric. The first of these is for giant branch stars from the Spaghetti survey (as in figure 1 of Starkenburg et al.

---

this treatment is not sensible at large angular separations.

[8] That is to say, a value large enough to confidently link together many stars, without creating spurious groups.

2009) and the second is for a much larger sample of BHB stars in SDSS DR6 extending[9] to ~ 60 kpc (Xue et al. 2008). These datasets are described in more detail in the following sections.

We also show in Fig. 4.6 the equivalent correlation functions setting $\eta_d = 1$ and $\eta_v = 1$ in Equation 4.4 as described above. These terms make interpretation of the metric distance more complicated. When they are included, pairs with larger errors have larger $\delta_{\rm 4d}$, and so are assigned to a higher-separation bin in the cumulative correlation function. Including these terms has a practical advantage if $\delta_{\rm 4d}$ is used only as a 'structure finder', as they 'clear out' dubious pairs from the smallest separation bins. However, $\delta_{\rm 4d}$ then depends not only on the physical phase-space coordinates of two stars, but on how well those coordinates are measured. For example, increasing the radial separation of a pair by 10 kpc and improving the measurement of distance for both stars by a factor of 10 (relative to the average of the sample) would result in the same $\delta_{\rm 4d}$. Thus DD/RR is not a straightforward measurement of physical clustering when these weighting factors are used. Fig. 4.6 shows that setting $\eta = 1$ affects the significance of the correlation function signal for these two surveys at the smallest separations but makes little difference to the overall shape. This is especially true in the case of the SDSS BHB stars.

Both samples show a significant signal in $\xi(<\delta_{\rm 4d})$ at small separations. Based on comparison to the simulations of Harding et al. (2001), Starkenburg et al. adopted $\delta_{\rm 4d} = 0.05$ as a suitable 'linking length' to identify meaningful groups in the Spaghetti survey. Here we are not concerned with the identification of individual groups. Instead, our aim is to use our $\xi(<\Delta)$ correlation function to quantify the *overall* nature of structure in the halo.

4.5 Observational samples: Spaghetti and SDSS

Spaghetti is a survey of the stellar halo in 134 pencil-beam fields covering $\sim 52\,\mathrm{sq.deg.}$ at high galactic latitudes (Morrison et al. 2000). Of these 134 fields, 101 were targeted randomly within the region defined in Galactic coordinates by $b > 30^\circ$ and $0 < l < 210^\circ$; the remaining 33 were targeted randomly in the region $b < -30^\circ$. Metal-poor red giant branch (RGB) halo star candidates were identified photometrically using a combination of Washington System filters (Morrison et al. 2001); each candidate was followed up spectroscopically to distinguish true giants from nearby metal-poor dwarfs. Radial velocities and metallicities were determined from the spectra of confirmed halo RGB stars with errors of $10\text{-}15\,\mathrm{km\,s^{-1}}$ and 0.25–0.3 dex respectively.

---

[9] In the case of the Xue et al. BHB stars we have set $\tilde{w}_d = 130$ kpc in Equation 4.4. Starkenburg et al. define $\tilde{w}_d$ as the maximum distance probed by the survey; the Xue et al. high-confidence sample extends to $w_d = 60$ kpc, and the most distant BHB found in the full SDSS sample lies at ~ 90 kpc. However, adjusting $\tilde{w}_d$ to these 'limits' makes a negligible difference to the correlation function.

Distances were determined from spectroscopic luminosity estimates as described by (Morrison et al. 2000, 2003). Errors associated with the spectroscopic metallicity measurements (used to select fiducial globular cluster colour-magnitude tracks) are the most significant contribution to a typical distance error of ~ 15 per cent.

Xue et al. (2008) have published a catalogue of 2558 stars from SDSS DR6 which they identify as halo BHBs with high confidence (contamination $< 10\%$), using a combination of colour cuts and Balmer line diagnostics. This sample ranges in distance from $4 - 60\,\mathrm{kpc}$; a cut on distance error excluded more distant stars observed in SDSS. The errors on distance ($\sim 5\%$) and radial velocity ($5 - 20\,\mathrm{km\,s^{-1}}$) for stars in the Xue et al. catalogue are comparable to or better than those of Spaghetti. Like the Spaghetti data, the Xue et al. BHBs are not a complete sample in any sense. In particular, as described by Xue et al., the targeting of SDSS spectroscopy disfavours follow-up of more distant BHBs. In both surveys, the probability of selecting a candidate star for spectroscopic follow-up is extremely difficult to quantify.

In the study of the Galactic escape velocity profile for which the Xue et al. sample was obtained, the authors further restricted the data to 2401 stars by selecting only stars with a height $|z| > 4\,\mathrm{kpc}$ above the Galactic plane. This cut was designed to exclude thick disc BHB stars. In our analysis of the data we retain the full high-confidence sample of 2558 BHBs and do not impose any restriction on $|z|$ in our mock observations, beyond that of the SDSS footprint.

Xue et al. (2009) studied the pairwise radial velocity distribution of the Xue et al. (2008) BHB sample as a function of distance separation, $\langle|\Delta v_r|\rangle(\Delta r)$. They found no significant deviation from a constant $|\Delta v_r|$ at any scale in Δr. From comparisons to the simulations of Bullock & Johnston (2005) Xue et al. concluded that this statistic is not capable of detecting structure against a more smoothly distributed background in phase space made up from well-mixed streams. However, the observed signal was not compared to the expected signal from random realisations.

4.6 Spaghetti survey mock catalogues

We use our stellar halo models and the procedure described in Section 4.2.1 to create mock catalogues of individual RGB stars, matched to the parameters of the Spaghetti survey described above. We locate fields randomly within the above constraints; we average over many different random sets of field positions when making comparisons based on a fixed observer position. In both model and data, the random sample $\langle RR\rangle$ is generated by reshuffling distances and velocities the mock catalogue 1000 times, following Starkenburg et al. (2009).

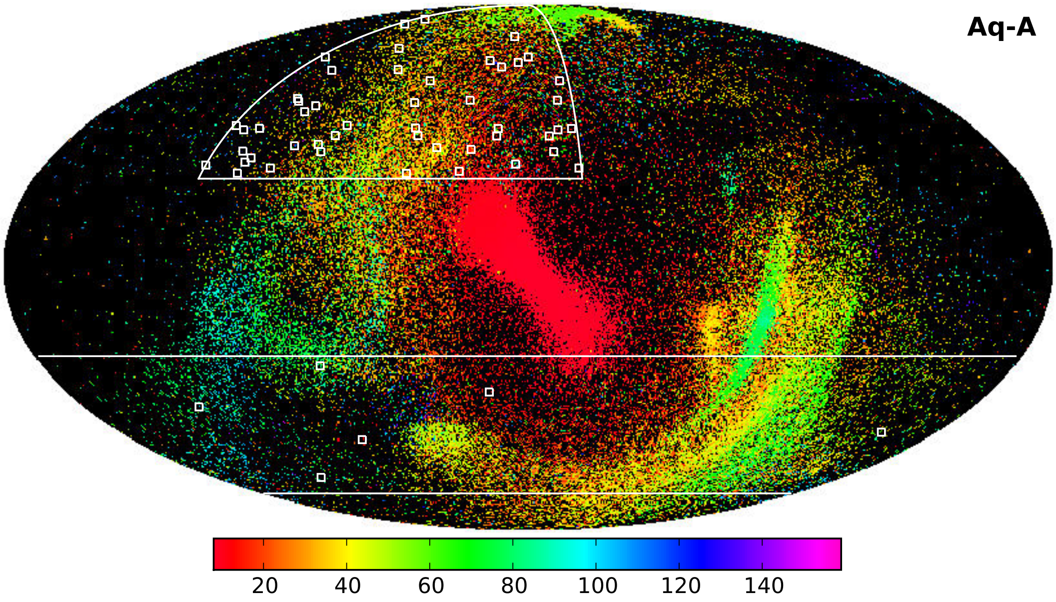

Figure 4.7: Sky distribution of halo RGB stars in simulation Aq-A. Colours indicate mean distance from the observer in kiloparsecs. Mollwiede projection in Galactic coordinates, centred on $(l, b) = (0, 0)$, taking $r_{\odot} = 8\,\mathrm{kpc}$. White lines show the Spaghetti survey target areas and white squares a fiducial set of 52 randomly located 1° fields (not to scale). The accreted component of the galactic bulge produces the elongated central feature at small distances. Here the major axis of this component is orientated from bottom right (further from the observer) to top left (closer to the observer).

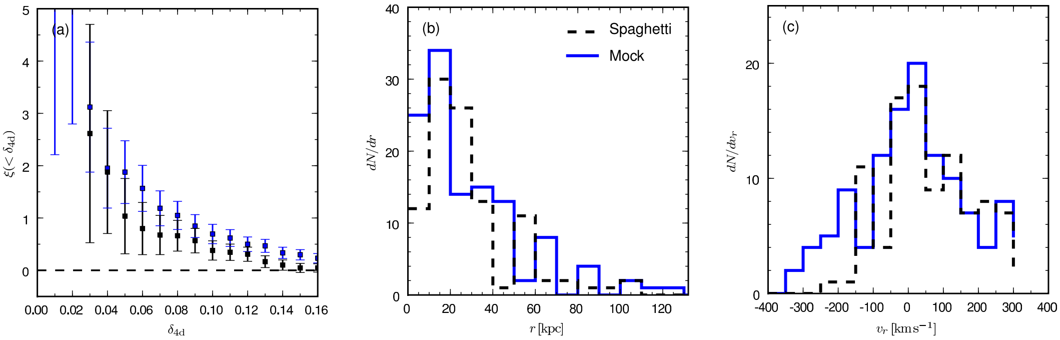

Figure 4.8: Fiducial realisation of a Spaghetti-like survey in halo Aq-A resembling the Spaghetti data (black dashed lines). The fiducial fields are those shown in Fig. 4.7. From left to right the panels show (a) the correlation function in the metric of Starkenburg et al. (2009) and distributions of (b) radial distance and (c) line-of-sight velocity (without correcting for the motion of the local standard of rest). Blue lines and points correspond to mock observations with our standard mock catalogue, sampled at a rate defined by $f_{\mathrm{T}}^{-1} = 3000\,M_{\odot}/\mathrm{star}$.

The correlation function results described below are independent of the choice of f_{T} we use to represent RGB stars, provided that the underlying distribution is well sampled at a given scale. We have therefore selected a fiducial value of $f_{\mathrm{T}}^{-1} = 3000\,M_{\odot}/\mathrm{star}$. This corresponds to the number of RGB stars expected down to approximately three magnitudes fainter than the tip of the red giant branch in the Marigo et al. (2008) model, for a typical halo stellar population (see Section 4.2.2). A single realisation of a mock RGB catalogue for halo Aq-A is shown in Fig. 4.7.

Fig. 4.8 shows that with this value of f_{T}, the normalisations of the radial velocity and distance histograms in a Spaghetti-like field are similar to those actually observed by Spaghetti. Morrison (1993) determined a value of $f_{\mathrm{RGB}}^{-1} \sim 620\ L_{V,\odot}/\mathrm{star}$ for halo giants (RGB and AGB) in the Solar neighbourhood, corresponding to a factor of $\sim 2-3$ more RGB stars per Solar mass than our value (assuming $M/L \sim 2$ and a minimal AGB contribution). There are many possible reasons for this discrepancy, most notably the incompleteness of the Spaghetti sample at faint magnitudes and large distances[10].

Fig. 4.8 verifies that our Aq-A model halo contains structures quantitatively similar to those seen by the Spaghetti survey. To illustrate this we have specifically chosen a set of fields for which the distributions of distance and velocity are well-matched. As we will show in the following section, however, there is a large amount of variance in the recovered signal among

---

[10] The Spaghetti survey is flux-limited, excluding the faintest giants at larger distances. In addition the candidate selection by colour may exclude some true giants, and not all stars selected as candidates were followed up successfully.

mock Spaghetti surveys adopting different placements of fields (for a fixed observer), and among different observer positions on the Solar shell.

4.7 Application of the Δ metric

In this section we describe our choice of the weight factor w_v in the Δ metric (Equation 4.3). We then analyse the clustering of the Spaghetti and SDSS using our mock catalogues, and discuss the limitations of Spaghetti.

4.7.1 Distance - velocity scaling

There is no clearly well-motivated way to choose a value of the velocity-to-distance scaling w_v; without a physical justification, it must be treated as a free parameter. The choice of w_v determines the scale of substructure to which the correlation function is most sensitive; naively we expect this to be the typical width and transverse velocity distribution of a ‘stream’. It is preferable to fix this parameter in a universal manner that does not depend on any particular survey parameters or geometry. We make a fiducial choice of w_v as follows.

In each simulated halo we adopt the SDSS-like survey configuration discussed below (without observational errors or assumptions about the location of the Sun). We construct (separately) one dimensional distributions of the separation in radial distance and velocity between stars. We generate many random realisations of these distributions by first convolving each simulated star with Gaussian kernels of width $8\,\mathrm{kpc}$ (distance) and $80\,\mathrm{km\,s^{-1}}$ (velocity), and then drawing from the equivalent ‘smoothed’ distributions. The kernel sizes were chosen as a compromise between signal (diminished by undersmoothing) and noise (increased by oversmoothing). Using these random realisations we construct correlation functions for each distribution. These two correlation functions are shown for halo Aq-A in Fig. 4.9. Although the signals are intrinsically weak, they have a very similar shape for both distributions, each with a characteristic ‘turnover’ scale. Matching this scale in the two correlation functions corresponds to $w_v \sim 0.04 \pm 0.01\,\mathrm{kpc\,km^{-1}\,s}$ for the six haloes, which we adopt as a fiducial value. We caution that although the scales on which we match the one-dimensional correlation functions are somewhat smaller than the smoothing scales we adopt to create the random distributions, this does not guarantee that w_v are unaffected by our choice of smoothing.

This is not a very satisfactory way of fixing w_v. However, in practice our conclusions are not strongly sensitive to the precise value we adopt. Values of w_v of the order of 0.01–$1.0\,\mathrm{kpc\,km^{-1}\,s}$ result in very similar $\xi(\Delta)$ correlation functions. Values lower than 0.01 recover very little sig-

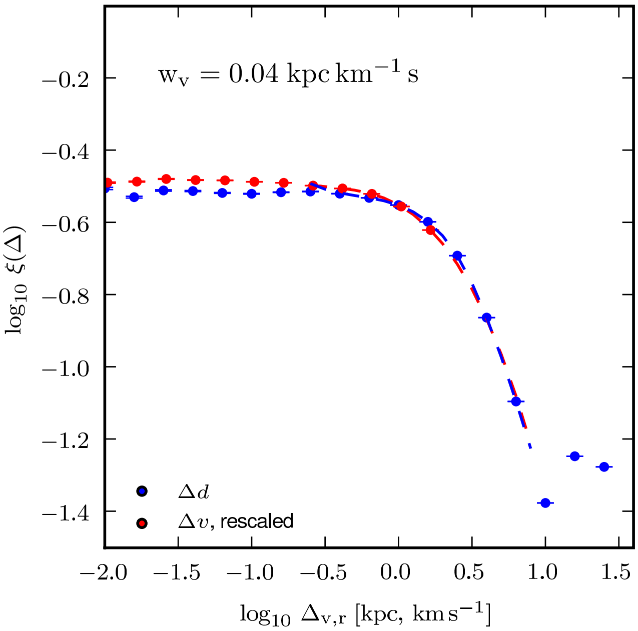

Figure 4.9: Correlation functions in space separation (blue) and velocity separation (red) for stars in halo Aq-A. The velocity separation correlation function has been scaled to match the turnover in the configuration space separation correlation function by a factor $w_v = 0.04\,\mathrm{kpc\,km^{-1}\,s}$.

nal; values above 1.0 treat $1\,\mathrm{km\,s^{-1}}$ velocity differences as equivalent to $> 1\,\mathrm{kpc}$ separations in space, and so make the cumulative correlation function very noisy on small scales for only a marginal increase in the overall signal (this noise in turn results in more scatter between the signals measured by different observers). We find that our choice of $w_v \sim 0.04\,\mathrm{kpc\,km^{-1}\,s}$ corresponds to a reasonable compromise. The above choices can be compared with the approach of Starkenburg et al. (2009), who take the (entirely arbitrary) ratio of the Spaghetti survey limits in radial distance and velocity to obtain $w_v = 0.26\,\mathrm{kpc\,km^{-1}\,s}$. Either value is acceptable to illustrate the utility of our approach. We therefore adopt $w_v \sim 0.04\,\mathrm{kpc\,km^{-1}\,s}$.

Fig. 4.10 shows the cumulative correlation function with the metric of Equation 4.3 averaged over many randomly placed observers for a mock Spaghetti survey[11]. We show results for $w_v = 0.26\,\mathrm{kpc\,km^{-1}\,s}$ and $w_v = 0.04\,\mathrm{kpc\,km^{-1}\,s}$. The scatter between observers is much larger for a Spaghetti-like survey than the SDSS-like surveys that we focus on below. This large scatter for individual surveys increases in the variation between observers at larger w_v in Fig. 4.10.

Starkenburg et al. 2009 find that for $\delta_{4\mathrm{d}} < 0.05$ over 80 per cent of pairs in their correlation function are made up of stars originating in the same progenitor satellite (so called 'true' pairs).

---

[11] When comparing our results with those of Starkenburg et al. (2009), it is important to note that the Δ metric distance has units of kiloparsecs, whereas $\delta_{4\mathrm{d}}$ defined by Equation 4.4 has units of [130 kpc].

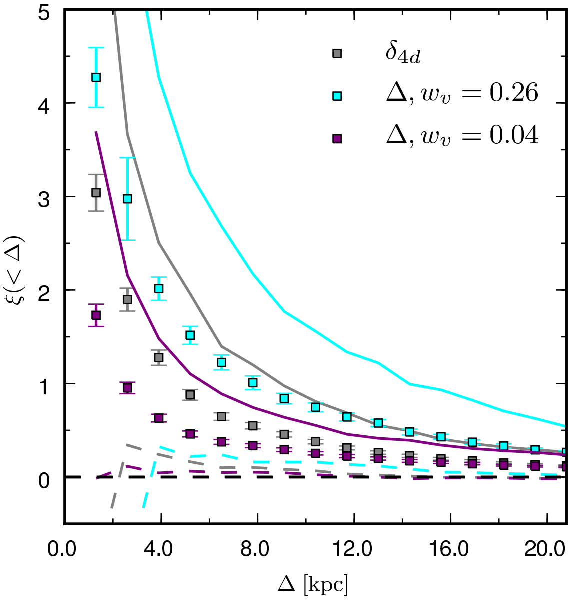

Figure 4.10: The Δ metric cumulative correlation function $\xi(<\Delta)$ for mock Spaghetti surveys in halo Aq-A. Each set of points with error bars show the mean and standard error of 200 random realisations; solid and dashed lines indicate 10^{th} and 90^{th} percentiles of the distribution in each bin. Colours correspond to different parameter choices in the metric. The $\delta_{4\mathrm{d}}$ metric of Starkenburg et al. (without η terms) is also shown (in grey). These correlation functions are those of mock catalogues with no observational errors.

We find that our choice of $w_v = 0.04$ finds a similar fraction (~ 70 per cent) of true pairs using the same method. In the largest-scale bin used in our cumulative correlation function, $\Delta < 21$ kpc, the fraction of true pairs is ~ 40 per cent. The efficiency with which true pairs are recovered is most relevant to structure-finding applications and is not important for our global statistic. However, such high fractions do indicate that the clustering of stars from individual progenitor galaxies makes a substantial contribution to the signals we recover.

We conclude that, as expected, the Δ metric is very similar to the $\delta_{4\mathrm{d}}$ metric of Starkenburg et al. in the limit of small angular separations and with $\eta = 1$ in Eqns. 4.5 and 4.6. The Δ metric has the advantage of a more straightforward definition. Furthermore, from the wide scatter around the mean signal in Fig. 4.10 it is clear that an individual Spaghetti-like survey cannot place any significant constraint on the structure of the halo using either statistic.

4.7.2 Observations of $\xi(<\Delta)$ Spaghetti and SDSS

In Fig. 4.11 we show $\xi(<\Delta)$ computed with the same observational data used in Fig. 4.6. In the case of the Spaghetti data, there is a clear reduction in the clustering signal relative to Fig. 4.6. This can be most easily understood in the limit of small angular separations as discussed above. In this limit, the transverse and perpendicular components of distance are coupled in the Δ metric. In effect, angular separations are translated to transverse distances, with a fixed angular scale corresponding to a larger '$r_\perp$' at larger $r_\parallel$. Pairs of a given ϕ_{ij} in the $\delta_{4\mathrm{d}}$ metric can therefore be displaced to a relatively higher- or lower-separation bin in the Δ metric, depending on their radial distance. This effect does not significantly reduce the number of $\langle DD \rangle$ pairs. However, the number of random pairs in small-separation bins increases on average in the Δ metric, where pairs physically close to the observer but separated by large angular distances can be assigned small transverse separations. This reduces the significance of observed pairs in small separation bins. Most of the signal in the Spaghetti survey comes from only a few excess data pairs, so this dilution has a significant effect.

The cumulative correlation function of the much larger SDSS BHB sample is very similar in both the $\delta_{4\mathrm{d}}$ and Δ metrics. This suggests that the differences between the two metrics are small in practice. This is not surprising; the weights in $\delta_{4\mathrm{d}}$ were selected, to within an order of magnitude, by maximising the signal in Spaghetti, which is similar in spirit to the empirical approach described in the previous section.

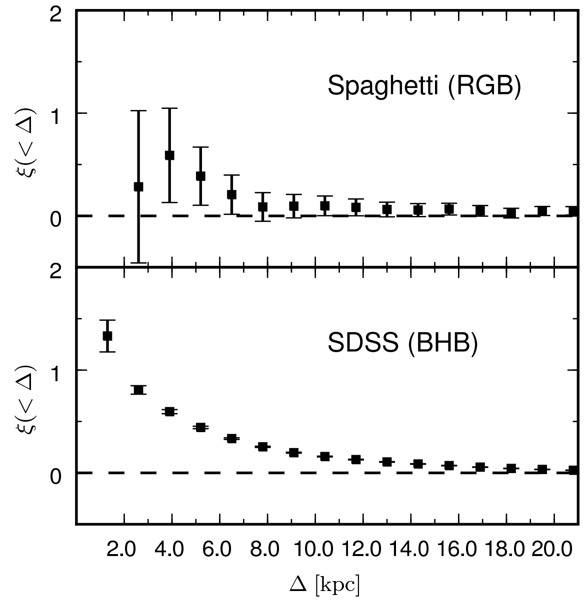

Figure 4.11: Upper panel: The Δ metric cumulative correlation function $\xi(<\Delta)$ (black squares with Poisson errorbars) of the Spaghetti survey. Lower panel: for the SDSS DR6 sample of Xue et al. (2008).

4.7.3 The halo-average signal and pencil-beam surveys

A useful survey should recover 'global' properties of the halo with high significance, i.e. properties that are insensitive to the observer's position on the surface of the Solar shell. We have shown that our metric can recover a clustering signal due to structure in the halo, using the data from a Spaghetti-like survey. However, Fig. 4.10 demonstrates that the signal from such a survey measured by any individual observer is extremely sensitive to the placement of its pencil beams. A corollary of this is that the 'halo average' signal of many observers also has a large scatter - in other words, the survey is limited by 'sample variance'. In this sense, 'blind' application of $\xi(<\Delta)$ to the data from Spaghetti cannot constrain the properties of the stellar halo, even if those data were complete in the surveyed fields.

The SDSS sample of BHB stars provides a much more significant measure of the global signal, as we demonstrate in the following section. However, SDSS is an expensive survey. Furthermore, in future it may be interesting to compare the correlation functions of different tracers that can be surveyed only in the manner of Spaghetti (in which costly spectroscopy of individual targets is required to construct the sample). In Fig. 4.12 we show a pencil beam survey covering both Galactic caps with 200 fields, using the distance limits of Spaghetti. Although the scatter remains large, the signal now deviates significantly from zero at small separations.

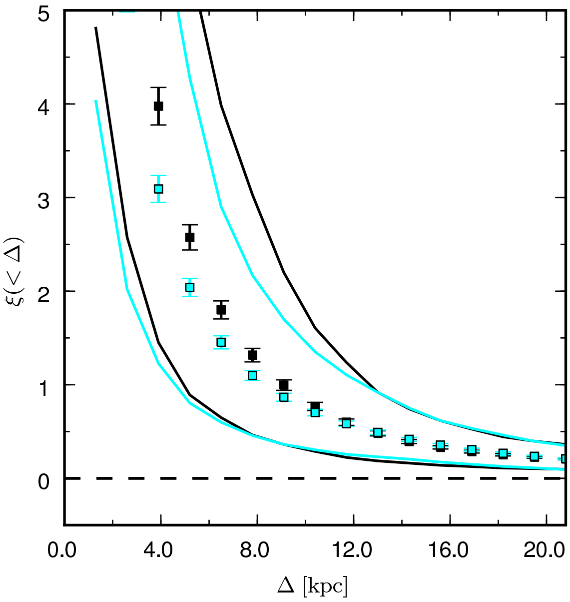

Figure 4.12: $\xi(<\Delta)$ for an 'enhanced' Spaghetti-like survey (in halo Aq-A) having 200 pencil beams at high latitude in each Galactic hemisphere. Black points show the mean signal (with its standard error), and black lines the 10–90 per cent range of the mean signal averaged over many observers. Cyan points and lines correspond to the distribution of signals for many surveys carried out by a single (randomly chosen) observer.

The local observer's signal is also a reasonable measure of the halo average. This is encouraging, because it suggests that only a relatively modest improvement is required over Spaghetti to provide useful constraints on halo structure. Halo simulations such as those presented in this thesis could be used to optimise a particular survey to detect clustering due to accreted substructures, accounting for the effects of observational errors and incompleteness, which we have not addressed here.

4.8 Clustering of SDSS BHB stars

We make mock SDSS surveys in a similar manner to the mock Spaghetti surveys described above using the same catalogues of tracer stars. Although the number density of BHB stars per halo is not equal to that of RGB stars even under our assumption of a uniform underlying population, the $\xi(<\Delta)$ statistic is not sensitive to the absolute number of tracers. Accounting for inhomogeneity in the stellar populations of the halo may introduce more significant differences between the distributions of BHB and RGB stars. The 'bias' that may be introduced by choosing particular tracer populations is beyond the scope of this thesis.

For a given observer location, we select all tracer stars in our catalogue within the SDSS DR6 footprint having distances $6 - 60\,\mathrm{kpc}$. We do not include any stars gravitationally bound to satellites. However, we do include stars in their tidal tails (which by our definition are part of the stellar halo). We note that in their study of the pairwise velocity distribution of their BHB catalogue, Xue et al. (2009) exclude nine stars deemed to belong to globular clusters. We do not exclude these stars from our analysis of the SDSS data.

In Fig. 4.13 we compare all six haloes with the observations of SDSS BHBs shown in Fig. 4.11. It is clear from Fig. 4.13 that the distribution of signals around the mean of many observers is much narrower than that for the Spaghetti survey show in Fig. 4.10. Because of the more extensive sky coverage of SDSS, fewer random orientations are required for the global halo signal to converge than in the case of Spaghetti. We find 80 randomly placed observers to be sufficient. For each of these observers, we compute the correlation function using 20 random 'shufflings' of the data.

Panel (a) of Fig. 4.13 shows that all haloes have an average signal clearly deviating from zero at small separations. Furthermore, significant differences are apparent in the average clustering signal between each of our six simulated haloes. This demonstrates that this statistic can distinguish between plausible alternatives for the structure of the MW halo in a ΛCDM model. In particular, halo Aq-C (purple) shows considerably more 'substructure' at all distances. Visually, this halo is dominated by a number of massive, dynamically young streams from recently-accreted satellites (see Fig. 3.1 and Fig. 3.2). By contrast halo Aq-B (cyan), which has the lowest clustering signal, is centrally concentrated, and contains only a small number of coherent low-mass streams. Halo Aq-E (blue) is similar to halo Aq-B, but differs in having a substantial accreted thick disc component. Haloes Aq-A (black) and Aq-D (green) are of intermediate mass and contain a variety of complex features in different stages of mixing. Halo Aq-A contains a Sagittarius-like stream and several widely dispersed clouds/shells, while Aq-D shows a highly elongated coherent complex of bright streams. Halo Aq-F is unusual; most of its stars are accreted in a late major merger and it is substantially brighter than the Milky Way at the Solar radius. For these reasons it more closely resembles the 'shell'-dominated haloes of some elliptical galaxies than those of Milky-Way like spirals. The signal is dominated by a much larger number of stars close to the observer and, other than the 'shell' system, very little coherent structure is apparent in this halo.

In summary, the clustering signal detected by our $\xi(<\Delta)$ statistic broadly reflects the visual impression of the amount of spatially coherent structure in each halo. However, to make a realistic comparison with the Milky Way data, it is important to account for the effects of observational errors (which become more significant at small scales). The consequences of including observational errors in the simulated data are shown in panel (b) of Fig. 4.13. Each distance and radial velocity is perturbed by representative Gaussian errors of $\sigma_d = 5\%$ and $\sigma_v = 15\ \mathrm{km\,s^{-1}}$ respectively (Xue et al. 2008). As expected, this smears out structure at small scales and suppresses the clustering signal in all haloes. Halo C in particular shows a much reduced signal, although the similarities and differences between the haloes are preserved.

It is also relevant that the sky distribution of structure in our simulated haloes stellar halo is not random with respect to the orientation of the galactic plane (and hence, with respect to the coverage of the Sloan survey). It is a strong prediction of our models that a planar alignment of halo debris will be observed in the Milky Way. This correlated alignment of tidal features is a natural consequence of structure formation in ΛCDM, because the direction from which most massive substructures are accreted is determined by the filamentary nature of the large-scale structure. These 'accretion axes' are correlated with the spin vector and shape of the main halo, and hence with the likely orientation of the galactic plane (Libeskind et al. 2005; Li & Helmi 2008; Lovell et al. 2010).

In panel (c) of Fig. 4.13 we show the clustering signals for the case in which we restrict the observer's position to a 'galactic plane'. We define this as the plane perpendicular to the minor principal axis of the inertia tensor for halo stars with galactocentric radii less than 3 kpc (see chapter 3). The observer is randomly located on a circle of radius 8 kpc in this plane, and the 'parity' of the galactic poles is also randomized (this is important, because SDSS coverage is mostly concentrated around only one Galactic pole and the halo need not be symmetric).

As described in Chapter 3, an 'accreted bulge' component is present in all of our haloes. In all cases the shape of this component is triaxial (oblate in the case of halo Aq-E) and is similar to the shape of the dark halo in the same region. The practical effect of restricting the observer to the 'galactic plane' is to prevent this (nearby) component from intruding into the SDSS footprint at high galactic latitudes. There are other plausible choices of galactic alignment (for example, relative to the shape or spin vectors of the entire dark halo). However, any choice is somewhat arbitrary in the absence of a self-consistent simulation of a galactic disc[12]. We choose to orient the galactic plane relative to the accreted bulge because, of all the plausible choices, it has the most significant influence on the clustering signal. Even in this case, the overall effect is modest. In some cases (e.g. halo C) the signal-to-noise increases slightly.

---

[12] In a full hydrodynamic simulation the effects of feedback and adiabatic contraction may also make the inner halo more spherical (Tissera et al. 2010; Abadi et al. 2010, e.g.).

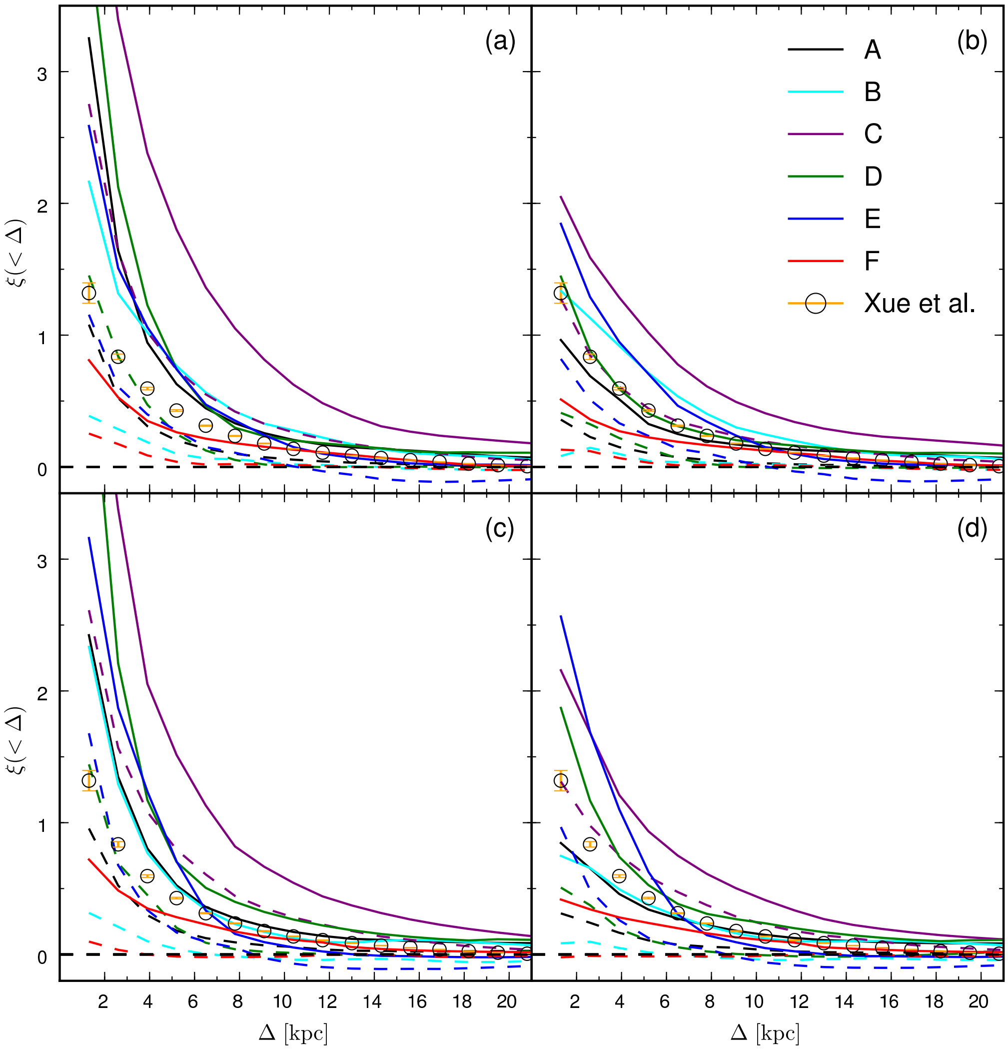

Figure 4.13: (a) The mean clustering signal $\xi(<\Delta)$ of 20 Solar-shell observers with a SDSS-like survey. Each halo simulation is represented by a pair of lines of the same colour (indicated in the legend): a solid line indicates the 90^{th} percentile of the distribution of $\xi(<\Delta)$ in each radial bin, and a dashed line the 10^{th} percentile. $\xi(<\Delta)$ for MW BHB stars from the catalogue of Xue et al. (2008) is shown with open circles and orange error bars (identical in all four panels). (b) Mock observations convolved with observational errors of $\sigma_d/d = 0.05$ and $\sigma_v = 15\,\mathrm{km\,s^{-1}}$. (c) Mock observations oriented such that the Galactic 'Z' direction is aligned with the minor axis of the halo ellipsoid within 3 kpc, but not convolved with errors.(d) Mock observations with errors of (b) and constrained alignment of (c).

Finally, in panel (d) of Fig. 4.13 we show the results of constraining the orientation of the galactic plane and also including observational errors. This provides a more realistic comparison with the observational data. Haloes with a high degree of coherent substructure on large scales (represented by our halo Aq-C) appear to be incompatible with the Milky Way. Our five remaining haloes are all broadly consistent with the data, with the MW having slightly more than the typical amount of substructure on the smallest scales in our analysis ($\Delta \sim 1\,\mathrm{kpc}$).

4.9 Conclusions

We began this chapter with a qualitative overview of the structure of our simulated stellar haloes as seen by a 'Solar' observer. We made a basic quantitative comparison to the photometric tomography of Bell et al. (2008), finding that our haloes produce overdensities on the sky that are much stronger than those apparent in a similar analysis of the SDSS data. There are tentative hints from this comparison that an additional halo component may be required to explain the apparent smoothness of the Milky Way halo. This conclusion is speculative, however, and we discuss this issue further in Chapter 6.

We have sought a more robust and sensitive means to quantify the degree of substructure in the Milky Way halo. We analysed the correlation function $\xi(<\Delta)$ of halo stars, defining their separations in four dimensions of phase space using a metric (which we call Δ) combining readily-obtained observables (angular and radial separation and radial velocity difference). A statistic of this type usefully quantifies kinematic and spatial substructure in the halo, and can easily be applied to observational data and catalogues generated from theoretical models. This analysis is particularly well suited to analysing the distant halo – other methods for studying clustering in many dimensions may be more suitable for the 'fine grained' data on the nearby halo that will soon be obtained by the *Gaia* mission (e.g. Gomez et al. 2010). We aim to apply other clustering statistics to our haloes in future work.

We have computed $\xi(<\Delta)$ for mock observations of six stellar haloes in the simulations described in the previous chapters. All of these haloes were formed from satellites disrupted within ΛCDM dark haloes selected as plausible hosts for the Milky Way. Our statistic distinguishes quantitatively between these six qualitatively different scenarios. On average, all six haloes show statistically significant correlations on scales in our metric equivalent to $\sim 1-10\,\mathrm{kpc}$.

We find that small pencil-beam surveys such as Spaghetti sample too few stars and cover too small an area to be well suited to analysis with our proposed statistic. Instead we have analysed a much larger catalogue of BHB star observations from the SDSS (Xue et al. 2008). The current Milky Way data are consistent with those simulated haloes having a moderate degree of spatial and kinematic substructure. Haloes dominated by massive coherent structures and haloes with little or no substructure appear less consistent with the Milky Way.

Our comparison between our models of ΛCDM stellar haloes and the Milky Way data demonstrates the potential of the statistical approach suggested by Starkenburg et al. (2009) and Xue et al. (2009). However, our application is very simple and can only serve as a basic consistency test for substructure kinematics in these models. Although the properties of our model stellar haloes may vary between different semi-analytic implementations, it is nevertheless encouraging that our fiducial model passes this basic test.

A number of aspects of this approach could be improved with further work. It seems desirable to use well-measured radial velocity data to boost a clustering signal (such as our correlation function) above that obtained from configuration space data alone (as demonstrated by Starkenburg et al. 2009). However, no means of including these velocity data is, as yet, well-supported by theory (including the simple approach we adopt here). The parametrised metric we have used to illustrate the concept of scaling radial velocity separations to 'equivalent' configuration space separations is a straightforward choice, and it is empirically useful in recovering a measurable signal. Nevertheless, we have not found any compelling or 'universal' way to select (or even justify the assumption of) the scaling parameter, w_v. Improving either definition of the metric itself or the means of fixing this parameter is a clear priority for extensions of this approach. A similar issue affects the weighting of velocity information in clustering algorithms (e.g. Sharma et al. 2010).

A full comparison between a stellar halo model and the observational data should also take account of effects such as spectroscopic incompleteness. In addition, the fraction of the stellar halo expected to be made up from components formed 'in situ' (i.e. within Milky Way-like galaxies themselves, rather than in accreted systems) is not well constrained (Abadi et al. 2006; Zolotov et al. 2009). It seems reasonable to expect in situ halo components to be distributed smoothly, with spherical or axial symmetry. The absence of these components in our models may therefore lead to an artificially high clustering signal. It is possible to place crude limits on the fraction of stars in a 'missing' smooth component, for example by comparing the RMS variation of projected star counts in our models, as we have done in Section 4.2.4. However, the uncertainties involved are substantial. Including an ad hoc smooth component in the clustering analysis above would also require assumptions about its velocity distribution, which are even less straightforward. There is a pressing requirement for complete observational samples, even if they do not probe the most distant halo. The LAMOST Galactic survey is likely to be the first to approach this goal.

In summary, we have taken a basic first step in adapting a well-studied cosmological statistic, the two-point correlation function, to an application in the study of the Milky Way halo. We have presented a very simple application making few modelling assumptions, using high-resolution simulations of stellar halo assembly. These simulations appear to be consistent in our comparison with currently available data. With further refinements, this approach may provide a practical and productive way to quantify the structure of the distant Milky Way halo for comparison with numerical models.

5

The bulk kinematics of stellar haloes

5.1 Introduction

Throughout previous chapters, we have discussed the possibility that some fraction of the stellar halo of the Milky Way (and by extension, all stellar haloes) has formed in situ, and hence is absent from our models of the accreted halo. In Section 1.3.1 we noted that in situ halo stars have been proposed as an origin of the apparent dichotomy in the properties of the Milky Way halo observed in the Solar neighbourhood (Carollo et al. 2010). This dichotomy is based on shape, metal enrichment and kinematics. In these multicomponent halo models, it is assumed that the accreted halo corresponds to the observed very metal poor component with mild net rotation, and the in situ stars produce the more metal-rich, non-rotating (or slightly prograde) inner halo.

In this chapter we examine the multicomponent nature of accreted haloes in CDM and the implications for kinematic observations of the Milky Way, using the high resolution simulations described in Chapters 2 and 3. We will explore the consistency of the bulk kinematics of our haloes with the Milky Way data and the presence of kinematically and chemically distinct components in the observations.

We will also examine one possible cause of the tension between different estimates of the mass of the Milky Way dark halo. 'Internal' estimates based on kinematic data for halo stars (e.g. Battaglia et al. 2005; Smith et al. 2007; Xue et al. 2008) favour systematically lower masses than those based on external data such as the M31 timing argument (Li & White 2008), the motions of satellite galaxies (Watkins et al. 2010) and halo abundance matching (Guo et al. 2010b). Hydrodynamic simulations have been used to support the assumptions underpinning the kinematic models of Smith et al. (2007) and Xue et al. (2008). Although these simulations may be reasonable (if highly uncertain) models of the in situ halo component, it is clear that they do not adequately resolve the accreted component. Studying the accreted contribution to the halo in isolation is one way to better understand the systematic uncertainties in these measurements.

In summary, this chapter addresses the following questions:

- Can inner/outer halo divisions of the type suggested (for example by Carollo et al. 2007) arise through accretion alone, or is an *in situ* component required to explain the existence of a flattened metal rich inner halo? (Section 5.3)
- Are single-component Gaussian distributions an adequate description of the halo star velocity ellipsoid, either in the Solar neighbourhood or overall? (Section 5.3 and Section 5.4)
- Are the shapes of the velocity ellipsoids of our simulated accreted haloes consistent with the Milky Way data? (Section 5.4)
- How much variation is there in the velocity ellipsoid of accreted stars around the Solar Circle? (Section 5.4)
- Do the assumptions of a relaxed system with a simple anisotropy profile (required to derive a MW dark halo mass from tracer star velocity dispersions, using the Jeans equation) hold for accreted halo stars? (Section 5.5 and Section 5.6)
- Does the velocity distribution of accreted halo stars extend to the escape velocity in the Solar neighbourhood, as assumed by recent studies using the local value of $v_{\rm esc}$ to constrain the dark halo mass? (Section 5.6)

A short discussion of our results is given in Section 5.7 and we summarise our conclusions in Section 5.8.

5.2 Halo models and rescaling

The models we use in this chapter are those presented in Chapters 2 and 3. We wish to compare to Solar neighbourhood data, so we again align the minor axis of the prolate distribution of halo stars in the inner 3 kpc of the halo to correspond to the Galactic Z axis. This is the same choice of 'galactic plane' used in Chapter 4.

In their study of the Solar neighbourhood escape velocity (see Section 5.6), Smith et al. (2007) use the simulations of Abadi et al. (2006) rescaled to a common circular velocity at the virial radius (r_{200}) of $V_{200} = 140\,\mathrm{km\,s^{-1}}$. To simplify our comparisons with Smith et al. (2007) and other Milky Way measurements, we adopt this same fiducial rescaling for all of our haloes, in *all* subsequent sections of this chapter. Note that this scaled V_{200} is consistent with current 'internal' estimates of the Milky Way dark halo mass (i.e. those based on halo star kinematics). However, as noted above, these are systematically lower than estimates obtained from 'external'

Table 5.1: Properties of the six Aquarius dark matter haloes/simulations (Springel et al. 2008a), *before rescaling*. The first column labels the simulations from A to F. From left to right, the remaining columns give the virial radius (r_{200}) at $z = 0$; the virial mass of the halo, M_{200}; the virial velocity $V_{200} = GM_{200}/r_{200}$; the maximum circular velocity, $V_{\max}$, and corresponding radius, $r_{\max}$; the rescaling factor γ used throughout this chapter (see text). The virial radius is taken to be that of a sphere with mean density equal to 200 times the critical density for closure.

	M_{200} $[10^{12}\mathrm{M}_\odot]$	r_{200} [kpc]	V_{200} $[\mathrm{km\,s^{-1}}]$	$V_{\max}$ $[\mathrm{km\,s^{-1}}]$	$r_{\max}$ [kpc]	γ
A	1.84	246	180	209	28	1.28
B	0.82	188	137	158	40	0.98
C	1.77	243	177	222	33	1.27
D	1.74	243	177	203	54	1.27
E	1.19	212	155	179	56	1.11
F	1.14	209	177	169	43	1.26

data ($V_{200} \sim 220\,\mathrm{km\,s^{-1}}$). Table 5.1 summarises the properties of the principal dark halo in the six simulations (without rescaling), and lists the rescaling factors $\gamma = v_{200}/140\,\mathrm{km\,s^{-1}}$ (distance and velocity are scaled by $1/\gamma$ and mass by $1/\gamma^3$). Throughout this chapter we assume $h = 0.73$, where the Hubble parameter $H_0 = 100\,h\,\mathrm{km\,s^{-1}\,Mpc^{-1}}$.

5.3 Global kinematic components of the halo

In Fig. 5.1 we give an overview of the stellar kinematics for each of our six haloes, for a wide annulus around the Solar circle ($3 < r < 14$ kpc) corresponding to the region used to define the Solar neighbourhood in the analysis of Smith et al. (2007). We limit our selection to stars within $|z| < 2.5$ kpc of the galactic plane (defined in Section 5.2). We refer to this region as the *Solar torus*. As in previous chapters, a *halo progenitor* in our models is defined as a satellite crossing the virial radius of the principal halo in the simulation and subsequently losing some or all of its stars through tidal stripping[1]. In our analysis we only include stars from progenitors contributing more than 2.5% of the total stellar mass in this torus. The coloured lines in each panel show velocity distributions for each of these significant progenitors individually, in a galactocentric spherical coordinate system. The rightmost column shows the corresponding metallicity distribution of each component[2]. We label the components with subscript letters a, b, c etc. ordered by the total mass of the progenitor (regardless of whether or not its stars fall

---

[1] In CDM, each infalling satellite will itself be the product of multiple mergers. Our definition groups all of the separate stellar populations making up a single satellite at the time of infall into one 'progenitor'.

[2] As discussed in Chapter 2, all metallicities are potentially too low in their absolute value by $\sim$ 1 dex, but relative metallicities are still meaningful.

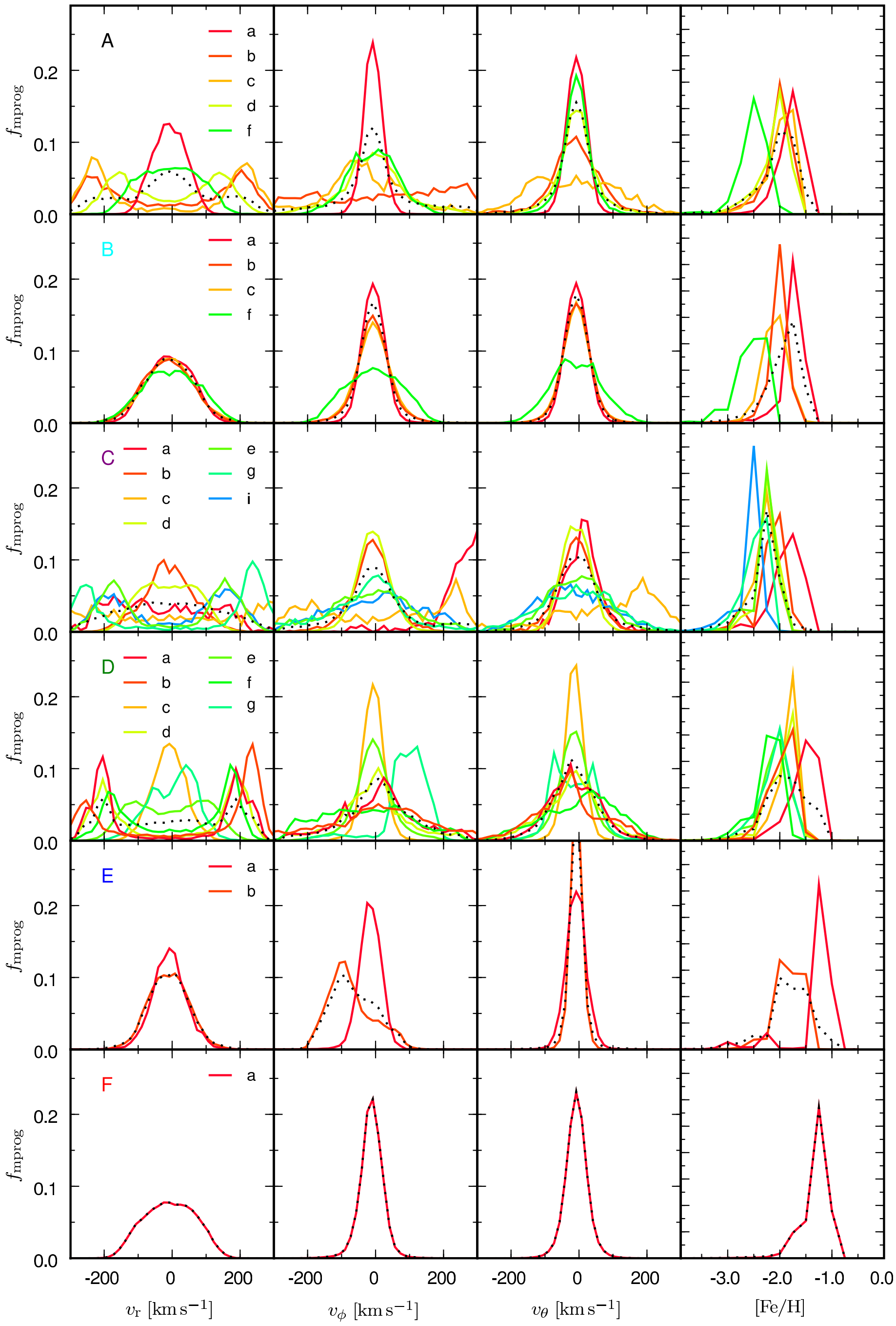

Figure 5.1: Velocity distribution functions in spherical polar coordinates (first three columns) and metallicity distribution functions (rightmost column) for individual components (i.e. the debris from unique progenitors) in each accreted stellar halo system (top to bottom, Aq-A – F). We include all stars in the radial range $3 < r < 14$ kpc and within $|z| < 2.5$ kpc of our choice of galactic plane. Within each halo, progenitors/components are colour-coded by their contribution to the *total* accreted stellar mass in the whole halo, from red (most significant) to blue (least significant). We include only progenitors contributing more than 2.5% of the total mass of accreted stars in the range $3 < r < 14$ kpc. The vertical scale shows the fraction of stars in each velocity bin normalized individually for each component. A black dotted line in each panel corresponds to the total distribution for all stars in the Solar torus.

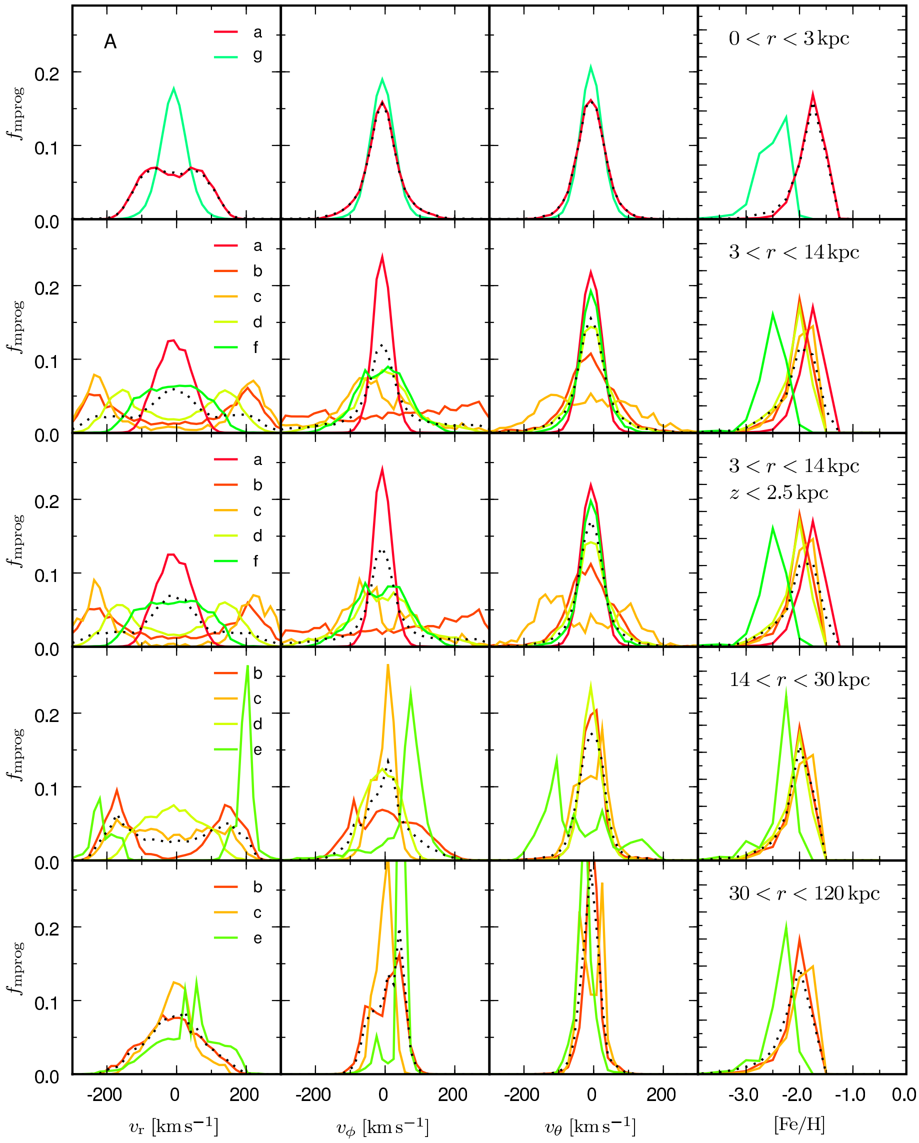

Figure 5.2: As Fig. 5.1, but here showing only halo Aq-A in the radial ranges $0 < r < 3$ kpc (bulge), $3 < r < 14$ kpc (Solar cylinder), $3 < r < 14$ kpc (restricting to stars $|z| < 2.5$ kpc from the galactic plane; Solar neighbourhood), $14 < r < 30$ kpc (inner halo) and $30 < r < 100$ kpc (outer halo).

within the Solar torus). Component 'Aa' is formed by stars belonging to the most significant progenitor in halo Aq-A, 'Ab' by the second most massive, and so on.

This figure shows that the mix of components present around the Solar circle can differ substantially between haloes. Broadly, the distribution of a given component can be classified either as relaxed (symmetric about zero velocity and approximately multivariate Gaussian) or unrelaxed (asymmetric or bimodal). In four of the six haloes one relaxed component is the most significant component both in the Solar torus and overall (components Aa, Ba, Ca and Fa). Haloes A, C, and D also contain a mix of unrelaxed components in the Solar torus (e.g. Ab, Cc, Da). These are most apparent from their bimodal radial velocity profiles[3]. In halo B all the significant components in the Solar torus are relaxed, as is conventionally assumed to be the case in the Milky Way. Although these different components resemble each other kinematically they show some separation in metallicity. However, it would not be easy to distinguish the contributions of the minor components from fluctuations in the metal poor tail of the component which overwhelmingly dominates. The majority of the stars in halo Aq-F come from only one accreted component, a late major merger (at $z \sim 0.7$). This illustrates the diversity of assembly histories for Milky Way mass haloes but is an unlikely scenario for the Milky Way itself. We do not discuss this halo further.

In halo Aq-E the unrelaxed component Eb dominates the Solar torus, although the more massive relaxed component Ea also contributes. Component Eb shows a strong net rotation (with a small 'counter-rotating' tail) and a low 'vertical' velocity dispersion. These features are reminiscent of the Milky Way's thick disc (this feature was also referred to in Chapter 3). Fig. 5.3 shows the velocity dispersion profiles of this component as a solid blue line, including all stars in this component regardless of their location in the halo. A solid red line shows the median distribution in spheres of radius 2.5 kpc surrounding observers at $R_{\odot} = 8\,\mathrm{kpc}$, averaging over 100 random azimuthal positions for the Sun. The shaded blue area shows the corresponding 10^{th}–90^{th} percentile range for these observers. For comparison, the solid black lines show the velocity distribution of Milky Way thick disc stars. Component Eb mimics the velocity distributions of the MW thick disc well, albeit with somewhat lower mean rotational speed, $\sim 100\,\mathrm{km\,s^{-1}}$, and a notably *colder* velocity dispersion in the Z direction. The v_{ϕ} distribution shows a significant tail to 'counter-rotating' velocities; MW thick disc stars selected

---

[3] The peaks in these bimodal stream distributions correspond to the 'wings' seen in 2D projections of the velocity ellipsoid at 8 kpc in other simulations, e.g. in figure 8 of Helmi & de Zeeuw (2000) – see also e.g. Re Fiorentin et al. (2005); Smith et al. (2009a) for similar plots for stars in the real Solar neighbourhood.

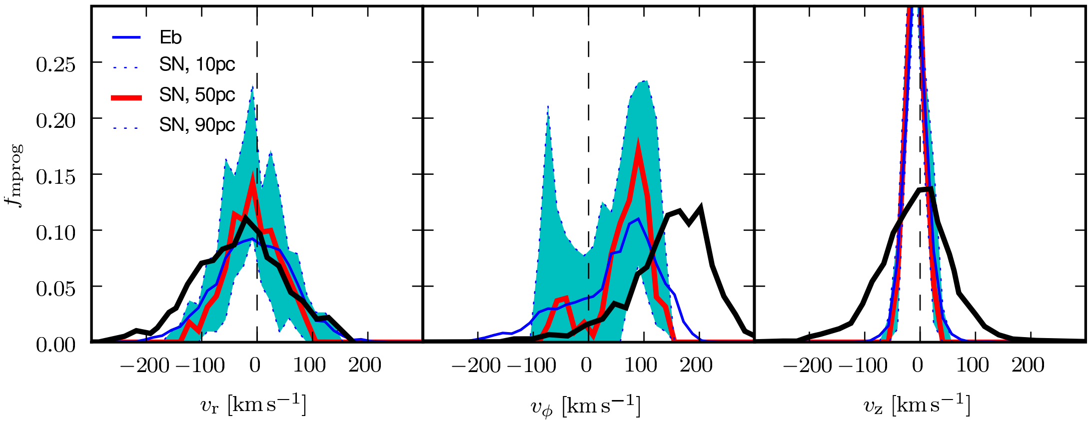

Figure 5.3: Velocity distributions in cylindrical coordinates for component Eb. The solid blue line includes all particles in this component; the solid red line shows the median distribution of particles in the Solar neighbourhood (see text), with the corresponding 10–90pc range indicated by the blue shaded region. For comparison, the black line shows the distribution of Milky Way thick disc stars in the Solar neighbourhood from the sample presented by (Navarro et al. 2010a).

by metallicity also show this tail, although it is debated whether these counter-rotating stars should be associated with the thick disc or another halo component (Navarro et al. 2010a).

The total mass of this component is $1.5 \times 10^8\,\mathrm{M}_\odot$ ($5.7 \times 10^8\,\mathrm{M}_\odot$ if halo Aq-E is rescaled to a virial velocity of $220\,\mathrm{km\,s^{-1}}$). This is approximately an order of magnitude less massive than the Milky Way's thick disc ($\sim 10^9\,\mathrm{M}_\odot$). In our Solar neighbourhood spheres, stars from component Eb contribute a large fraction of all accreted stars $0.98^{+0.01}_{-0.2}$ (5-95% range).

The mix of progenitors varies with radius in each halo. As an example we show in Fig. 5.2 velocity distributions in halo Aq-A split into four wide radial bins: from 0–3 kpc (the 'accreted bulge' discussed in previous chapters), 3–14 kpc (the Solar neighbourhood), 14–30 kpc (the 'inner halo') and 30–120 kpc (the 'outer halo'). These subdivisions are those conventional for the Milky Way: they are not based on specific features in the structure of halo Aq-A. We do not impose the restriction $|z| < 2.5$ kpc in this figure. We repeat the 3–14 kpc bin including this cut from Fig. 5.1 for comparison.

In the accreted bulge region of Aq-A the quasi-relaxed component Aa dominates (if the radial range is restricted to $0 < r < 1$ kpc the radial velocity distribution becomes bimodal). A second more metal-poor component of much lower mass is also present (Ag), with an isotropic velocity ellipsoid. The Solar region was discussed above: component Aa continues to dominate here but other less relaxed and more metal poor components make significant contributions to the overall velocity distribution. These distributions nevertheless remain symmetrical and centred on zero velocity. In the inner and outer haloes the overall distribution becomes increasingly asymmetric as sharp spikes due to individual coherent streams (e.g. Ae) appear. A mild

	$\langle v_{\rm r}\rangle$		$\langle v_{\phi}\rangle$		$\langle v_{\theta}\rangle$		$\sigma_{\rm r}$		σ_{ϕ}		σ_{θ}		$N_{\rm prog}$		$f_{\rm sat}$	
A	−37.6	$^{+97}_{-78}$	2.3	$^{+94}_{-25}$	−2.4	$^{+10}_{-9}$	208	$^{+135}_{-77}$	97	$^{+63}_{-24}$	50	$^{+8}_{-21}$	84	$^{+33}_{-10}$	0.007	$^{+0.011}_{-0.004}$
B	−1.0	$^{+15}_{-17}$	2.4	$^{+8}_{-7}$	−0.4	$^{+3}_{-2}$	69	$^{+8}_{-11}$	57	$^{+21}_{-19}$	37	$^{+4}_{-2}$	39	$^{+3}_{-10}$	0.025	$^{+0.106}_{-0.009}$
C	10.0	$^{+31}_{-47}$	−5.9	$^{+85}_{-19}$	−0.7	$^{+22}_{-18}$	141	$^{+29}_{-93}$	79	$^{+105}_{-15}$	57	$^{+9}_{-8}$	104	$^{+27}_{-40}$	0.123	$^{+0.552}_{-0.079}$
D	−25.5	$^{+269}_{-62}$	12.3	$^{+25}_{-23}$	−5.9	$^{+33}_{-23}$	180	$^{+138}_{-96}$	75	$^{+71}_{-17}$	48	$^{+10}_{-14}$	65	$^{+15}_{-10}$	0.467	$^{+0.166}_{-0.203}$
E	−3.4	$^{+9}_{-7}$	−64.1	$^{+16}_{-24}$	0.5	$^{+2}_{-2}$	49	$^{+2}_{-3}$	37	$^{+16}_{-8}$	17	$^{+5}_{-0}$	49	$^{+9}_{-7}$	0.000	$^{+0.001}_{-0.000}$
F	−1.7	$^{+13}_{-12}$	−5.3	$^{+3}_{-16}$	0.3	$^{+8}_{-2}$	59	$^{+13}_{-3}$	31	$^{+22}_{-1}$	28	$^{+7}_{-55}$	54	$^{+8}_{-5}$	0.000	$^{+0.003}_{-0.000}$
A	−11.4	(−0.4)	6.3	(3.3)	−1.3	(0.3)	290	(136)	127	(115)	62	(98)	197		0.006	
B	−2.4	(−0.2)	1.4	(1.6)	0.0	(0.0)	74	(126)	40	(108)	38	(91)	63		0.024	
C	5.6	(−0.6)	−2.8	(0.5)	−1.3	(0.1)	167	(142)	83	(120)	64	(101)	243		0.110	
D	92.7	(−0.2)	23.9	(1.2)	−5.1	(−0.3)	357	(130)	86	(111)	63	(99)	135		0.532	
E	−2.1	(−1.2)	−49.4	(−37.3)	0.2	(0.0)	55	(114)	51	(98)	19	(85)	82		0.002	
F	0.7	(−1.6)	−4.1	(−6.8)	0.4	(0.1)	62	(104)	32	(93)	31	(77)	84		0.000	

Table 5.2: Median values of the first and second moments of the velocity distribution in spherical polar coordinates, for halo stars in 50 spheres of radius 2.5 kpc centred on the Solar circle (see text). The rightmost columns give the total number of progenitor satellites contributing to each volume ($N_{\rm prog}$) and the fraction of halo stellar mass in each volume associated with a surviving satellite core ($f_{\rm sat}$). The 10–90 per cent range is indicated alongside each value. The lower half of the table gives the equivalent values for all stellar particles in the Solar torus. Values in brackets correspond to all dark matter particles in the same region.

net rotation is apparent in the outer halo, driven by this component. These unrelaxed components are more metal poor than the inner relaxed components despite their (presumably) later arrival in the halo. This reinforces our conclusion in Chapter 3 (also e.g. Robertson et al. 2005) that although the outer halo is *dynamically* young, its progenitors typically have low masses, slow star formation rates and/or star formation histories truncated prior to infall (resulting in metal-poor populations). By contrast the inner halo is dynamically old, but formed from massive populations with rapid enrichment histories (giving them relatively high metallicities despite their old stellar ages).

In summary, these figures suggest that the *accreted* component of the stellar halo can produce *multiple* relaxed, non-rotating components in the Solar neighbourhood. These components may even have similar metallicity distribution functions, making them hard to distinguish from one another without detailed chemical analysis. As expected, the distant halo (beyond $r = 14$ kpc) includes larger contributions from unrelaxed metal-poor structures, with a tendency for stronger bulk rotation. Many of these distant halo structures *also* contribute to the region around the Sun. In particular they tend to broaden the local radial velocity distribution. The following section further examines this complex halo composition in the Solar neighbourhood. Subsequent sections discuss the implications for dark halo mass measurements based on the assumption of a simple relaxed stellar halo.

5.4 The Solar neighbourhood velocity ellipsoid

In this section we examine the velocity ellipsoid of the Solar neighbourhood in more detail. We fit a single Gaussian profile to each component of the velocity ellipsoid in fifty spheres of radius 2.5 kpc, each centred at a random point on a circle of radius $8\,\mathrm{kpc}$ around the centre of the halo. Each of these Solar neighbourhoods yields a local bulk velocity for halo stars, $(\langle v_r \rangle, \langle v_\theta \rangle, \langle v_\phi \rangle)$, and a corresponding velocity dispersion tensor specified by its diagonal elements $(\sigma_\mathrm{r}, \sigma_\theta, \sigma_\phi)$ under the assumption that it is aligned with the spherical coordinate system and polar axis that we adopt[4]. We calculate these values from the tagged dark matter particles in our model, weighting each particle by the stellar mass it carries. In Table 5.2 we give, for each halo, the median values of these bulk velocities and dispersions over fifty Solar neighbourhoods, and an estimate of the scatter between neighbourhoods (10–90 percentile range). We compute these

---

[4] Observations show the velocity ellipsoid in the Solar neighbourhood to be very closely aligned with the axes of a spherical polar coordinate system (Smith et al. 2009b). However, in our simulations the velocity ellipsoid will almost certainly not be aligned with our assumed coordinate system in all mock Solar neighbourhoods. The values we discuss are those that an observer assuming this alignment would infer.

Table 5.3: Observational estimates of the principle axes of the halo velocity ellipsoid in spherical polar coordinates, ordered approximately by the radial distance probed (from the Sun). A list of previous results for the Solar neighbourhood velocity ellipsoid are given in table 3 of Smith et al. (2009a).

σ_r	σ_θ	σ_ϕ	Notes	Ref
143 ± 2	77 ± 2	82 ± 2	$r < 2.5$ kpc	Smith et al. (2009a)
141 ± 5	75 ± 5	85 ± 5	$r < 10$ kpc	Bond et al. (2010)
160 ± 3	83 ± 2	102 ± 2	Inner halo	Carollo et al. (2010)
101 ± 3	98 ± 16	107 ± 17	SDSS BHB	Sirko et al. (2004)
178 ± 9	127 ± 6	149 ± 7	Outer halo	Carollo et al. (2010)

same moments of the velocity distribution for tagged particles in the entire Solar torus (defined in Section 5.3) and also for *all* dark matter particles in the same region. For comparison we list some recent measurements of the halo velocity ellipsoid in Table 5.3.

The mean radial and 'vertical' (θ) motions observed in the Solar neighbourhood are close to zero in all haloes except Aq-D. This is consistent with SDSS subdwarf stars in the Solar neighbourhood from the work of Smith et al. (2009a), who found a small radial bulk motion of $\langle v_\mathrm{r} \rangle \sim 8.9 \pm 2.7\,\mathrm{km\,s^{-1}}$, with $\langle v_\phi \rangle$ and $\langle v_\theta \rangle$ approximately zero. Haloes Aq-A and Aq-C contain a significant number of volumes with strong radial bulk motions and in Aq-D an unrelaxed component dominates over the whole Solar torus (component Da in Fig. 5.1). This component is associated with a surviving satellite core, as indicated by the high value of f_sat in Table 5.2. The velocity distribution of this component is not at all Gaussian in the radial coordinate. These bulk motions are not evident in the dark matter, for which $\langle v_\mathrm{r} \rangle$ and $\langle v_\theta \rangle$ deviate no more than $\pm 3\,\mathrm{km\,s^{-1}}$ from zero over all sample volumes in all haloes.

There are indications of bulk rotation (nonzero $\langle v_\phi \rangle$) in some haloes. This is most apparent in Aq-E, which is dominated in the Solar torus by an accreted 'thick disc' (component Eb in Fig. 5.1). This component also appears to dominate in the full dark matter distribution. Haloes Aq-A and Aq-F show a very weak dark matter bulk rotation of $|\langle v_\phi \rangle| < 10\,\mathrm{km\,s^{-1}}$ and the remaining haloes are consistent with zero rotation for the dark matter. The stellar haloes Aq-A and Aq-C show a wide distribution of $\langle v_\phi \rangle$ across different Solar neighbourhoods. This suggests that some streams only cross restricted regions of the Solar torus.

With regards to velocity dispersion, haloes A, C and D show the same approximately 2:1 ratio of radial and azimuthal (ϕ) velocity dispersions measured in the Milky Way. The two tangential components appear to be roughly isotropic in the Milky Way, with evidence for σ_θ smaller than σ_ϕ by $\sim 5\,\mathrm{km\,s^{-1}}$ (Smith et al. 2009a). However, the v_θ distribution in our simulated haloes is always notably colder than the v_ϕ distribution, hence in general our simulated

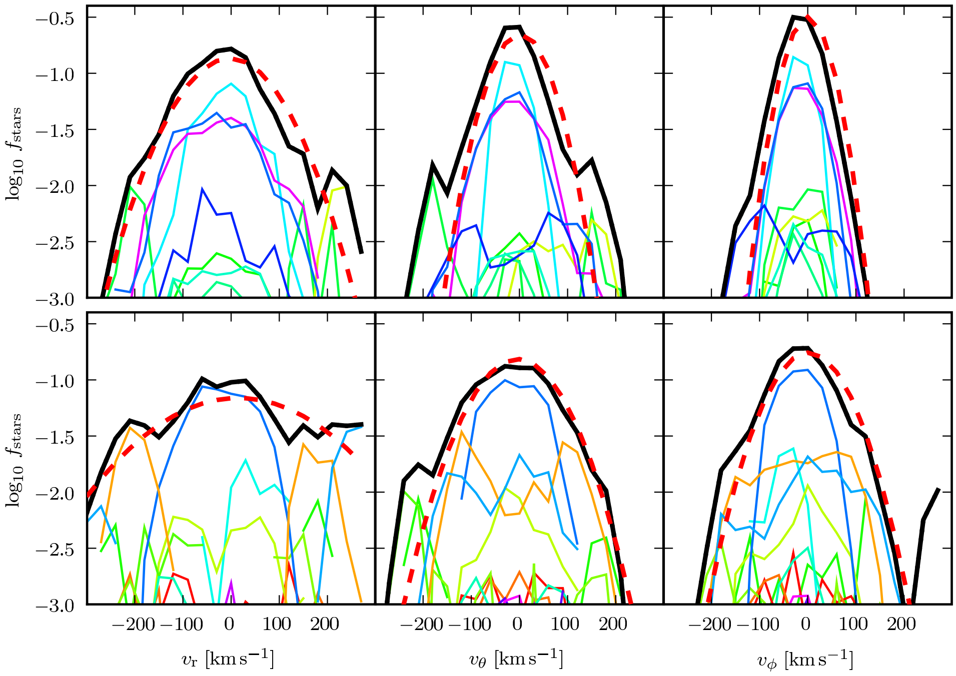

Figure 5.4: Velocity distributions (on a logarithmic scale) for stars in a sphere of radius $2.5\,\rm kpc$ located at a random point at $r = 8\,\rm kpc$ in halo Aq-B (upper panel) and halo Aq-C (lower panel). A black line corresponds to the total distribution for all stars, and coloured lines indicate individual contributions. The red dashed line shows a Gaussian fit to each distribution.

velocity ellipsoids are more triaxial than that of the Milky Way. This triaxiality is also apparent, but weaker, in the dark matter velocity ellipsoid.

The typical dark matter distribution in the Solar neighbourhood is close to (but not exactly) a multivariate Gaussian (Vogelsberger et al. 2009). However, typically only ~ 1000 (10 per cent) of the dark matter particles in our Solar volumes are 'tagged' by our stellar model. In a small number of cases ($\leq 10\%$) a Gaussian fit fails altogether in one or more coordinates. We discard these extremely non-Gaussian volumes when computing averages. In practice, even in those cases where a Gaussian fit is 'successful', it is not always a good description of the distribution – hints of this are apparent in Fig. 5.1.

To illustrate this point further we show velocity distributions for two individual Solar neighbourhood spheres in Fig. 5.4 (from Aq-B and from Aq-C). In the Aq-B example, relaxed components dominate and the sum of the individual distributions results in an approximately isotropic Gaussian ellipsoid. In the Aq-C example, the presence of an unrelaxed component substantially broadens the velocity ellipsoid, particularly in the radial direction.

Smith et al. (2009a) find that both the v_ϕ and v_θ distribution are better fit by two-component Gaussians in their sample of subdwarf stars in the Solar neighbourhood. They attribute this to the presence of substructure. Their v_θ distribution shows broad wings that are better fit by combining one wide and one narrow Gaussian both with zero mean motion, while their v_ϕ distribution requires nonzero mean motion for the two components (of $\sim +20\,\mathrm{km\,s^{-1}}$ and $\sim -20\,\mathrm{km\,s^{-1}}$). Both of these scenarios are qualitatively similar to many of our haloes shown in Fig. 5.1. These observed distributions are also smoothed by velocity errors ($\sim 30\,\mathrm{km\,s^{-1}}$ in the sample of Smith et al.), which we have not accounted for in our comparisons.

From this quantitative analysis of the Solar neighbourhood velocity ellipsoid we conclude that a pure accretion model has some difficulty reproducing the observed behaviour of nearby Milky Way halo stars despite many qualitative similarities. The main differences are the greater triaxiality of the simulated ellipsoids and the frequency with which unrelaxed streams result in strong deviations from Gaussian distributions. We consider some possible reasons for these discrepancies in Section 5.7. Another conclusion drawn from Table 5.2 is that accreted halo stars may not be reliable tracers of dark matter. In the following two sections we examine the consequences of this, considering first the complexity in the velocity structure of the outer halo, and then the escape velocity of the Solar neighbourhood.

5.5 Velocity dispersion profile

If Milky Way halo stars trace the underlying dark matter distribution, they can be used to determine the circular velocity profile of the dark halo, $v_\mathrm{c}(r)$ (where r denotes galactocentric radius), and hence to constrain the total halo mass. This requires a significant sample of tracers at large galactocentric distances, with accurate distance and radial velocity measurements. In recent years several samples of tracers (giant and horizontal branch stars and globular clusters) have been obtained and used to estimate the halo mass in this way (Battaglia et al. 2005; Xue et al. 2008; Brown et al. 2010; Gnedin et al. 2010).

In practice, $v_\mathrm{c}(r)$ is not measured directly. It is inferred from the galactocentric radial velocity dispersion of the tracers, $\sigma_\mathrm{r}(r)$, under the assumptions that the halo is in dynamical equilibrium, that its stars trace the dark matter, and that it has a particular velocity anisotropy profile. Anisotropy here is defined as

$$\beta(r) = 1 - \frac{\sigma_\theta^2(r) + \sigma_\phi^2(r)}{2\sigma_\mathrm{r}(r)}. \tag{5.1}$$

The 'radial' velocity actually observed is that component measure along the line of sight in the heliocentric frame ($v_{\mathrm{r},\odot}$). This can be converted to a 'pseudo-galactocentric' radial velocity in the Galactic rest frame, $v_\mathrm{r,GSR}$ if the local circular velocity, the distance to the Galactic centre and the Solar motion with respect to the local standard of rest are known (as discussed in Battaglia et al. 2005; Xue et al. 2008; Brown et al. 2010; Gnedin et al. 2010). These $v_{\mathrm{r,GSR}}$ are still not true galactocentric radial velocities, v_{r} (which can only be determined with proper motion data for the tracers). However, $v_{\mathrm{r,GSR}}$ is a close approximation to v_{r} at large radii ($r \gtrsim 30\,\mathrm{kpc}$).

In practice the constraint on $v_{\mathrm{c}}(r)$ from the velocity dispersion profile may be weak and suffers from several systematic uncertainties (Dehnen et al. 2006). In particular, as we will demonstrate in the case of our accreted haloes, the assumptions of a relaxed halo and a 'well-behaved' anisotropy profile are questionable[5] . Measurements of the local velocity ellipsoid constrain the anisotropy $\beta(R_{\odot})$ in the Solar neighbourhood, but $\beta(r)$ is unknown elsewhere in the halo. In the absence of data, cosmological simulations have been used to justify the assumption that halo stars trace dark matter and to determine plausible $\beta(r)$ profiles. In particular Xue et al. (2008) use simulations from Abadi et al. (2003a, 2006) in an attempt to circumvent many of the systematic uncertainties inherent in deriving $v_{\mathrm{c}}(r)$ from the distribution[6] of line-of-sight velocities $v_{\mathrm{r,GSR}}$. From two hydrodynamical simulations of Milky Way-like haloes (total mass $2.1 \times 10^{12}\,\mathrm{M}_{\odot}$ and $8.6 \times 10^{11}\,\mathrm{M}_{\odot}$) they construct two probability distributions $P[v_{\mathrm{los}}/v_{\mathrm{c}}(r)]$ in several radial bins. Their best estimate of $v_{\mathrm{c}}(r)$ in each bin is then taken to be the value which scales the *observed* v_{los} distribution such that its similarity to the *simulated* distribution is maximised (under a KS-test).

This approach is only valid if the underlying simulations are themselves realistic representations of the Milky Way stellar halo. The stellar haloes in these simulations match the gross properties of the Milky Way (Abadi et al. 2006), but have much lower resolution than those in this thesis. Unlike our haloes, these simulations contain an (unquantified) *in situ* contribution from scattered disc stars and starbursts in accreted gas. As we discuss below, simulations such as those of Abadi et al. (2003a) may not have resolved the full complexity of the accreted stellar halo and estimates of the Milky Way halo mass that rely on them may be biased as a result.

In Fig. 5.5 we show the profile of the *true galactocentric* radial velocity dispersion, $\sigma_{\mathrm{r}}(r)$, in spherical shells measured in each of our six haloes. To emphasise intrinsic variations rather than systematic differences in halo mass, we scale all of our haloes to a common virial velocity

---

[5] In addition to the assumptions discussed above, the density profile of tracers must be specified to calculate $v_{\mathrm{c}}(r)$. In principle this is directly measurable, but nontrivial corrections must be made for selection effects and incompleteness. Gnedin et al. (2010) use the data of Brown et al. (2010) to show how the maximum likelihood circular velocity at 80 kpc, $v_{\mathrm{c}}(80)$, varies under a range of reasonable assumptions for the halo density profile and a constant anisotropy value. They demonstrate that assuming shallow tracer density profiles and radially biased velocities results in lower mass estimates for the Milky Way dark halo.

[6] If Gaussian, the distribution of $v_{\mathrm{r,GSR}}$ is specified simply by the dispersion $\sigma_{\mathrm{r}}(r)$.

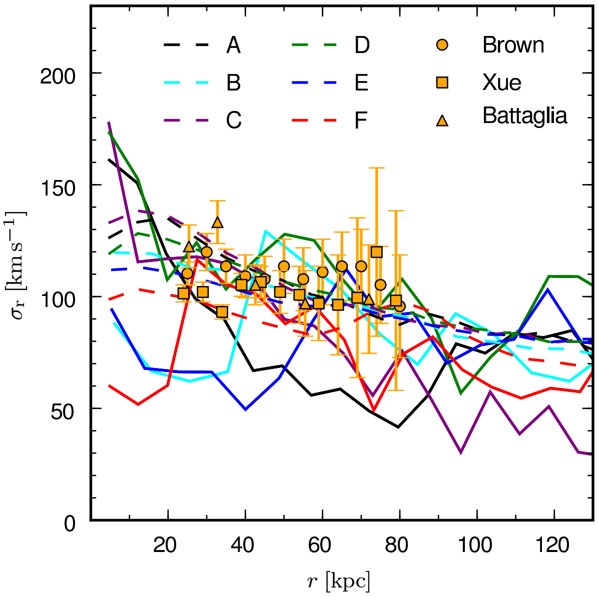

Figure 5.5: Solid lines show the true galactocentric velocity dispersion of accreted halo stars, $\sigma_{\mathrm{r}}(r)$, in spherical shells. Dashed lines show the corresponding profiles for all dark matter particles. Orange lines with error bars show observations of Battaglia et al. (2005), Xue et al. (2008) and Brown et al. (2010) as plotted by Gnedin et al. (2010).

(V_{200}) of $140\,\mathrm{km\,s^{-1}}$, as discussed in Section 5.2. Regardless of rescaling, haloes Aq-C and Aq-D have similar V_{200}, and comparing these two haloes in Fig. 5.5 makes clear the significance of halo-to-halo variations. Dashed lines in Fig. 5.5 are the corresponding $\sigma_{\mathrm{rDM}}(r)$ profiles for all dark matter particles. These show more regular behaviour and substantially less halo-to-halo scatter than the stars. Only in halo Aq-D does $\sigma_{\mathrm{r}}(r)$ resemble $\sigma_{\mathrm{rDM}}(r)$ over most of the radial range shown. Stars in the other haloes show systematically lower velocity dispersion than the dark matter. Interestingly, the accreted stars in the SPH simulations of Abadi et al. (2006) show slightly *higher* radial velocity dispersions than the dark matter at large radii.

Fig. 5.5 also shows observational data (compiled by Gnedin et al. 2010) from Battaglia et al. (2005), Xue et al. (2008) and Brown et al. (2010). The observations suggest $\sigma_{\mathrm{r}}(r)$ in the Milky Way is flat or very slowly declining with radius (a shallower slope implies a larger halo mass; e.g. Gnedin et al. 2010). The observed profile appears smoother than the simulations (more closely resembling the dark matter), although the error in each point is large. The majority of the observational data is derived from BHB stars in SDSS (Xue et al. 2008; Brown et al. 2010). Distance errors in these samples are small but still capable of smoothing local fluctuations and the SDSS footprint only partly samples large structures in the halo (e.g. Sagittarius, Virgo, Hercules-Aquila, Triangulum-Andromeda). By contrast our simulated profiles are 'all sky' and

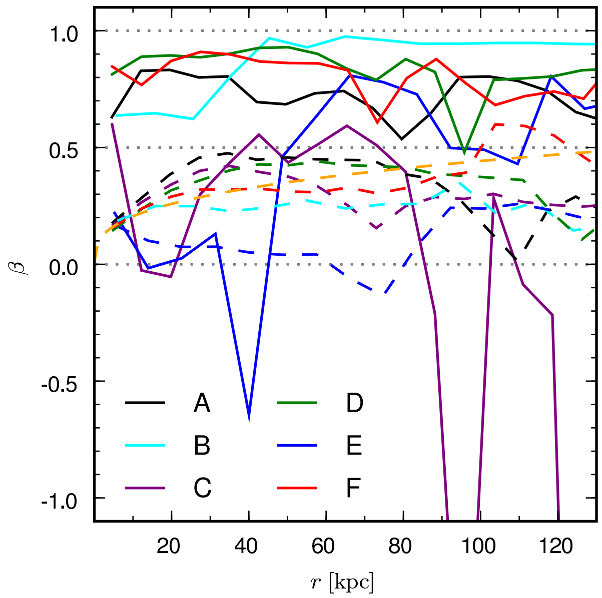

Figure 5.6: Solid lines show the velocity anisotropy profiles of accreted halo stars, $\beta(r)$, in the six Aquarius stellar haloes described in Chapter 3. Dashed lines show the corresponding profiles for all dark matter particles. An orange dashed line shows the radially anisotropic model used by Battaglia et al. (2005, their equation 5).

are not selected to avoid streams.

Haloes Aq-D and Aq-C are closest to the Milky Way data (given our fiducial scaling). In Chapter 3 we showed that Aq-D has some consistency with other Milky Way data, notably the halo density profile (although its kinematic structure in the Solar neighbourhood is unlike the Milky Way, as discussed in Section 5.4). Within 20 kpc, both these haloes and Aq-A show a strong rise in velocity dispersion that is not seen in Aq-B, Aq-E and Aq-F. Observed radial velocities alone are insufficient to constrain the galactocentric profile in this region. Proper motion data from *Gaia* will be particularly helpful in discriminating between the two classes of halo profile seen in our model.

We show the spherically averaged velocity anisotropy in Fig. 5.6. Three of our stellar haloes are consistent with $\beta \sim 0.5 \pm 0.1$ in the Solar neighbourhood, but all show very different profiles at larger radii. In general haloes Aq-A, B, D and F show strong radial bias from 30–100 kpc; haloes Aq-C and Aq-E are dominated by localised 'excursions' to strong tangential bias. None of the haloes is consistent with an isotropic dispersion profile, nor with strictly uniform or even monotonic anisotropy (halo Aq-B comes closest, with $\beta \sim 1$ beyond 60 kpc). In all cases, $\beta(r)$ fluctuates throughout the halo. The trend towards increasing radial bias for accreted stars (relative to the dark matter) is in agreement with average profiles shown by Abadi et al. (2006). These authors also note the difference between the velocity structure of halo stars and dark matter.

We also show the underlying dark matter anisotropy profile, $\beta_{DM}(r)$. As expected the dark matter anisotropy varies much more smoothly and is essentially constant over the range 30–$100\,\mathrm{kpc}$ in haloes Aq-A, B, C, D and F. The mean anisotropy differs only slightly between these haloes in the range $0.2 < \beta_{DM}(r) < 0.5$. Aq-E is more isotropic on average than the other haloes, and shows a strong dip to tangential bias in the dark matter distribution at $\sim 80\,\mathrm{kpc}$: the *opposite* trend is seen in halo stars at the same radius. As in the case of the radial velocity dispersion profile, we conclude (as Abadi et al. 2006) that accreted halo stars are *not* reliable tracers of the underlying dark matter velocity distribution. We further caution that individual (accreted) haloes can differ substantially from the 'average' anisotropy behaviour. Simulations may not be a reliable guide to the discrepancy between stars and dark matter in the outskirts of the Milky Way halo.

As the systematic uncertainty in the assumption of a $\beta(r)$ profile and a relaxed halo dominate attempts to constrain v_{c} from velocity dispersion data, Gnedin et al. (2010) advocate the approach of (Xue et al. 2008), comparing directly with simulations. We have shown that when streams are resolved in detail in a realistic accreted stellar halo, the outlook for this approach is rather bleak. The regularity of the observed Milky Way halo radial velocity dispersion profile may be due to undersampling or smoothing by errors, or else the majority of mass (at least in BHB stars) may indeed belong to a velocity component not included in our simulations. We discuss these possibilities further in Section 5.7.

5.6 Hypervelocity stars and the local escape velocity

In this final section, we return to the Solar neighbourhood. Smith et al. (2007) use high-velocity stars from the RAVE survey to constrain the local escape speed v_{esc}. They determine a maximum likelihood estimate of the median value of $v_{\mathrm{esc}} = 544\,\mathrm{km\,s^{-1}}$ with a 90% confidence range of $498 < v_{\mathrm{esc}} < 608\,\mathrm{km\,s^{-1}}$. Their method, which follows that of Leonard & Tremaine (1990), uses only radial velocity measurements and assumes a relaxed system with isotropic velocities (it also assumes that the contribution from other sources of high velocity stars, such as three-body encounters and measurement errors, are negligible). Furthermore the method must assume a particular form for the stellar velocity distribution function in its high-velocity tail. This approach is valid only if this tail is populated all the way up to v_{esc}. If the actual velocity distribution is truncated well below v_{esc}, the result will be an underestimate of the true escape speed.

A suitable form to assume for the high-velocity distribution function is a powerlaw $f(v|v_{\rm esc},k) \propto (v_{\rm esc}-v)^k$ for $v < v_{\rm esc}$ ($f(v|v_{\rm esc},k) = 0$ for $v \geq v_{\rm esc}$). The appropriate value of k is unknown (Leonard & Tremaine 1990). In their maximum likelihood approach to determining $v_{\rm esc}$, Smith et al. obtain a prior probability distribution for k from a series of four hydrodynamical cosmological simulations of Milky Way-mass haloes ($\sim 1.25 \times 10^{12}\,{\rm M}_{\odot}$), including those of Abadi et al. (2003b, 2006) described in Section 5.5. The stellar velocity distributions in these simulations were found to be populated up to $v/v_{\rm esc} \geq 0.9$.

Smith et al. use only particles in their simulation set that are classified as belonging to a non-rotating spheroid (the observational sample is assumed to have negligible contamination from thin and thick disc stars). Having rescaled the simulations as described in Section 5.2, they calculate $v_{\rm esc}$ in the Solar neighbourhood, defining the zero of the potential at $3\,{\rm r}_{200}$. Because stars are not uniform tracers of the DM, stars and DM particles may behave differently in the high velocity tail, as $v \rightarrow v_{\rm esc}$. Smith et al. find that stars are less likely than DM particles to reach the escape velocity. The fraction of stars at a given $v/v_{\rm esc}$ becomes systematically smaller than the corresponding fraction of dark matter at the same $v/v_{\rm esc}$. Their maximum likelihood values for k differ systematically between stars and DM, and from simulation to simulation.

Here we examine the assumptions underlying the Smith et al. $v_{\rm esc}$ estimate in the context of our high resolution models. We are restricted to examining the accreted stars only, although Smith et al. claim their selection of particles in the Abadi et al. (2006) simulations isolates the same contribution to the halo. In addition, we do not capture the change in the shape of the halo and its potential as the result of disc growth (e.g. Abadi et al. 2010). Our 'stars' trace the unmodified dark halo, which is expected to become more spherical in its outer regions and more oblate in the centre if baryons are included. A compact disc component should raise the escape velocity in the Solar neighbourhood. Stars falling into this modified potential would reach correspondingly higher velocities, although this need not be the case for halo stars in place *prior* to the formation of the disc.

For each of our simulations we assume an NFW potential with individual parameters for each halo given by Navarro et al. (2010b)[7], rescaling as described in Section 5.2. For all star particles in the range $3 < r < 14$ kpc considered by Smith et al., we compute the total velocity, v,

---

[7] We have used an accurate reconstruction of the non-spherical potential based on the self-consistent field method (Lowing et al. 2010) to determine that the variations in $v_{\rm esc}$ over a sphere of 8 kpc radius are less than $\sim 15\,{\rm km\,s^{-1}}$.

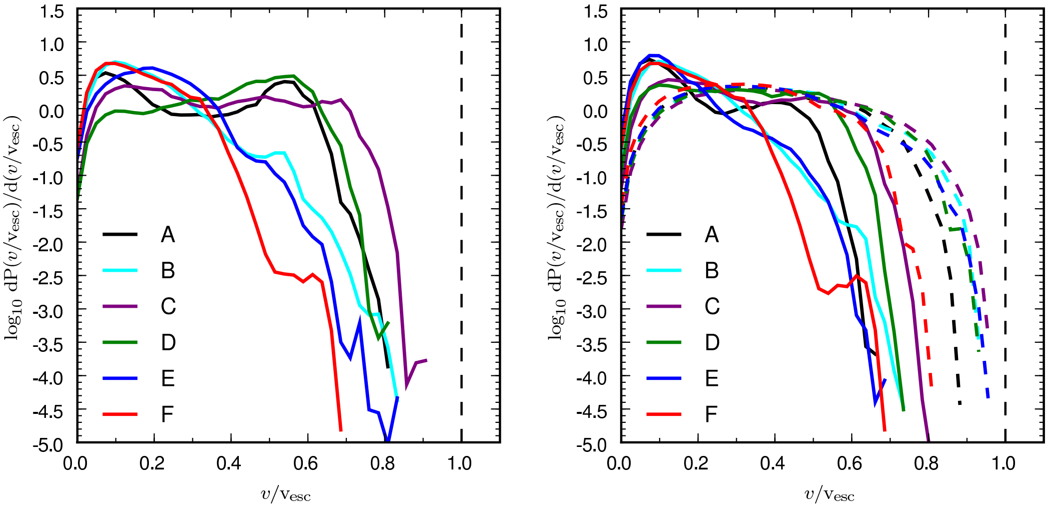

Figure 5.7: *Left*: Stellar-mass weighted probability distribution of tagged dark matter particles in the Solar neighbourhood moving with speeds in the interval v to $v+dv$, where v is expressed as a fraction of the escape velocity, v_{esc}, at their current position. *Right*: in this panel we exclude stars (tagged particles) stripped from surviving satellites and those belonging to components with high mean motions (see text). Dashed lines show the corresponding PDFs for all dark matter particles in the Solar torus.

relative to the escape velocity (to infinity) at the radius of that particle in our assumed potential. The mass-weighted probability density function of v/v_{esc} is show in the left-hand panel Fig. 5.7.

The tails of the v/v_{esc} distributions roughly follow the power-law form given above, with exponents in the interval $[2.7, 4.7]$ used as prior on k in the analysis of Smith et al. (2007). However, the distribution of v/v_{esc} does not extend beyond $v/v_{\mathrm{esc}} > 0.9$ in any of our haloes. In the right-hand panel of Fig. 5.7 we have included only particles belonging to components with peak rotational velocity of $|v_\phi| < 30\,\mathrm{km\,s^{-1}}$. Note that this excludes both strongly 'co-rotating' and 'counter-rotating' stars. If unrelaxed components are excluded in this way, the stellar distributions are truncated between $0.6 < v/v_{\mathrm{esc}} < 0.8$. We conclude that if the stars in the RAVE sample of Smith et al. (2007) belong to analogous components, their analysis is likely to underestimate the escape velocity (and hence underestimate the dark halo mass).

This analysis also demonstrates that most high-velocity stars ($v/v_{\mathrm{esc}} > 0.85$) in the Solar neighbourhood do not belong to the relaxed components of the halo. Instead they belong to unrelaxed components with high mean motions. This was suggested by Abadi et al. (2009) based on the presence of high-velocity streams in the simulations of Abadi et al. (2003a, 2006). In Fig. 5.8 we show $v_{\mathrm{r}}(r)$ for the tagged particles in three of our simulations (Aq-C, Aq-D and Aq-E). High-velocity stars ($v/v_{\mathrm{esc}} > 0.85$) are indicated by filled stars symbols. Many have high *tangential* rather than radial motions. Although we observe some features reminiscent of

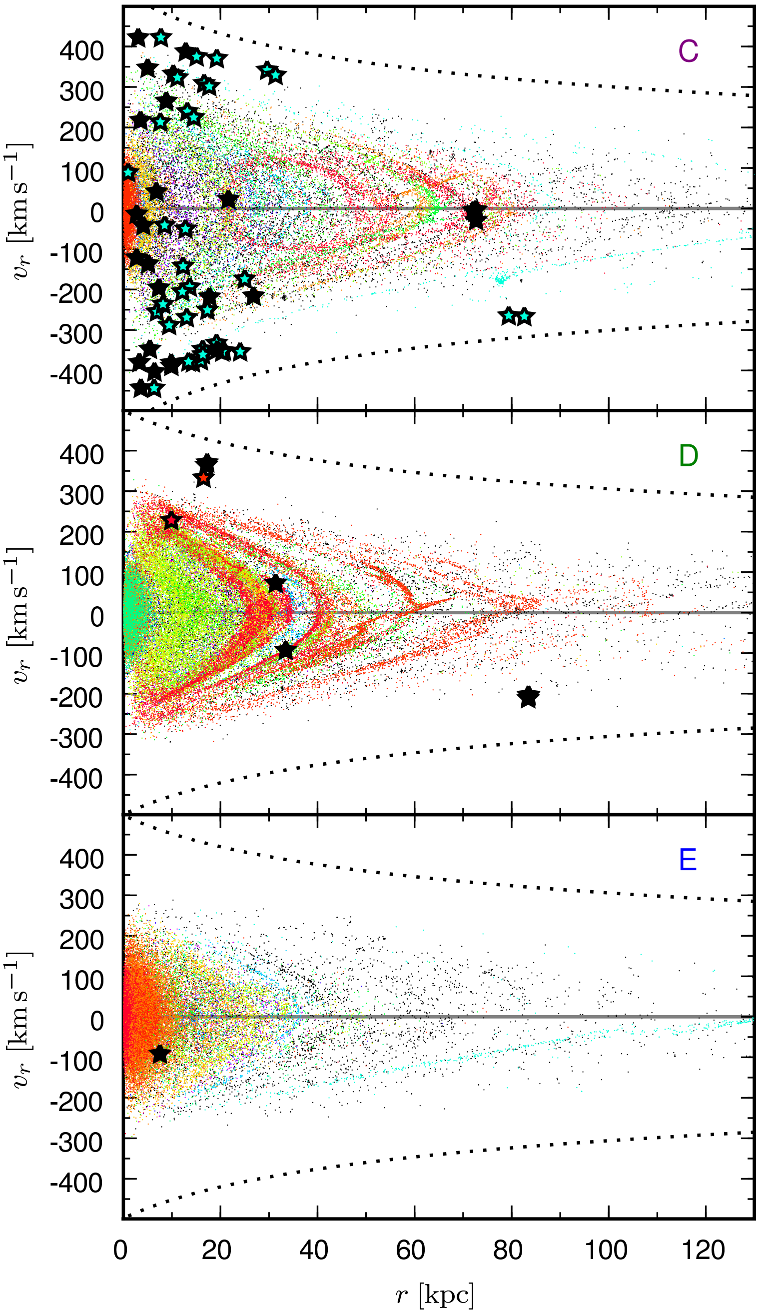

Figure 5.8: Points show galactocentric radial velocity and distance for all particles in the haloes Aq-C, Aq-D and Aq-E (top to bottom). Colours indicate different progenitors (chosen in the same manner as Fig. 5.1; black points correspond to minor progenitors). Dotted lines indicate the escape velocity. Although these distributions are downsampled for clarity at rate of $1:100$, we explicitly highlight all stars with $v/v_{\rm esc} > 0.85$ (with filled star symbols, the colour of which corresponds to those of the points). There are very few such stars in the radial range shown, and not all of them have high $v_{\rm r}$ motions.

the streams shown by Abadi et al. (2009) (particularly in Aq-C and Aq-D, which have recently accreted bright satellites), none of these extend beyond the escape velocity[8]. However, the simulation snapshot shown by Abadi et al. (2009) was chosen to be close in time to the disruption of the satellite responsible for the high velocity stream – it may be that the signatures of these events do not persist for long in the $v_{\rm r}(r)$ diagram. Xue et al. (2008) also find that the radial velocities of particles in one of the two simulations they analyse rarely approach the escape velocity (their figure 11)[9].

5.7 Discussion

We have presented a basic kinematic decomposition of the accreted stellar halo models we presented in Chapter 3. These haloes are dominated by debris from a small number of significant progenitors. In their centres the debris is dynamically relaxed and follows roughly isotropic Gaussian velocity ellipsoids. A number of relaxed components with similar kinematic and chemical profiles exist in these inner regions, which would be difficult to disentangle observationally. With increasing galactocentric distance, the halo becomes dominated by more complex kinematic structures associated with recently stripped streams.

In our simulations, stars in the outer halo are not dynamically relaxed, do not trace the dark matter and exhibit strong variations in velocity anisotropy with radius. In the Solar neighbourhood halo stars do not always populate the velocity distribution up to the escape velocity: those hypervelocity stars that do are overwhelmingly associated with extant or recently disrupted satellites. The variation in the velocity ellipsoid around the Solar circle is substantial, as it can be locally biased by the presence of individual massive streams.

These results contradict the assumptions of relaxation and simple $\beta(r)$ models often used when reconstructing the circular velocity profile of the Milky Way dark halo (and hence measure its mass) from velocity dispersion data. Previous simulations have supported these assumptions. The bias we find between halo stars and dark matter may explain why measurements of the Milky Way dark halo mass based on velocity dispersion data favour systematically lower masses. Further investigation of these biases will require more realistic mock observa-

---

[8] We note that attempts to fit the envelope of high velocity stars in order to constrain the escape velocity beyond the Solar neighbourhood, as suggested by Brown et al. (2010), will also be compromised if high velocity halo stars in the Milky Way behave as those in our simulations.

[9] In the other simulation, the highest velocity particles seem to belong to groups at a single radius with some internal velocity dispersion (appearing as vertical lines of points in these plots), reminiscent of satellites (which were removed from the simulations in the analysis Xue et al.).

tions of the simulations, taking account of the distributions of individual stellar tracer types (which depend on age and metallicity) and the effects of instrumental and systematic errors, limited depth and sky coverage.

Why have earlier simulations (based on SPH) come to different conclusions? First of all, low-resolution SPH models may simply not resolve accreted substructure in the halo adequately. For example, the absence of structure in the v_{r} diagrams shown in figure 11 of Xue et al. (2008) can be contrasted with Fig. 5.8. The discrepancy is particularly clear at large radii, where many of our halo particles are clearly concentrated into streams.

More significantly, our models consider only the *accreted* contribution to stellar haloes. As discussed in Section 1.3.1 in situ formation processes may be responsible for some fraction of the halo. These contributions are poorly understood in comparison to accretion. If stars are formed in situ in the distant halo more-or-less uniformly (e.g. in an unstable cooling flow), then they may indeed trace the dark matter more closely than accreted stars. For example, large numbers of in situ stars can be formed through cooling instabilities in SPH simulations, although physical effects are hard to disentangle from numerical artifacts in this regime[10]. The kinematics of these stars could provide an insight into the behaviour of possible in-situ halo populations, even if their origin in the simulations is unphysical.

Disc disruption is another possible source of in situ stars (e.g. Purcell et al. 2010). Gradual heating by satellite bombardment (often proposed as a means of forming the thick disc) seems unlikely to contribute to the halo far beyond the disc. However, more catastrophic events could plausibly build the inner halo. The Solar neighbourhood measurements we discuss here will be particularly sensitive to these stars. Studying this mechanism in detail will require simulations in which the growth of a realistic stellar disc is modelled together with the assembly history of the dark halo. The next generation of ab initio hydrodynamic simulations (which should resolve galactic satellites, produce stable discs with realistic halo baryon and stellar fractions, and demonstrate robust numerical convergence) will be better suited to studying this process.

Our accreted haloes reproduce the radial elongation of the velocity ellipsoid in the Solar neighbourhood. In many cases this may be due to the broadening of the radial component by the symmetric bimodal distributions associated with streams (as illustrated in Fig. 5.4). In our models we find a stronger asymmetry between the tangential components of the velocity ellipsoid than is observed in the Solar neighbourhood. Hydrodynamic simulations suggest that overall halo potential becomes more spherical when baryons are included (e.g. Abadi et al.

---

[10] This may be one explanation for the unusual clumps shown in figure 11 of Xue et al. (2008), noted above.

2010; Tissera et al. 2010). This effect is neglected in our simulations, which may explain the greater triaxiality of the simulated velocity ellipsoids.

Changes to the star formation (semi analytic) model may also have some impact. Fig. 2.1 shows that the fiducial Bower et al. (2006) model used in this work tends to underpredict the number of bright (SMC/LMC) surviving satellites relative to the mean of the Milky Way and M31 systems. This may be due in part to the Aquarius haloes having a lower mass than the Milky Way. If this is not the case, then our models may not be assigning sufficient luminosity to the halo components associated with the most massive disrupted galaxies. The implications of this effect are unclear: in some haloes, correcting it would boost the contribution of relaxed halo components; in others it would enhance the unrelaxed components.

Finally, we note that most of the features of the Milky Way halo are observed in our simulations, but not all in the same halo. Our models (which were not attempting to exactly replicate the Milky Way) demonstrate substantial halo to halo scatter. This scatter is driven by their sensitivity to the most massive of their progenitors, the properties of which are essentially independent of one another and of the host halo. It is therefore not unreasonable to imagine that the Milky Way simply represents a different combination of the ‘ingredients’ found across our six examples. Furthermore, if the halo masses derived by Smith et al. (2007) and Xue et al. (2008) are indeed underestimates, then the Aquarius haloes may themselves be less massive than the Milky Way halo by up to a factor of two. The mix of progenitors in the inner regions of more massive haloes may be different from those in the Aquarius sample, as a few more large satellites may be accreted on average. Haloes B and E seem to match the apparent absence of unrelaxed components in the Solar neighbourhood, but their dispersions are too small in absolute terms and their density profiles are too concentrated (see Chapter 3, Fig. 3.8). In addition their overall halo stellar mass (or density in the Solar neighbourhood) is too low. A more massive version of Aq-B with the addition of one or two massive later-infalling components (to create a shallower density profile and introduce some radial bias to the local velocity ellipsoid) would be a reasonable match to the Milky Way.

5.8 Conclusions

The main conclusions of this chapter are summarised as follows:

- Inner/outer halo divisions of the type suggested (for example by Carollo et al. 2007) can arise through accretion alone, without having to invoke an *in situ* component to explain the dichotomy between a (flattened) non-rotating metal-rich inner halo and an overlapping, weakly rotating, metal-poor outer halo.

- Single-component Gaussian distributions are generally an inadequate description of the velocity ellipsoids of accreted stars in the Solar neighbourhood, particularly in the radial coordinate. Although some halo configurations can produce velocity ellipsoids consistent with the Milky Way data, in others significant contributions are made by unrelaxed components. The radial elongation of the velocity ellipsoid in the Solar neighbourhood may be a manifestation of a 'symmetric' velocity perturbation due to an unrelaxed halo component.
- There is substantial variation around the Solar circle in the mix of kinematic components present in the accreted halo (distinguished by their mean motion and velocity dispersion).
- In the distant halo, the velocity dispersion and anisotropy profiles of stars differ significantly from those of the bulk of the dark matter. The kinematics of outer halo stars differ from halo to halo, so the results of individual simulations are unlikely to provide accurate templates for the behaviour of these stars in the Milky Way.
- In the Solar neighbourhood, the velocity distribution of accreted halo stars does not extend to the escape velocity. Caution is necessary when interpreting measurements of the Milky Way dark halo mass that make this assumption. Such assumptions would benefit from further testing against high resolution simulations including baryons.

6
Conclusions

6.1 Summary

In this thesis we have explored the formation of galactic stellar haloes through the tidal disruption of satellite galaxies. To do this we have used a novel combination of semi-analytic models and N-body simulations. Much of the data to which we have compared our models has been obtained from the Milky Way, although throughout we have attempted to set our work in the wider context of galaxy formation in the Cold Dark Matter cosmogony. In Chapter 1 we discussed the historical background to this work and gave an overview of recent observational results concerning the stellar haloes of the Milky Way, M31 and other galaxies.

In Chapter 2 we described our simulations, which were based on tagging dark matter particles in N-body simulations with stellar populations according to a semi-analytic galaxy formation model. The advantage of our approach over previous work is the combination of high numerical resolution with a fully cosmological context (both in the dynamics and initial conditions of the N-body simulation and in the constraints imposed on the semi-analytic model). This combination allows us to study the bulk properties of the halo and its substructure as explicit predictions of a given CDM galaxy formation model. We applied our technique to the Aquarius simulations (Springel et al. 2008a) using the GALFORM semi-analytic model of Bower et al. (2006). In Chapter 3 we examined many properties of the resulting stellar haloes, such as their density, surface brightness and metallicity profiles. We found our simulations to be in broad agreement with observational data from the Milky Way and M31. However, we also found that the stochastic nature of halo mergers in CDM leads to large variations in these observable stellar halo properties between different dark haloes of a given mass. This variation is a natural expectation of halo growth in the CDM cosmogony.

In Chapters 4 and 5 we examined the spatial distribution and kinematics of accreted halo stars in more detail. The first part of Chapter 4 highlighted the difficulty of comparing directly to the simple SDSS tomographic results of Bell et al. (2008), where systematic errors in the observations (such as quasar and disc star contamination) are not well understood. Despite these difficulties, our comparison suggested that a smoothly distributed component (possibly formed in situ and hence not modelled by our approach) could make a significant contribution to the inner halo of the Milky Way. In the second part of Chapter 4 we developed a new statistical method to quantify kinematic substructure in spectroscopic surveys of luminous halo tracers, based on a two-point correlation function in phase space. We found that this technique could distinguish differences in the 'phase space substructure' of our different Aquarius halo models. Applying this same analysis to BHB star catalogue of Xue et al. (2008) suggests that the Milky Way halo contains a modest degree of kinematic and spatial structure. It lies close to the median of our sample of simulated haloes in this respect.

In Chapter 5 we examined the bulk kinematic properties of our simulated stellar haloes. We demonstrated that multicomponent haloes like those of the Milky Way and M31 arise naturally in our satellite accretion model. Our simulations reproduce the gross properties of the velocity ellipsoid measured in the Solar neighbourhood. We found that overall, accreted halo stars do not behave as the bulk of the dark matter. Although this is anticipated, our findings suggest that assumptions about the relationship between halo stars and dark matter deserve further investigation. In particular halo stars do not trace the dark matter velocity distribution up to the escape velocity in the Solar neighbourhood. If the stellar halo is built largely though accretion, these results suggest that mass estimates of the Milky Way based on these kinematic measurements will underestimate the true mass.

6.2 Further Work

Here we outline several outstanding questions raised in this thesis and discuss some possibilities for further work.

6.2.1 Quantifying halo structure in the Milky Way and beyond

Our results suggest that each individual galactic stellar halo is a complicated mix of morphological and kinematic features created by different progenitors. Indeed, the variety and complexity of stellar haloes is one of the overarching themes of the work in this thesis. This rich structure is created by hierarchical merging, one of the defining features of galaxy formation in the CDM model. The information encoded by this structure is thus complementary to more basic (and much more easily measured) quantities such as galaxy luminosity, colour and bulge/disc morphology. This information is particularly interesting because it preserves an observable record of the past dynamical history of galaxies. Diagnostics of the assembly history of individual galaxies based on their stellar haloes might help, for example, in understanding the stability of massive discs, and the role of mergers in determining star formation history and morphology. Reading this record will almost certainly be possible, to some extent, in the Milky Way and M31. Unfortunately the stellar haloes of other galaxies are extremely hard to study at a comparable level of detail.

Many nearby early-type galaxies show tidal features (streams, shells and diffuse clouds; van Dokkum 2005; Kaviraj 2010). The challenges and possibilities of recovering useful information from these data have been recognised for many years (e.g. Schweizer & Seitzer 1992). Further progress could be made by collecting larger statistical samples of basic data on these features, quantified in a uniform way. This has proven to be difficult in practice (e.g. Tal et al. 2009). Limited depth will always prevent a full observational 'census' to compare directly with simulations. As we have shown in Chapter 3, the true extent and complexity of a typical Milky Way-like stellar halo only becomes apparent below a V-band surface brightness of $\mu \sim 28\,\mathrm{mag\,arcsec^{-2}}$. This is the limit of the best current integrated-light measurements and requires excellent control of systematic effects.

This limit can be surpassed by resolving individual halo stars. This technique has met with spectacular success in the context of M31 and M33, thanks to the latest generation of wide-field instruments such as MegaCam[1] (McConnachie et al. 2009) and SuprimeCam[2] (Tanaka et al. 2010) – and, of course, to the proximity of these two galaxies. Only the Hubble Space Telescope (HST) is capable of carrying out similar work in more distant (but still, in cosmological terms, very nearby) galaxies (e.g. de Jong et al. 2008). Mapping stellar haloes in the manner of the PANDAS survey of M31 (McConnachie et al. 2009) is practically impossible with the small field of view of HST and is likely to be highly impractical even with JWST[3]. The promised next generation of Extremely Large Telescopes may offer some hope for such a project.

In the short term, it will undoubtedly be useful to develop better statistical techniques for analysing information that is readily obtained – relatively 'shallow' images of faint tidal debris around many galaxies in the low-redshift universe, in the spirit of Schweizer & Seitzer (1992). Simulations such as those in this thesis (also applied to larger samples) should be helpful in calibrating these techniques and interpreting them in relation to other galactic properties.

---

[1] `http://www.cfht.hawaii.edu/Instruments/Imaging/Megacam/`

[2] `http://www.naoj.org/Observing/Instruments/SCam/`

[3] The James Webb Space Telescope

This approach will benefit from realistic mock observations of the simulations that can exploit their full predictive power. Detailed mock catalogues of individual halo stars will be even more important in the study of the Milky Way, where sampling issues can be particularly complex. The simple statistical comparisons we presented in Chapter 4 made very crude assumptions in this respect. In particular we did not account for the fact that the density of particular tracer populations (such as RR Lyrae and BHB stars) depend on age and metallicity (Bell et al. 2010).

To improve on the work we have presented here, we intend to combine our models with the `Galfast` code (developed by M. Jurić et al.). This code will resample the density field of tagged particles in a more sophisticated manner, interpolating each population in space and velocity and drawing individual tracers at each point in the density field from an appropriate combination of isochrones. `Galfast` also allows theoretical or empirical galactic stellar foregrounds to be incorporated in our halo models (Jurić et al. 2008; Ivezić et al. 2008; Bond et al. 2010). We hope to construct tailored mock catalogues for SDSS, PanSTARRS and other current surveys, which can be used to refine statistical techniques for detecting and quantifying substructure.

Given the uncertainties in the current generation of hydrodynamical simulations, hybrid semi-analytic and N-body techniques will continue to be a useful way to study the stellar halo. The power of the semi-analytic method is the ability to rapidly explore the effects of different modelling assumptions. In this thesis we have developed techniques that make it easy to carry out this exploration in the context of the stellar halo. However, we have not yet examined alternatives to our fiducial model, or results from other semi-analytic models that perform well on large-scale data (e.g. Guo et al. 2010a).

The interaction between halo assembly and chemical enrichment (explored in simpler halo models by Robertson et al. 2005; Font et al. 2006a) is a particularly interesting topic that would test the star formation physics in the models. As discussed in Section 1.3.1, [α/Fe] and other chemical abundance ratios are now widely used as diagnostics of the star formation histories of dwarf galaxies and halo populations, and also as 'chemical tags' for separating distinct populations with similar kinematics (e.g. Nissen & Schuster 2010). We are working to include comparable chemical abundance information in our semi-analytic model. We aim to compare the results for different models in the context of dwarf galaxies and stellar haloes.

Many aspects of our hybrid approach to stellar halo simulations could also be improved – in particular, one could adopt other criteria for particle tagging (beyond our selection of the 1% most bound particles in a halo). In principle a semi-analytic model *predicts* the appropriate binding energies of stars (and also their angular momenta). One could make use of this information by adopting a method akin to the weighted distribution function technique of Bullock & Johnston (2005). With such a method, assignment of stars to dark matter could be tied more closely to the structural properties of the galaxies in the semi-analytic model, such as their disc sizes. Making use of this information would eliminate the free parameter we have introduced in our tagging method ($f_{\mathrm{mb}} = 0.01$ in Chapter 2). Apart from the practical difficulties, however, this improvement requires a semi-analytic model that can predict reliable structural properties for the faintest dwarf galaxies – a daunting challenge, as we discuss further below.

Higher resolution and a closer coupling between the galaxy model and the simulation could also be achieved by seeding test particles directly into the N-body integration, based on a 'first pass' with the semi-analytic model (fully coupling a semi-analytic code and an N-body simulation remains a more distant goal). Such improvements may be necessary to apply this technique to the study of diffuse light in high-resolution cluster simulations, where massive baryon-dominated galaxies are being stripped.

However, the most pressing issue in the current debate about the nature of the stellar halo concerns the extent to which observational samples are dominated by halo stars formed 'in situ'. As described in the following section, clarifying this point is at least as important as improving models of the accreted halo.

6.2.2 The contribution of in situ halo stars

Although we have focused on the process of stellar accretion in this thesis, we have not argued that this process alone is sufficient to build the entire stellar halo. It is clear that populations of stars on eccentric orbits can arise in a variety of ways, and there is no reason to expect that only one of these has been active in the Milky Way and M31. Nevertheless, as we demonstrated in Chapter 5, although in situ star formation is not strictly required to build structurally and kinematically complex haloes consistent with observations. In Section 1.3.1 we briefly described the two mechanisms for in situ halo growth, disc disruption and extragalactic star formation. Until well-constrained estimates can be made of the importance of these contributions, it is not clear how much weight should be given to results such as ours, based on the accreted stars alone.

Quantifying in situ star formation is therefore a crucial outstanding issue in the study of galactic stellar haloes. This problem is much harder than the simple gravitational dynamics of satellite accretion. Hydrodynamical simulations seem the natural way to proceed, although they suffer from substantial uncertainties in the implementation of the relevant physics[4]. No simulation has yet reached the resolution at which halo and satellite structure can be fully resolved with robust numerical convergence. The push to higher resolution will present more challenges. For example, experience has show that it is all too easy for such simulations to form 'spurious' stars on 'halo' orbits through numerically-seeded instabilities and the unintended consequences of subgrid models for star formation and feedback. Only $\sim 1\%$ of the stars in a Milky Way-scale simulation will belong to the stellar halo, demanding that the number of erroneous stars be reduced even below this low level. Finally, we note that attempts to distinguish between different formation scenarios for the thick disc (e.g. Sales et al. 2009) suggest one way to make progress may be to explore the kinematic signatures of in situ stars in the simulations[5].

Having questioned our models of the stellar halo, we now turn to some important uncertainties in the underlying model of galaxy formation and some interesting directions for related work.

6.2.3 Do CDM models produce an acceptable satellite population?

The satellite luminosity function of Milky Way-like galaxies is a strong constraint on the CDM model, so long as the data themselves are well understood. In Chapter 2 we demonstrated an adequate (though far from 'perfect') match to the observed luminosity function of Koposov et al. (2008), using the Bower et al. (2006) semi-analytic model[6]. We used this agreement to argue for the plausibility of our stellar halo model. However, this apparent success of CDM and Bower et al. (2006) can be challenged on several grounds.

Firstly, all current models claiming to produce an 'acceptable' satellite luminosity function assume that the Milky Way system is representative of haloes of its assumed mass. At the faint end of this luminosity function (which is only constrained by Milky Way data), the extrapolation from the actual observations is severe (up to two orders of magnitude) and based on uncertain assumptions about the surface brightness and radial distribution of dwarf galaxies. At the bright end it is usually assumed that the *mean* of the Milky Way and M31 systems is representative (at least by studies comparing to Koposov et al. 2008). The data here are taken to be essentially complete. However, the Milky Way and M31 satellite systems differ substan-

---

[4] For example, the simulations of Zolotov et al. (2009) have unrealistically high baryon fractions. These authors still find a limited contribution from in situ halo stars.

[5] We also note that Morrison et al. (2009) use the high degree of clustering in angular momentum space of nearby halo stars on highly eccentric orbits to argue against a substantial smooth component.

[6] Modified in accord with recent estimates of an ionizing background on gas accretion and cooling in small haloes

tially from one another (e.g. McConnachie & Irwin 2006; Martin et al. 2009). Furthermore the dark halo masses of the two galaxies remain uncertain, as we discussed in Chapter 5, and it is likely that the absolute abundance of satellites depends to some extent on halo mass. It is not yet clear that matching the shape and normalization of the composite MW/M31 satellite luminosity function is a reliable and well-constrained calibration for the models. More data on the satellite systems of other Milky Way-like galaxies will be particularly helpful in addition to tighter constraints on the Milky Way and M31 dark halo properties.

With the above caveat, semi-analytic (and now hydrodynamic) modelling has shown that populating the right *number* of dark subhaloes with satellites of a given luminosity is not a problem for the CDM model. However, whether or not this agreement is robust and meaningful awaits further, more rigorous investigation. Aside from the cut-off imposed by galaxy formation physics in very small subhaloes, the present agreement between subhalo and satellite abundances[7] is a manifestation of the fact that current models (both semi-analytic and SPH) assign the highest luminosities to those subhaloes that attain the highest masses over their lifetimes. In other words, luminosity and 'peak mass' are more-or-less matched in rank order. In observational terms, the models predict that the brightest satellites should live in haloes with rotation curves peaking at the highest velocities (V_{max}), or (almost) equivalently, those with the highest velocity dispersions (σ). This strong prediction cannot be tested by comparing number counts alone.

Presently only the Fornax dwarf has a constrained V_{max}, of $\sim 20\,\mathrm{km\,s^{-1}}$, obtained from the kinematics of individual stars in data from radii (possibly) beyond the peak circular velocity (Walker et al. 2009a). Importantly, this value is far lower than that of $\sim 40\,\mathrm{km\,s^{-1}}$ predicted by models that match the abundances of subhaloes, such as the model we presented in Chapter 2. Taking this result at face value raises an immediate problem for CDM. If all subhaloes of $\sim 20\,\mathrm{km\,s^{-1}}$ in a simulation like Aquarius were associated with galaxies as luminous as Fornax, then the resulting luminosity function would be in clear disagreement with the data. Furthermore, many haloes *more* massive than this are present in the model, raising the additional problem of why these did not form galaxies even more luminous than Fornax.

This 'mismatch' breaks the correspondence between halo mass and luminosity that has been well-established (at least theoretically) on larger scales (Guo et al. 2010b). In both hydrodynamical and semi-analytic models, galaxy luminosity is found to increase monotonically with the peak circular velocity of a dark matter halo. In the context of CDM galaxy formation,

---

[7] As discussed for example in a recent review by Kravtsov (2010)

there is no obvious mechanism for producing stochastic variations in the luminosities of dwarf galaxies large enough to explain the low circular velocity of Fornax[8].

This discrepancy was highlighted in Chapter 2 (Fig. 2.3). Even our simple 'most-bound particles' model of the distribution of stars in dwarf galaxies could reproduce the shape of the Fornax surface brightness profile for a large number of simulated galaxies. However, only satellite haloes heavily stripped of their dark matter could match *simultaneously* the normalization of this profile and the velocity dispersion profile of Fornax measured by Walker et al. (2009a). In our models, this severe tidal stripping lowered the velocity dispersion of a $\sim 40\,\mathrm{km\,s^{-1}}$ halo to $\sim 20\,\mathrm{km\,s^{-1}}$ without affecting the surface brightness of its stars. There is currently no compelling observational evidence for Fornax having been stripped in this manner, although this merits further investigation.

A similar unexplained discrepancy concerns the tilt in the relation between the mass within the inner $300\,\mathrm{pc}$ of dwarf galaxies and their total luminosity, shown in Fig. 2.6. This tilt is present in almost all published models and is absent in the data[9]. At face value it implies a similar problem to the kinematic measurements discussed above: the relationship between halo mass and luminosity in the models is in disagreement with the apparent mass of the halo of Fornax.

Of course, very little can be concluded from one observation. The discrepancy with the predictions of CDM may be due to some peculiarity of Fornax itself, or the observations (such as unrecognised stripping, or a breakdown of the assumptions of the Jeans modelling used to derive dark halo properties from stellar kinematics). This issue highlights the important role that *individual* dwarf galaxies like Fornax now play in efforts to constrain CDM. Unfortunately the modelling uncertainties are also substantial: as we discuss below, it is unlikely that any current model accurately represents the physics governing star formation in dwarf galaxies.

6.2.4 The margins of galaxy formation

On the scale of dwarf galaxies, important aspects of the physics of star formation may be missing from current semi-analytic and hydrodynamic models. These models treat star formation in dwarf galaxies in the same globally-averaged (subgrid) manner to larger galaxies, and ignore small scale effects relevant to individual star-forming regions. These small scale effects may

---

[8] One possibility is to appeal to highly inhomogeneous local reionization in the early universe, or other modes of localised suppression such as feedback from the first stars.

[9] M_{300} may not the most useful diagnostic of this 'problem': Wolf et al. (2010); Walker et al. (2010); McGaugh & Wolf (2010)

'average out' in models of massive galaxies, but they could easily leave an imprint on dwarf galaxies (some of which have stellar masses equivalent to only a handful of large molecular clouds in the Milky Way). Environmental effects are also mostly unaccounted for, including feedback from the first stars and an enhanced 'local' background of ionizing photons in the regions surrounding the first galaxies. These effects may have created more inhomogeneity in the Milky Way and M31 dwarf galaxy populations than models currently predict.

Together with their star formation histories, the morphological properties of dwarf irregular and dwarf spheroidal galaxies in the Local Group (beyond the Milky Way and M31 systems) could be a strong test of the treatment of faint galaxies in simulations. The dwarf irregulars show clumpy, thick discs with patchy star formation (e.g. Roychowdhury et al. 2010). The cause of their (supposed) transformation to dwarf spheroidals (widely believed to be related to tidal interactions) has still not been conclusively identified.

Despite their apparent 'simplicity', to date these galaxies have been studied by only a handful of hydrodynamical models[10] (e.g. Revaz et al. 2009; Sawala et al. 2010a,b). One possible reason for this is that the observational data are somewhat limited. This situation should improve rapidly as interest in nearby galaxies increases and more examples are discovered by deep large-area surveys. Given the centre-stage position occupied by the Milky Way and M31 satellites in recent debates about CDM, it is surprising that their cousins '*outside* the virial radius' have received so little attention.

6.2.5 The globular cluster connection

Finally, as we have already noted in Chapter 3, galactic globular cluster (GC) systems are curious 'doppelgangers' of stellar haloes. They share similar spatial and kinematic distributions and can be subdivided in a similar manner (Zinn 1993). The theory of the formation of individual globular clusters (and GC systems) has a long and complex (and largely inconclusive) history, dominated by the dichotomy between in situ formation and accretion, again in parallel to debates about the halo. GCs are of particular interest in the context of this thesis because, from a practical point of view, their luminosity functions, colours and radial distributions can be quantified in distant galaxies more easily than diffuse haloes and other tidal features. With a better understanding of their role as tracers of hierarchical assembly, the statistical 'archaeology' of globular clusters could be a powerful means of constraining CDM structure formation.

---

[10] To our knowledge, dIrrs in the Local Group have been ignored by all semi-analytic models.

The debate over the processes governing the formation and survival of GCs obscures their usefulness as probes of galaxy formation. Typical models of in situ GC formation mirror the 'extragalactic star formation' mechanisms we outlined for halo stars in Section 1.3.1 – namely instabilities in a halo cooling flow and starbursts triggered in gas-rich mergers. However, it is not at all clear whether clusters produced in this way will survive over a Hubble time, or if the resulting GC population would be consistent with any subset of the GCs in the Milky Way. The stellar dynamics (and hydrodynamics) of these extreme systems are much studied but still very poorly understood (in a cosmological context). Given these uncertainties, it would be interesting to ask what role the accretion of 'primordial' clusters from progenitor galaxies plays in determining the properties of the GC system in a galaxy like the Milky Way (or, indeed, a galaxy like the LMC), and how these accreted GC systems relate to the stellar halo.

Most dwarf galaxies more massive than Fornax contain one or more globular clusters (Fornax itself hosts five clusters, an unusually high abundance for its luminosity). Given the simple star formation histories of these dwarf galaxies and their limited number of hierarchical progenitors, they seem to be the best systems in which to study cluster formation. As discussed in Chapter 3, analogues (but not identical twins) of these galaxies are the building blocks of the stellar halo, so it is reasonable to assume that some fraction of the GC population is a relic of hierarchical assembly rather than in situ formation (e.g. Lynden-Bell & Lynden-Bell 1995; Mackey & Gilmore 2004). For example, Bellazzini et al. (2003) find evidence that the disrupting Sagittarius dwarf is contributing clusters to the Milky Way halo and Mackey et al. (2010) show that groups of GCs around M31 are associated with extensive overdensities and streams of halo stars. With an improved understanding of (or at least, simple hypotheses for) the formation of 'primordial' clusters in dwarf galaxies, it should be possible to construct models of this accreted GC population. Such models can now be compared against a wealth of data from a wide variety of galactic environments, from the Fornax dwarf to the Fornax cluster.

6.3 Conclusion

In the concordance CDM cosmogony, most galaxies are small and mergers between galaxies are important. In this thesis, we have addressed the nature of the faintest galaxies and simulated their disruption in the potential wells of larger galaxies like the Milky Way. Observations have revealed first-hand evidence of this hierarchical assembly in the Milky Way and its neighbours. New perspectives on the dynamical nature of CDM galaxy formation are emerging rapidly from the faint stellar systems at is margins – galactic stellar haloes, dwarf galaxies and globular clusters. The field of galactic archaeology seeks to tie together these different strands of evidence and reconstruct the assembly history of the Milky Way and other nearby galaxies, opening a local window into the high-redshift universe. Progress in this field requires the synthesis of data across a huge range of scales, from the Solar neighbourhood to the Local Group and beyond. Our simulations have demonstrated that accreted stellar haloes are richly-structured and diverse systems: excellent hunting-grounds in which to search for archaeological insights into galactic evolution. Further simulations in a cosmological context will be vital tools for interpreting the extremely complex picture of our own Galaxy that observations are already painting, soon to be revolutionised once more by *Gaia*. We stand on the brink of answering the fundamental questions about galactic assembly raised by Searle & Zinn more than three decades ago.

Bibliography

Abadi M. G., Navarro J. F., Fardal M., Babul A., Steinmetz M., 2010, MNRAS, 407, 435

Abadi M. G., Navarro J. F., Steinmetz M., 2006, MNRAS, 365, 747

—, 2009, ApJ, 691,

Abadi M. G., Navarro J. F., Steinmetz M., Eke V. R., 2003a, ApJ, 591, 499

—, 2003b, ApJ, 597, 21

Adén D., Wilkinson M. I., Read J. I., Feltzing S., Koch A., Gilmore G. F., Grebel E. K., Lundström I., 2009, ApJ, 706,

Allgood B., Flores R. A., Primack J. R., Kravtsov A. V., Wechsler R. H., Faltenbacher A., Bullock J. S., 2006, MNRAS, 367, 1781

Baade W., 1944, ApJ, 100, 137

Bahcall N. A., Soneira R. M., 1983, ApJ, 270, 20

Barker M. K., Ferguson A. M. N., Irwin M., Arimoto N., Jablonka P., 2009, AJ, 138, 1469

Battaglia G., Helmi A., Morrison H., Harding P., Olszewski E. W., Mateo M., Freeman K. C., Norris J., Shectman S. A., 2005, MNRAS, 364, 433

Baugh C. M., 2006, Reports on Progress in Physics, 69, 3101

Baugh C. M., Lacey C. G., Frenk C. S., Granato G. L., Silva L., Bressan A., Benson A. J., Cole S., 2005, MNRAS, 356, 1191

Beers T. C., Christlieb N., 2005, ARA&A, 43, 531

Bekki K., Chiba M., 2001, ApJ, 558, 666

Bell E. F., Xue X. X., Rix H. W., Ruhland C., Hogg D. W., 2010, ArXiv e-prints, astro-ph/1010.2239

Bell E. F., Zucker D. B., Belokurov V., Sharma S., Johnston K. V., Bullock J. S., Hogg D. W., Jahnke K., de Jong J. T. A., Beers T. C., Evans N. W., Grebel E. K., Ivezić v. Z., Koposov S. E., Rix H. W., Schneider D. P., Steinmetz M., Zolotov A., 2008, ApJ, 680, 295

Bellazzini M., Ferraro F. R., Ibata R., 2003, AJ, 125, 188

Belokurov V., Evans N. W., Bell E. F., Irwin M. J., Hewett P. C., Koposov S., Rockosi C. M., Gilmore G., Zucker D. B., Fellhauer M., Wilkinson M. I., Bramich D. M., Vidrih S., Rix H. W., Beers T. C., Schneider D. P., Barentine J. C., Brewington H., Brinkmann J., Harvanek M., Krzesinski J., Long D., Pan K., Snedden S. A., Malanushenko O., Malanushenko V., 2007a, ApJ, 657, L89

Belokurov V., Evans N. W., Irwin M. J., Lynden-Bell D., Yanny B., Vidrih S., Gilmore G., Seabroke G., Zucker D. B., Wilkinson M. I., Hewett P. C., Bramich D. M., Fellhauer M., Newberg H. J., Wyse R. F. G., Beers T. C., Bell E. F., Barentine J. C., Brinkmann J., Cole N., Pan K., York D. G., 2007b, ApJ, 658, 337

Belokurov V., Walker M. G., Evans N. W., Gilmore G., Irwin M. J., Just D., Koposov S., Mateo M., Olszewski E., Watkins L., Wyrzykowski L., 2010, ApJ, 712,

Belokurov V., Zucker D. B., Evans N. W., Gilmore G., Vidrih S., Bramich D. M., Newberg H. J., Wyse R. F. G., Irwin M. J., Fellhauer M., Hewett P. C., Walton N. A., Wilkinson M. I., Cole N., Yanny B., Rockosi C. M., Beers T. C., Bell E. F., Brinkmann J., Ivezić v. Z., Lupton R., 2006, ApJ, 642, L137

Benson A. J., 2010, ArXiv e-prints, astro-ph/1006.5394

Benson A. J., Bower R., 2010, MNRAS, 405, 1573

Benson A. J., Bower R. G., Frenk C. S., Lacey C. G., Baugh C. M., Cole S., 2003, ApJ, 599, 38

Benson A. J., Frenk C. S., Lacey C. G., Baugh C. M., Cole S., 2002a, MNRAS, 333, 177

Benson A. J., Lacey C. G., Baugh C. M., Cole S., Frenk C. S., 2002b, MNRAS, 333, 156

Benson A. J., Lacey C. G., Frenk C. S., Baugh C. M., Cole S., 2004, MNRAS, 351, 1215

Binney J., Tremaine S., 1987, Galactic dynamics. Princeton University Press

Bond J. R., Cole S., Efstathiou G., Kaiser N., 1991, ApJ, 379, 440

Bond N. A., Ivezić v. Z., Sesar B., Jurić M., Munn J. A., Kowalski A., Loebman S., Roˇ skar R., Beers T. C., Dalcanton J., Rockosi C. M., Yanny B., Newberg H. J., Allende Prieto C., Wilhelm R., Lee Y. S., Sivarani T., Majewski S. R., Norris J. E., Bailer-Jones C. A. L., Re Fiorentin P., Schlegel D., Uomoto A., Lupton R. H., Knapp G. R., Gunn J. E., Covey K. R., Allyn Smith J., Miknaitis G., Doi M., Tanaka M., Fukugita M., Kent S., Finkbeiner D., Quinn T. R., Hawley S., Anderson S., Kiuchi F., Chen A., Bushong J., Sohi H., Haggard D., Kimball A., McGurk R., Barentine J., Brewington H., Harvanek M., Kleinman S., Krzesinski J., Long D., Nitta A., Snedden S., Lee B., Pier J. R., Harris H., Brinkmann J., Schneider D. P., 2010, ApJ, 716, 1

Bower R. G., 1991, MNRAS, 248, 332

Bower R. G., Benson A. J., Malbon R., Helly J. C., Frenk C. S., Baugh C. M., Cole S., Lacey C. G., 2006, MNRAS, 370, 645

Boylan-Kolchin M., Springel V., White S. D. M., Jenkins A., 2010, MNRAS, 406, 896

Boylan-Kolchin M., Springel V., White S. D. M., Jenkins A., Lemson G., 2009, MNRAS, 398, 1150

Bromm V., Larson R. B., 2004, ARA&A, 42, 79

Brown A. G. A., Velázquez H. M., Aguilar L. A., 2005, MNRAS, 359, 1287

Brown W. R., Geller M. J., Kenyon S. J., Beers T. C., Kurtz M. J., Roll J. B., 2004, AJ, 127, 1555

Brown W. R., Geller M. J., Kenyon S. J., Diaferio A., 2010, AJ, 139, 59

Bullock J. S., Johnston K. V., 2005, ApJ, 635, 931

Bullock J. S., Kravtsov A. V., Weinberg D. H., 2001, ApJ, 548, 33

Bullock J. S., Stewart K. R., Kaplinghat M., Tollerud E. J., Wolf J., 2010, ApJ, 717, 1043

Busha M. T., Alvarez M. A., Wechsler R. H., Abel T., Strigari L. E., 2009, ArXiv e-prints, astro-ph/0901.3553

Carollo D., Beers T. C., Chiba M., Norris J. E., Freeman K. C., Lee Y. S., Ivezić v. Z., Rockosi C. M., Yanny B., 2010, ApJ, 712, 692

Carollo D., Beers T. C., Chiba M., Norris J. E., Freeman K. C., Lee Y. S., Ivezic Z., Rockosi C. M., Yanny B., 2009, ArXiv e-prints, astro-ph/0909.3019

Carollo D., Beers T. C., Lee Y. S., Chiba M., Norris J. E., Wilhelm R., Sivarani T., Marsteller B., Munn J. A., Bailer-Jones C. A. L., Fiorentin P. R., York D. G., 2007, Nature, 450, 1020

Chabrier G., Baraffe I., Allard F., Hauschildt P., 2000, ApJ, 542, 464

Chapman S. C., Ibata R., Irwin M., Koch A., Letarte B., Martin N., Collins M., Lewis G. F., McConnachie A., Peñarrubia J., Rich R. M., Trethewey D., Ferguson A., Huxor A., Tanvir N., 2008, MNRAS, 390, 1437

Chiba M., Beers T. C., 2000, AJ, 119, 2843

—, 2001, ApJ, 549, 325

Christlieb N., Schörck T., Frebel A., Beers T. C., Wisotzki L., Reimers D., 2008, A&A, 484, 721

Cole S., 1991, ApJ, 367, 45

Cole S., Helly J., Frenk C. S., Parkinson H., 2008, MNRAS, 383, 546

Cole S., Lacey C., 1996, MNRAS, 281, 716

Cole S., Lacey C. G., Baugh C. M., Frenk C. S., 2000, MNRAS, 319, 168

Collins M. L. M., Chapman S. C., Ibata R. A., Irwin M. J., Rich R. M., Ferguson A. M. N., Lewis G. F., Tanvir N., Koch A., 2010, ArXiv e-prints, astro-ph/1010.5276

Couchman H. M. P., Rees M. J., 1986, MNRAS, 221, 53

Croton D. J., Springel V., White S. D. M., De Lucia G., Frenk C. S., Gao L., Jenkins A., Kauffmann G., Navarro J. F., Yoshida N., 2006, MNRAS, 365, 11

Davis M., Efstathiou G., Frenk C. S., White S. D. M., 1985, ApJ, 292, 371

de Jong J. T. A., Yanny B., Rix H. W., Dolphin A. E., Martin N. F., Beers T. C., 2010, ApJ, 714, 663

de Jong R. S., Radburn-Smith D. J., Sick J. N., 2008, in Astronomical Society of the Pacific Conference Series, Vol. 396, Formation and Evolution of Galaxy Disks, Funes J. G., Corsini E. M., eds., p. 187

De Lucia G., Helmi A., 2008, MNRAS, 391, 14

De Lucia G., Springel V., White S. D. M., Croton D., Kauffmann G., 2006, MNRAS, 366, 499

Deason A. J., Belokurov V., Evans N. W., 2010, ArXiv e-prints, astro-ph/1008.3067

Dehnen W., McLaughlin D. E., Sachania J., 2006, MNRAS, 369, 1688

Doinidis S. P., Beers T. C., 1989, ApJ, 340,

Du C., Ma J., Wu Z., Zhou X., 2006, MNRAS, 372, 1304

Eggen O. J., Lynden-Bell D., Sandage A. R., 1962, ApJ, 136, 748

Fall S. M., Efstathiou G., 1980, MNRAS, 193, 189

Faúndez-Abans M., Reshetnikov V. P., de Oliveira-Abans M., Fernandes I. F., 2009, Astronomy Letters, 35, 25

Fellhauer M., Belokurov V., Evans N. W., Wilkinson M. I., Zucker D. B., Gilmore G., Irwin M. J., Bramich D. M., Vidrih S., Wyse R. F. G., Beers T. C., Brinkmann J., 2006, ApJ, 651, 167

Ferguson A. M. N., Irwin M. J., Ibata R. A., Lewis G. F., Tanvir N. R., 2002, AJ, 124, 1452

Flynn C., Holmberg J., Portinari L., Fuchs B., Jahreiß H., 2006, MNRAS, 372, 1149

Font A. S., Bower R. G., McCarthy I. G., Benson A. J., Frenk C. S., Helly J. C., Lacey C. G., Baugh C. M., Cole S., 2008, MNRAS, 389, 1619

Font A. S., Johnston K. V., Bullock J. S., Robertson B. E., 2006a, ApJ, 638, 585

—, 2006b, ApJ, 646, 886

Font A. S., Navarro J. F., Stadel J., Quinn T., 2001, ApJ, 563, L1

Forbes D. A., Strader J., Brodie J. P., 2004, AJ, 127, 3394

Frebel A., Kirby E. N., Simon J. D., 2010a, Nature, 464, 72

Frebel A., Simon J. D., Geha M., Willman B., 2010b, ApJ, 708, 560

Freeman K., Bland-Hawthorn J., 2002, ARA&A, 40, 487

Frenk C. S., White S. D. M., 1980, MNRAS, 193, 295

Fuchs B., Jahreiß H., 1998, A&A, 329, 81

Fulbright J. P., 2002, AJ, 123, 404

Galleti S., Bellazzini M., Federici L., Buzzoni A., Fusi Pecci F., 2007, A&A, 471, 127

Galleti S., Federici L., Bellazzini M., Buzzoni A., Fusi Pecci F., 2006, A&A, 456, 985

Galleti S., Federici L., Bellazzini M., Fusi Pecci F., Macrina S., 2004, A&A, 416, 917

Gao L., Theuns T., Frenk C. S., Jenkins A., Helly J. C., Navarro J., Springel V., White S. D. M., 2010, MNRAS, 403, 1283

Gilmore G., Reid N., 1983, MNRAS, 202, 1025

Gilmore G., Wyse R. F. G., 1991, ApJ, 367,

—, 1998, AJ, 116, 748

Gnedin N. Y., 2000, ApJ, 542, 535

Gnedin O. Y., Brown W. R., Geller M. J., Kenyon S. J., 2010, ApJ, 720,

Gould A., 2003, ApJ, 592,

Gould A., Flynn C., Bahcall J. N., 1998, ApJ, 503, 798

Grebel E. K., Gallagher I. I. I. . J. S., Harbeck D., 2003, AJ, 125, 1926

Guo Q., White S., Boylan-Kolchin M., De Lucia G., Kauffmann G., Lemson G., Li C., Springel V., Weinmann S., 2010a, ArXiv e-prints, astro-ph/1006.0106

Guo Q., White S., Li C., Boylan-Kolchin M., 2010b, MNRAS, 404, 1111

Guth A. H., 1981, Phys. Rev. D, 23, 347

Harding P., Morrison H. L., Olszewski E. W., Arabadjis J., Mateo M., Dohm-Palmer R. C., Freeman K. C., Norris J. E., 2001, AJ, 122, 1397

Harris W. E., 1996, AJ, 112, 1487

Hatton S., Devriendt J. E. G., Ninin S., Bouchet F. R., Guiderdoni B., Vibert D., 2003, MNRAS, 343, 75

Helly J. C., Cole S., Frenk C. S., Baugh C. M., Benson A., Lacey C., 2003, MNRAS, 338, 903

Helmi A., 2008, A&A Rev., 15, 145

Helmi A., de Zeeuw P. T., 2000, MNRAS, 319, 657

Helmi A., Irwin M. J., Tolstoy E., Battaglia G., Hill V., Jablonka P., Venn K., Shetrone M., Letarte B., Arimoto N., Abel T., Francois P., Kaufer A., Primas F., Sadakane K., Szeifert T., 2006, ApJ, 651, L121

Helmi A., White S. D. M., 1999, MNRAS, 307, 495

Hodge P. W., 1961, AJ, 66, 83

Hoeft M., Yepes G., Gottlöber S., Springel V., 2006, MNRAS, 371, 401

Hofmann S., Schwarz D. J., Stöcker H., 2001, Phys. Rev. D, 64, 083507

Huxor A. P., Tanvir N. R., Ferguson A. M. N., Irwin M. J., Ibata R., Bridges T., Lewis G. F., 2008, MNRAS, 385, 1989

Ibata R., Chapman S., Ferguson A. M. N., Lewis G., Irwin M., Tanvir N., 2005, ApJ, 634, 287

Ibata R., Irwin M., Lewis G., Ferguson A. M. N., Tanvir N., 2001a, Nature, 412, 49

Ibata R., Irwin M., Lewis G. F., Stolte A., 2001b, ApJ, 547, L133

Ibata R., Martin N. F., Irwin M., Chapman S., Ferguson A. M. N., Lewis G. F., McConnachie A. W., 2007, ApJ, 671, 1591

Ibata R., Mouhcine M., Rejkuba M., 2009, MNRAS, 395, 126

Ibata R. A., Gilmore G., Irwin M. J., 1994, Nature, 370, 194

Ibata R. A., Irwin M. J., Lewis G. F., Ferguson A. M. N., Tanvir N., 2003, MNRAS, 340,

Irwin M., Hatzidimitriou D., 1995, MNRAS, 277, 1354

Irwin M. J., Ferguson A. M. N., Ibata R. A., Lewis G. F., Tanvir N. R., 2005, ApJ, 628, L105

Ishigaki M., Chiba M., Aoki W., 2010, PASJ, 62, 143

Ivans I. I., Sneden C., James C. R., Preston G. W., Fulbright J. P., Höflich P. A., Carney B. W., Wheeler J. C., 2003, ApJ, 592, 906

Ivezić v. Z., Goldston J., Finlator K., Knapp G. R., Yanny B., McKay T. A., Amrose S., Krisciunas K., Willman B., Anderson S., Schaber C., Erb D., Logan C., Stubbs C., Chen B., Neilsen E., Uomoto A., Pier J. R., Fan X., Gunn J. E., Lupton R. H., Rockosi C. M., Schlegel D., Strauss M. A., Annis J., Brinkmann J., Csabai I., Doi M., Fukugita M., Hennessy G. S., Hindsley R. B., Margon B., Munn J. A., Newberg H. J., Schneider D. P., Smith J. A., Szokoly G. P., Thakar A. R., Vogeley M. S., Waddell P., Yasuda N., York D. G., 2000, AJ, 120, 963

Ivezić v. Z., Sesar B., Jurić M., Bond N., Dalcanton J., Rockosi C. M., Yanny B., Newberg H. J., Beers T. C., Allende Prieto C., Wilhelm R., Lee Y. S., Sivarani T., Norris J. E., Bailer-Jones C. A. L., Re Fiorentin P., Schlegel D., Uomoto A., Lupton R. H., Knapp G. R., Gunn J. E., Covey K. R., Smith J. A., Miknaitis G., Doi M., Tanaka M., Fukugita M., Kent S., Finkbeiner D., Munn J. A., Pier J. R., Quinn T., Hawley S., Anderson S., Kiuchi F., Chen A., Bushong J., Sohi H., Haggard D., Kimball A., Barentine J., Brewington H., Harvanek M., Kleinman S., Krzesinski J., Long D., Nitta A., Snedden S., Lee B., Harris H., Brinkmann J., Schneider D. P., York D. G., 2008, ApJ, 684, 287

Ivezic Z., Tyson J. A., Allsman R., Andrew J., Angel R., Collaboration f. t. L., 2008, ArXiv e-prints, astro-ph/0805.2366

Johnston K. V., Bullock J. S., Sharma S., Font A., Robertson B. E., Leitner S. N., 2008, ApJ, 689, 936

Johnston K. V., Hernquist L., Bolte M., 1996, ApJ, 465, 278

Jurić M., Ivezić v. Z., Brooks A., Lupton R. H., Schlegel D., Finkbeiner D., Padmanabhan N., Bond N., Sesar B., Rockosi C. M., Knapp G. R., Gunn J. E., Sumi T., Schneider D. P., Barentine J. C., Brewington H. J., Brinkmann J., Fukugita M., Harvanek M., Kleinman S. J., Krzesinski J., Long D., Neilsen Jr. . E. H., Nitta A., Snedden S. A., York D. G., 2008, ApJ, 673, 864

Kalirai J. S., Gilbert K. M., Guhathakurta P., Majewski S. R., Ostheimer J. C., Rich R. M., Cooper M. C., Reitzel D. B., Patterson R. J., 2006, ApJ, 648, 389

Kang X., Jing Y. P., Mo H. J., Börner G., 2005, ApJ, 631, 21

Kant I., 1755, Allgemeine Naturgeschichte und Theorie des Himmels, Vol. 1. J. F. Peterson, Königsberg and Leipzig

Kapteyn J. C., 1922, ApJ, 55, 302

Kapteyn J. C., van Rhijn P. J., 1922, ApJ, 55, 242

Kauffmann G., Colberg J. M., Diaferio A., White S. D. M., 1999, MNRAS, 303, 188

Kauffmann G., White S. D. M., Guiderdoni B., 1993, MNRAS, 264, 201

Kautsch S. J., Grebel E. K., Barazza F. D., Gallagher I. I. I. . J. S., 2006, åp, 445, 765

Kaviraj S., 2010, MNRAS, 406, 382

Kazantzidis S., Bullock J. S., Zentner A. R., Kravtsov A. V., Moustakas L. A., 2008, ApJ, 688, 254

Kim S. C., Lee M. G., Geisler D., Sarajedini A., Park H. S., Hwang H. S., Harris W. E., Seguel J. C., von Hippel T., 2007, AJ, 134, 706

Kirby E. N., Simon J. D., Geha M., Guhathakurta P., Frebel A., 2008, ApJ, 685, L43

Klement R. J., 2010, åpr, 9

Klypin A., Kravtsov A. V., Valenzuela O., Prada F., 1999, ApJ, 522, 82

Koch A., Rich R. M., Reitzel D. B., Martin N. F., Ibata R. A., Chapman S. C., Majewski S. R., Mori M., Loh Y. S., Ostheimer J. C., Tanaka M., 2008, ApJ, 689, 958

Kollmeier J. A., Gould A., Shectman S., Thompson I. B., Preston G. W., Simon J. D., Crane J. D., Ivezić v. Z., Sesar B., 2009, ApJ, 705,

Komatsu E., Dunkley J., Nolta M. R., Bennett C. L., Gold B., Hinshaw G., Jarosik N., Larson D., Limon M., Page L., Spergel D. N., Halpern M., Hill R. S., Kogut A., Meyer S. S., Tucker G. S., Weiland J. L., Wollack E., Wright E. L., 2009, ApJS, 180, 330

Koposov S., Belokurov V., Evans N. W., Hewett P. C., Irwin M. J., Gilmore G., Zucker D. B., Rix H. W., Fellhauer M., Bell E. F., Glushkova E. V., 2008, ApJ, 686, 279

Koposov S. E., Yoo J., Rix H. W., Weinberg D. H., Macciò A. V., Escudé J. M., 2009, ApJ, 696, 2179

Kormendy J., Kennicutt Jr. . R. C., 2004, ARA&A, 42, 603

Kravtsov A., 2010, Advances in Astronomy, 2010

Lacey C., Cole S., 1993, MNRAS, 262, 627

—, 1994, MNRAS, 271, 676

Larson D., Dunkley J., Hinshaw G., Komatsu E., Nolta M. R., Bennett C. L., Gold B., Halpern M., Hill R. S., Jarosik N., Kogut A., Limon M., Meyer S. S., Odegard N., Page L., Smith K. M., Spergel D. N., Tucker G. S., Weiland J. L., Wollack E., Wright E. L., 2010, ArXiv e-prints, astro-ph/1001.4635

Larson R. B., 1974, MNRAS, 169, 229

Law D. R., Johnston K. V., Majewski S. R., 2005, ApJ, 619, 807

Layden A. C., Sarajedini A., 2000, AJ, 119, 1760

Lemon D. J., Wyse R. F. G., Liske J., Driver S. P., Horne K., 2004, MNRAS, 347, 1043

Leonard P. J. T., Tremaine S., 1990, ApJ, 353, 486

Li Y.-S., De Lucia G., Helmi A., 2009a, ArXiv e-prints, astro-ph/0909.1291

—, 2010, MNRAS, 401, 2036

Li Y.-S., Helmi A., 2008, MNRAS, 385, 1365

Li Y.-S., Helmi A., De Lucia G., Stoehr F., 2009b, MNRAS, 397,

Li Y.-S., White S. D. M., 2008, MNRAS, 384, 1459

Libeskind N. I., Frenk C. S., Cole S., Helly J. C., Jenkins A., Navarro J. F., Power C., 2005, MNRAS, 363, 146

Lindblad B., 1925, Arkiv f. Mat.ematik, Astr. o. Fysik, 19A

—, 1927, MNRAS, 87, 553

Lovell M., Eke V., Frenk C., Jenkins A., 2010, ArXiv e-prints, astro-ph/1008.0484

Lowing B., Jenkins A., Eke V., Frenk C., 2010, ArXiv e-prints, astro-ph/1010.6197

Lynden-Bell D., Lynden-Bell R. M., 1995, MNRAS, 275, 429

Macciò A. V., Kang X., Moore B., 2009, ApJ, 692, L109

Maciejewski M., Colombi S., Alard C., Bouchet F., Pichon C., 2009, MNRAS, 393, 703

Mackey A. D., Gilmore G. F., 2004, MNRAS, 355, 504

Mackey D., Huxor A., Ferguson A., Irwin M., Tanvir N., McConnachie A., Ibata R., Chapman S., Lewis G., 2010, ArXiv e-prints, astro-ph/1005.3812

Majewski S. R., 1993, ARA&A, 31, 575

Malin D., Hadley B., 1999, in Astronomical Society of the Pacific Conference Series, Vol. 182, Galaxy Dynamics - A Rutgers Symposium, D. R. Merritt M. Valluri . J. A. S., ed., p. 445

Marigo P., Girardi L., Bressan A., Groenewegen M. A. T., Silva L., Granato G. L., 2008, åp, 482, 883

Martin N. F., de Jong J. T. A., Rix H. W., 2008, ApJ, 684, 1075

Martin N. F., Ibata R. A., Bellazzini M., Irwin M. J., Lewis G. F., Dehnen W., 2004, MNRAS, 348, 12

Martin N. F., McConnachie A. W., Irwin M., Widrow L. M., Ferguson A. M. N., Ibata R. A., Dubinski J., Babul A., Chapman S., Fardal M., Lewis G. F., Navarro J., Rich R. M., 2009, ArXiv e-prints, astro-ph/0909.0399

Martínez-Delgado D., Peñarrubia J., Gabany R. J., Trujillo I., Majewski S. R., Pohlen M., 2008, ApJ, 689, 184

Martínez-Delgado D., Pohlen M., Gabany R. J., Majewski S. R., Peñarrubia J., Palma C., 2009, ApJ, 692, 955

Mateo M. L., 1998, ARA&A, 36, 435

Mateu C., Vivas A. K., Zinn R., Miller L. R., Abad C., 2009, AJ, 137, 4412

Matteucci F., Brocato E., 1990, ApJ, 365, 539

McConnachie A. W., Chapman S. C., Ibata R. A., Ferguson A. M. N., Irwin M. J., Lewis G. F., Tanvir N. R., Martin N., 2006, ApJ, 647, L25

McConnachie A. W., Irwin M. J., 2006, MNRAS, 365, 902

McConnachie A. W., Irwin M. J., Ibata R. A., Dubinski J., Widrow L. M., Martin N. F., Côté P., Dotter A. L., Navarro J. F., Ferguson A. M. N., Puzia T. H., Lewis G. F., Babul A., Barmby P., Bienaymé O., Chapman S. C., Cockcroft R., Collins M. L. M., Fardal M. A., Harris W. E., Huxor A., Mackey A. D., Peñarrubia J., Rich R. M., Richer H. B., Siebert A., Tanvir N., Valls-Gabaud D., Venn K. A., 2009, Nature, 461, 66

McGaugh S. S., Wolf J., 2010, Local group dwarf spheroidals: Correlated deviations from the baryonic tully-fisher relation

Merrett H. R., Merrifield M. R., Douglas N. G., Kuijken K., Romanowsky A. J., Napolitano N. R., Arnaboldi M., Capaccioli M., Freeman K. C., Gerhard O., Coccato L., Carter D., Evans N. W., Wilkinson M. I., Halliday C., Bridges T. J., 2006, MNRAS, 369, 120

Meza A., Navarro J. F., Abadi M. G., Steinmetz M., 2005, MNRAS, 359, 93

Mo H. J., Mao S., White S. D. M., 1998, MNRAS, 295, 319

Moore B., Ghigna S., Governato F., Lake G., Quinn T., Stadel J., Tozzi P., 1999, ApJ, 524,

Morrison H. L., 1993, AJ, 106, 578

Morrison H. L., Helmi A., Sun J., Liu P., Gu R., Norris J. E., Harding P., Kinman T. D., Kepley A. A., Freeman K. C., Williams M., Van Duyne J., 2009, ApJ, 694, 130

Morrison H. L., Mateo M., Olszewski E. W., Harding P., Dohm-Palmer R. C., Freeman K. C., Norris J. E., Morita M., 2000, AJ, 119, 2254

Morrison H. L., Norris J., Mateo M., Harding P., Olszewski E. W., Shectman S. A., Dohm-Palmer R. C., Helmi A., Freeman K. C., 2003, AJ, 125, 2502

Morrison H. L., Olszewski E. W., Mateo M., Norris J. E., Harding P., Dohm-Palmer R. C., Freeman K. C., 2001, AJ, 121, 283

Narlikar J. V., Padmanabhan T., 1991, ARA&A, 29, 325

Navarro J. F., Abadi M. G., Venn K. A., Freeman K. C., 2010a, ArXiv e-prints, astro-ph/1009.0020

Navarro J. F., Frenk C. S., White S. D. M., 1996, ApJ, 462, 563

—, 1997, ApJ, 490, 493

Navarro J. F., Ludlow A., Springel V., Wang J., Vogelsberger M., White S. D. M., Jenkins A., Frenk C. S., Helmi A., 2008, ArXiv e-prints, astro-ph/0810.1522

—, 2010b, MNRAS, 402, 21

Neto A. F., Gao L., Bett P., Cole S., Navarro J. F., Frenk C. S., White S. D. M., Springel V., Jenkins A., 2007, MNRAS, 381, 1450

Newberg H. J., Yanny B., 2006, Journal of Physics Conference Series, 47, 195

Newberg H. J., Yanny B., Grebel E. K., Hennessy G., Ivezić v. Z., Martinez-Delgado D., Odenkirchen M., Rix H. W., Brinkmann J., Lamb D. Q., Schneider D. P., York D. G., 2003, ApJ, 596, L191

Newberg H. J., Yanny B., Rockosi C., Grebel E. K., Rix H. W., Brinkmann J., Csabai I., Hennessy G., Hindsley R. B., Ibata R., Ivezić Z., Lamb D., Nash E. T., Odenkirchen M., Rave H. A., Schneider D. P., Smith J. A., Stolte A., York D. G., 2002, ApJ, 569, 245

Niederste-Ostholt M., Belokurov V., Evans N. W., Peñarrubia J., 2010, ApJ, 712, 516

Nissen P. E., Schuster W. J., 2010, åp, 511, Norris J. E., Wyse R. F. G., Gilmore G., Yong D., Frebel A., Wilkinson M. I., Belokurov V., Zucker D. B., 2010, ApJ, 723, 1632

Okamoto T., Frenk C. S., 2009, MNRAS, 399, L174

Okamoto T., Frenk C. S., Jenkins A., Theuns T., 2009, ArXiv e-prints, astro-ph/0909.0265

Okamoto T., Gao L., Theuns T., 2008, MNRAS, 390, 920

Oort J. H., 1926, Publications of the Kapteyn Astronomical Laboratory Groningen, 40, 1

—, 1927, Bull. Astron. Inst. Netherlands, 3, 275

Parkinson H., Cole S., Helly J., 2008, MNRAS, 383, 557

Parry O. H., Eke V. R., Frenk C. S., 2009, MNRAS, 396, 1972

Peacock J. A., 1999, Cosmological Physics. Cambridge University Press

Peacock J. A., Dodds S. J., 1994, MNRAS, 267, 1020

Peñarrubia J., McConnachie A., Babul A., 2006, ApJ, 650, L33

Peñarrubia J., McConnachie A. W., Navarro J. F., 2008a, ApJ, 672, 904

Peñarrubia J., Navarro J. F., McConnachie A. W., 2008b, ApJ, 673, 226

Peñarrubia J., Navarro J. F., McConnachie A. W., Martin N. F., 2009, ApJ, 698, 222

Perryman M. A. C., de Boer K. S., Gilmore G., Høg E., Lattanzi M. G., Lindegren L., Luri X., Mignard F., Pace O., de Zeeuw P. T., 2001, åp, 369, 339

Power C., Navarro J. F., Jenkins A., Frenk C. S., White S. D. M., Springel V., Stadel J., Quinn T., 2003, MNRAS, 338, 14

Press W. H., Schechter P., 1974, ApJ, 187, 425

Pritchet C. J., van den Bergh S., 1994, AJ, 107, 1730

Purcell C. W., Bullock J. S., Kazantzidis S., 2010, MNRAS, 404, 1711

Quinn P. J., 1984, ApJ, 279, 596

Quinn P. J., Hernquist L., Fullagar D. P., 1993, ApJ, 403, 74

Re Fiorentin P., Helmi A., Lattanzi M. G., Spagna A., 2005, A&A, 439, 551

Read J. I., Lake G., Agertz O., Debattista V. P., 2008, MNRAS, 389, 1041

Revaz Y., Jablonka P., Sawala T., Hill V., Letarte B., Irwin M., Battaglia G., Helmi A., Shetrone M. D., Tolstoy E., Venn K. A., 2009, åp, 501, 189

Richardson J. C., Ferguson A. M. N., Mackey A. D., Irwin M. J., Chapman S. C., Huxor A., Ibata R. A., Lewis G. F., Tanvir N. R., 2009, MNRAS, 396, 1842

Robertson B., Bullock J. S., Font A. S., Johnston K. V., Hernquist L., 2005, ApJ, 632, 872

Rocha-Pinto H. J., Majewski S. R., Skrutskie M. F., Crane J. D., Patterson R. J., 2004, ApJ, 615, 732

Roederer I. U., 2009, AJ, 137, 272

Roman N. G., 1954, AJ, 59, 307

Roychowdhury S., Chengalur J. N., Begum A., Karachentsev I. D., 2010, MNRAS, 404,

Ryan S. G., Norris J. E., 1991, AJ, 101, 1865

Sackett P. D., Morrisoni H. L., Harding P., Boroson T. A., 1994, Nature, 370, 441

Sales L. V., Helmi A., Abadi M. G., Brook C. B., Gómez F. A., Roˇ skar R., Debattista V. P., House E., Steinmetz M., Villalobos Á., 2009, MNRAS, 400,

Sales L. V., Navarro J. F., Abadi M. G., Steinmetz M., 2007a, MNRAS, 379, 1475

—, 2007b, MNRAS, 379, 1464

Sandage A., 1990, JRASC, 84, 70

Sawala T., Guo Q., Scannapieco C., Jenkins A., White S. D. M., 2010a, ArXiv e-prints, astro-ph/1003.0671

Sawala T., Scannapieco C., Maio U., White S., 2010b, MNRAS, 402, 1599

Scheiner J., 1899, ApJ, 9, 149

Schlaufman K. C., Rockosi C. M., Allende Prieto C., Beers T. C., Bizyaev D., Brewington H., Lee Y. S., Malanushenko V., Malanushenko E., Oravetz D., Pan K., Simmons A., Snedden S., Yanny B., 2009a, ApJ, 703, 2177

Schlaufman K. C., Rockosi C. M., Beers T. C., Bizyaev D., Brewington H., Lee Y. S., Malanushenko V., Malanushenko E., Oravetz D., Pan K., Simmons A., Snedden S., Yanny B., 2009b, ArXiv e-prints, astro-ph/0908.2627

Schöerck T., Christlieb N., Cohen J. G., Beers T. C., Shectman S., Thompson I., McWilliam A., Bessell M. S., Norris J. E., Melendez J., Solange Ramirez S., Haynes D., Cass P., Hartley M., Russell K., Watson F., Zickgraf F., Behnke B., Fechner C., Fuhrmeister B., Barklem P. S., Edvardsson B., Frebel A., Wisotzki L., Reimers D., 2008, ArXiv e-prints, astro-ph/0809.1172

Schweizer F., 1980, ApJ, 237, 303

Schweizer F., Seitzer P., 1992, AJ, 104, 1039

Searle L., Zinn R., 1978, ApJ, 225, 357

Sesar B., Ivezić v. Z., Lupton R. H., Jurić M., Gunn J. E., Knapp G. R., DeLee N., Smith J. A., Miknaitis G., Lin H., Tucker D., Doi M., Tanaka M., Fukugita M., Holtzman J., Kent S., Yanny B., Schlegel D., Finkbeiner D., Padmanabhan N., Rockosi C. M., Bond N., Lee B., Stoughton C., Jester S., Harris H., Harding P., Brinkmann J., Schneider D. P., York D., Richmond M. W., Vanden Berk D., 2007, AJ, 134, 2236

Sesar B., Vivas A. K., Duffau S., Ivezić v. Z., 2010, ApJ, 717, 133

Shang Z., Zheng Z., Brinks E., Chen J., Burstein D., Su H., Byun Y. I., Deng L., Deng Z., Fan X., Jiang Z., Li Y., Lin W., Ma F., Sun W. H., Wills B., Windhorst R. A., Wu H., Xia X., Xu W., Xue S., Yan H., Zhou X., Zhu J., Zou Z., 1998, ApJ, 504, L23

Shapley H., 1918, ApJ, 48, 154

—, 1919, ApJ, 49, 311

Sharma S., Johnston K. V., 2009, ApJ, 703, 1061

Sharma S., Johnston K. V., Majewski S. R., Muñoz R. R., Carlberg J. K., Bullock J., 2010, ArXiv e-prints, astro-ph/1009.0924

Shetrone M. D., Côté P., Sargent W. L. W., 2001, ApJ, 548, 592

Simon J. D., Geha M., 2007, ApJ, 670, 313

Sirko E., Goodman J., Knapp G. R., Brinkmann J., Ivezić v. Z., Knerr E. J., Schlegel D., Schneider D. P., York D. G., 2004, AJ, 127, 914

Skrutskie M. F., Cutri R. M., Stiening R., Weinberg M. D., Schneider S., Carpenter J. M., Beichman C., Capps R., Chester T., Elias J., Huchra J., Liebert J., Lonsdale C., Monet D. G., Price S., Seitzer P., Jarrett T., Kirkpatrick J. D., Gizis J. E., Howard E., Evans T., Fowler J., Fullmer L., Hurt R., Light R., Kopan E. L., Marsh K. A., McCallon H. L., Tam R., Van Dyk S., Wheelock S., 2006, AJ, 131, 1163

Smith M. C., Evans N. W., Belokurov V., Hewett P. C., Bramich D. M., Gilmore G., Irwin M. J., Vidrih S., Zucker D. B., 2009a, MNRAS, 1376

Smith M. C., Ruchti G. R., Helmi A., Wyse R. F. G., Fulbright J. P., Freeman K. C., Navarro J. F., Seabroke G. M., Steinmetz M., Williams M., Bienaymé O., Binney J., Bland-Hawthorn J., Dehnen W., Gibson B. K., Gilmore G., Grebel E. K., Munari U., Parker Q. A., Scholz R. D., Siebert A., Watson F. G., Zwitter T., 2007, MNRAS, 379, 755

Smith M. C., Wyn Evans N., An J. H., 2009b, ApJ, 698, 1110

Smith R. W., 1985, in IAU Symposium, Vol. 106, The Milky Way Galaxy, H. van Woerden R. J. Allen . W. B. B., ed., p. 43

Somerville R. S., 2002, ApJ, 572,

Sommer-Larsen J., Zhen C., 1990, MNRAS, 242, 10

Spergel D. N., Verde L., Peiris H. V., Komatsu E., Nolta M. R., Bennett C. L., Halpern M., Hinshaw G., Jarosik N., Kogut A., Limon M., Meyer S. S., Page L., Tucker G. S., Weiland J. L., Wollack E., Wright E. L., 2003, ApJS, 148, 175

Springel V., 2005, MNRAS, 364, 1105

Springel V., Wang J., Vogelsberger M., Ludlow A., Jenkins A., Helmi A., Navarro J. F., Frenk C. S., White S. D. M., 2008a, MNRAS, 391, 1685

Springel V., White S. D. M., Frenk C. S., Navarro J. F., Jenkins A., Vogelsberger M., Wang J., Ludlow A., Helmi A., 2008b, Nature, 456, 73

Springel V., White S. D. M., Jenkins A., Frenk C. S., Yoshida N., Gao L., Navarro J., Thacker R., Croton D., Helly J., Peacock J. A., Cole S., Thomas P., Couchman H., Evrard A., Colberg J., Pearce F., 2005, Nature, 435, 629

Springel V., White S. D. M., Tormen G., Kauffmann G., 2001, MNRAS, 328, 726

Starkenburg E., Helmi A., Morrison H. L., Harding P., van Woerden H., Mateo M., Olszewski E. W., Sivarani T., Norris J. E., Freeman K. C., Shectman S. A., Dohm-Palmer R. C., Frey L., Oravetz D., 2009, ApJ, 698, 567

Strigari L. E., Bullock J. S., Kaplinghat M., Diemand J., Kuhlen M., Madau P., 2007, ApJ, 669, 676

Strigari L. E., Bullock J. S., Kaplinghat M., Simon J. D., Geha M., Willman B., Walker M. G., 2008, Nature, 454, 1096

Stringer M., Cole S., Frenk C. S., 2010, MNRAS, 404, 1129

Tal T., van Dokkum P. G., Nelan J., Bezanson R., 2009, AJ, 138, 1417

Tanaka M., Chiba M., Komiyama Y., Guhathakurta P., Kalirai J. S., Iye M., 2009, ArXiv e-prints, astro-ph/0908.0245

—, 2010, ApJ, 708, 1168

Tegmark M., Silk J., Rees M. J., Blanchard A., Abel T., Palla F., 1997, ApJ, 474, 1

Tinsley B. M., 1979, ApJ, 229, 1046

Tissera P. B., White S. D. M., Pedrosa S., Scannapieco C., 2010, MNRAS, 406, 922

Tollerud E. J., Bullock J. S., Strigari L. E., Willman B., 2008, ApJ, 688, 277

Tolstoy E., Hill V., Tosi M., 2009, ARA&A, 47, 371

Tolstoy E., Venn K. A., Shetrone M., Primas F., Hill V., Kaufer A., Szeifert T., 2003, AJ, 125, 707

Toth G., Ostriker J. P., 1992, ApJ, 389, 5

Tremonti C. A., Heckman T. M., Kauffmann G., Brinchmann J., Charlot S., White S. D. M., Seibert M., Peng E. W., Schlegel D. J., Uomoto A., Fukugita M., Brinkmann J., 2004, ApJ, 613, 898

Unavane M., Wyse R. F. G., Gilmore G., 1996, MNRAS, 278, 727

van Dokkum P. G., 2005, AJ, 130, 2647

Velazquez H., White S. D. M., 1999, MNRAS, 304, 254

Venn K. A., Irwin M., Shetrone M. D., Tout C. A., Hill V., Tolstoy E., 2004, AJ, 128, 1177

Vivas A. K., Zinn R., 2006, AJ, 132, 714

Vogelsberger M., Helmi A., Springel V., White S. D. M., Wang J., Frenk C. S., Jenkins A., Ludlow A., Navarro J. F., 2009, MNRAS, 395, 797

Walker M. G., Mateo M., Olszewski E. W., Peñarrubia J., Wyn Evans N., Gilmore G., 2009a, ApJ, 704, 1274

—, 2009b, ArXiv e-prints, astro-ph/0906.0341

Walker M. G., McGaugh S. S., Mateo M., Olszewski E. W., Kuzio de Naray R., 2010, ApJ, 717,

Wang J., Navarro J. F., Frenk C. S., White S. D. M., Springel V., Jenkins A., Helmi A., Ludlow A., Vogelsberger M., 2010, ArXiv e-prints, astro-ph/1008.5114

Watkins L. L., Evans N. W., An J. H., 2010, MNRAS, 406, 264

Watkins L. L., Evans N. W., Belokurov V., Smith M. C., Hewett P. C., Bramich D. M., Gilmore G. F., Irwin M. J., Vidrih S., Wyrzykowski . L., Zucker D. B., 2009, MNRAS, 398, 1757

White S. D. M., Frenk C. S., 1991, ApJ, 379, 52

White S. D. M., Rees M. J., 1978, MNRAS, 183, 341

White S. D. M., Springel V., 2000, in The First Stars, Weiss A., Abel T. G., Hill V., eds., p. 327

Wolf J., Martinez G. D., Bullock J. S., Kaplinghat M., Geha M., Munoz R. R., Simon J. D., Avedo F. F., 2009, ArXiv e-prints, astro-ph/0908.2995

Wolf J., Martinez G. D., Bullock J. S., Kaplinghat M., Geha M., Muñoz R. R., Simon J. D., Avedo F. F., 2010, MNRAS, 406, 1220

Wright T., 1750, An Original Theory or New Hypothesis of the Universe. Publisher unknown, London

Xue X. X., Rix H. W., Zhao G., 2009, Research in Astronomy and Astrophysics, 9, 1230

Xue X. X., Rix H. W., Zhao G., Re Fiorentin P., Naab T., Steinmetz M., van den Bosch F. C., Beers T. C., Lee Y. S., Bell E. F., Rockosi C., Yanny B., Newberg H., Wilhelm R., Kang X., Smith M. C., Schneider D. P., 2008, ApJ, 684, 1143

Yanny B., Newberg H. J., Grebel E. K., Kent S., Odenkirchen M., Rockosi C. M., Schlegel D., Subbarao M., Brinkmann J., Fukugita M., Ivezic v. Z., Lamb D. Q., Schneider D. P., York D. G., 2003, ApJ, 588, 824

Yanny B., Newberg H. J., Kent S., Laurent-Muehleisen S. A., Pier J. R., Richards G. T., Stoughton C., Anderson Jr. . J. E., Annis J., Brinkmann J., Chen B., Csabai I., Doi M., Fukugita M., Hennessy G. S., Ivezić v. Z., Knapp G. R., Lupton R., Munn J. A., Nash T., Rockosi C. M., Schneider D. P., Smith J. A., York D. G., 2000, ApJ, 540, 825

Yanny B., Rockosi C., Newberg H. J., Knapp G. R., Adelman-McCarthy J. K., Alcorn B., Allam S., Allende Prieto C., An D., Anderson K. S. J., Anderson S., Bailer-Jones C. A. L., Bastian S., Beers T. C., Bell E., Belokurov V., Bizyaev D., Blythe N., Bochanski J. J., Boroski W. N., Brinchmann J., Brinkmann J., Brewington H., Carey L., Cudworth K. M., Evans M., Evans N. W., Gates E., Gänsicke B. T., Gillespie B., Gilmore G., Gomez-Moran A. N., Grebel E. K., Greenwell J., Gunn J. E., Jordan C., Jordan W., Harding P., Harris H., Hendry J. S., Holder D., Ivans I. I., Ivezič v. Z., Jester S., Johnson J. A., Kent S. M., Kleinman S., Kniazev A., Krzesinski J., Kron R., Kuropatkin N., Lebedeva S., Lee Y. S., Leger R. F., Lépine S., Levine S., Lin H., Long D. C., Loomis C., Lupton R., Malanushenko O., Malanushenko V., Margon B., Martinez-Delgado D., McGehee P., Monet D., Morrison H. L., Munn J. A., Neilsen E. H., Nitta A., Norris J. E., Oravetz D., Owen R., Padmanabhan N., Pan K., Peterson R. S., Pier J. R., Platson J., Fiorentin P. R., Richards G. T., Rix H. W., Schlegel D. J., Schneider D. P., Schreiber M. R., Schwope A., Sibley V., Simmons A., Snedden S. A., Smith J. A., Stark L., Stauffer F., Steinmetz M., Stoughton C., Subba Rao M., Szalay A., Szkody P., Thakar A. R., Thirupathi S., Tucker D., Uomoto A., Vanden Berk D., Vidrih S., Wadadekar Y., Watters S., Wilhelm R., Wyse R. F. G., Yarger J., Zucker D., 2009, AJ, 137, 4377

Yoachim P., Dalcanton J. J., 2005, ApJ, 624, 701

—, 2008, ApJ, 682, 1004

Zibetti S., Ferguson A. M. N., 2004, MNRAS, 352,

Zibetti S., White S. D. M., Brinkmann J., 2004, MNRAS, 347, 556

Zinn R., 1993, in The Globular Cluster-Galaxy Connection, Smith G. H., Brodie J. P., eds., Vol. 48, p. 38

Zolotov A., Willman B., Brooks A. M., Governato F., Brook C. B., Hogg D. W., Quinn T., Stinson G., 2009, ApJ, 702, 1058

Colophon

The main text of this thesis is set in Pagella, created by the TeX Gyre project[*], modelled on Palatino (Zapf). The LaTeX style has been modified from the `phdthesis` style created by J. Stevens[†]. Excluding front-matter there are 163 pages.

The work in this thesis made extensive use of the COSMA-III (OCTOR) supercomputer at the University of Durham, managed by Lydia Heck. As well as COSMA, the machines of the Leibniz Computing Centre (Garching, Germany) and the LOFAR 'STELLA' machine (University of Groningen) were used to run the original Aquarius simulations.

Most figures produced by the author were created with the Python `matplotlib` package. The skyplots shown in Chapter 4 were made with `HEALPy` implementation of `HEALPix`[‡] (Gorski et al. 2005). Extensive use was made of the `IPython` environment. The maintainers of Python, Ruby, Linux, LaTeX and their many open-source packages are gratefully acknowledged.

If you're not reading it already, then an electronic copy of this thesis with amendments, corrections and maybe even one or two additions can be obtained directly from the author (see `http://www.mpa-garching.mpg.de/~acooper`).

歡言得所憩
美酒聊共揮
長歌吟松風
曲盡河星稀
我醉君復樂
陶然共忘機

– 李白

---

[*] `http://www.gust.org.pl/projects/e-foundry/tex-gyre/`

[†] `http://www-ra.phys.utas.edu.au/~jstevens/code_thesis_style.html`

[‡] `http://healpix.jpl.nasa.gov`